universität wien

DISSERTATION

Titel der Dissertation

„Hysteresis Properties of Soft Magnetic Materials“

Verfasser

Nasir Mehboob

angestrebter akademischer Grad

Doktorin der Naturwissenschaften (Dr. rer.nat.)

Wien, 2012

Studienkennzahl lt. Studienblatt:	A 091 411
Dissertationsgebiet lt. Studienblatt:	411 Physik
Betreuerin / Betreuer:	Univ. Prof. Dipl.-Ing. Dr. Techn. Roland Grössinger

Abstract

Soft magnetic materials belong to the most important and most investigated materials in modern world technology. Particularly in the last years the interest was focused on nano size particles (< 100 nm) of magnetic materials because of their unique magnetic properties and potential for many applications. In order to understand these material better the frequency dependence of the Hysteresis loop was measured and analyzed for all kind of soft magnetic materials.

For determining the hysteresis the magnetization M (or the induction B) has to be measured as a function of the applied magnetic field *H*. Hysteresis loops were measured by an induction method on ring shaped samples. Alternating periodic magnetic (*ac*) field is generated (where *H(t)* can be chosen) with a primary coil. A signal proportional to *dB/dt* is measured on a secondary coil. The hysteresis B(H) is then registered with a full automized hysteresisgraph using a Labview program. Temperature dependent hysteresis can be obtained in a temperature controlled furnace and the sample temperature is determined using a Pt 100 sensor.

This work concentrates on the investigation of the effect of "Severe Plastic Deformation" on Hysteresis properties of various kinds of soft magnetic materials. Therefore in this thesis the experimental part consist of hysteresis loop measurements of severe plastic deformed (SPD) soft magnetic materials such as Fe and its alloy with Si, Co, Al, Ga and steel. These samples were SPD treated by a technique which is the so-called high pressure torsion (HPT). The aim of the investigation of SPD soft magnetic materials is to study and analyze the deformation effect on the magnetic properties such as coercivity, permeability, remanence and also on the shape (which means the area) of the hysteresis loop. Additionally an analytical model based on the Maxwell equation and the material parameters (electrical resistivity) was developed in order to describe the change of the coercivity with frequency and also a dynamic correlation between the coercivity and the permeability of the material was deduced. Losses are calculated by integrating the area

of hysteresis loop and then analyzed by a general second order polynomial equation. The fitted coefficients are compared with similar results which are based on well established models for Fe-Si electro-steel e.g. Mosses, Bertotti.

Hysteresis loops of Fe, Fe-3 wt%Si, Fe-6.5 wt%Si, and Fe-17 wt%Co, and Ni were measured in the frequency range from 0.25 Hz to 1 kHz at room temperature up to 220°C on ring shaped samples. All the samples were investigated in the as cast as well as HPT-deformed state which was achieved at liquid nitrogen (N_2) room temperature and also at 450°C (723 K). The as cast sample (un-deformed) was also investigated as a reference sample.

Soft magnetic material with high magnetostriction $Fe_{100-x}Al_x$ ($15 \leq x \leq 25$) were studied after a Severe Plastic Deformation (SPD) treatment at room temperatures and liquid nitrogen temperature. The hysteresis loops on ring shaped samples were measured in the frequency range from 0.25 Hz to 1 kHz at room temperature up to 200°C. Moreover the hysteresis loops of different heat treated $Fe_{81}Ga_{19}$ ring shaped samples were measured and analysed as a function of the frequency.

Pearlitic rail steel R260 was investigated magnetically by hysteresis measurements. The samples were plastically deformed by HPT technique with shear rate ϵ= (0, 1, 2, 4, 8, 16) at room temperature.

Frequency dependence of coercivity data as well as frequency dependence of losses of all samples are analyzed and explained by different eddy current based models. This delivers a good understanding of the frequency behavior of soft magnetic materials. From these models also a medium average relative permeability (which is reciprocal to the coercivity) was calculated and compared with experimental data. Severe Plastic Deformation causes generally an increase of the coercivity as well as a reduced frequency dependence. Similar is valid for the frequency dependence of the losses.

Kurzfassung

Weich magnetische Materialien gehören zu den wichtigsten und am häufigsten untersuchten Werkstoffen moderner Technologie. In den letzten Jahren hat sich das Interesse speziell auf magnetische "Nano-Teilchen" (< 100 nm) konzentriert, da diese einmalige magnetische Eigenschaften aufweisen und daher potentiell interessant sind für viele Anwendungen. Um diese Werkstoffe besser zu verstehen, wurde die Frequenzabhängigkeit der Hysteresisschleife von verschiedensten weichmagnetischen Materialien gemessen und analysiert.

Um die Hysteresisschleife zu bestimmen, muß die Magnetisierung M (oder Induktion B) als Funktion des angelegten Magnetfeldes H gemessen werden. Die Hysteresisschleife wird mittels Induktionsmethode an ringförmigen Proben gemessen. Es wird ein zeitlich, periodisch veränderliches Feld mit einer Primärspule erzeugt (wobei *H(t)* wählbar ist). An einer Sekundärspule wird dann ein Signal das proportional zu *dB/dt* ist, gemessen. Die Hysteresisschleife B(H) wird mit einem vollautomatisiertem Hysteresograph der mit einem Labview Programm bedient wird, registriert. Die Temperaturabhängigkeit der Hysteresisschleife kann in einem temperaturgeregelten Ofen gemessen werden, wobei die Probentemperatur mit einem Pt 100 Sensor bestimmt wird.

Diese Arbeit konzentriert sich auf die Untersuchung des Einflusses der "Severe Plastic Deformation" (Starke plastische Verformung) auf die Hysteresiseigenschaften verschiedener weichmagnetischer Materialien. Daher besteht der experimentelle Teil der Dissertation aus Hysteresisschleifenmessungen an plastisch deformierten weichmagnetischen Materialien wie Fe und seinen Legierungen mit Si, Co, Al, Ga sowie Stahl. Diese Proben wurden mit einer Technik die man Hoch Druck Torsion (HPT) nennt, "SPD" behandelt. Das Ziel der Untersuchung von SPD behandelten weichmagnetischen Materialien ist den Einfluß der Deformation auf magnetische Eigenschaften wie z.B. Koerzitivfeld, Permeabilität, Remanenz sowie auch die Form der Hysteresis (d.h. die Fläche) zu messen und zu analysieren. Ausserdem wurde ein analytisches Modell basierend auf den Maxwell Gleichungen und den Materialparametern (elektrischer Widerstand) entwickelt um die Frequenzabhngigkeit des Koerzitivfeldes sowie auch die dynamische Korrelation mit der

Permeabilität zu beschreiben.

Die Verluste werden mittels Integration der Fläche der Hysteresisschleife berechnet und dann mit einem allgemeinen Polynom 2. Ordnung analysiert. Die gefitteten Koeffizienten werden mit wohlbekannten ähnlichen Resultaten basierend auf Modellen für Fe-Si Elektrostählen verglichen z.B. Moses, Bertotti.

Hysteresisschleifen von Fe, Fe-3 wt%Si, Fe-6.5 wt%Si, und Fe-17 wt%Co, und reinem Ni wurden im Frequenzbereich von 0.25 Hz bis 1 kHz von Raumtemperatur bis 220°C an ringförmigen Proben gemessen. Alle Proben wurden im Ausgangszustand sowie nach einer HPT Verformung bei flüssiger Stickstofftemperatur (N_2), bei Raumtemperatur und auch bei 450°C (723 K) gemessen. Das Material im Ausgangszustand wurde als Referenzprobe untersucht.

Hochmagnetostriktives, weichmagnetisches Material wie $Fe_{100-x}Al_x$ ($15 \leq x \leq 25$) wurde ebenfalls nach einer SPD Verformung bei Raumtemperatur und bei flüssigem Stickstoff (N_2) untersucht. Die Hysteresisschleife an ringförmigen Proben wurde im Frequenzbereich von 0.25 Hz bis 1 kHz von Raumtemperatur bis zu 200°C gemessen. Zusätzlich wurde auch die Frequenzabhängigkeit der Hysteresisschleife an ringförmfgen $Fe_{81}Ga_{19}$ Proben gemessen und analysiert.

Perlitischer Schienenstahl (R260) wurde ebenfalls magnetisch mittels Hysteresismessungen untersucht. Auch diese Proben wurden mittels HPT Methode mit Scherraten von ϵ= (0, 1, 2, 4, 8, 16) bei Raumtemperatur plastisch verformt.

Die Frequenzabhängigkeit des Koerzitivfeldes sowie auch jene der Verluste aller Proben wurde analysiert und mittels verschiedener auf Wirbelströmen basierenden Modellen erklärt. Daraus folgt ein gutes Verständnis des Freqenzverhaltens weichmagnetischer Materialien. Aus diesen Modellen folgte auch eine mittlere relative Permeabilität (die sich reziprok zum Koerzitivfeld verhält) die dann mit experimentellen Daten verglichen wurde. Der Effekt der plastischen Deformation manifestiert sich im Allgemeinen in höheren Koerzitivfeldwerten, aber auch einer geringeren Frequenzabhängigkeit. Ähnliches gilt für die Frequenzabhängigkeit der Verluste.

Contents

1 Introduction **1**

1.1 Ferromagnetism 1

1.2 Types of Magnetic Materials 3

1.2.1 Hard Magnetic Materials 3

1.2.2 Soft Magnetic Materials 4

1.2.2.1 Soft Magnetic Crystalline Materials 6

1.2.2.2 Soft Magnetic Amorphous Materials 6

1.2.3 Magnetization Curves and Hysteresis Loops 7

1.2.4 Frequency Dependence of Losses 9

1.3 Severe Plastic Deformation 12

1.3.1 Effect of Severe Plastic Deformation 14

1.3.2 Effect of HPT Deformation Temperature 16

1.4 Tasks for the present work 17

2 Experimental **20**

2.1 Severe Plastic Deformation (SPD) Set-up 20

2.2 Magnetic Measurement Methods 22

2.2.1 Measurements on Hysteresigraph 22

2.3 Magnetic Measurements in Toroid 23

2.3.1 Different Configurations of Windings 25

2.3.2 Effect of Winding Density 26

2.3.3 Effect of Sample Geometry on Magnetic Hysteresis and Optimization of Geometry parameters 27
2.3.4 Pulse Field Magnetometer 30
2.3.5 Vibrating Sample Magnetometer VSM 31

3 Frequency Dependence of the Coercivity Modeled by Eddy Currents 33

3.1 Analysis of the Frequency Dependence of Coercivity: 38

4 Magnetic studies of Severe Plastically Deformed Soft-Magnetic Materials 41

4.1 Microstructure at Different Processing Temperatures 44
4.2 Microhardness Measurements 45
4.3 Magnetic Hysteresis Measurements of HPT Deformed Fe and Fe-Si/Co Alloys 46
4.3.1 Temperature Dependence of Hysteresis 59
4.3.2 Analysis of the Frequency Dependence of Coercivity 61
4.3.3 Analysis of the Frequency Dependence of Losses 68
4.4 Hysteresis Measurements of HPT-Deformed Ni 71
4.4.1 Temperature Dependence of Hysteresis 77
4.4.2 Analysis of the Frequency Dependence of Coercivity 77
4.4.3 Analysis of the Frequency Dependence of Losses 80
4.5 Discussion and Conclusions 81

5 Magnetic Hysteresis Measurements of High Magnetostrictive Materials 84

5.1 Hysteresis Measurement of HPT Treated Fe-Al 85
5.1.1 Temperature Dependence of Hysteresis 91
5.1.2 Analysis of the Frequency Dependence of Coercivity at room temperature 92
5.1.3 Analysis of the Frequency Dependence of Losses 96
5.2 Quenched and Annealed Fe-Ga 99
5.2.1 Hysteresis Measurements of Quenched and Annealed $Fe_{81}Ga_{19}$ . . . 99
5.2.2 Analysis of the Frequency Dependence of Coercivity 102

5.2.3 Analysis of the Frequency Dependence of Losses 106
5.3 Discussion and Conclusions 108

6 Magnetic and Microstructural Investigation of SPD Pearlitic Steel 110

6.1 Microstructure 111
6.2 Magnetic Hysteresis Measurements of SPD Pearlitic Steel R260 112
6.2.1 Analysis of the Frequency Dependence of Coercivity 116
6.2.2 Analysis of the Frequency Dependence of Losses 119
6.3 Conclusions 121

7 Magnetic Measurements of Pipeline Steels 122

7.1 Microstructure 123
7.2 Magnetic Hysteresis of X52, X56 and X60 Pipeline Steels 125
7.2.1 Analysis of the Frequency Dependence of Coercivity 133
7.2.2 Analysis of the Frequency Dependence of Losses 135
7.3 Conclusions 137

8 Magnetization and Microstructural Investigation of Resin coated Fe-Powder 138

8.1 Microstructure of Resin coated Fe-Powder 139
8.2 Magnetization Measurements of Resin coated Fe-Powder 140
8.3 Hysteresis Measurements of Resin coated Fe-Powder 143
8.4 Conclusions 149

List of Figures

1.1 (a) Randomly oriented ferromagnetic domains $H_{ext} = 0$ (b) Oriented ferromagnetic domains. 2

1.2 A magnetic hysteresis loop for soft and hard ferromagnetic materials. . . . 3

1.3 Hysteresis loop of ferromagnetic materials. 7

1.4 Separation of core losses. 10

1.5 Schematic diagram of: (a) HPT (b) ECAP 13

1.6 BSE images of HPT deformed P800 in radial direction; the samples were deformed at different temperatures (see insets) [1]. 17

1.7 TEM micrographs of P800 deformed at low temperatures (293 K and 77 K) [1]. 17

2.1 Photograph of HPT set up [2] 21

2.2 Schematic illustration of the used HPT equipment for hot (left) and cold (right) processing [3]. 21

2.3 Diagram of the LabVIEW controlled hysteresigraph. 22

2.4 Hysteresis loops at different configurations of windings. “a”, “b”, “c”, “d”, corresponds to the different configurations mentioned in text. 26

2.5 (a) Hysteresis loops measured at 1 Hz on pure Fe with different numbers of primary windings (b) Magnetization as a function of the number of the primary windings (N_1). 27

2.6 Ring and Window frame. 28

2.7 Hysteresis loops measured on the ring and the window frame samples. . . . 30

2.8 Block diagram of the pulse field magnetometer [4]. 31

2.9 Pulse field magnetometer photograph available in TU Wien [4]. 31
2.10 Block diagram of the vibrating sample magnetometer (VSM) [4]. 32
2.11 Vibrating sample magnetometer (VSM) photograph available in TU Wien [4]. 32

3.1 Schematic diagram for Eddy current model. 34
3.2 Comparison between model and experimental curve of H_c versus *f*. Solid line (experimental) and dotted line (model) 36
3.3 *dB/dt* versus *H(t)* loop and triangular form of field *H(t)*. 40

4.1 Grain size maps for Fe-17 wt% Co alloy correspond (a) 723 K, (b) 293 K and (c) 77 K [5]. 44
4.2 Vickers hardness as a function of the HPT processing temperature. 45
4.3 The frequency dependence hysteresis loops of HPT-trated pure Fe (a) un-deformed, (b) deformed at 300 K (RT), (c) deformed at 723 K and (d) deformed at liquid (N_2) temperature. 48
4.4 The frequency dependence hysteresis loops HPT-treated Fe-3 wt%Si (a) un-deformed, (b) deformed at 300 K (RT), (c) deformed at 723 K and (d) deformed at liquid (N_2) temperature. 49
4.5 The frequency dependence hysteresis loops of HPT-treated Fe-6.5 wt%Si (a) un-deformed, (b) deformed at 300 K (RT), (c) deformed at 723 K and (d) deformed at liquid (N_2) temperature. 50
4.6 The frequency dependence hysteresis loops of HPT-treated Fe-17 wt%Co (a) un-deformed, (b) deformed at 300 K (RT), (c) deformed at 723 K, and (d) deformed at liquid (N_2) temperature. 51
4.7 Dependence of the zero extrapolated coercivity versus the HPT-deformation temperature for: pure Fe, Fe-3 wt%Si, Fe-6.5 wt%Si, Fe-17 wt%Co (P800) and Ni. 51
4.8 Frequency versus coercivity of HPT-treated (a) Fe, (b) Fe-3 wt%Si, (c) Fe-6.5 wt%Si and (d) Fe-17 wt%Co. 52

4.9 Coercivity as a function of the grain size (D) for Fe, Fe-3 wt%Si, Fe-6.5 wt%Si, Fe-17 wt%Co and Ni, after HPT-deformation [5]. 53
4.10 Relative permeability versus the field for HPT-treated Fe samples at room temperature. 55
4.11 Relative permeability versus the field for HPT-treated Fe-3 wt%Si samples at room temperature. 56
4.12 Relative permeability versus the field for HPT-treated Fe-6.5 wt%Si samples at room temperature. 57
4.13 Relative permeability versus the field for HPT-treated Fe-17 wt%Co (P800) samples at room temperature. 58
4.14 Temperature dependent coercivity of HPT-treated (a) Fe, (b) Fe-3 wt%Si and (c) Fe-6.5 wt%Si samples. 60
4.15 Relative initial permeability versus Temperature of HPT-treated (a) Fe, (b) Fe-3 wt%Si and (c) Fe-6.5 wt%Si samples. 61
4.16 Fitting on the frequency dependent coercivity of HPT-treated Fe at different temperature by Eqs. (4.3) and (4.4) (a) un-deformed, (b) deformed at RT, (c) deformed at 450°C and (d) deformed at N_2. 62
4.17 Fitting on frequency dependent coercivity of HPT-treated samples at room temperature by Eqs. (4.3) and (4.4) (a) Fe, (b) Fe-3 wt%Si, (c) Fe-6.5 wt%Si and (d) Fe-17 wt%Co. 63
4.18 Fitting according to model Eq. 4.7 on the data coercivity verses frequency of HPT-treated Fe, Fe-3 wt%Si, Fe-6.5 wt%Si and Fe-17 wt%Co samples, whereas Δk described the error in k. 67
4.19 Fitting applying Eq. 4.8 on the frequency dependence of the losses; HPT-treated (a) Fe, (b) Fe-3 wt%Si, (c) Fe-6.5 wt%Si and (d) Fe-17 wt%Co samples. 69
4.20 Hysteresis loops of HPT-treated Ni (a) un-deformed, (b) deformed at RT (300 K), (c) deformed at 450°C (723 K) and (d) deformed at liquid N_2 temperature (77 K). 72

4.21 Hysteresis loops of Ni (a) Bulk, (b) HPT deformed and heat treated (420°C for 1 hr) and (c) Nano-crystalline Ni. 73
4.22 Coercivity versus square root of the frequency of (a) HPT-treated Ni and (b) Ni(Bulk), HPT-deformed with heat treatment Ni(HT)$_{HPT}$, nano-crystalline Ni(nc) samples. 74
4.23 Relative permeability versus the field of HPT-treated Ni samples at room temperature. 75
4.24 Relative permeability versus the field (a) Ni(Bulk),(b) HPT-deformed and heat treated Ni(HT)$_{HPT}$ and (c) Nano-crystalline Ni(nc) samples at room temperature. 76
4.25 Temperature dependent (a) coercivity $H_c(T)$, (b) Relative permeability of HPT-Treated Ni 77
4.26 (a)Fitting frequency dependent coercivity for HPT-Treated Ni by Eq. 4.3 and 4.4 (a) at room temperature and (b) 100°C (373 K). 78
4.27 Fitting applying model Eq. (4.7) on the coercivity versus frequency data, indicated by dotted line. 79
4.28 Frequency dependence of the losses calculated by integrated hysteresis loops of HPT treated Ni (dotted line indicate fitting). 80

5.1 Hysteresis loops of HPT-treated Fe-Al system (a) $Fe_{85}Al_{15}$ (RT), (b) $Fe_{85}Al_{15}$ (N_2), (c) $Fe_{80}Al_{20}$ (RT), (d) $Fe_{80}Al_{20}$ (N_2), (e) $Fe_{78}Al_{22}$ (RT), (f) $Fe_{78}Al_{22}$ (N_2), (g) $Fe_{75}Al_{15}$ (RT) and (h) Magnetization as a function of Al concentration. 87
5.2 Coercivity versus square root of frequency of HPT-treated $Fe_{100-x}Al_x$ (x = 15$\leq$ x $\leq$ 25) samples. 88
5.3 Relative permeability versus the field of HPT treated $Fe_{100-x}Al_x$ (x = 15 $\leq$ x $\leq$ 25) samples. 90
5.4 (a) coercivity versus temperature (b) saturation magnetization versus temperature and (c) initial relative permeability versus temperature (K) of HPT treated $Fe_{100-x}Al_x$ (x = 15 $\leq$ x $\leq$ 25) samples. 92

5.5 Fitting applying Eqs. (5.3) and (5.4) on experimental data of coercivity versus frequency of HPT treated $Fe_{100-x}Al_x$ ($15 \leq x \leq 25$) samples. 93
5.6 Fit applying the model Eq. (5.6) on experimental data of the coercivity versus frequency of of HPT-treated $Fe_{100-x}Al_x$ ($15 \leq x \leq 25$) samples. . . 95
5.7 Fitting according to equation (5.8) and (5.9) on the frequency dependence of the losses of HPT-treated $Fe_{100-x}Al_x$ ($15 \leq x \leq 25$) samples. 97
5.8 Hysteresis loop of $Fe_{81}Ga_{19}$ measured at different frequencies: (a) on quenched (Q) and (b) on annealed (A) at room temperature. 100
5.9 Extrapolated coercivity as a function of square root of frequency of $Fe_{81}Ga_{19}$ quenched (Q) and annealed (A) samples. 101
5.10 Relative permeability versus the field at room temperature measured at 0.5 Hz of $Fe_{81}Ga_{19}$ (a) quenched (Q) and (b) annealed (A) samples. 102
5.11 Fitting according to Eqs. 5.3 and 5.4 on experimental data of coercivity versus frequency of quenched and annealed $Fe_{81}Ga_{19}$ samples. 103
5.12 Fitting according to Eq. (5.6) on experimental data of coercivity versus frequency of $Fe_{81}Ga_{19}$ quenched (Q) and annealed (A) samples. 104
5.13 Fitting applying model Eq. 5.12 on the experimental data of the coercivity versus frequency of $Fe_{81}Ga_{19}$ (Q) and (A). 106
5.14 Fitting using Eq. 5.9 on the frequency dependence of losses of $Fe_{81}Ga_{19}$ quenched (Q) and annealed (A) samples. 107

6.1 Microstructure photographs of SPD treated pearlitic steel (R260). 111
6.2 Hysteresis loops of SPD treated pearlitic steel (R260) (a) $P_1(\epsilon=0)$, (b) $P_2(\epsilon=1)$, (c) $P_3(\epsilon=2)$, (d) $P_4(\epsilon=4)$, (e) $P_5(\epsilon=8)$ and (f) $P_6(\epsilon=16)$. 113
6.3 Coercivity versus square root of frequency of SPD treated pearltic steel (R260). 114
6.4 Relative permeability versus the field of SPD treated pearlitic steel (R260) (a) $P_1(\epsilon=0)$, (b) $P_2(\epsilon=1)$, (c) $P_3(\epsilon=2)$,(d) $P_4(\epsilon=4)$, (e) $P_5(\epsilon=8)$ and (f) $P_6(\epsilon=16)$. 115

6.5 Fitting according to Eqs. (3.16) and (3.17) on coercivity versus frequency data of SPD treated pearlitic steel (R260). 117
6.6 Fitting according to Eq. (6.1) on the coercivity versus frequency data of SPD pearlitic steel (R260). 118
6.7 Total losses versus frequency for SPD pearlitic steel (R260) and analyzed by applying Eq.(6.2) shown by dotted line. 120

7.1 Microstructure of a longitudinal (left) and transversal (right) section of X52 (a, b), X56 (c, d) and X60 (e, f). 124
7.2 Hysteresis loops for X52 steel (a) *L*, (b) *M*, (c) *T* and (d) Comparison of texture of X52 at 0.5 Hz. 127
7.3 Hysteresis loops for X56 steel (a) *L*, (b) *M*, (c) *T* and (d) Comparison of texture at 0.5 H. 128
7.4 Hysteresis loops for X60 steel (a) *L*, (b) *M*, (c) *T* and (d) Comparison of texture at 0.5 H. 129
7.5 Coercivity versus square root of frequency of X52, X56, X60. 129
7.6 Relative permeability μ_r versus field *H(t)* for pipeline steel X52 (a) X52 (L), (b) X52 (M), (c) X52 (T). 130
7.7 Relative permeability μ_r versus field *H(t)* for pipeline steel X56 (a) X56 (L), (b) X56 (M) and (c) X56 (T). 131
7.8 Relative permeability μ_r versus field *H(t)* for pipeline steel X60 (a) X60 (L), (b) X60 (M) and (c) X60 (T). 132
7.9 fit according to Eqs.3.16 and 3.17 on coercivity versus frequency of X52, X56, and X60 steel pipeline samples. 133
7.10 Fitting according to Eq. (3.15) on experimental data of coercivity versus frequency of X52, X56, and X60 pipeline steel. 135
7.11 Total losses per cycle with frequency of X52 (L), X56 (L), and X60 (L). The dotted indicates the fitting result. 136

8.1 Microstructure of resin coated Fe-Powder samples (a) S_3, (b) S_8 and (c) S_9. 139

8.2 Magnetization M(H) loops of resin coated Fe-Powder. 141
8.3 Schematic diagram for resin coated Fe-Powder sample to show applied field directions. 141
8.4 Magnetization loops of resin coated Fe-Powder to see demagnetizing effect. 142
8.5 Frequency dependent hysteresis loops of resin coated Fe-Powder samples (a) S_1, (b) S_2, (c) S_3 and (d) S_4. 144
8.6 Frequency dependent hysteresis loops of resin coated Fe-Powder (e) S_5, (f) S_6, (g) S_7, (h) S_8, (i) S_9 and (j) S_{10}. 145
8.7 Hysteresis loops at 0.5 Hz of all resin coated Fe-Powder samples. 146
8.8 Coercivity versus frequency of resin coated Fe-Powder. 146
8.9 Relative permeability versus field of resin coated Fe-powder samples (a) S_1, (b) S_2, (c) S_3 and (d) S_4. 147
8.10 Relative permeability versus field of resin coated Fe-powder samples (e) S_5 (f), S_6, (g) S_8, and (h) S_9. 148

List of Tables

2.1 Geometry Parameters of ring and window frame samples. 29

4.1 HPT parameters as used for the Fe, Fe-3 wt%Si, Fe-6.5 wt%Si, Fe-17wt %Co samples, T_{HPT}-HPT treatment temperature; n-number of turns; t-thickness of sample before HPT; d_o-outer diameter; d_i-inner diameter. . . . 43

4.2 Geometry dimensions and Parameters of HPT-treated Fe, Fe-Si/Co samples as used for the hysteresis measurements. 47

4.3 Magnetic properties of HPT-treated Fe, Fe-3 wt%Si, Fe-6.5 wt%Si and Fe-17 wt%Co samples, the number in (..) indicate the field where μ_{max} was determined. 59

4.4 Fit parameters at different temperatures for HPT treated Fe samples using Eq.4.3; Δa, Δb and Δc describes the error to a, b and c. 64

4.5 Fit parameters at room temperature for HPT-treated Fe-3 wt%Si, Fe-6.5 wt%Si and Fe-17 wt%Co samples using Eq. 4.3; Δa, Δb and Δc describes the error to a, b and c. 65

4.6 Fit parameters at different temperatures for HPT-treated Fe samples using Eq. 4.4; Δd, Δe and Δg describes the error to d, e and g. 65

4.7 Fit parameters at room temperature for HPT-treated, Fe-3 wt%Si, Fe-6.5 wt%Si and Fe-17 wt%Co samples using Eq. 4.4; Δd, Δe and Δg describes the error to d, e and g. 66

4.8 Fit parameters according to model Eq. 4.8 for HPT-treated Fe Fe-3 wt%Si, Fe-6.5 wt%Si and Fe-17 wt%Co samples, where as Δn, Δk describe the error in n, k. 68

4.9 Fit parameters applying Eq. 4.9 for HPT-treated Fe, Fe-Si, Fe-Co samples and the calculated values of B_2 and V_o; ΔW_h, ΔB_1 and ΔB_2 describes the error to ΔW_h, ΔB_1 and ΔB_2. 70

4.10 HPT parameters as used for the Ni samples; T_{HPT}-HPT treatment temperature, n-number of turns; t-thickness of sample; d_o-outer diameter; d_i-inner diameter. 71

4.11 Parameters as used for the hysteresis measurements for pure HPT-treated Ni. N_1-Primary windings, N_2-Secondary windings; $l_{eff}(m)$-Magnetic path length; $A(m^2)$-Cross-sectional area. 71

4.12 Magnetic parameters extracted form the hysteresis loop of HPT-treated Ni and Ni(Bulk), HPT-deformed with heat treated (420°C for 1 hr) Ni(HT)$_{HPT}$ and nano-crystalline Ni(nc) samples. The number in (..) are the field values where μ_{max} was determined. 76

4.13 Fit parameters for HPT treated Ni samples using Eq. 4.13; Δa, Δb and Δc describe the error to a, b and c. 78

4.14 Fit parameters for HPT treated Ni samples using Eq. 4.14; Δd, Δe and Δg describe the error to d, e and g. 79

4.15 Fit parameters by using model (4.7) and calculated permeability at $f = 0$ from $k/[H_c(f)]^n$ for HPT-deformed Ni. Δn and Δk represent errors in n and k. 80

4.16 Parameters obtained by fitting Eq.(4.8) on frequency dependence of the losses of HPT treated Ni. ΔW_h and ΔB_1 and ΔB_2 represent errors in W_h,B_1 and B_2. 81

5.1 *HPT* parameters as used for the Fe-Al samples. d-sample diameter; h-sample height before *HPT*; h_{HPT}-sample height after *HPT* treatment; n-number of turns during deformation; T_{HPT}-treatment temperature. 85

5.2 Parameters as used for the hysteresis measurements. N_1-Primary Windings; N_2-Secondary Windings; $l_{eff}(m)$-Magnetic Path length; $A(m^2)$-Cross-sectional Area. 86

5.3 Magnetic hysteresis Parameters of HPT-treated $Fe_{100-x}Al_x$ (x = 15 ≤ x ≤ 25) samples. 91

5.4 Fitting parameters applying Eq. (5.3) on the frequency dependence of the coercivity for HPT treated $Fe_{100-x}Al_x$ (15 ≤ x ≤ 25) samples; Δa, Δb and Δc describes the error to a, b and c. 94

5.5 Fitting parameters applying Eq. (5.4) on the frequency dependence of the coercivity for HPT treated $Fe_{100-x}Al_x$ (15 ≤ x ≤ 25) samples; Δd, Δe and Δg describes the error to d, e and g. 94

5.6 Fitting parameters applying model Eq. (5.6) on the frequency dependence of the coercivity for HPT-treated $Fe_{100-x}Al_x$ (15 ≤ x ≤ 25) samples; Δa and $\Delta\mu_r$ describes the error to a, and μ_r. 96

5.7 Fit parameters applying Eq. (5.8) on the frequency dependence of the losses of HPT-treated $Fe_{100-x}Al_x$ (15 ≤ x ≤ 25) samples; ΔW_{h1}, ΔB_1 and ΔB_2 are estimated errors of W_{h1}, B_1 and B_2. 98

5.8 Fit parameters applying Eq. (5.9) on the frequency dependence of the losses of HPT-treated $Fe_{100-x}Al_x$ (15 ≤ x ≤ 25) samples; ΔW_h, ΔB_1 and ΔB_2 are estimated errors of W_h, B_1 and B_2. 98

5.9 Parameters as used for the hysteresis measurements. N_1-Primary windings, N_2-Secondary windings, l_{eff} *(m)*-Magnetic path length, $A(m^2)$-Cross-sectional area. 100

5.10 Magnetic hysteresis Parameters of $Fe_{81}Ga_{19}$ quenched (Q) and annealed (A) samples. The number in (..) is the field values where μ_{max} was determined. 102

5.11 Fit parameters according to Eqs. (5.3) and (5.4) on experimental data of coercivity versus frequency of $Fe_{81}Ga_{19}$(Q) and (A) samples, where Δb, Δc, Δe, Δg describe the errors of b c, e,and g respectively. 103

5.12 Fit parameters according to model Eq. 5.12 assuming n=1 on experimental data of coercivity versus frequency of $Fe_{81}Ga_{19}$(Q) and $Fe_{81}Ga_{19}$(A) samples. 106

5.13 Fit parameters according to model Eq. 5.12 using n as a free parameter on experimental data of coercivity versus frequency of $Fe_{81}Al_{19}$(Q) and $Fe_{81}Ga_{19}$(A). 106

5.14 Fit parameters applying Eq. (5.9) on the frequency dependence of the losses for $Fe_{81}Ga_{19}$ (Q) and (A)samples; ΔW_h, ΔB_1 and ΔB_2 are estimated errors to W_h, B_1 and B_2. 107

6.1 Parameters as used for the hysteresis measurements of pearlitic steel (R260). N_1-Primary Windings, N_2-Secondary Windings, $l_{eff}(m)$-Magnetic Path length, $A(m^2)$-Cross-sectional Area. 112

6.2 Magnetic Properties of SPD treated pearlitic steel (R260), the number in (..) describes the field where the relative permeability μ_{max} was determined. 116

6.3 Fit parameters according to Eq. (3.16) on the coercivity versus frequency data of SPD pearlitic steel (R260). Δa, Δb and Δc describe error to a, b and c. 117

6.4 Fit parameters according to Eq. (3.17) on the coercivity versus frequency data of SPD pearlitic steel (R260). Δd, Δe and Δg describe error to d, e and g. 117

6.5 Fit parameters according to equation (6.1) on the coercivity versus frequency data of SPD treated pearltic steel (R260) and the calculated permeability μ_r at $f = 0$ from $\mu_r(f) = k/[Hc(f)]^n$. 118

6.6 Fit parameters according to Eq. (6.3) on frequency of dependence total losses for pearlitic steel (R260). ΔW_h, ΔB_1 and ΔB_2 describe error to W, e and g. 120

7.1 Chemical composition of pipeline steels X-52, X-56, X-60. 123

7.2 Parameters as used for the hysteresis measurements. N_1-Primary Windings, N_2-Secondary Windings, $l_{eff}(m)$-Magnetic Path length, $A(m^2)$-Cross-sectional Area of the thin leg. 125

7.3 Magnetic properties derived from hysteresis loops of samples X52, X56 and X60. 132
7.4 Fit parameters according to Eq. (3.16) for X52, X56, and X60 pipeline steel samples.Whereas, Δa, Δb and Δc describe error to a, b and c. 134
7.5 Fit parameters according to Eq. (3.17) for X52, X56, and X60 pipeline steel samples. Whereas, Δd, Δe and Δg describe error to d, e and g. . . . 134
7.6 Fit parameters according to model (3.15) for X52, X56, and X60 pipeline steel samples. Δn and Δk describe error to n and k. 135
7.7 Fit parameters according to Eq. (6.3) on frequency of dependence total losses for X52, X56, and X60 pipeline steel. ΔW_h, ΔB_1 and ΔB_2 describe error to W_h, e and g. 137

8.1 Data according to ISO standard for Sample S_8. 142
8.2 Saturation magnetization and % of Fe-contents resin coated Fe-powder. . . 142
8.3 Dimensions and parameters used for the hysteresis measurements of Fe-Powder. N_1-Primary Windings, N_2-Secondary Windings, $l_{eff}(m)$-Magnetic Path length, $A(m^2)$-Cross-sectional Area. 143
8.4 Magnetic properties of risen coated Fe-powder, the number in (..) are the field values where μ_{max} was determined. 148

Chapter 1

Introduction

1.1 Ferromagnetism

Ferromagnetic materials such as the transition elements Iron (Fe), Nickel (Ni), Cobalt (Co), and rare earth metals like Gadolinium (Gd), Terbium (Tb), Dysprosium (Dy), Holmium (Ho), and Erbium (Er), are "spontaneous magnetized" by a parallel alignment of magnetic moments even in absence of external magnetic field. This magnetic ordering occurs due to exchange which can be only explained by quantum mechanics. From "outside" this magnetic behavior cause a magnetic Hysteresis measuring the magnetization as function of the magnetic field. Such a hysteresis is caused by the movement and alignment of magnetic domains. The parallel alignment of magnetic moments in one direction is subdivided into small regions (microscopic) within a material, known as domains in order to minimize the magnetostatic stray field energy of the system. Adjacent domains are separated by domain boundaries or walls called Bloch walls (180°walls) or Neel walls (90°walls) in which the direction of the magnetic moment gradually and continuously changes from that of one domain to adjacent domains. The thickness of the domain wall is much smaller than the domains itself and roughly proportional to the $\sqrt{A/K}$ (A-exchange stiffnes constant, K-anisotropy energy) [6]. Different energy contribute to the formation of domains and determine its size i.e. magnetostatic (stray field) energy, crystal anisotropy, magnetoelastic energy etc. Normally the domain size can range from a few micrometers to 1 mm in a demagnetized material as whole. Nevertheless the parallel

arrangements of magnetic moments within domains depend on the ambient temperature. At the Curie temperature (depends on the type of ferromagnetic materials), the parallel alignment of moments breaks down because of thermal agitation and the material is no more ferromagnetic.

In the absence of external field H_{ext}=0, the domains are oriented in random directions such that the net magnetization of material as a whole become zero as shown in Figure 1.1a. When a demagnetized ferromagnetic material well below the Curie temperature (having a net magnetization zero) is brought into an external magnetic field, the domains lying more or less in the direction of the applied field start to grow at the expense of other domains until most favorably oriented domains remains when the external field is high enough. Further increase in the magnetic field causes the domains to rotate and align parallel to the applied field. At this stage the material is saturated as shown in Figure 1.1b. During the growth of magnetic domains there has been no change in the magnitude of the local magnetization only the domain walls move and the external field provides the force required for this movement.

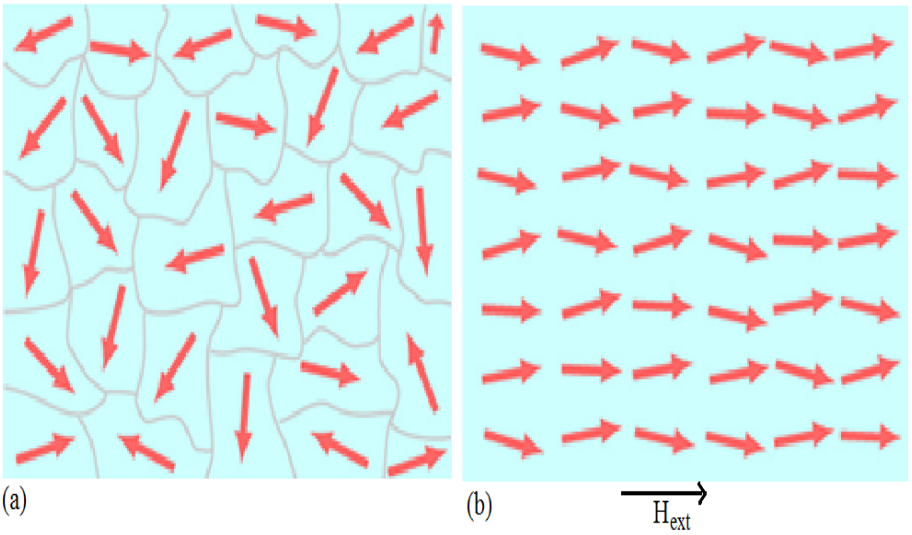

Figure 1.1: (a) Randomly oriented ferromagnetic domains $H_{ext} = 0$ (b) Oriented ferromagnetic domains.

1.2 Types of Magnetic Materials

From application point of view magnetic materials can be classified as hard magnetic materials (Permanent Magnets) and Soft Magnetic Materials. This classification is made on the basis of coercive value. Figure 1.2 illustrates the usual way to distinguish between two types of materials.

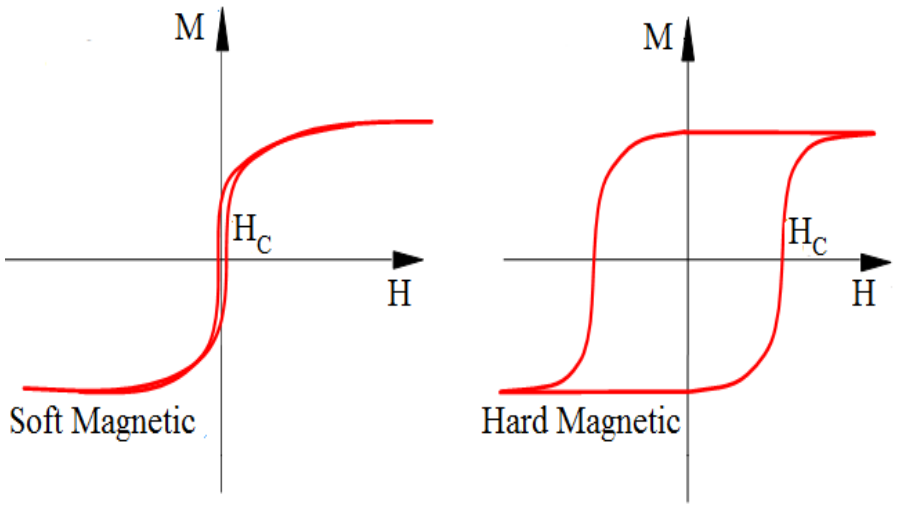

Figure 1.2: A magnetic hysteresis loop for soft and hard ferromagnetic materials.

1.2.1 Hard Magnetic Materials

Materials with a high coercivity (H_c >10 kA/m) are consider as a hard magnetic materials [7]. Due to the high coercivity, a strong magnetic field is required to magnetize the material. Once such material being magnetized, they exhibit and retain a strong net magnetization without external field, that means that these materials not only have a high coercivity but also a high saturation (B_s) and remnant inductions (B_r) [8]. These materials are used for permanent magnets in order to generate strong static fields (up to about 1T). Magnets used for different applications such as transforming energy from one form to another i.e converting mechanical energy to electrical energy and vice versa for example generators, motors and microphones, loudspeakers etc. Engineers are more interested in a part of the hysteresis loop which lies in the second quadrant commonly called "Demagnetizing curve" in order to determine the suitability and performance of a permanent magnet for a particular device. Fe-carbon steel and special alloys such as Al-

comax, Alnico, and Ticonal, which contain various amounts of aluminium, nickel, cobalt, and copper, are used to make low cost permanent magnets. The strongest permanent magnets are nowadays rare earth intermetallics based on Sm-Co or Nd-Fe-B, produced by a sintering technology [9, 10]. Ceramics such as Ba- or Sr-ferrites are interesting for dynamic applications [11]. They are produced using a wet chemical route (sol gel) and afterward sintered at high pressure and high temperatures from powders [12, 13].

1.2.2 Soft Magnetic Materials

The magnetic materials having coercivity less than 1 kA/m are considered as magnetically soft. These materials are easy to magnetize and demagnetize. The main characteristics of soft magnetic materials are low core losses, high permeability and high induction. Depending on the application and its requirements, soft magnetic materials are selected on the basis of these characteristic. The most common application lies in transformers and generators which use soft magnetic Fe-3 wt%Si sheets [14]. High frequency applications of soft magnetic materials uses soft magnetic ferrites: in all cases low core losses are required. Therefore low coercivity combined with a high permeability and low magnetocrystalline anisotropy are necessary for soft magnetic materials [15]. The most important conventional and new soft magnetic materials are given in the following list:

- Fe-Ni alloys e.g. "Permalloy", "Mumetal",(for television, telephons, micromachines and small transformers with special utilization, transducers, magnetic recording heads, computer peripherals, microwave installations etc. Fe- Ni alloys are the most representative materials for this category [14]. These alloys exhibit a very high permeability which is most favorable for shielding applications.

- Fe-Si alloys one of the most extensively used soft magnetic materials in electrical industry with typically operating frequency 50/60 Hz. The main applications for these soft magnetic materials are in generators, motors, transformers, electromagnets and relays. These applications need high-induction, low losses and high permeability magnetic materials. The most common material used for these applications is non-oriented and oriented 3%silicon-iron but many smaller motors use silicon-free low-

carbon steel for economic reasons. Grain oriented iron-silicon alloys are mostly used for high energy transformers because of low core losses. High-frequency transformers use ferrites although this represents only a small volume of the total transformer market [7]. The addition on nonmagnetic silicon in iron enhance its properties in many respects, most important is the increase of the electrical resistivity of the material due to the addition of Si into Fe for example, Fe-3 wt%Si has four time higher resistivity than pure iron [7]. Consequently the dynamic losses due to eddy currents are reduced thats why it is suitable for transformers. Additionally the magnetostriction decreases with increasing Si content [16–18]. Also this causes a reduction of the coercive field and the hysteresis losses. Consequently the mechanical noise of operating transformers is reduced. From this magnetic point of view, the best composition is around 6-wt% Si which reduces the magnetocrystalline anisotropy and the magnetostriction. This material has the highest permeability and the lowest coercivity, however it is too brittle for standard applications. Nevertheless addition of silicon in iron also have two harmful effects: first it reduces the saturation magnetization, second it influences the mechanical workability. The reduction of the Curie temperature below 10-wt%Si is of no practical importance.

- Fe-Al alloys ("Sendust" FeSiAl) exhibit the lowest magnetocrystalline anisotropy combined with a nearly zero magnetostriction. These alloys have a high resistivity, lower density and a higher hardness and a good resistance against corrosion which is better than those of nickel- iron and many other soft magnetic alloys as silicon iron steel. That is why these alloys are more suitable for special environment such as nuclear radiation, shock, acceleration, etc and also have significant industrial application in the fields of aviation, space flight, navigation, and other civilian and military industries. However due to higher costs than silicon iron these alloys are unlikely to replace silicon-iron for general electrical applications. Additionally this material is very brittle and needs special production methods which causes also additional costs.

- Soft magnet Iron-cobalt (Fe-Co) is the only alloy with increased saturation mag-

netization (up to 2.4 T) [19] as well as the highest Curie temperature of all other binary alloys with iron. The high saturation magnetization is about 2.45 T with 35-wt% Co. Therefore this alloy is suitable for high induction application and elevated temperatures. The material is very corrosion stable. Drawback of these alloys is that they are mechanically very hard, furthermore cobalt is also expensive.

- Soft ferrites (Mn-Zn ferrites) are ceramic materials. There chemical composition is (metal oxides) + (iron oxide)- $M.Fe_2O_3$ where M represents transition metal such as iron (Fe), manganese (Mn), magnesium (Mg) nickle (Ni), zinc (Zn).

1.2.2.1 Soft Magnetic Crystalline Materials

Materials with grain size less than 100 nm [20,21] are considered as "nanocrystalline" materials with very specific magnetic properties (such as magnetic softening due to exchange coupling) . The use of nanocrystalline technology provided a new path to tailoring the soft magnetic properties. It is well known that the hysteresis loop of ferromagnetic materials depends on the microstructure, particularly when the grain size become comparable to the exchange length, exchange coupling occurs which causes a dramatic reduction of the coercivity [22].

1.2.2.2 Soft Magnetic Amorphous Materials

Amorphous materials have no periodic arrangement of the atoms because they are produced by rapid cooling (quenching) of the molten alloys of usually Fe, Co, or Ni with a metalloid such as B, C, Si, P, or Al. Metalloid is added in order to stabilize the amorphous phase. An example of such an amorphous alloy is $Fe_{80}B_{20}$ (Metglass 2605). The amorphous alloys have usually excellent soft magnetic properties even in the as-cast state which exhibit a highly stressed state. Magnetic properties of amorphous materials are different from those found in their crystalline counterparts. The basic reason is that some magnetic properties are particularly structure sensitive that is why the properties of amorphous materials strongly depends on the fabrication process. In general, amorphous materials show excellent soft magnetic properties due to the averaging of magnetocrystalline anisotropy

and microstructural defects (grain boundaries, dislocations or precipitates) on which domain walls could be pinned even in the as-cast state.

1.2.3 Magnetization Curves and Hysteresis Loops

The hysteresis loop express a non linear, irreversible relationship between the magnetic flux density B and the applied magnetic field H_{ext}. Generally the external field has to be corrected for demagnetizing field effects. Only in the case of a magnetically closed circuit the external field is equal to the internal field. A typical hysteresis loop for a ferromagnetic material as shown in Figure 1.3 exhibits the following steps:
Point O (origin) presents the demagnetized, initial state of the material, with increasing applied field (H_{ext}) in positive direction, the favorable domains of the material start to increase in the direction of H_{ext} as shown in Figure from O to a.

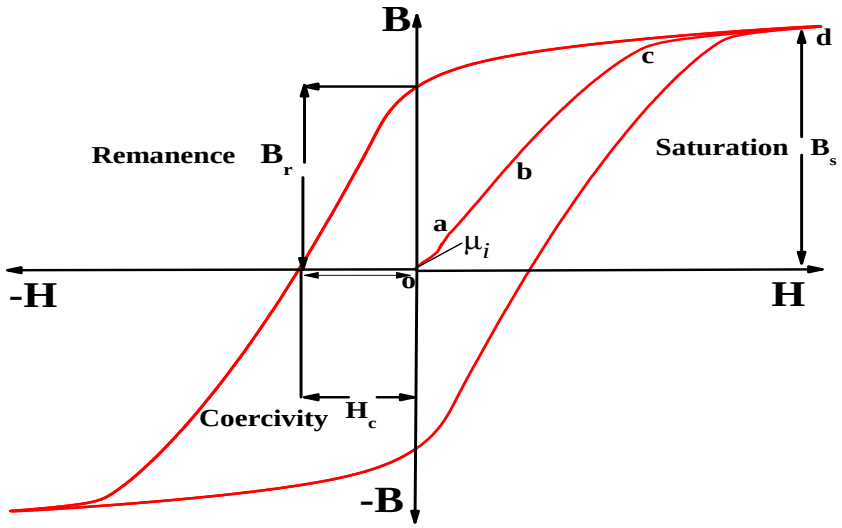

Figure 1.3: Hysteresis loop of ferromagnetic materials.

When the external field H_{ext} is sufficiently high, the induction B(H) in the material becomes saturated (+B_s) by aligning all domains in the direction of H_{ext} and a further increase in the external field produce no significant change in the magnetic induction B. The first B(H) curve from the demagnetized state "O" to the saturation point B_s is called "virgin curve" of the B(H) hysteresis.
After saturation, when the external field (H_{ext}) is reduce to zero the magnetic induction

B does not reduce to zero but it retains in a remanent state which is known as remanence (+B_r). This is valid in a magnetically closed system.

Now to demagnetized the material that means to reduce B_r to zero, the external field H_{ext} has to be applied in the negative direction. This negative value of H_{ext} where the induction B becomes zero is described by H_c and is called coericive force or coercivity. A further increase of H_{ext} in the negative direction can saturate the material but in the opposite direction (-B_s). If now the negative H_{ext} field reduces to zero the material achieves again a remanent magnetization (-B_r). The hysteresis loop traced out from +B_s to -B_s is called the major hysteresis loop. If the field H_{ext} is not sufficient to saturate the sample also a loop is formed which is called minor loop.

For a ferromagnetic material, the magnetic induction B inside the sample is defined as:

$$B = \mu_o(H + M) \tag{1.1}$$

Where μ_o is the permeability in free space and its value is $4\pi \times 10^{-7}$ Vs/Am and M is the magnetization which is spontaneously induced in a ferromagnetic material by exchange and which becomes visible by applying field H_{ext}. In free space M = 0

B and H are related as:

$$B = \mu_r \mu_o H_{ext} \tag{1.2}$$

Where μ_r is the relative permeability and in vacuum $\mu_r = 1$.

In general, a material becomes magnetized as response to an external field H_{ext} and can be measured through its susceptibility and permeability. Hence, M can be expressed as

$$M = \chi_m H_{ext} \tag{1.3}$$

Where χ_m is the magnetic susceptibility (unitless) "response function" of the magnetization of a material due to an applied magnetic field. Relative permeability and magnetic

susceptibility are related as follows:

$$\mu_r = 1 + \chi_m \tag{1.4}$$

A numbers of characteristic properties of a ferromagnetic material can be determined from the hysteresis loop.

- Remanence - It is the amount of magnetic induction which retain in a material when the magnetic field is removed after achieving saturation (The value of B_r on the hysteresis curve). This value depends on the magnetic material (microstructure) and plays an important role in all application.

- Coercive force - The amount of reverse magnetic field which has to be applied to a magnetic material to reduce the magnetic flux to zero. (The value of H_c on the hysteresis curve).

- Permeability, *$\mu(H)$* - This property represents the slope of the B(H) curve. It describes the ease with which a magnetic flux is established at a certain field value in the component.

1.2.4 Frequency Dependence of Losses

All the irreversible energies utilized in the magnetization and demagnetization process during hysteresis measurements are termed as losses. The total losses depend not only on the type of magnetic material used in the core, but also upon the maximal induction and magnetization frequency. Conventionally total core losses in a soft magnetic metallic material are divided into, hysteresis loss or static loss (P_h), classical loss (dynamic) or eddy current loss (P_e) and anomalous losses (P_a) or excess losses [23].

Hysteresis losses (P_h) occur due to the motion of magnetic domain walls and Barkhausen jumps under external magnetic field [24]. The material compositions, grain size, grain boundaries, mechanical strains, dislocations and impurities all play a part in domain wall

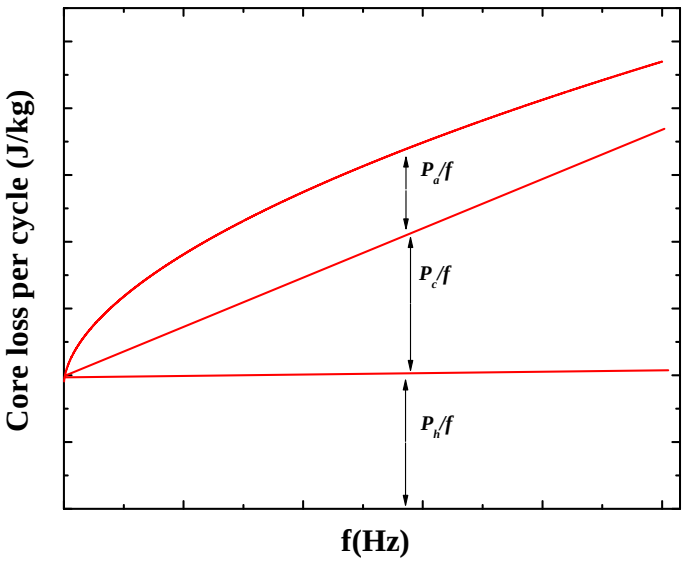

Figure 1.4: Separation of core losses.

movement and hence in hysteresis losses.

Steinmetz empirically expressed hysteresis loss for normally sinusoidal flux wave B(t) form with varying frequency [25], nevertheless in case of major loops hysteresis loss depends on the maximum value of the flux density, B_{max} irrespective to magnetic waveform.

$$P_h = k_h f B_{max}^n (J/m^3) \tag{1.5}$$

The parameters k_h are material dependent and can be determined by fitting the experimental data. Steinmetz exponent n range from 1.5 to 2 [23], but for most of soft magnetic materials (Fe 3 wt%Si) its value is 1.6 [26] The dependence of P_h on B_{max} is predicted by the theory of magnetic domains.

The origin of the classical losses in the material are *eddy currents* due to an alternating magnetic (AC) field produced by an excitation current in the primary windings (according to lenz's law). The magnetic flux generated by the induced currents opposes the flux changes Φ(t) produced by excitation current in the core, thus preventing the flux from penetrating the core. The eddy current in general is unfavorable because it weakens the flux inhomogeneous and heats the material [27]. The induced current is proportional to the rate of change of the induction B, with time (dB/dt). Therefore eddy current losses increases with increasing frequency in dB/dt. The eddy current losses can be reduced

by increasing the resistivity of the material. Since ferrites have a high resistivity, eddy currents are small until higher frequencies are encountered [28].
The classical eddy current loss was described by the Steinmetz law :

$$P_{ec} = k_{ec} f^2 B_{max}^2 (J/m^3) \tag{1.6}$$

According to the statistical theory described by Bertotti [23] and Fiorillo [29] the expression for calculating the classical eddy currents losses:

$$P_{ec} = \frac{\pi^2 d^2 f^2 B_{max}^2}{\rho\beta} (J/m^3) \tag{1.7}$$

Where d is thickness of the lamination, ρ is the electrical resistivity of the material and β is a constant which depends on the shape of driving field.

The third contribution to the losses are the anomalous or excess losses. They are usually the difference of the total losses from the sum of hysteresis losses and classical losses. In reality this point of the losses occur due to the local damping of the movement of domain walls.
The expression for the excess losses can be written as:

$$Pex = k_{ex} (f B_{max})^{1.5} (J/m^3) \tag{1.8}$$

Where k_{ex} is a fitting parameter.

Equations 1.5, 1.6, and 1.8 empirically describe the separation of losses [30]. In 1984 Bertotti developed [23, 31, 32] a statistical loss theory, describing the magnetization dynamics based on the concept of randomly distributed magnetic correlation regions called magnetic objects (MO). These magnetic objects (MO) lead to a physical description for separation of losses. It assumes that the excess loss is governed by the statistical distribution of the local threshold fields at which different MOs become magnetically active.

According to this theory, the simplified form of excess loss valid for most soft magnetic materials is given as [33–35]

$$P_{exc} = CB_{max}^{1.5}\sqrt{f} = 8\sqrt{\frac{GAV_o}{\rho}}B_{max}^{1.5}\sqrt{f}. \tag{1.9}$$

Where A is the cross sectional area of the lamination, G is a dimensionless coefficient of the eddy current damping which is about 0.2 and ρ is electrical resistivity. V_0 is a parameter characterizes the statistical distribution of the magnetic objects responsible for the anomalous eddy currents.

1.3 Severe Plastic Deformation

Severe plastic deformation (SPD) has become a well established technique for the production of ultrafine grained (UFG) materials in order to attain superior mechanical and other physical properties. Ultrafine grained (UFG) even down to nanostructure (nc) range can be attained through this technique by imposing large strains leading to significant microstructural refinement in bulk crystalline solids with no significant change in the overall dimensions of the sample. Large strain is introduced by hydrostatic pressure through a special tool geometry that prevents free flow of the material. The typical average grain size of UFG for submicrocrystalline is about ∼100-200 nm and for nanocrystalline is in range ∼10 - $<$ 100 nm [36, 37]. When the grain sizes reach nanometer range their boundaries area increases which lead to enhancement in mechanical and physical properties of a material [38]. Specially in the nanometer range the magnetic moments interact across the grain boundaries which lead to a significant enhance of soft magnetic properties. There are several SPD techniques used in refining the microstructure - High Pressure Torsion (HPT) and Equal Channel Angular Pressing (ECAP) are probably the most common and standard SPD techniques for achieving large plastic deformations (with true strains $\geq$10) and a formation of a nanostructures [38, 39]. A schematic diagram of HPT and ECA is shown in Figure 1.5

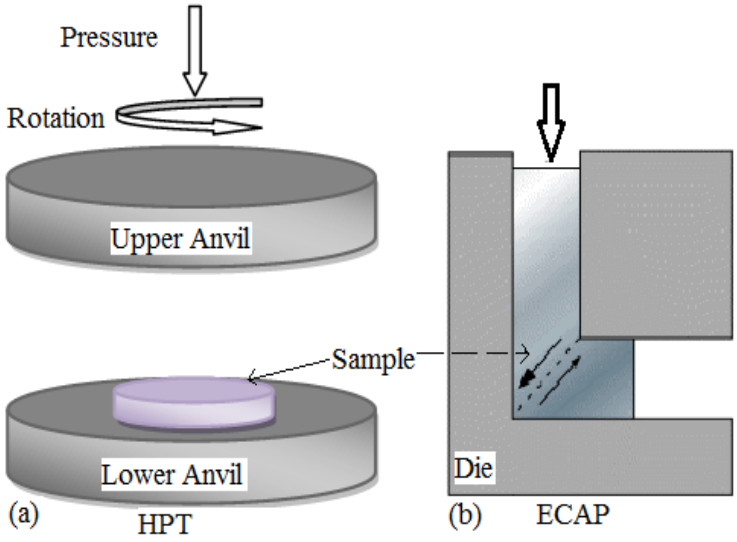

Figure 1.5: Schematic diagram of: (a) HPT (b) ECAP .

1. High Pressure Torsion: a sample in a shape of a thin disc typically 10-20 mm diameter and 0.2 - 0.5 mm thick [40] is deformed under high hydrostatic pressure by rotating the two anvils with respect to each other with pure shear strain. The necessary torsion-momentum is provided by friction forces at constant areas anvil-material. Basic structure refinement is obtained after half- or one complete (360°) turn deformation [41]. However, several turns are necessary for creating a homogeneous nanostructure deformation [40]. The advantage of this technique is that the parameters like hydrostatic pressure, strain rate and deformation temperature can effectively be controlled [42] and gives high quality UFG materials with grain sizes up to 100 nm.

2. Equal Channel Angular Pressing: a rod or bar shaped sample (length ∼100mm, diameter ∼20mm) is pressed through two intersecting channels of identical cross-section. Strain on the sample depends on the die angle between the intersecting channels. A shear strain is introduced when the sample passes through the die angle of two intersection channels. Since during the pressing process the cross-sectional area of the sample remain unchanged therefore the process can be repeated several times to achieve extremely high strains [43].

1.3.1 Effect of Severe Plastic Deformation

Over the last two decades, much research has been carried out to the engineering of innovative nanostructured materials because of their outstanding characteristics such as mechanical or magnetic properties [44, 45]. There are two effects of SPD: *i*) extreme plastic deformation up to a saturated state with a high density of all kinds of dislocations and *ii*) the high density of dislocations is accompanied with a nanocrystallization. This cause "new" magnetic properties. They arise from the fact that the grain size becomes comparable with the magnetic exchange length, which causes exchange coupling between the magnetic moments going over the grain boundaries. This leads to an averaging of the magnetic anisotropy and consequently improved soft magnetic properties (reduction of coercivity, increase of the susceptibility). Also the domain structure changes leading to so-called "exchange-domains" resulting in strongly modified magnetic properties compared to coarse grained materials.

In the last 15 years it has been shown that severe plastic deformation (SPD) represents a method that is suitable for processing large quantities of pure and fully dense small scaled micro- or even nanostructures [45–47]. Many publications in this scientific field comment on the change in mechanical properties with different combinations of SPD and subsequent annealing [6, 48]. The changes in material properties, such as magnetic or electrical properties, are rarely investigated. Severe plastic deformation (SPD) affects the magnetic properties of magnetic materials in two ways: *i*) It changes the shape and area of the hysteresis loop due to the increasing influence of magneto-elastic energy. The residual stresses induced during the SPD deformation resist the domains to rotate in order to align themselves with applied magnetic field. Therefore extra work is needed to overcome the magnetoelastic energy. This effect can be explained in a simple formula which describes the coercivity of soft magnetic materials.

$$H_c = \frac{\lambda\sigma + < K >}{\mu_o . M_s} \tag{1.10}$$

Where λ describes an average magnetostriction constant, $< K >$ a mean crystalline

anisotropy σ- internal or external stress, μ_o and M_s denote the permeability and the saturation magnetization, respectively.

ii) because of the SPD induced nano-crystallization, exchange coupling can cause a reduction of the effective anisotropy thus causing magnetic softening. The coercivity of exchange coupled magnetic material scales after Herzer with the 6^{th} power of the grain size [49, 50].

$$H_c \approx Pc \frac{K_1^4 . D^6}{\mu_o . M_s . A^2} \tag{1.11}$$

Where P_c is a dimensionless prefactor close to unity, A is the exchange stiffness, and D the grain size. This causes for soft magnetic materials with decreasing grain size drastically decreasing coercivity . Such a behaviour was found for different nano-crystalline materials produced by rapidly quenching [6]. Recently a similar behavior was also detected for SPD treated materials. The coercivity of a soft-magnetic material is determined by the formation and mobility of domain walls, which depends on the actual microstructure. Therefore, the ratio of the domain wall width (50-100 nm in soft Fe) to the dimensions of the local stress field is very important. Below a grain size of about 100 nm it can be expected that the grains couple magnetically over the grain boundaries. This causes a magnetic softening as soon as the grain size of the alloy becomes smaller than the ferromagnetic exchange length, which is of the order of the domain wall width [51]. The maximum in H_c occurs at a grain size of about 100 nm which correspond to single domain particles. For smaller grains the exchange coupling reduces the effective anisotropy as well as the coercivity [52]. Exchange coupled materials show naturally no super paramagnetism which occurs for decoupled nano-sized grains only. The complex situation in a severely deformed material is determined by the interplay between domain walls and dislocations or stresses.

1.3.2 Effect of HPT Deformation Temperature

Different studies of SPD treatment temperature effect on the microstructure shows that the grain size increased with increasing temperature of deformation [1, 53–55]. The grain refinement is achieved at all temperatures but there is a transition from arrays of high angle boundaries at lower temperatures to low angle boundaries at high temperatures [54]. For example A. Vorhauer et al. [1] observed that with an equivalent strain of $\varepsilon_{vM} \sim 32$ during warm and cold HPT for ferritic steel P800, the mean size of the crystallites was about 120 nm and 270 nm at 293 K and 723 K, respectively and refined to a mean structural size of about 40 to 80 nm when deformed at liquid nitrogen temperature. BSE and TEM images for warm and cold HPT are shown in Figures 1.6 and 1.7 respectively. The grains are mostly elongated parallel to the shear direction with decreasing temperature, especially after SPD at liquid nitrogen temperature.

Yamashita et al. [55] investigated the effect of processing temperature of equal channel angular extrusion (ECAE) on pure aluminum and Al-Mg alloys. He showed that the sub-grain size increased with increasing extrusion temperature. According to Yamashita et.al. the distribution of boundary misorientation as a function of extrusion temperature generated boundaries decreasing with increasing extrusion temperature. Y.Y. Wang et al. [53] observed on ECAE deformed commercial aluminum (AA1050) samples to a strain of 8 at extrusion temperatures from 298 to 523 K that an increasing deformation temperature causes an increasing of the subgrain size, the sub-grain shape becomes more equiaxed-like lamellar structure and nearly parallel to the extrusion direction.

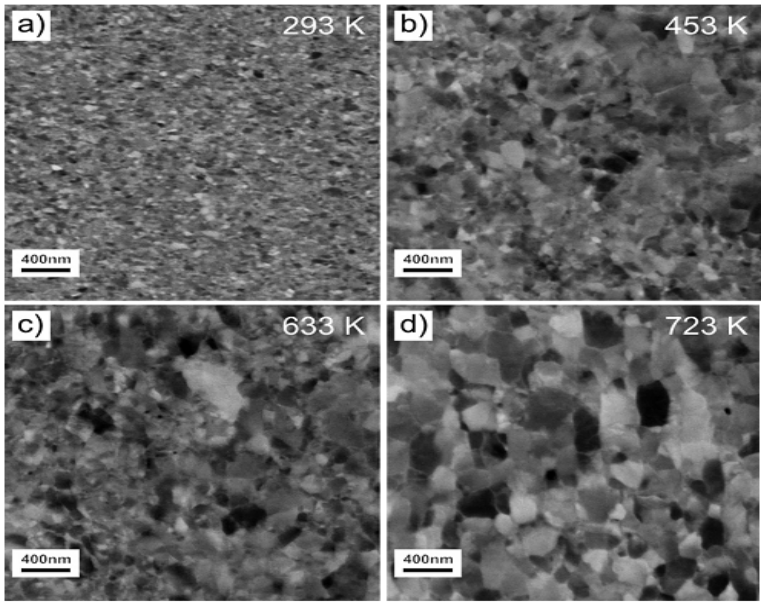

Figure 1.6: BSE images of HPT deformed P800 in radial direction; the samples were deformed at different temperatures (see insets) [1].

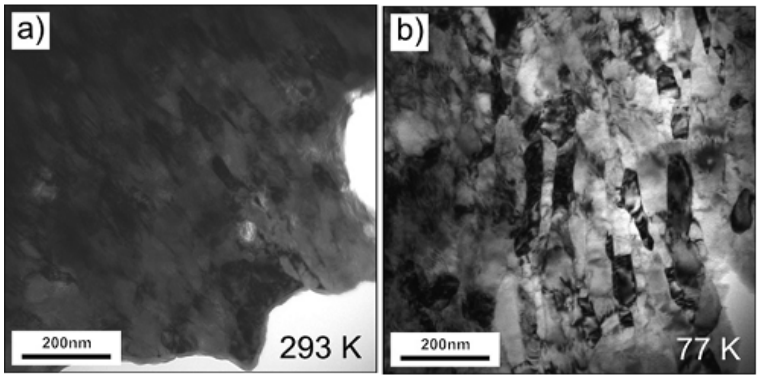

Figure 1.7: TEM micrographs of P800 deformed at low temperatures (293 K and 77 K) [1].

1.4 Tasks for the present work

Hysteresis characteristics of magnetic materials play an important role to investigate the magnetization mechanism with respect of possible applications of the material. The study of the hysteresis loops is of great benefit to check general theories explaining the magnetization phenomenon and to develop analytical or numerical models for the magnetization process as well as for the optimum design of innovative electromagnetic devices.

For determining the hysteresis, the magnetization (M) (or the induction B) has to be measured as a function of the applied magnetic field (H). The field can be determined

either directly by using a sensor (Hall probe for field strength meters, measuring coils for flux meter) [7] or indirectly by current and voltage measurements. The induction B is measured using an induction coil. For measuring a hysteresis loop a magnetic ac-field is applied and a hysteresisgraph or Magnetometer is used to measure the hysteresis loop of a magnetic material at a constant temperature, generating as its output a hysteresis loop M(H) or B(H). Despite the long history of investigating the influence of mechanical stresses on the magnetic behavior of ferromagnetic materials [26,56] the issue of magnetic evaluation of plastic deformation and residual stress is still a topical and open question. There is strong need of non-destructive testing (NDT) of structural changes of steels during production processes: rolling, extrusion, cutting or punching. Gas pipeline industry and other steel producers are also interested in reliable estimates of the remaining lifetime of steel constructions and industrial plants [57–59].

The aim of the thesis is to evaluate magnetic hysteresis properties of wide range of soft magnetic materials which are important from industrial point of view. For this purpose a hysteresigraph is used to measure hysteresis loops including minor loops as a function of frequency and magnetic field. Parameters i.e coerecivity, permeability, remanence etc, were calculated (determined) from the hysteresis loops.

To see the effect of grain size and dislocations the samples were plastically deformed by HPT at different temperatures. Hysteresis loop measurement were made on ring shaped samples of as cast, machined, SPD deformed soft magnetic materials (steel etc) produced at well-defined conditions. A theoretical model was developed to analyse the experimental data especially frequency dependence of coercivity, frequency dependcence of losses and comparisons were made between experimental and theoretical results.

The work was accomplished by investigating following materials:

- SPD deformed at different temperatures by using the so-called HPT method pure iron (99.98% purity), pure nickel (99.97% purity) and Fe alloy with silicon and cobalt were investigated by measuring their frequency dependence of hysteresis at room temperature as well as elevated temperature up to 220°C. Stress effect due to HPT deformation and temperature on the magnetic hysteresis parameters were discussed

by comparing the result with corresponding un-deformed samples. The frequency dependence of coercivity was analyzed applying general formulas as well as by a self developed eddy current model and compared with the obtained results. Moreover losses were analyzed by models suggested by Mosses and Bertotti [31, 34, 60].

- High magnetostrictive material which exhibits soft magnetic behavior are of great important for applications in sensors and actuators. Substituting Fe by non magnetic Al or Ga causes a strong increase in magnetostriction [61–63] . $Fe_{1-x}Al_x$ ($15 \leq x \leq 25$) with the range of x. The samples were HPT-deformed in liquid nitrogen temperature and at room temperature such a HPT treatment causes a local disorder which may enhance the magnetostriction in these systems. Analyzing the frequency dependence of the hysteresis loop shall give a basic understandings of the stress and frequency effects on the hysteresis properties of materials with high magnetostrictions. $Fe_{81}Ga_{19}$ as quenched in cold water and annealed (slowly cooled in oven) were also investigated by magnetic measurements via hysteresis.

- Rail steel is an iron-carbon alloys. SPD deformed rail steel grade R260 with shear rate $\epsilon = (0, 1, 2, 4, 8, 16)$ at room temperature were studied applying severe plastic deformation. Here the microstructure and correlations with the magnetic hysteresis properties such as coercivity, permeability etc were studied.

- Pipeline steel is one of the vital part of petroleum and chemical industry used for transporting oil and other chemicals. Out-of-service standard grad pipe X52, X56, and X60 were investigated magnetically along longitudinal, transverse, and between these two axis of preferential orientation. Hysteresis loops were measured in a magnetically closed circuit by making window frames in order to see the effect of texture induced anisotropy and compare with their corresponding microstructure.

- On iron powder coated with epoxy resin or glass the frequency dependence of hysteresis and saturation magnetization was measured by a Pulse field magnetometer (PFM). Additionally, microstructure and the powder morphology were examined by scanning electron microscopy.

Chapter 2

Experimental

2.1 Severe Plastic Deformation (SPD) Set-up

High Pressure Torsion (HPT) is one of the techniques used for severe plastic deformation (SPD) for producing ultra fine grain samples in a bulk state without changing overall dimensions strongly. In the present work most of the the samples studied were SPD deformed by HPT at different temperatures in order to investigate the effect of plastic deformation on the magnetic properties. Figure 2.1 presents a brief introduction of the HPT setup available in the Erich Schmid Institute of Materials Science, Austrian Academy of Sciences, Department Materials Physics, University of Leoben. A typical specimen for HPT treatment is in the shape of a thin disc which is deformed under high hydrostatic pressure by rotating the two anvils with respect to each other with pure shear strain. The necessary torsion-momentum is provided by friction forces at constant areas of the anvil-material (see Figure 2.2).

In order to study the effect of the temperature on the deformation of the sample, the two anvils of HPT with the sample is subjected into a chamber flushed with liquid nitrogen called cold HPT and for warm HPT the same parts of tool with the sample is placed into the inductor of an induction heating system. With the help of these two additional tools the sample can be deformed in a temperature range between 77 K and 873 K. Moreover, the tool allows variations in the applied strain, pressure and rotation speed and enables the direct measurement of the torque applied to the sample. Figure 2.2 shows a sketch of

the used warm and cold HPT setup.

Figure 2.1: Photograph of HPT set up [2]

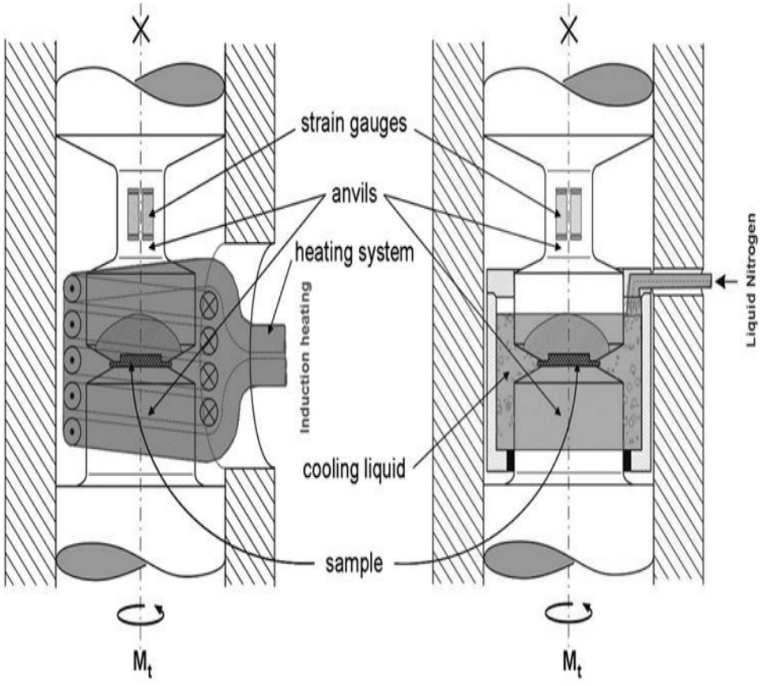

Figure 2.2: Schematic illustration of the used HPT equipment for hot (left) and cold (right) processing [3].

2.2 Magnetic Measurement Methods

2.2.1 Measurements on Hysteresigraph

A complete setup for measuring and recording hysteresis loops is called a hysteresigraph or hysteresosgraph. The hysteresograph used in this work consist of a standard PC with a National Instruments measurement (PCI-6120) data-acquisition card, a connector block and a power amplifier (APEX or KEPCO). The KEPCO bipolar operational power amplifier (Model BOP 100-4M) is suitable to generate 100 V and 4 A bipolar signals and the OPV of APEX, sends up to a maximum current of 6.3 A, with a maximum voltage of 24 V supplies with optional signal shapes. The whole measurement is handled by a LabVIEW program [64]. The block diagram of the whole set-up can be seen in Figure 2.3.

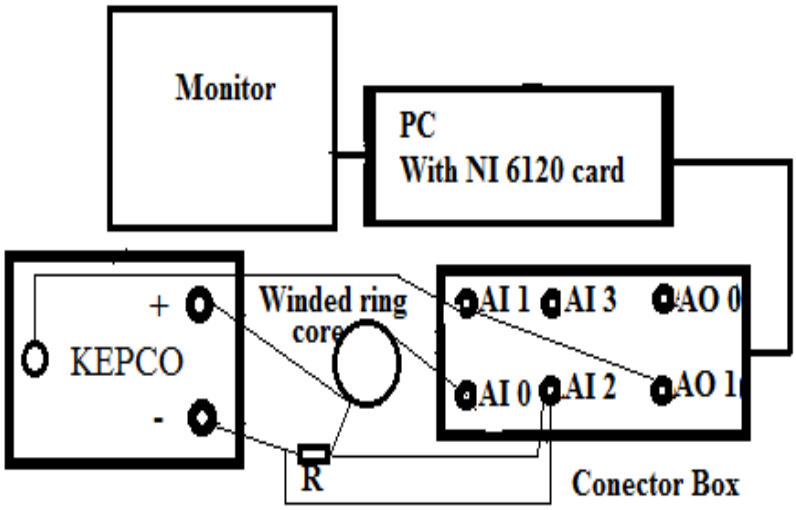

Figure 2.3: Diagram of the LabVIEW controlled hysteresigraph.

With the National Instruments data acquisition card PCI 6120, it is possible simultaneously sent out two signals and record four input-signals. There are three different control programs. These require one output channel and up to 4 input channels. From the output channel the required waveform voltage signal is sent. The voltage *U(t)* sent by the output channel is converted into electric current using the power amplifier (APEX or KEPCO). The generated current passes through the primary winding of the ring shaped sample

or the yoke, and causes a magnetic field *H(t)*. This magnetic field magnetizes the ring shaped sample or the Yoke. The magnetic field strength has been calculated from the current of the primary winding by the following formula

$$H = U_1 \frac{N_1}{R l_m} \tag{2.1}$$

Where *U (t)* is a voltage set by KEPCO amplifier through a shunt resistor R which excites the primary coil of known current. N_1 is the number of primary turns and l_m is the mean magnetic path length. The alternately magnetized sample induces a voltage in the secondary winding. This voltage is picked up by the data acquisition card and is integrated by the LabVIEW program. The induction B is calculated by using the formula:

$$B = \frac{1}{N_2 A} \int U_2 dt \tag{2.2}$$

The measured results are further processed by the LabVIEW program, and the hysteresis characteristics are plotted by LabVIEW functios as well. Results can be saved into files for further use. The whole setup is shown in Figure 3.4.
The advantage of a such a system are:

- The current *I(t)* can be chosen freely as e.g. triangular, sinusoidal, etc.
- Average over several loops which improves the signal - noise ratio.
- Automatic demagnetization of the sample.
- Frequency dependent measurements up to $f = 1000$ Hz.

2.3 Magnetic Measurements in Toroid

Magnetic hysteresis measurements on ring or toroidal core sample equipped with primary winding (excitation) and secondary (pick up) windings have the advantage that the mag-

netic field remains inside the core of the magnetic material and no stray field is produced because no magnetic poles are formed. Ring shaped samples only provide an option for the measurements of average directional magnetic properties of the sample. For measuring magnetic properties along different crystallographic directions (single crystal) or different texture it is appropriate to have geometrically closed set-ups like the square or rectangle called picture or window frame [65].

For magnetic hysteresis measurements on ring or window frame sample equipped with primary and secondary windings some important factors must be considered:

- Before winding the ring, square or window frame sample having sharp edges must be wraped with thin tape to avoid short circuits between sample and winding due to removal of the isolation.

- Windings should be uniformly distributed over the circumference of the closed sample particularly primary windings. However, it is mentioned in the introduction to magnetic Materials by B. D Cullity that if the material is homogeneous and nondirectional, the secondary windings need not to be extended around the sample [65]. Moreover avoid overlapping and twisting.

- Great care is required in counting the number of turns when one has to wind a large number of windings, particularly in number of pick-up windings because this affects the induction field calculation (Eq. 2.2).

- Generally the wire diameter for primary windings is thicker than secondary windings but in some suitable ratio. The main purpose of the selection of suitable wire diameter is to avoid an air gap between sample body and wire as well as between successive windings. Selection of wire diameter for both windings depend on the area of cross-section, sample height to width ratio, outer to inner diameter ratio of the sample, for example the samples measured in this thesis work have outer diameter 10 mm - 8 mm, inner diameter 7 mm - 5 mm and thickness 2 mm - 0.4 mm. The wire diameter used for primary windings was 0.3 mm - 0.5 mm and for secondary windings 0.15 mm - 0.3 mm.

Although a ring specimen is free of demagnetizing (stray) fields, however there are a few disadvantages. The main disadvantage of a toroidal core is the fact that it is difficult to wind, especially for sample small in size and as well as time consuming. Every sample to be measured need new windings. High magnetic field cannot be applied to the sample. This means that sometimes the true saturation can not be achieved. Measurements on ring reveal the average magnetic properties over the various directions.

2.3.1 Different Configurations of Windings

The question here is what is the most exact way to minimize the losses of induction field and to obtain also the high field behavior for measurements of hysteresis on ring shaped samples using primary and secondary windings. For this purpose in order to determine the optimum winding configuration, a ring shaped sample of Fe-Si alloy was wound using different configurations scheme of windings:

(a) Primary windings (N_1) were directly wound homogenously around the circumference of the ring while the secondary (N_2) windings were wound over this.

(b) Secondary windings (N_2) were wound directly onto ring and primary windings over it, both were evenly distributed around the circumference of the ring.

(c) One half of the circumference of the ring was wound by the primary (N_1) and the other half with secondary (N_2) windings.

(d) In this configuration the circumference of ring was divided into four parts. Each part was evenly wound by primary (N_1) and secondary (N_2) windings consecutively.

In all winding configurations the number of primary (N_1) and secondary (N_2) windings were kept constant. The hysteresis loops obtained for these winding configurations are shown in Figure 2.4. It can be seen from hysteresis loop "a" that the low induction magnetization obtained when the secondary (pick up) windings were not directly incontact with sample body because in that case some part of magnetizing flux leakage through the air which cause a reduction in induce voltage in secondary windings. In configuration "c" and "d" the flux is not uniformly distributed over the ring. The highest induction

magnetization was obtained in the second type of configuration "b" where secondary windings (N_2) were directly onto the ring and primary windings over it because in this configuration there is very low leakage inductance when the winding covers the entire magnetic path. The maximum difference in the magnetic field strength was found to be about 3 % and therefore the error in the coercivity was 3 % at a given frequency. However the error in B was up to 4 % depending on the configuration.

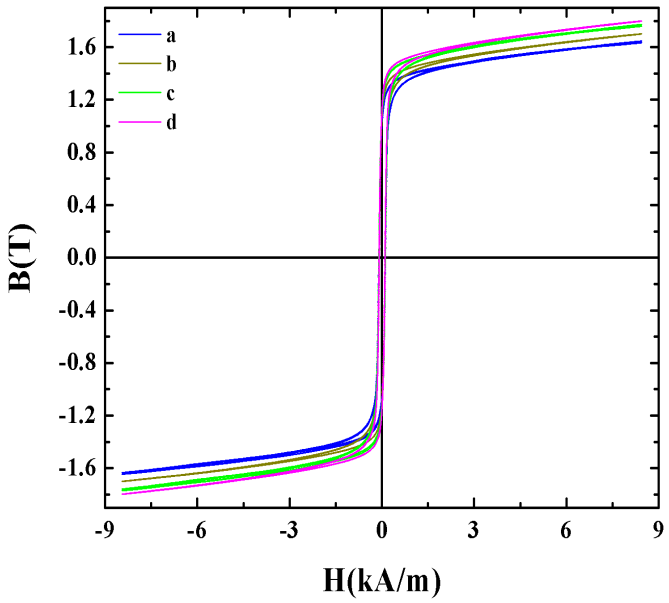

Figure 2.4: Hysteresis loops at different configurations of windings. "a", "b", "c", "d", corresponds to the different configurations mentioned in text.

2.3.2 Effect of Winding Density

The basic question of how accurate and also an appropriate applied field behavior can be established in the tested core to achieve saturation magnetization, was investigated on a ring-shaped sample by using different numbers of primary windings (N_1) while the secondary windings (N_2) were kept constant. Both windings were uniformly distributed around the circumference with secondary below and primary windings above it. For the experiment a pure iron sample was used with the following dimensions: the magnetic path length l_m = 0.0785 m, cross-sectional area A= 2.1×10^{-5} m^2 and secondary turns N_2 = 100. These experiments showed that with increasing winding density a systematic increase of the achieved magnetization is accompanied. Figure 2.5 (a) shows the saturation

induction achieved with the field and (b) shows magnetization as a function of the number of primary windings.

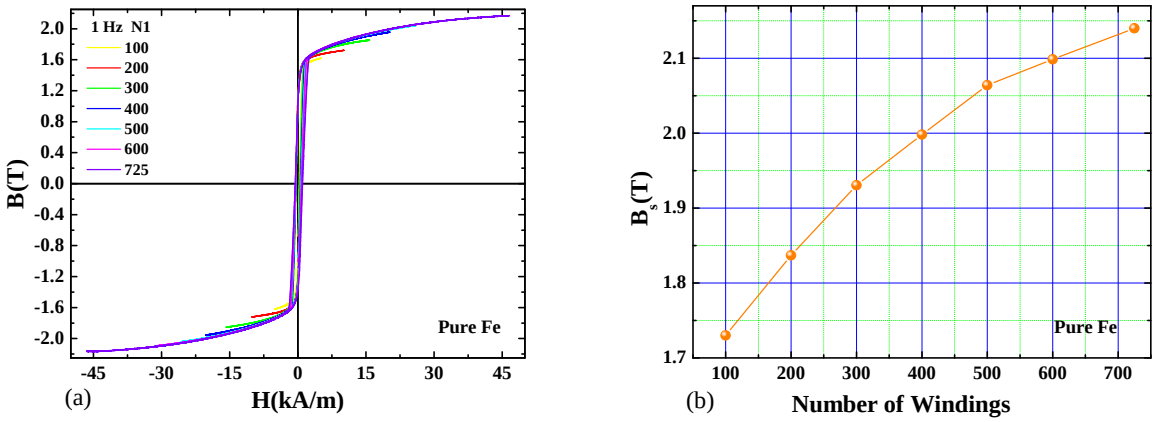

Figure 2.5: (a) Hysteresis loops measured at 1 Hz on pure Fe with different numbers of primary windings (b) Magnetization as a function of the number of the primary windings (N_1).

The magnetic field H produced by the current I is given by the simple formula: $H = N_1 I/l_m$ which shows that by increasing the number of the primary turns (N_1) the maximum field is also increasing. However this is not sufficient as visible by comparing the shapes of the loops measured with different winding numbers; the such obtained hysteresis curves are not identical. This demonstrates that the use of a careful winding scheme is very important for measuring correct and accurate full magnetization curve . Comparative investigations using a single sheet tester gave strong deviations in the shape and magnitude of the loop values [64]. The main problem there is that the unavoidable air gap influences the shape of the loops. In this case also the "true" magnetic field inside of the sample can not be estimated accurately [64].

2.3.3 Effect of Sample Geometry on Magnetic Hysteresis and Optimization of Geometry parameters

In order to measure the directional dependent magnetic properties on closed magnetic circuit a window or picture frame sample is used. The geometrical parameters and winding

configuration used for magnetic hysteresis measurements on window frame shaped samples are problematic in case the window sample have different cross-sections along the length and width dimension. As on magnetic hysteresis measurement the geometry parameters such as magnetic path length, area of cross-section and also winding configuration greatly affects the accuracy of measurements. Therefore the main idea of this investigation was to find an optimum winding configuration for frame shaped samples. Also the correct geometry parameters apply for magnetic hysteresis measurements. For this purpose ring shaped and rectangular window samples were made from the same piece of iron sheet. The rectangle window frame was dimensioned in the way that the cross-sectional area of the width of window was 5 times the cross-section of its length. The cross-section of the ring sample was equal to the cross-section area of the length of the window frame sample. The sketch of each geometry is shown in Figure 2.6. Both samples were equipped with same gauge of copper wire. The ring was first wound with secondary windings and onto it primary windings, both windings were evenly distributed over the whole circumference of the ring. However, for rectangular sample two different winding configurations were considered.

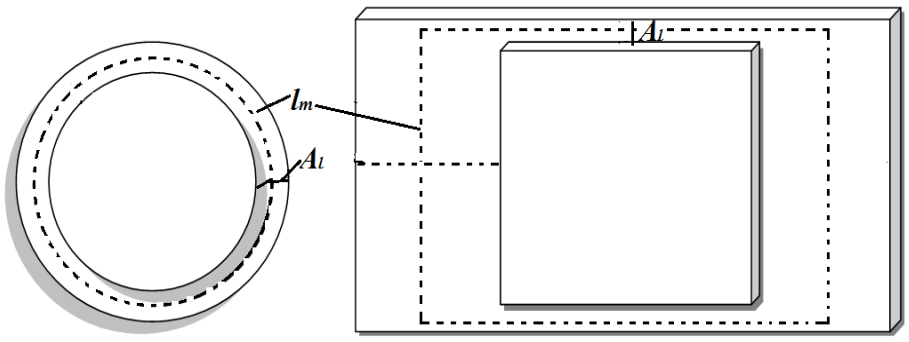

Figure 2.6: Ring and Window frame.

1. In the first configuration the secondary winding was on one thin leg (length) and the primary winding on the other thin leg (length) of the window evenly distributed on entire leg.

2. In second configuration the secondary winding were wound directly on both thin legs sides while primary windings were wound over it on both legs of the window frame.

In both configurations there were no windings on connecting region (bigger cross-sectional area) of the legs. The geometry parameters taken for magnetic hysteresis measurement are given in table 2.1.

Dimensions	*Ring* (m)	*Widow frame* (m)
Mean magnetic path length l_m	0.0786	1.44×10^{-1}
Cross-sectional area of length A_l	-	9.21×10^{-6}
Cross-sectional area of width A_w	-	4.63×10^{-5}
Average cross-sectional area A_{av}	9.23×10^{-6}	2.80×10^{-5}
Total cross-sectional area A_t	-	9.23×10^{-6}

Table 2.1: Geometry Parameters of ring and window frame samples.

For the each measurement the mean magnetic path length of window frame was considered which is equal to the total distance around the middle part of all four side of window (the mean perimeter of frame) shown by dotted line in schematic sketch but taking different cross-sectional areas of window frame. The hysteresis loops were measured at 1 Hz on the ring as well as on the window frame samples as shown in Figure 2.7.

- Loop "a" is measured on a ring sample which is considered as reference. Loops "b" "c" "d" and "e" are measured on window frame sample with different cross-sectional areas and different winding configurations.

- Loop "b" is the result of a measurement by considering the average cross-sectional area of window and winding configuration No. (1)

- Loop "c" is the result of a measurement by considering the cross-sectional area of length (thin leg) of window and winding configuration No. (1)

- Loop "d" is the result of a measurement by considering the average cross-sectional area of window and winding configuration No.(2)

- Loop "e" is the result of a measurement by considering the cross-sectional area of length (thin leg) of window and winding configuration No.(2)

It can be seen from the hysteresis loop "c" that magnetization induction and coercivity comparable to the reference (Ring) could be achieved by considering only the cross-sectional area of the length (thin leg) and using wind winding configuration where secondary windings are placed directly onto the sample and primary windings onto it on both legs uniformly (length). Optimum results were obtained i.e. saturation

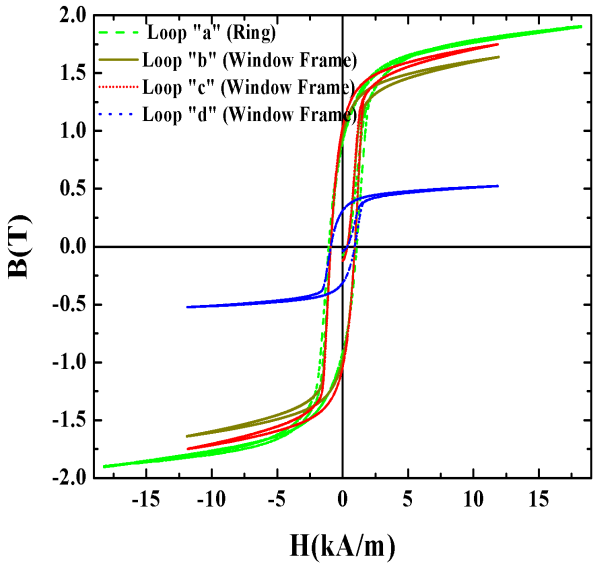

Figure 2.7: Hysteresis loops measured on the ring and the window frame samples.

2.3.4 Pulse Field Magnetometer

A Pulse Field Magnetometer (Hirst Industrial system PFM11) that could charge a 22.5 kJ capacitor bank (5 mF) to 3000 V in approximately 25 seconds using thyristor switches can be used for measuring the hysteresis loop of large samples at room temperature. The whole charging process of PFM, (f/2f)selection (40 ms and 57 ms) and the data acquisition is computer controlled using a Z80 microprocessor which is linked to the PC. The signal is integrated with a stable analogue integrator with selectable time constants. The signals are connected to a 14 bit 5M sample/s two channel ADC card from Datel (model: PCI-416N) directly to the computer. The system is capable of accepting samples up to a 30 mm diameter and 10 mm length within a 1 % pickup homogeneity range. The maximum field is 5 T. It is calibrated with an absolute error in H and M of 1.5 %. Figure

2.9 shows the PFM set available at TU Wien.

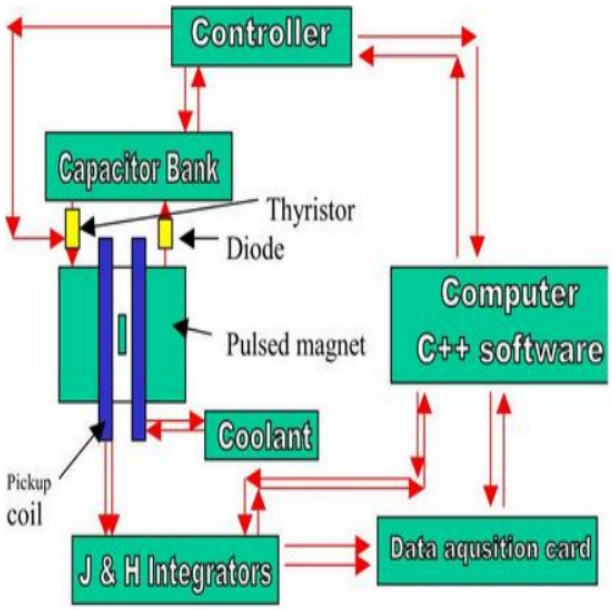

Figure 2.8: Block diagram of the pulse field magnetometer [4].

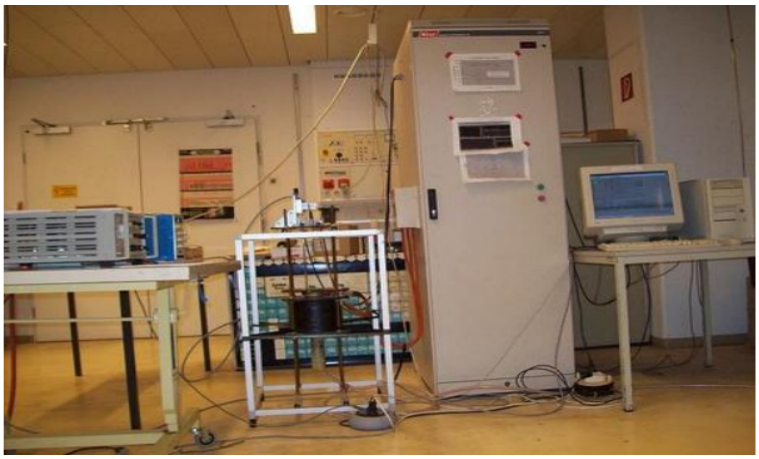

Figure 2.9: Pulse field magnetometer photograph available in TU Wien [4].

2.3.5 Vibrating Sample Magnetometer VSM

Vibrating sample magnetometers (VSM) are used to measure the magnetic properties of soft and hard magnetic materials as a function of magnetic field, temperature and time. A vibrating sample magnetometer (VSM) operates on Faraday's Law of Induction, which tells that a changing magnetic field will produce an electric induction voltage. This voltage can be measured and gives information about the changing magnetic field. The block diagram of a VSM is shown in Figure 2.10. The vibrating sample magnetometer (VSM)

PPMS Q6000 (Quantum Design) available at TU Wien is shown in Figure 2.11. The PPMS Q6000 consists of a liquid Helium Dewar containing a longitudinal superconducting magnet capable of producing a 9 T field and a temperature controller which can operate in the range of 1.9 K to 1000 K.

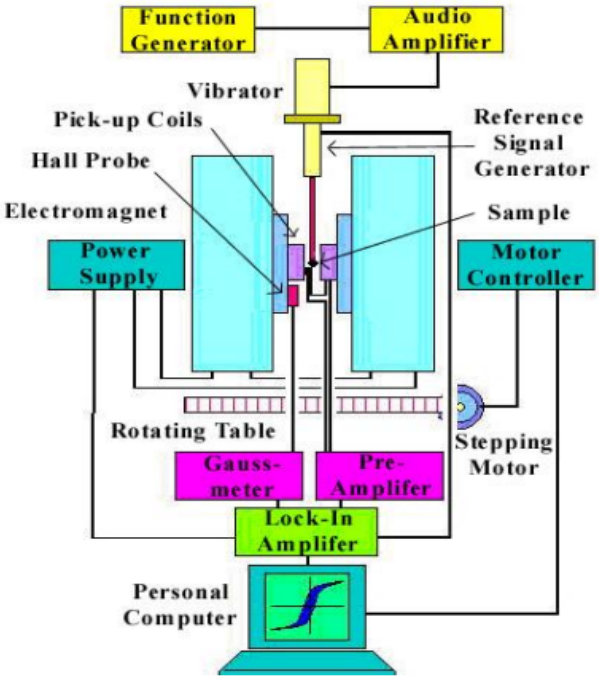

Figure 2.10: Block diagram of the vibrating sample magnetometer (VSM) [4].

Figure 2.11: Vibrating sample magnetometer (VSM) photograph available in TU Wien [4].

Chapter 3

Frequency Dependence of the Coercivity Modeled by Eddy Currents

A simple eddy current model based on the Maxwell equation and the material parameters (electrical resistivity) was developed in order to describe the change of the coercivity with frequency. The model is mathematical (analytic) relatively simple leading to equations that calculates the increase of the coercivity of the material under alternating magnetic field assuming a shielding due to classical eddy currents. The model is based on the fact that in metallic components magnetic flux is reduced due to finite skin depth. The field is maximum at the surface of the material (adjacent to an excitation coil) and decreases exponentially with depth. This behavior of eddy current is known as skin effect and the depth at which eddy current density has decreased to 1/e in material is called Skin depth or standard depth of penetration and is described by the following function.

$$\delta = \sqrt{\frac{\rho}{\pi . f \mu_o \mu_r}} \tag{3.1}$$

δ = *Standard Depth of penetration (meter)*

ρ = *Material electric resistivity [ohm-meter]*

μ_o = *Absolute permeability [Henry/meter]* $4\pi \times 10^{-7}$

μ_r = *Relative permeability*

f = *Frequency [Hertz]*

Eddy current model for μ_r = *constant*:

In the model we assume a cylindrical metallic sample with radius R. The effective coercivity in terms of skin depth which is measured at different radii (x) of the metallic sample is represented by simple geometry shown in Figure 3.1:

The equation describing the coercivity varying with x can be written as:

$$H_c(x) = H(R).exp[\frac{-(R-x)}{\delta}] \tag{3.2}$$

R is calculated as

$$R = \sqrt{\frac{A}{\pi}} \tag{3.3}$$

Where A is the cross-sectional area of the sample

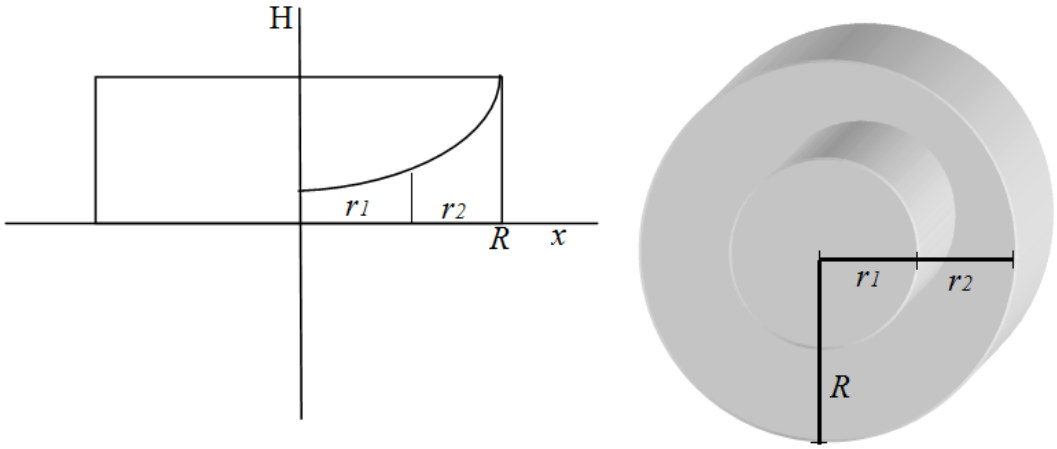

Figure 3.1: Schematic diagram for Eddy current model.

Now the cylindrical sample is divided into two concentric shells with r_1 as a radius of inner shell and r_2 as thickness of the outer shell as shown in Figure 3.1.

Since H_c increases with frequency, the eddy current effect will also increase with frequency

and the shielding effect inside the material becomes stronger since the skin depth decreases with the operating frequency. Equation (3.2) can be written as in term of operating frequency and radii of the cylindrical sample:

$$H_c(f,r) = H(R).exp[\frac{-(R-r)}{\delta}] \tag{3.4}$$

The volume of outer shell and inner core shell are assumed to be equal if: the coercivity is reached if the outer shell of the cylinder is switched and the volume of the outer shell is the same as the inner core. As the volume of the inner core is equal to the outer shell:

$$\pi R^2 h - \pi r_1^2 h = \pi r_2^2 h \tag{3.5}$$

Since the volume of outer cylinder is equal to inner cylinder. Therefore $r_1^2 = r_2^2$. Hence equation 3.5 implies:

$$r_1 = \sqrt{\frac{1}{2}}R \tag{3.6}$$

The condition when an external field H_{ext} which is applied parallel to the symmetry axis decreases within the magnetic cylinder at position r due to eddy currents Eq. 3.4 can be written as:

$$H_c(f,r) = H_{ext}.exp[\frac{-(R-r)}{\delta}] \tag{3.7}$$

$$H_{ext} = H_c(f,r).exp[\frac{(R-r)}{\delta}] \tag{3.8}$$

Due to eddy currents we expect the outer core to switch first since the field decays according to Eq. (3.8) towards the center. Hence H_{ext} is equal to the frequency dependent coercive field $H_c(f)$ *i.e*, $H_{ext} = H_c(f)$

The condition for the applied field H_{ext} in order to reduce the magnetization to zero is

given by: $H(r,f) = H_c(0)$

Where $H_c(0)$ is the coercivity field in the limit of $f = 0$.

Now Eq. 3.8 can be written as with condition $H(r_1,f) = H_c(0)$:

$$H_{ext} = H_c(f) = H_c(0).exp[R(1 - \frac{1}{\sqrt{2}}).\sqrt{\frac{\pi.f\mu_o\mu_r}{\rho}}] \tag{3.9}$$

The most important parameter in Eq. (3.9) is the relative mean permeability which can be estimated from this model. A comparison between a modeled curve behavior (considering a relative permeability (μ_r) as constant as in Eq. (3.9)) and the experimentally determined H_c versus f shows that H_c increases with the square root of f as described by Eq. (3.9), whereas the experimental curve starts to saturate for high frequency values. Therefore this model is not satisfying the general trend of frequency dependence of the coercivity as shown in Figure 3.2.

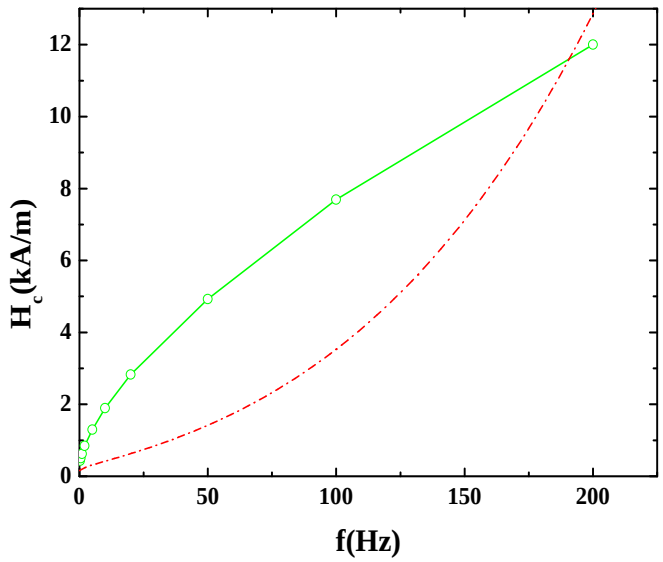

Figure 3.2: Comparison between model and experimental curve of H_c versus f. Solid line (experimental) and dotted line (model)

Eddy current model for $\mu_r = k/[H_c(f)]^n$:

Generally it can be assumed that the permeability scales reciprocal with the coercivity [66]. Therefore an increasing coercivity due to an increase of the frequency may cause

a reciprocal decreasing permeability. This leads to an improved eddy current model by assuming $\mu_r(f)$ as a function of $H_c(f)$ which can be described by the simple formula:

$$\mu_r = k/[H_c(f)]^n \tag{3.10}$$

Where k is a chooseable fit parameter

With this assumption equation (3.9) can be rewritten as:

$$H_{ext} = H_c(f) = H_c(0).exp[R(1 - \frac{1}{\sqrt{2}}).\sqrt{\frac{\pi.f\mu_o k}{[H_(f)]^n \rho}}] \tag{3.11}$$

To simplify the equation one can take the log on both sides

$$\ln H_{ext} = \ln H_c(0).exp[R(1 - \frac{1}{\sqrt{2}}).\sqrt{\frac{\pi.f\mu_o k}{[H_(f)]^n \rho}}] \tag{3.12}$$

$$\ln H_{ext} = \ln H_c(0) + R(1 - \frac{1}{\sqrt{2}}).\sqrt{\frac{\pi.f\mu_o k}{[H_(f)]^n \rho}} \tag{3.13}$$

$$\ln H_{ext} - \ln H_c(0) = R(1 - \frac{1}{\sqrt{2}}).\sqrt{\frac{\pi.f\mu_o k}{[H_(f)]^n \rho}} \tag{3.14}$$

Squaring both sides we get new equation

$$f = [\frac{\ln H_{ext} - \ln H_c(0)}{R(1 - \frac{1}{\sqrt{2}})}]^2.\frac{\rho}{k\pi\mu_o} \tag{3.15}$$

The model Eq. (3.15) describes much better the frequency dependent magnetic behavior (coercivity) of soft magnetic materials measured in this thesis. Additionally by fitting the model equation on experimental data allows to determine the average relative permeability of the materials.

3.1 Analysis of the Frequency Dependence of Coercivity:

The coercivity (H_c) is an important parameter of magnetic materials for defining their role in technical applications. The coercivity of a magnetic material depends upon the domain-wall movement, which is greatly influenced by the microstructural changes induced by mechanical and thermal treatments. At quasi static frequencies the increase in coercivity is due to structural defects such as particles of a nonmagnetic phase or voids in the magnetic material tend to restrict the motion of domain walls.

An analysis of the frequency dependence of coercivity is helpful in understanding the dynamic coercivity mechanism in soft magnetic materials. There are several possibilities to analyze the frequency dependence of H_c very general:

1. One can assume that H_c scales with some power of frequency *(f)* which leads to Eq. (3.16) or

2. One can develop $H_c(f)$ into different powers of frequency (see Eq. 3.17).

$$H_c(f) = a + b.f^c \tag{3.16}$$

$$H_c(f) = d + e.\sqrt{f} + g.f \tag{3.17}$$

Where parameters a and d in the equations correspond to the coercivity at 0 Hz i.e. *Hc(f=0)* and b, c, e and g are free fit-parameters. These parameters depend on the microstructure as well as the magnetic field amplitude H_o and also on *H(t)*. In equation (3.16) coefficient e described the normal "classical" eddy currents whereas the anomalous eddy current damping represented by g becomes dominant especially at higher external fields .

A. Zhukov and coworker [67] analyzed the frequency behavior of the coercivity in amor-

phous materials with the general formula 3.18 which was derived for triangular wave form of the field with : *H(t)=4fH$_o$t*:

$$H_c(f) = H_c(0) + B.(f.H_o)^{1/n} \tag{3.18}$$

Where H_o is the field amplitude and n can vary between 1 and 3 depending on the geometry and on the microstructure of the material as well as on the frequency range considered. Formula (3.18) is equivalent with a fit using Eq. (3.16); with the parameter B corresponding to b/[H$_o$]$^{1/n}$ which correlates to the dynamic coercivity field.

The term *H$_c$(0)* corresponds always to the zero frequency extrapolated which is the "true" coercivity. The power factor c in equation (3.16) that correspond to a high frequency solution or to the effect that also anomalous eddy current damping of the domain walls occur as described in [67], therefore its value should be comparable to n in Eq. (3.18).

It can be shown that formula (3.9) and (3.17) are equivalent. If one makes a series expansion of formula (3.9):

$$H_{ext} = H_c(0)[1 + R(1 - \frac{1}{\sqrt{2}})\sqrt{\frac{\pi f \mu_o \mu_r}{\rho}} + R^2(1 - \frac{1}{\sqrt{2}})^2 \frac{\pi f \mu_o \mu_r}{\rho} ....] \tag{3.19}$$

By comparing the Eqs (3.19) and (3.17) that the coefficients e and g have the following *meaning*:

$$e = H_c|_{f=0} R(1 - \frac{1}{\sqrt{2}})\sqrt{\frac{\pi.\mu_o \mu_r}{\rho}} \tag{3.20}$$

$$g = H_c|_{f=0} R^2(1 - \frac{1}{\sqrt{2}})^2 \frac{\pi.\mu_o \mu_r}{\rho} \tag{3.21}$$

The parameters e and g obtained by fitting Eq. (3.17) on the experimental data are used to get the relative permeability of the materials from relations (3.20) and (3.21), which can be compared with the experimentally determined values.

The relative permeability μ_r can be determined experimentally directly by using minor loop measurements from which the plot of *dB/dt* versus the field *H(t)* can be derived and then according to formula (3.25) μ_r(H) can be calculated.

$$B = \mu_o \mu_r H \tag{3.22}$$

$$\frac{\Delta B}{\Delta t} = \mu_o \mu_r \frac{\Delta H}{\Delta t} \tag{3.23}$$

$$\mu_r = \frac{1}{\mu_o} \Delta B/\Delta t \frac{1}{\Delta H/\Delta t} \tag{3.24}$$

$$\mu_r = \frac{1}{\mu_o} \Delta B/\Delta t \frac{4}{f H_{max}} \tag{3.25}$$

Applied triangular field *H(t)* allows to calculate $\Delta H/\Delta t$ from H_{max}/T/4 as shown in Figure 3.3; $\Delta B/\Delta t$ is taken directly from the measurement.

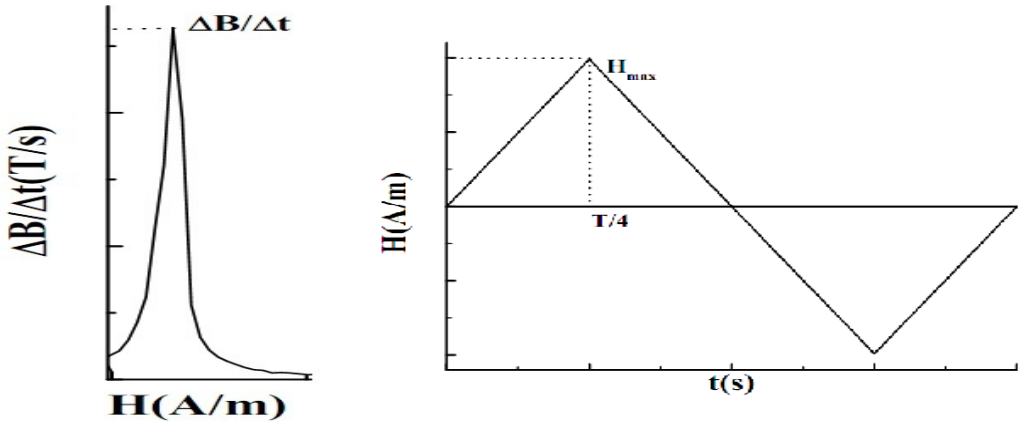

Figure 3.3: *dB/dt* versus *H(t)* loop and triangular form of field *H(t)*.

Chapter 4

Magnetic studies of Severe Plastically Deformed Soft-Magnetic Materials

A number of studies show that the severe plastic deformation (SPD) strongly influences the magnetic hysteresis characteristics of soft magnetic metals [68–70]. The extrinsic magnetic properties *i.e.* coercivity, remanence, permeability and losses are affected by stress, strain, grain size, heat treatment and the presence of impurities. The severe plastic deformation (SPD) induces residual stresses and influences the magneto-elastic energy. The coercivity, one of the important parameter of a soft-magnetic material, is determined by the formation and mobility of domain walls, which depends on the actual microstructure. Therefore the ratio of the domain wall width (50-100 nm in soft-magnetic Fe) to the dimensions of the local stress field is very important. Below a grain size of about 100 nm it can be expected that the grains couple magnetically over the grain boundaries. This causes a magnetic softening as soon as the grain size of the alloy becomes smaller than the ferromagnetic exchange length, which is of the order of the domain wall width [51]. The maximum in H_c occurs at a grain size of about 100 nm (single domain particles). For smaller grains the exchange coupling reduces the effective anisotropy as well as the coercivity. Exchange coupled materials show naturally no super paramagnetism. The

complex situation in a severely deformed material is determined by the interplay between domains and domain walls with dislocations or local stresses areas.

In this work the severe plastic deformation effects on the magnetic properties of soft magnetic materials such as, pure iron (Fe), iron alloys with silicon (Si) and Cobalt (Co) and pure nickel (Ni) has been investigated via the frequency dependence of magnetic hysteresis measurements. For this purpose pure Fe of 99.98% purity, Fe-3wt% Si, Fe-6.5wt% Si, and Fe-17wt% Co were processed by a High Pressure Torsion (HPT) technique described in the experimental chapter. Prior deformation the rod-shaped materials were annealed at 800°C for 2 hours in a vacuum furnace to guarantee an initial state which is free of any pre-deformation. From each material a set of four samples were produced and all samples had a diameter of 8 mm. These samples were HPT deformed at liquid nitrogen temperature (77 K), ambient temperature (298 K), and 723 K, 0.4 T_{hom}(= T_{HPT} /$T_{melting}$) under a pressure of 40t and the pressing tool made 3 complete turns with the shear strain about $\epsilon = 35$. One sample from each set kept un-deformed as a reference. Ring shaped samples were made from the outside of the thin HPT deformed plates, which are in the saturated state of deformation and magnetically the best choice for hysteresis measurements. The HPT processing parameters are given in Table 4.1.

Iron has different phases, at room temperature up to 912°C iron is in the form of ferrite, or α-iron, a body-centered cubic structure (bcc) corresponding to the ferromagnetic ferritic phase. At 912°C it changes to γ-iron and range up to 1394°C, which is face-centered cubic called the austenitic phase and is somewhat softer [71] . At 1535°C iron melts, and boils at 3000°C. The density of α-iron is 7.86 g/cc. Saturation magnetization is about 2.15 T at room temperature [29]. Body centered cubic (bcc) Fe exhibits anisotropic magnetostriction constants of different signs: λ_{100} = 20 ppm and λ_{111} = -16 ppm (1 ppm corresponds to a relative change in length of $1x10^{-6}$) at room temperature [72]. These considerations reveal that in (polycrystalline) steel a very complex situation determines the interplay between hysteresis parameters (domain walls) and dislocations or stresses.

Sample	T_{HPT}	n	t	d_o	d_i
Fe	-	0	0.772	7.053	5
Fe	RT	3	0.516	7.010	5
Fe	450^{o}C	3	0.770	7.026	5
Fe	N_2	3	0.510	6.910	5
Fe-3wt%Si	-	0	0.810	7.053	5
Fe-3wt%Si	RT	3	0.638	7.010	5
Fe-3wt%Si	450^{o}C	3	0.637	7.026	5
Fe-3wt%Si	N_2	3	0.653	6.910	5
Fe-6.5wt%Si	-	0	0.781	7.053	5
Fe-6.5wt%Si	RT	3	0.640	7.010	5
Fe-6.5wt%Si	450^{o}C	3	0.657	7.026	5
Fe-6.5wt%Si	N_2	3	0.653	6.910	5
Fe-17wt%Co	-	0	0.781	7.053	5
Fe-17wt%Co	RT	3	0.640	7.010	5
Fe-17wt%Co	450^{o}C	3	0.657	7.026	5
Fe-17wt%Co	N_2	3	0.653	6.910	5

Table 4.1: HPT parameters as used for the Fe, Fe-3 wt%Si, Fe-6.5 wt%Si, Fe-17wt %Co samples, T_{HPT}-HPT treatment temperature; n-number of turns; t- thickness of sample before HPT; d_o-outer diameter; d_i-inner diameter.

Silicon is a non magnetic element, considered as one of the most effective alloying element for soft magnetic materials. The main purpose of addition of silicon to Fe is to get high electric resistance, high permeability and as possible as low steel's hysteresis loss [26]. Iron alloys with silicon are widely used in transformers, motors, and power generators. The 3-4wt% content of Si in Fe is known as a electrical steel or transformer steel. The saturation polarization of this material is about 2 T, its coercivity is about 10 A/m. The magnetic losses of iron-silicon alloys can be improved by increasing the Si to 6.5-wt% Si thus achieving a high permeability, acceptable saturation magnetization, high specific resistivity, accompanied by a nearly zero magnetostriction combined with low core loss [73]. When compared with the conventional Fe-(3 wt%)Si alloys, the specific electric resistivity increases from 4.5$\times$ 10^{-7} to 8.0$\times$ 10^{-7} $\mu\Omega$ m, anisotropy lowered from K = 3.6 x 10^4 J/m^3 to 2.1 x 10^4 J/m^3 [65, 73, 74].

4.1 Microstructure at Different Processing Temperatures

Microstructural studies of the severely deformed discs were made on a Philips CM12 transmission electron microscope operating at 120 kV. Figure 4.1 presents sequence of TEM-based grain size maps for Fe-17 wt% Co alloy. All deformation states processed at different HPT temperatures correspond to an equivalent strain of $\epsilon_{eq} \sim 45$ (see insets). It can be seen clearly from Figure 4.1 that in the initial state the coarse grains are mostly in polygonal shape and the larger grains are surrounded by smaller ones. In alloy composition Fe-17 wt% Co, the coarse grains are mostly polygonal in shape before HPT deformation and larger grains are surrounded by smaller ones with mean grain sizes around 20.18 μm. Crystallite sizes extremely decreased in the highly deformed states. Deformed microstructures are shown in Figure 4.1 following HPT at 723, 293 and 77 K, respectively [5].

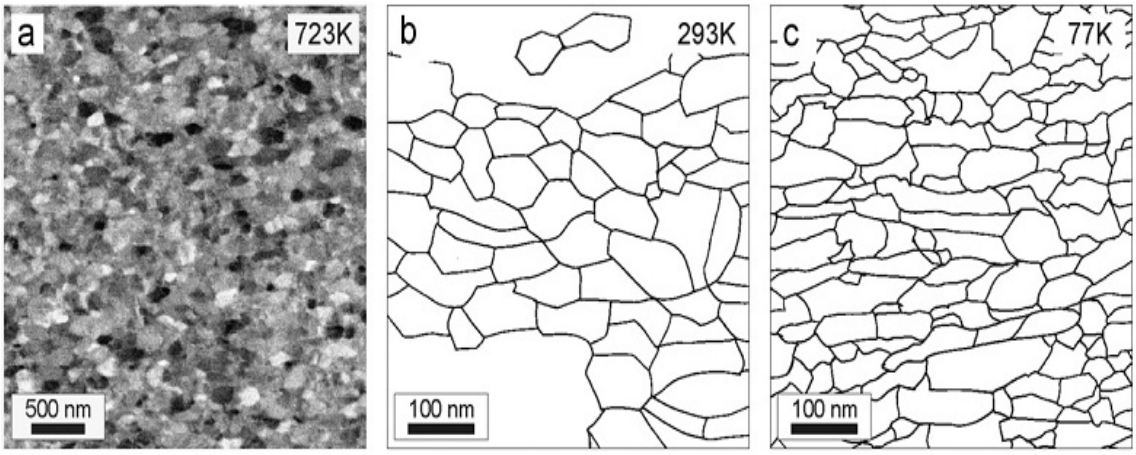

Figure 4.1: Grain size maps for Fe-17 wt% Co alloy correspond (a) 723 K, (b) 293 K and (c) 77 K [5].

The TEM measurements were performed in tangential direction of the disc. After HPT the mean crystallite size as calculated by the area fraction method decreased from 270 to 83 and 72 nm after HPT deformation at 723, 293 and 77 K respectively.One can clearly see by comparing the microstructures of Fe-17 wt% Co in Figure 4.1(b,c) that both the grain size and the grain shape have changed. Crystallites formed as result of HPT deformation

at 723 K are more polygonal in shape but at lower processing temperature (77 K), the grains mostly become elongated parallel to the shear direction as depicted in Figure 4.1c. This can be attributed to an increase in dynamic recovery rate at higher processing temperatures. Thermally activated cross slip of screw and climb of edge dislocations are enhanced with increasing processing temperatures, which ensure the annihilation and rearrangement of glide dislocations in low energy dislocation walls. Moreover materials with high stacking fault energies, as in the present work, tend to large extents of dynamic recovery, which affects the resulting saturation microstructure.

4.2 Microhardness Measurements

The Vickers hardness tests were performed by interval of 0.5 mm along the circumference of sample using a load of 1000 g and a dwell time of 15 s. The results of the microhardness measurements are summarized in Figure 4.2 where the Vickers hardness (at a radius of 3 mm) is plotted as function of the HPT temperature.

Since the deformation is based on the torsional straining of the small discs, characteristic feature in HPT deformation is the development of a highly inhomogeneous radial dependent microstructure.

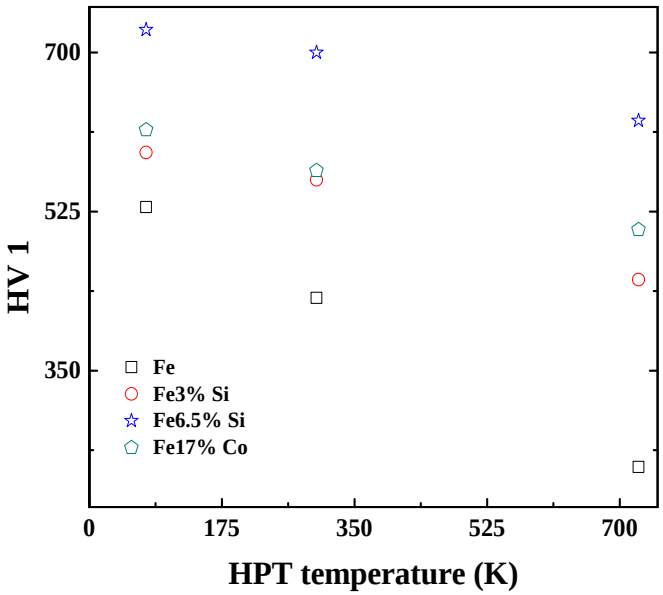

Figure 4.2: Vickers hardness as a function of the HPT processing temperature.

The induced microstructural refinement strongly depends on the local strain at any point within the disk. Therefore in order to ensure homogeneous microstructures in the sample, the rings for the magnetic characterizations were fabricated from the region between radii of 2.5 mm and 3.5 mm. It is obvious from the data presented in Figure 4.2, corresponding to the same total strain but different HPT temperatures, that the microhardness decreases with increasing processing temperatures.

It should be noted that the high temperature state corresponds to 0.4 T_{hom} and result in the shift in the nickel data point. The lowest microhardness values after HPT deformation were found in pure Ni followed by pure Fe. The main difference in these two materials is based on their different crystal structures and different Peierls potential which results in higher Vickers hardness for Fe. The influence of alloying is reflected from higher micro hardness values for the materials Fe-17 wt% Co, Fe-3 wt% Si and Fe-6.5 wt% Si where the highest micro-hardness values were found for Fe-6.5 wt% Si composition. It seems that silicon is one of the most effective alloying elements for soft-magnetic materials as compared to cobalt. The high potential of iron alloys containing 6-7 wt% Si as high permeability, an acceptable saturation magnetization, low magnetostriction and low power loss for ferromagnetic applications has been known for some time [73]. Alloy compositions Fe-3 wt% Si and Fe-17 wt% Co gives almost the same microhardness [5].

4.3 Magnetic Hysteresis Measurements of HPT Deformed Fe and Fe-Si/Co Alloys

Magnetic hysteresis were measured on hysteresigraph described in chapter 2. Ring shaped samples were exhibited with primary and secondary windings. Samples with their geometry dimensions and parameters used for hysteresis measurements are listed in Table 4.2. All magnetic measurements were performed under triangular magnetizing current in order to obtain constant dH/dt. The samples were demagnetized before each measurement.

Figures 4.3, 4.4, 4.5 and 4.6 present hysteresis loops of un-deformed and HPT-deformed

Sample	*Cross-Sectional Area* $A(m^2)$	*Magnetic Path Length* $l_{eff}(m)$	*Primary Turns* (N_1)	*Secondary Turns* (N_2)
Fe(Und)	$8.35*10^{-7}$	0.019	89	61
Fe(RT)	$4.87*10^{-7}$	0.0187	64	64
Fe(450°C)	$6.5*10^{-7}$	0.019	93	63
Fe(N_2)	$5.04*10^{-7}$	0.019	95	64
Fe-3wt%Si(Und)	$7.7*10^{-7}$	0.0187	90	50
Fe-3wt%Si(RT)	$5.8*10^{-7}$	0.019	92	63
Fe-3wt%Si(450°C)	$5.6*10^{-7}$	0.019	94	63
Fe-3wt%Si(N_2)	$5.6*10^{-7}$	0.0186	92	61
Fe-6.5wt%Si(Und)	$5.6*10^{-7}$	0.187	90	60
Fe-6.5wt%Si(RT)	$7.5*10^{-7}$	0.0187	94	63
Fe-6.5wt%Si(450°C)	$6.4*10^{-7}$	0.019	95	63
Fe-6.5wt%Si(N_2)	$6.3*10^{-7}$	0.0188	96	64
Fe-17wt%Co(Und)	$7.5*10^{-7}$	0.019	80	62
Fe-17wt%Co(RT)	$5.8*10^{-7}$	0.019	93	63
Fe-17wt%Co(450°C)	$6.3*10^{-7}$	0.019	98	66
Fe-17wt%Co(N_2)	$6.6*10^{-7}$	0.019	92	61

Table 4.2: Geometry dimensions and Parameters of HPT-treated Fe, Fe-Si/Co samples as used for the hysteresis measurements.

Fe, Fe-3 wt% Si, Fe-6.5 wt% Si and Fe-17 wt%Co (P800) samples respectively. Measurements were performed at room temperature in the frequency range of 0.25 Hz to 1 kHz. The maximum average applied field was about 20000 A/m. It can be seen from the width of the hysteresis loops that the coercivities (H_c) of all samples increased slightly at low frequencies 0.25-20 Hz, but at higher frequencies *i.e.* 50 Hz and above it increased sharply. The sharp increase in coercivity (H_c) at high frequencies is well known in iron (conductive material) due to the increasing effect of eddy currents induced in the material with increasing frequency [29]. The coercivity of Fe deformed at 450°C (723 K) was much higher than that of other deformed Fe samples, which can be seen from hysteresis loops (see Fig.4.3c).

Although addition of non magnetic silicon lowers the saturation flux but significantly decreased the coercivity. For example the coercivity reduced up to factor 2.5 with 3 wt%Si as compared to pure un-deformed iron whereas the electrical resistivity of pure iron increases 4.5 times with the 3-wt%Si and 8 times with 6.5-wt%Si [73, 74] thereby reducing the eddy current. Moreover with increasing Si contents also decreases the magnetocrystalline anisotropy constant K_1 [29] which is obvious from the width of the hysteresis loops

shown in Figure 4.4, and 4.5.

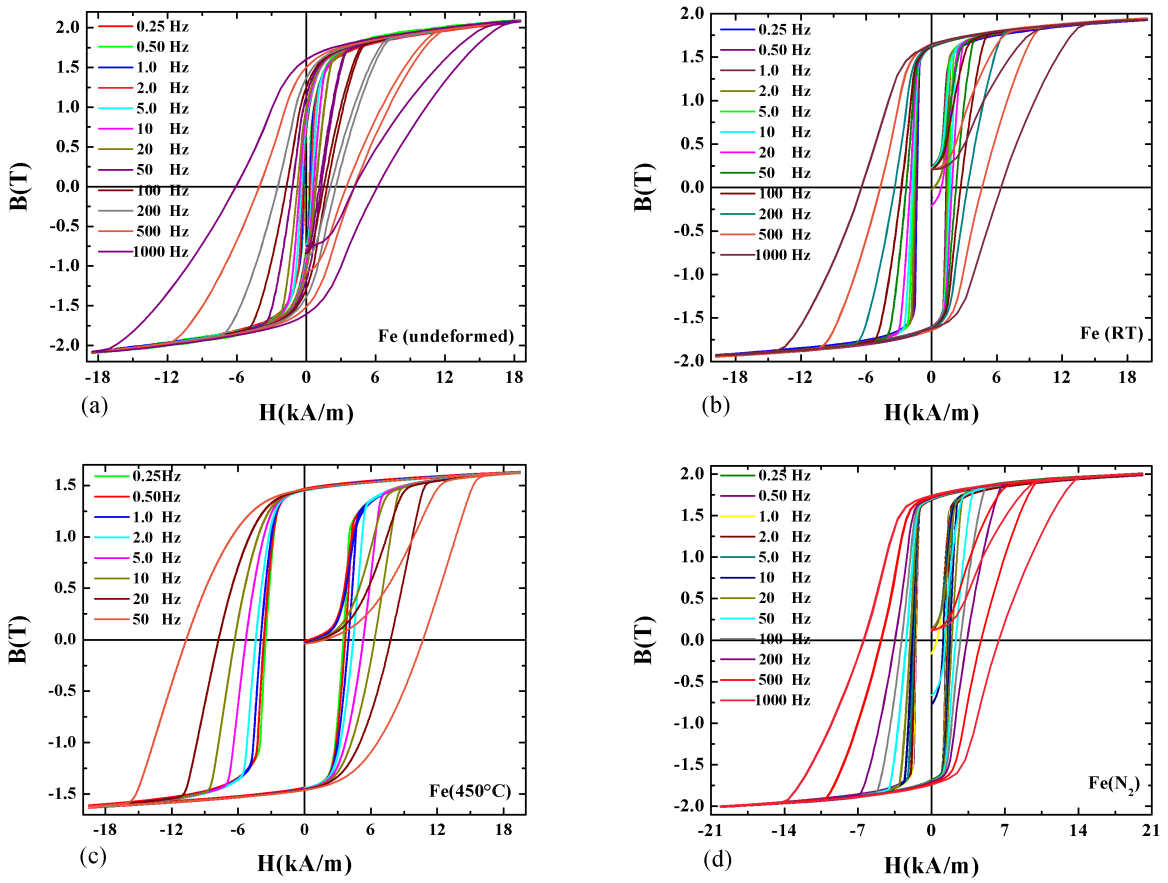

Figure 4.3: The frequency dependence hysteresis loops of HPT-trated pure Fe (a) un-deformed, (b) deformed at 300 K (RT), (c) deformed at 723 K and (d) deformed at liquid (N_2) temperature.

The coercivity of all HPT-deformed samples at low frequencies for example at 0.25 Hz is considerably high as compared to un-deformed material because although the grain size reduced up to nano scale with SPD deformation but still the size is much higher than the exchange coupling length. Moreover the induced microstresses during the deformation increased the number of dislocations and lattice defects which lead to domain wall pinning. The deformation also increased the magnetoelastic energy ($\lambda.\sigma$) which resulted in an increase of the coercivity. However at higher frequencies the effect of eddy current is comparatively less in HPT-deformed samples as compared to un-deformed because the deformation induced dislocations also enhance the resistivity of the material. It

was observed that the coercivity of HPT-treated samples increased with increasing HPT processing temperature except Fe-6.5%wt Si.

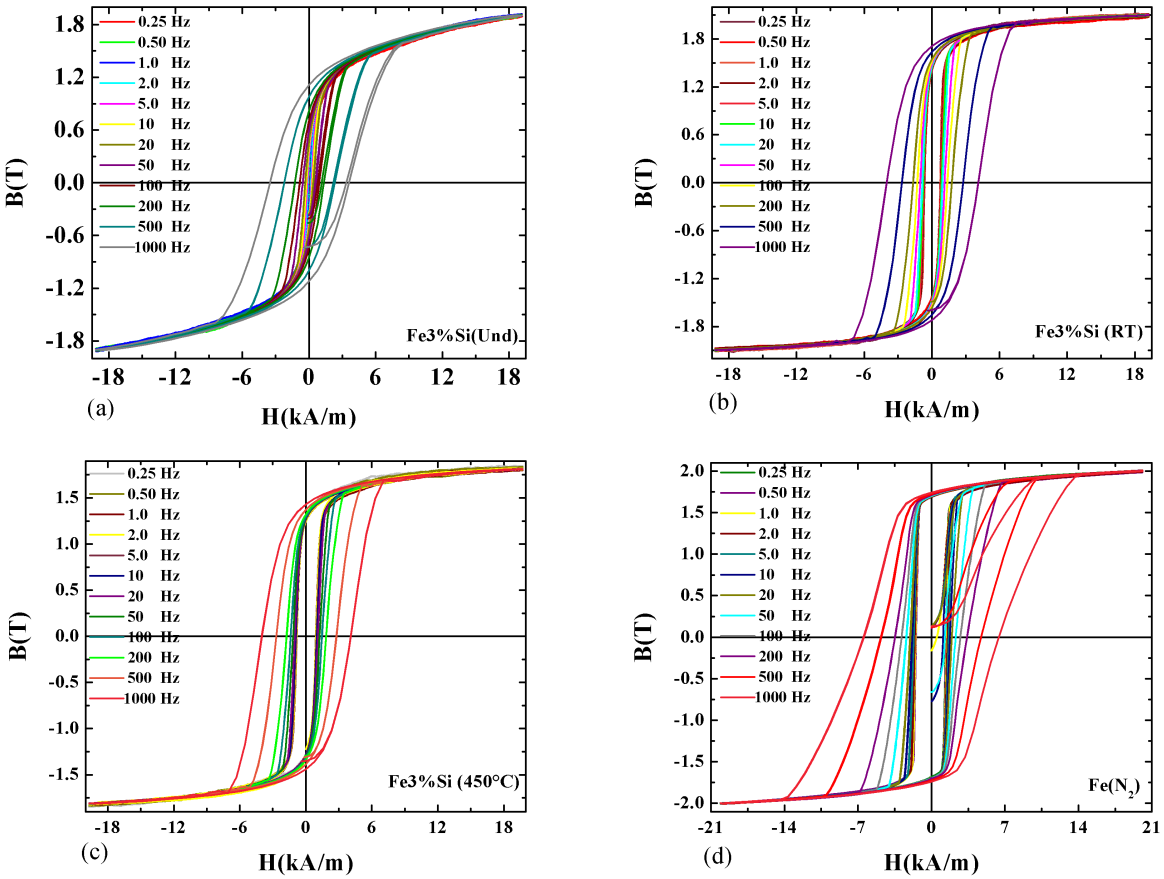

Figure 4.4: The frequency dependence hysteresis loops HPT-treated Fe-3 wt%Si (a) undeformed, (b) deformed at 300 K (RT), (c) deformed at 723 K and (d) deformed at liquid (N_2) temperature.

The coercivity of samples that were HPT-deformed at 450°C was significantly higher (except Fe-6.5 wt%Si) as compared to samples deformed at room temperature and 77 K, particularly the coercivity of Fe (450°C) which can be observed from the width of the hysteresis loops (see Figure 4.3c) and can also be seen from the dependence of the coercivity on the HPT processing temperature (Figure 4.7). The high coercivity of samples deformed at 450°C might be due to commencement of crystallization, larger internal stresses or to a larger inhomogeneity. The grain size increases with increasing deformation temperature for example as can be seen from TEM analysis Figure 4.1 that the mean grain

size Fe-17 wt%Co found to be 270 nm, 83 nm and 72 nm at 450°C, RT, and N_2, HPT processing temperature respectively and also the grain size and the grain shape changed with HPT processing temperature. The grains are more polygonal in shape at 450°C (723 K) but at liquid nitrogen (77 K) the grains are mostly elongated parallel to the shear direction. The most pronounced sensitivity on the deformation temperature has been observed for pure iron, where the crystallites after 450°C processing were determined to be about 450 nm [38].

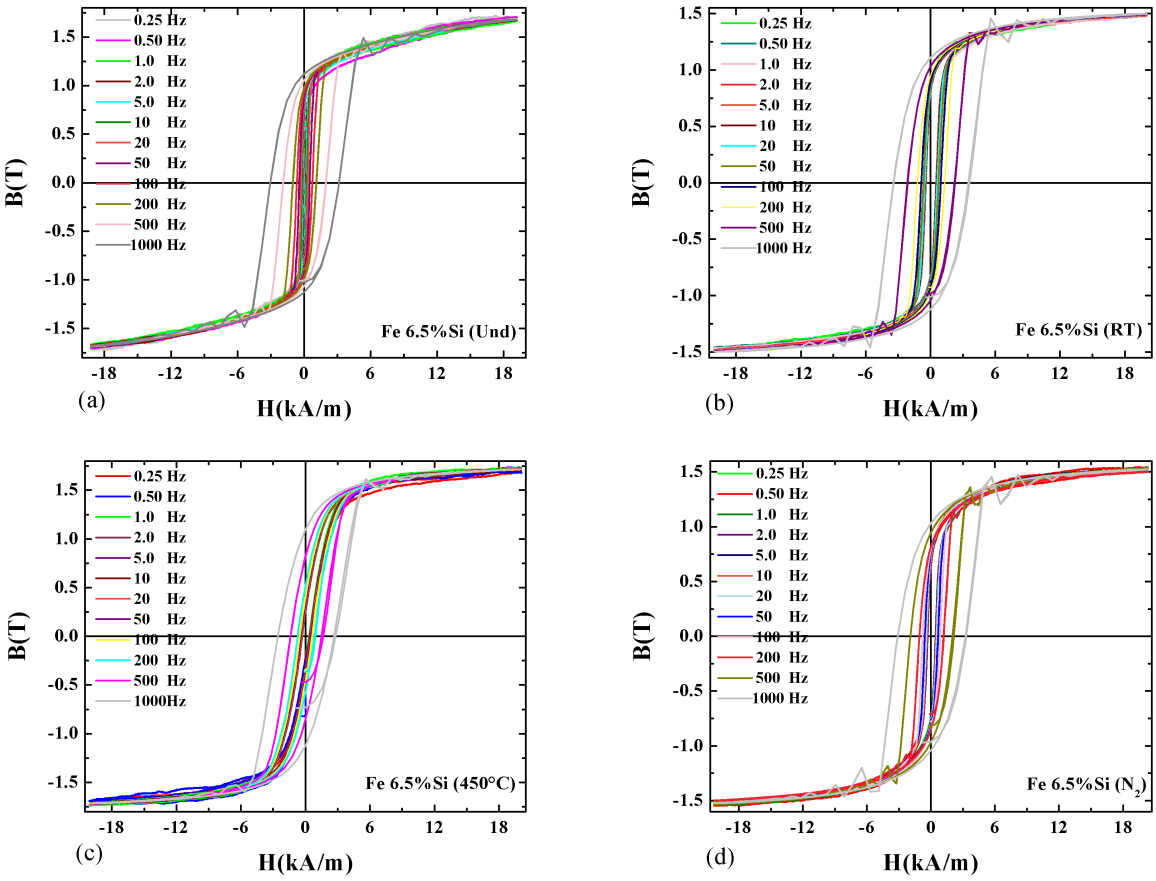

Figure 4.5: The frequency dependence hysteresis loops of HPT-treated Fe-6.5 wt%Si (a) un-deformed, (b) deformed at 300 K (RT), (c) deformed at 723 K and (d) deformed at liquid (N_2) temperature.

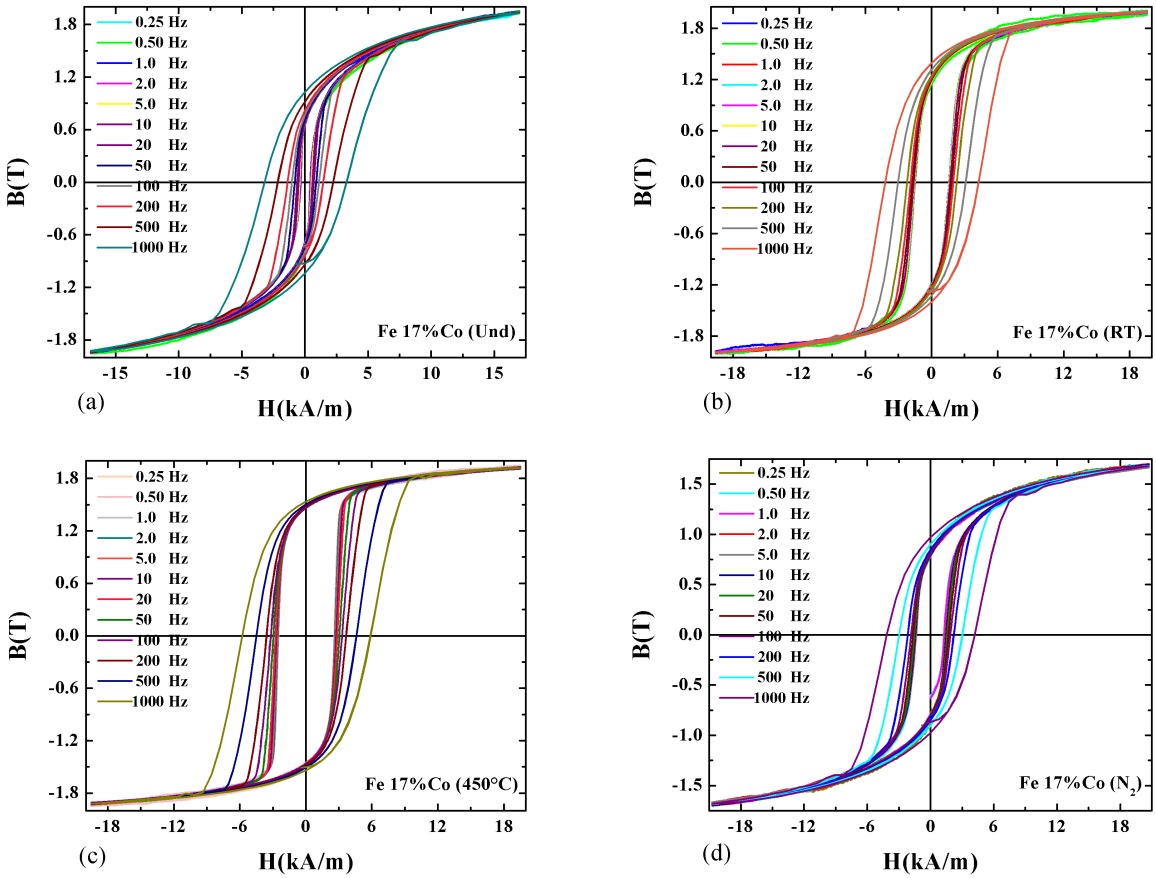

Figure 4.6: The frequency dependence hysteresis loops of HPT-treated Fe-17 wt%Co (a) un-deformed, (b) deformed at 300 K (RT), (c) deformed at 723 K, and (d) deformed at liquid (N_2) temperature.

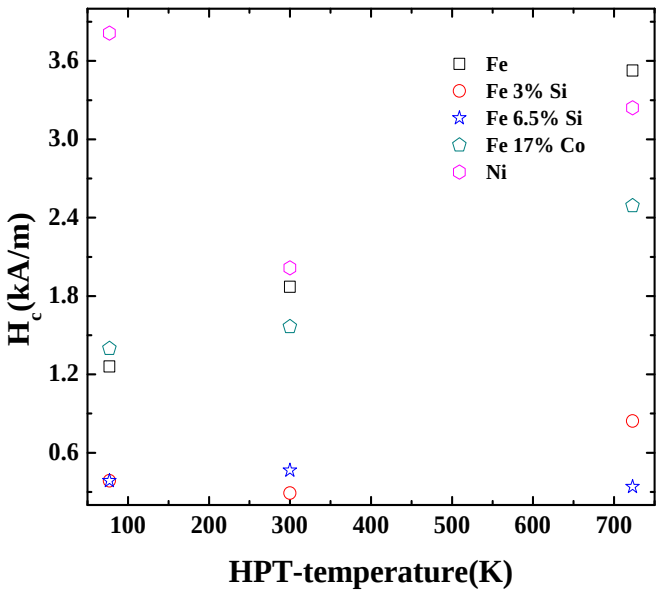

Figure 4.7: Dependence of the zero extrapolated coercivity versus the HPT-deformation temperature for: pure Fe, Fe-3 wt%Si, Fe-6.5 wt%Si, Fe-17 wt%Co (P800) and Ni.

Figure 4.8 shows the dependence of the coercivity on the square root of the frequency *f*. The coercivity (H_c) of all samples was evaluated from the width of hysteresis loops with an accuracy of ± 4 A/m at the measured frequencies. The linear dependence of coercivity with the square root of frequency shows classical eddy current behavior [75–77]. Iron samples, shows more linear behavior of coercivity with square root of frequency particularly at higher frequencies as compared to Fe-Si samples (see Figure 4.8, which indicates that mainly eddy currents are responsible for the strong increase in the coercivity with increasing frequency in Fe samples.

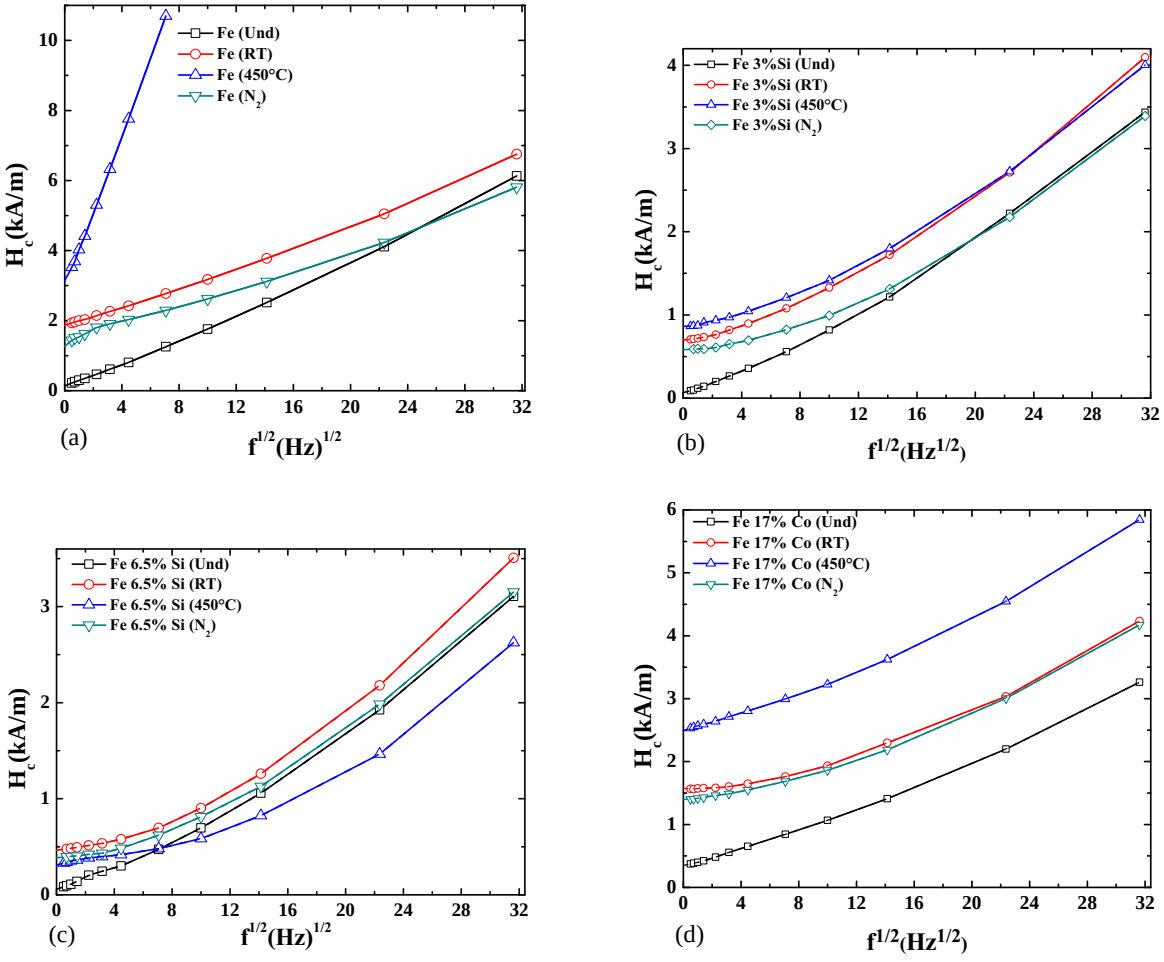

Figure 4.8: Frequency versus coercivity of HPT-treated (a) Fe, (b) Fe-3 wt%Si, (c) Fe-6.5 wt%Si and (d) Fe-17 wt%Co.

H_c curves for deformed samples are less steep as compared to un-deformed samples. Since

the slope of the H_c curve is reciprocally proportional to the square root of the electric resistivity of the material this implies that the resistivity of the material increases with deformation, which is in line with the fact that deformation induced dislocations enhance the resistivity.

The coercivity at 0 Hz the "true" coercivity which is physically relevant coercivity was obtained by linearly extrapolating the data for $f = 0$ Hz. It is obvious from coercivity (H_c) values that the coercivity at $f = 0$ Hz increases due to the severe plastic deformation (SPD). On the other side the mean grain size decreases due to the SPD treatment from micrometers to 50-200 nm. This should cause a reduction of H_c. However from the graph of coercivity H_c as a function of the grain size (D) (so called Herzer plot) as shown in Figure 4.9 [5] reveals that the power law D^6 is not fulllfilled. This might be an effect of stresses due to the HPT deformation, which increase the coercivity generally [78].

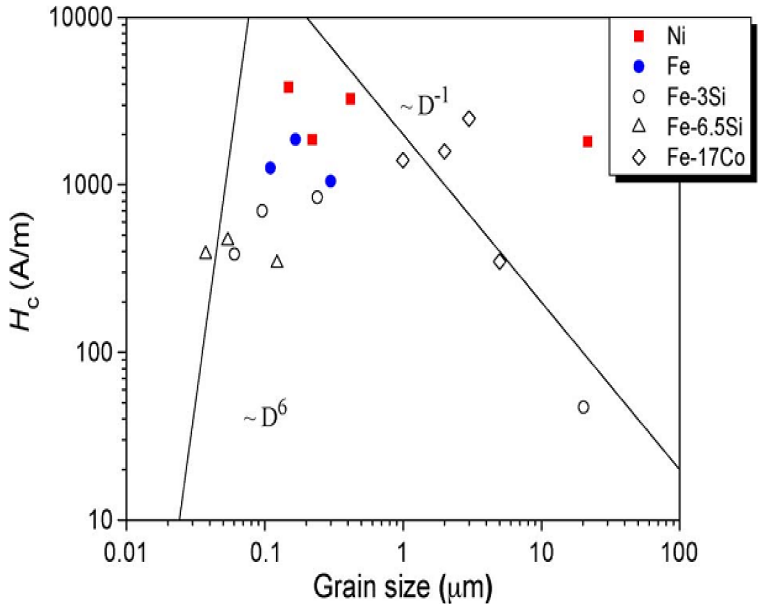

Figure 4.9: Coercivity as a function of the grain size (D) for Fe, Fe-3 wt%Si, Fe-6.5 wt%Si, Fe-17 wt%Co and Ni, after HPT-deformation [5].

The relative permeability μ_r is defined as the ratio between magnetic induction B and magnetic field strength H of the normal magnetization curve $B(H)$. The initial permeability μ_i was determined by the slope of the initial B-H-curve and the relative permeability (μ_r) was calculated by μ_i/μ_o. The magnetic parameters extracted from hysteresis loops are given in Table 4.3. A significant decrease in initial relative permeability is observed in

HPT-deformed samples, which might be the result of dislocations and other imperfections generated by internal stresses that tend to pin domain walls and limit their movement resulting in increase of coercivity which in turn is reciprocal related to permeability [49]. However, from Table 4.3 it can be seen that with the addition of Si the initial relative permeability is increased because the crystalline anisotropy decreased. The squareness (the ratio of remanence to saturation magnetization i.e. B_r/B_s) increased with deformation due to increasing the defects that hinder the magnetic domain wall motion in the grains.

The relative permeability was also determined from the minor loop measurements *i.e. dB/dt (T/s)* versus the field *H (A/m)* by using the relation 4.1. The triangular wave form of field *H (t)* that allows to calculate $\Delta\ H_{max}/\Delta\ t$ from $H_{max}/T/4$ (see section 3.1); $\Delta\ B/\Delta\ t$ is a maximum value taken directly from the minor loop measurement *dB/dt* versus *H(t)*.

$$\mu_r = \frac{1}{\mu_o}\Delta B/\Delta t\frac{1}{\Delta H/\Delta t} \tag{4.1}$$

Figures 4.10, 4.11, 4.12, 4.13 present the relative permeability μ_r versus field H obtained from the *dB/dt* versus field *H(t)* data. The maximum differential permeability μ_{max} was determined from a direct differentiation (dB/dH) of the hysteresis loop. The magnetic parameters determined from the hysteresis loops of all samples are given in Table 4.3.

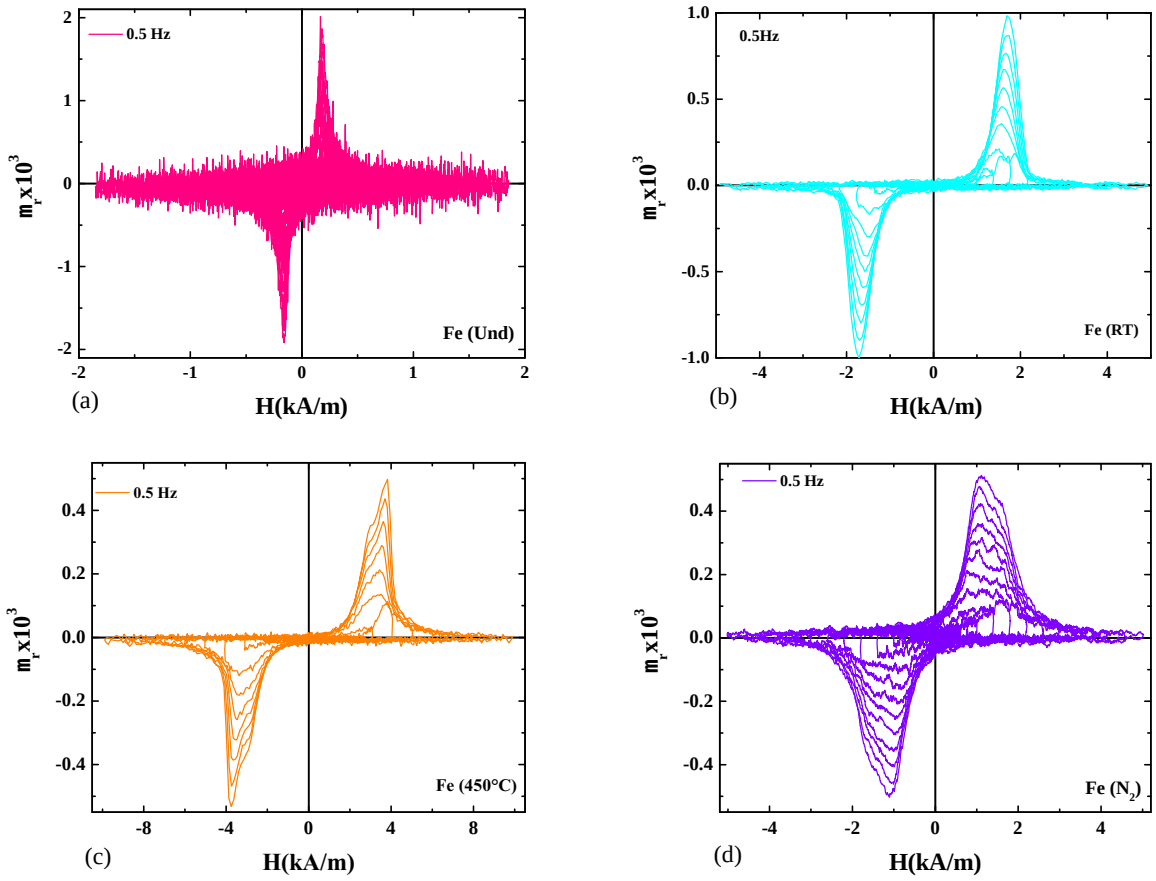

Figure 4.10: Relative permeability versus the field for HPT-treated Fe samples at room temperature.

The external stresses were estimated by the general formula of the type [5]:

$$H_c = \frac{\lambda \times \sigma}{\mu_o \times M_s} \tag{4.2}$$

Where as in above formula λ is effective magnetostriction, σ stress and M_s saturation magnetization. It should be noted that the "true" ($f = 0$) coercivity of a soft magnetic materials depend generally on the microstructure (grain size) and additionally on external stress [49]. Following data were used to estimate the stress for Fe: λ = -14 ppm [78] and $\mu_o M_s$ = 2.15 T. It should be mentioned here that body centered cubic (bcc) Fe exhibits anisotropic magnetostriction constants of different signs: λ_{100} = 20 ppm and λ_{111} = -16 ppm at room temperature. These considerations reveal that in (polycrystalline) iron for a torque type deformation a very complex situation determines the interplay between

hysteresis parameters (domain walls) and dislocations or stresses. The estimated stresses from relation 4.2 are given in Table 4.3.

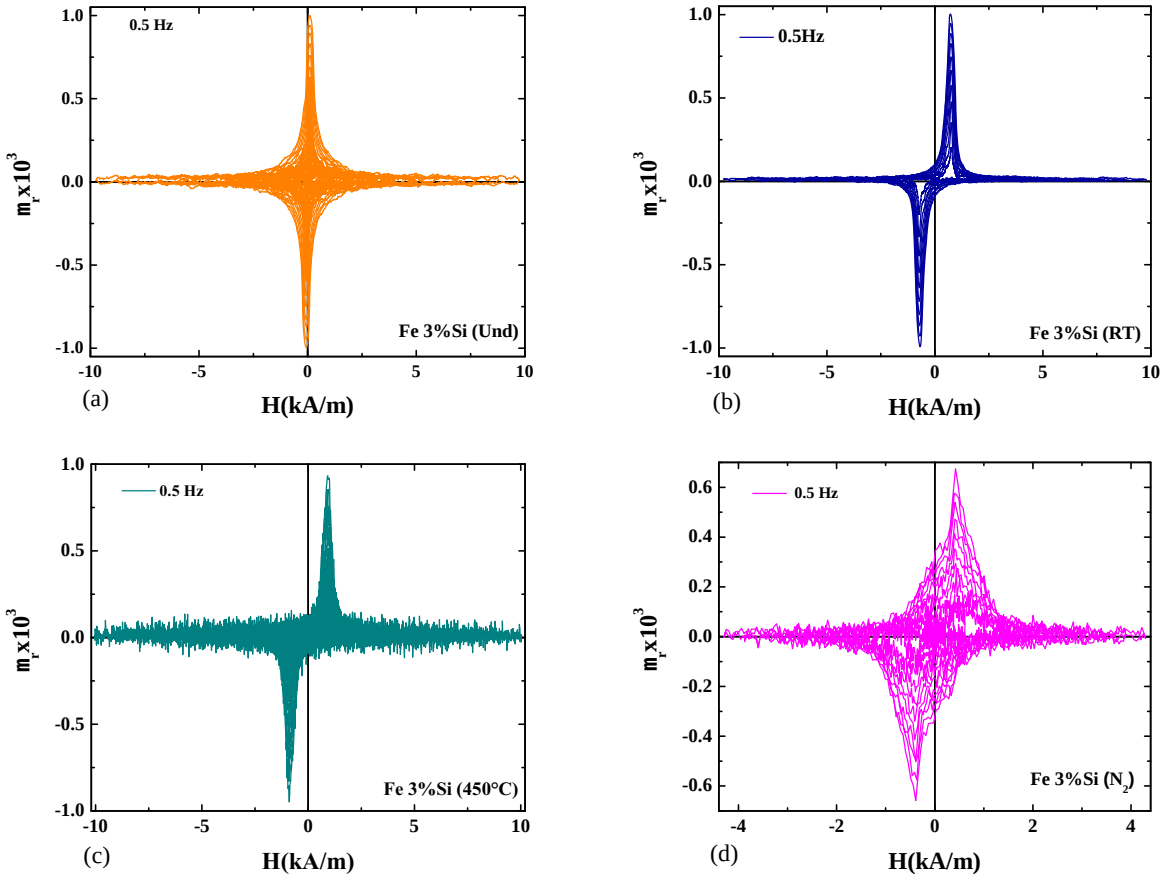

Figure 4.11: Relative permeability versus the field for HPT-treated Fe-3 wt%Si samples at room temperature.

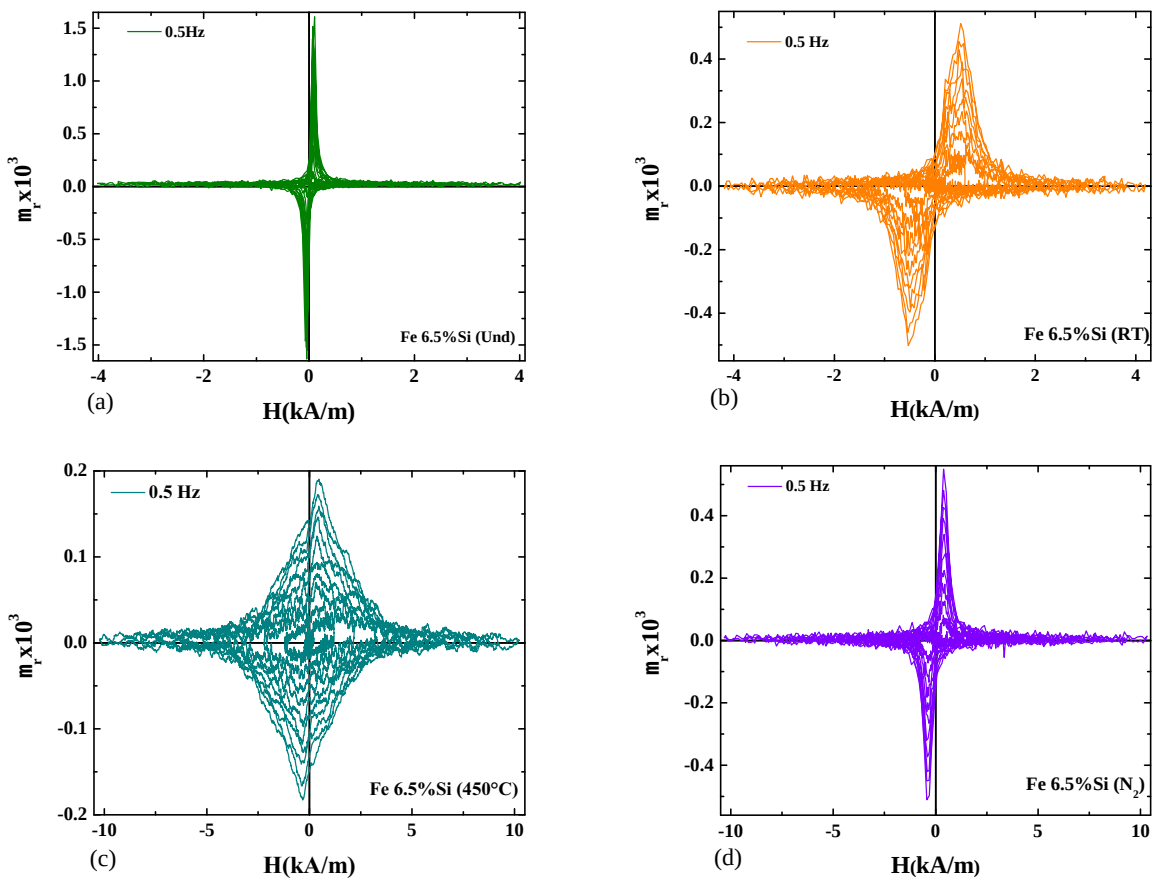

Figure 4.12: Relative permeability versus the field for HPT-treated Fe-6.5 wt%Si samples at room temperature.

It can be observed from the values (see Table 4.3) that initial permeability of HPT-deformed samples decreased as compared to un-deformed material, which indicates well the effect of the stresses caused by HPT deformation and this become also visible from the coercivity estimated stress values. It can also be seen from the values given in table that the coercivity is reciprocal propertional to the initial and maximum relative permeability.

The broadening of the peak of $\mu_r(H)$ versus H (A/m) curve is due to HPT treatment. This can be explained as by the deformation caused increasing stress distribution. The grain size distribution may play also a role.

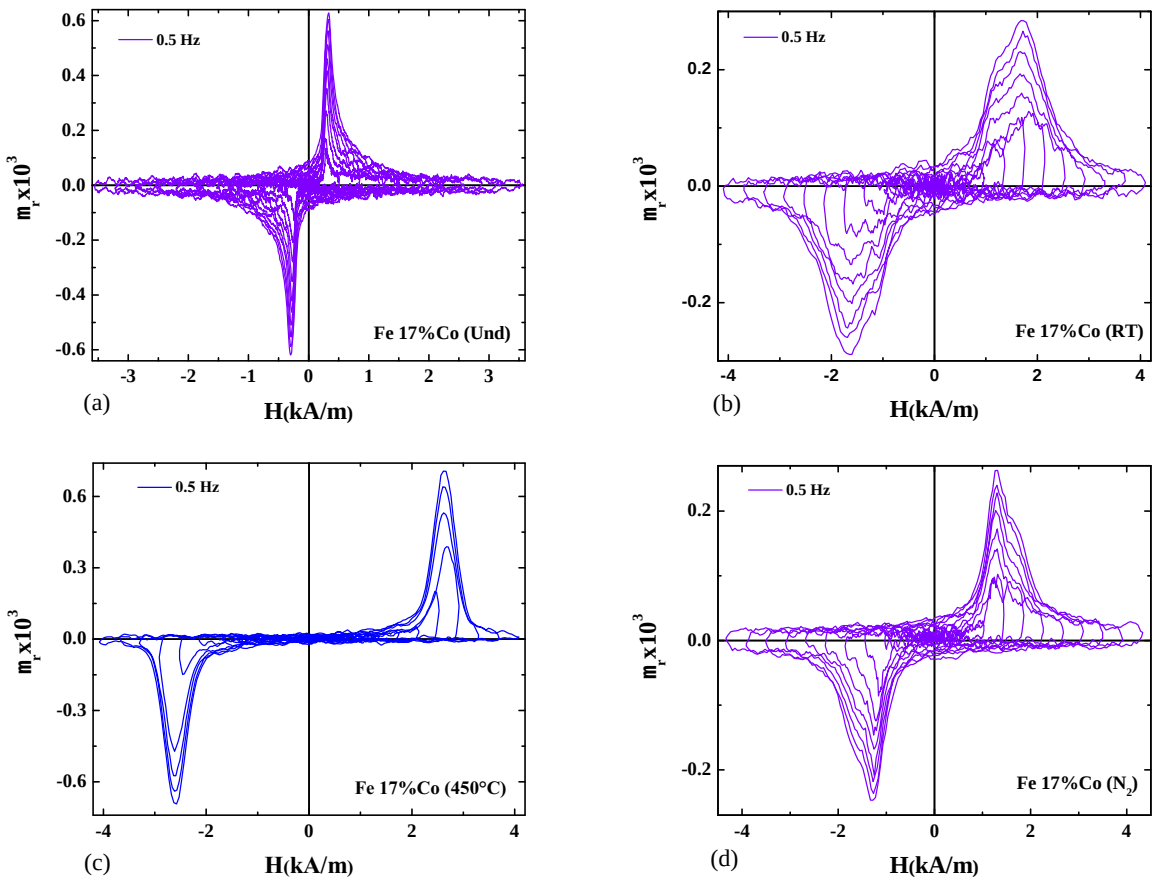

Figure 4.13: Relative permeability versus the field for HPT-treated Fe-17 wt%Co (P800) samples at room temperature.

Sample	H_c*(f=0Hz)* *(A/m)*	H_c*(f=50Hz)* *(A/m)*	B_r/B_s	σ *(MPa)*	μ_{ri}	μ_{max} *dB/dt vs H(t)*	μ_{max} *dB/dH*
Fe(Und)	150	1250	0.38	23	1190	2000(166)	667(270)
Fe(RT)	1870	2750	0.83	287	90	1000(1693)	318(1452)
Fe(450°C)	3526	3686	0.88	541	43	500(3800)	163(3098)
Fe(N_2)	1260	2290	0.86	194	87	500(1130)	177(1186)
Fe3wt%Si(Und)	47	550	0.12	11	1000	1000(115)	714(228)
Fe3wt%Si(RT)	700	1070	0.68	163	290	1000(710)	732(657)
Fe3wt%Si(450°C)	840	1200	0.70	196	120	900(920)	622(871)
Fe3wt%Si(N_2)	385	650	0.37	90	360	650(422)	355(394)
Fe6.5wt%Si(Und)	60	480	0.37	13	950	1600(104)	963(355)
Fe6.5wt%Si(RT)	465	700	0.55	103	370	500(515)	337(374)
Fe6.5wt%Si(450°C)	340	490	0.20	76	175	170(465)	175(871)
Fe6.5wt%Si(N_2)	386	625	0.46	86	150	540(390)	289(394)
Fe17wt%Co(Und)	374	844	0.35	47	255	628(333)	305(333)
Fe17wt%Co(RT)	1562	1761	0.60	198	121	284(1673)	334(1520)
Fe17wt%Co(450°C)	2532	2995	0.76	321	113	70(2610)	181(2818)
Fe17wt%Co(N_2)	1402	1686	0.50	178	32	262(1261)	167(1195)

Table 4.3: Magnetic properties of HPT-treated Fe, Fe-3 wt%Si, Fe-6.5 wt%Si and Fe-17 wt%Co samples, the number in (..) indicate the field where μ_{max} was determined.

4.3.1 Temperature Dependence of Hysteresis

Temperature dependent hysteresis loops of un-deformed and HPT-deformed pure Fe, Fe-3 wt%Si, and Fe-6.5 wt%Si alloys were measured in order to analyze temperature effect on the stresses produced during HPT-Treatment. Measurements were performed in a temperature controlled furnace and the sample temperature was determined using Pt 100 from room temperature (300 K) up to 220°C (493 K) with an accuracy of ± 2°C at selected temperatures. The temperature dependence of coercivity $H_c(T)$ at constant frequency f = 0.5 Hz is shown in Figure 4.14. It can be seen that the coercivity (H_c), in Fe and Fe-3 wt%Si is decreasing whereas in Fe-6.5 wt%Si increasing with increasing temperature. The increment in coercivity with temperature in HPT-deformed Fe-6.5 wt%Si is in accordance with literature [79].

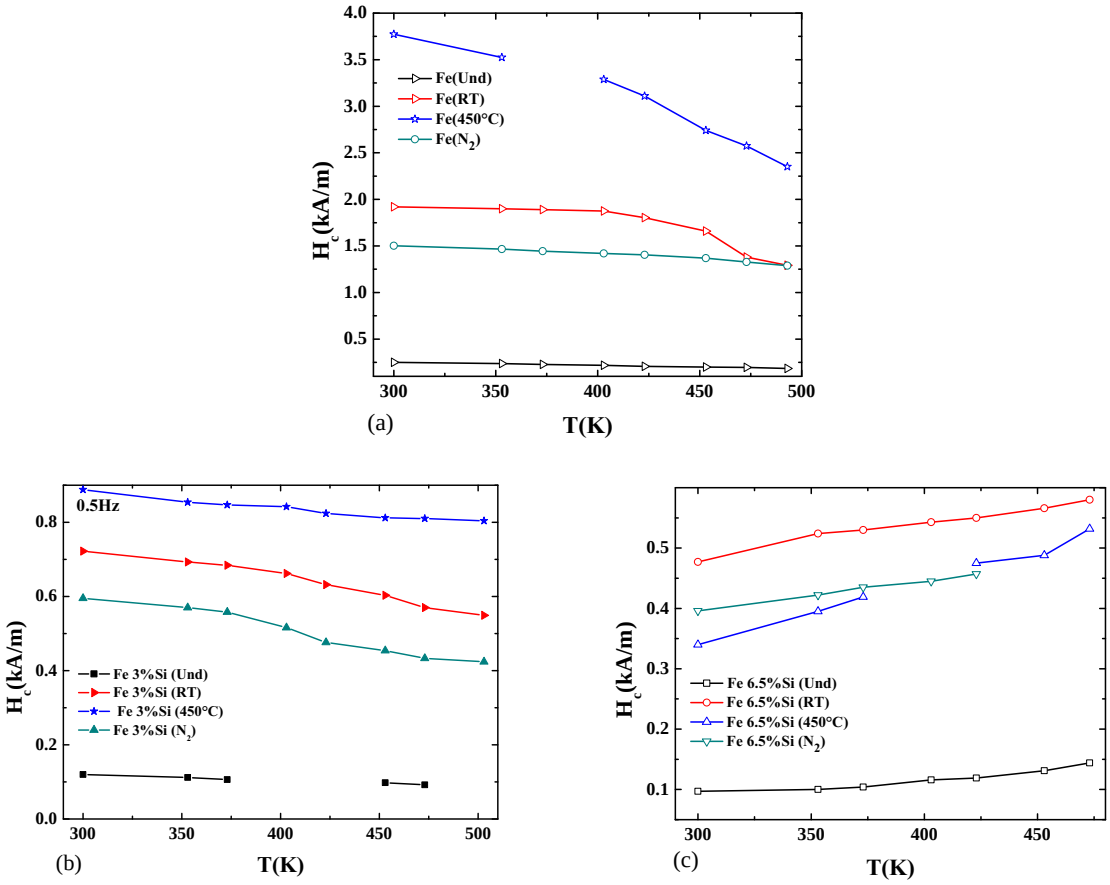

Figure 4.14: Temperature dependent coercivity of HPT-treated (a) Fe, (b) Fe-3 wt%Si and (c) Fe-6.5 wt%Si samples.

Figure 4.15 shows the plot of initial relative permeability as a function of temperature at constant frequency $f = 0.5$ Hz. The initial relative permeability was determined from the slope of initial B(H) curve of the hysteresis loop at 0.5 Hz. The permeability increases with increasing temperature and reaches a maximum just before the Curie temperature of the material, and then fall abruptly to unity at T_c [80,81] but here the measured temperature range is well below the Curie temperature. It can be seen from Figure 4.15 that μ_i increases with increasing temperature and also the rate of increase of μ_i with temperature is higher in un-deformed samples. The permeability is related to crystal anisotropy constant and the magnetostriction which is decreasing with increasing temperature this may leads to an increase in μ_i. The permeability of the deformed samples increased less due to induced crystal anisotropy because of deformations.

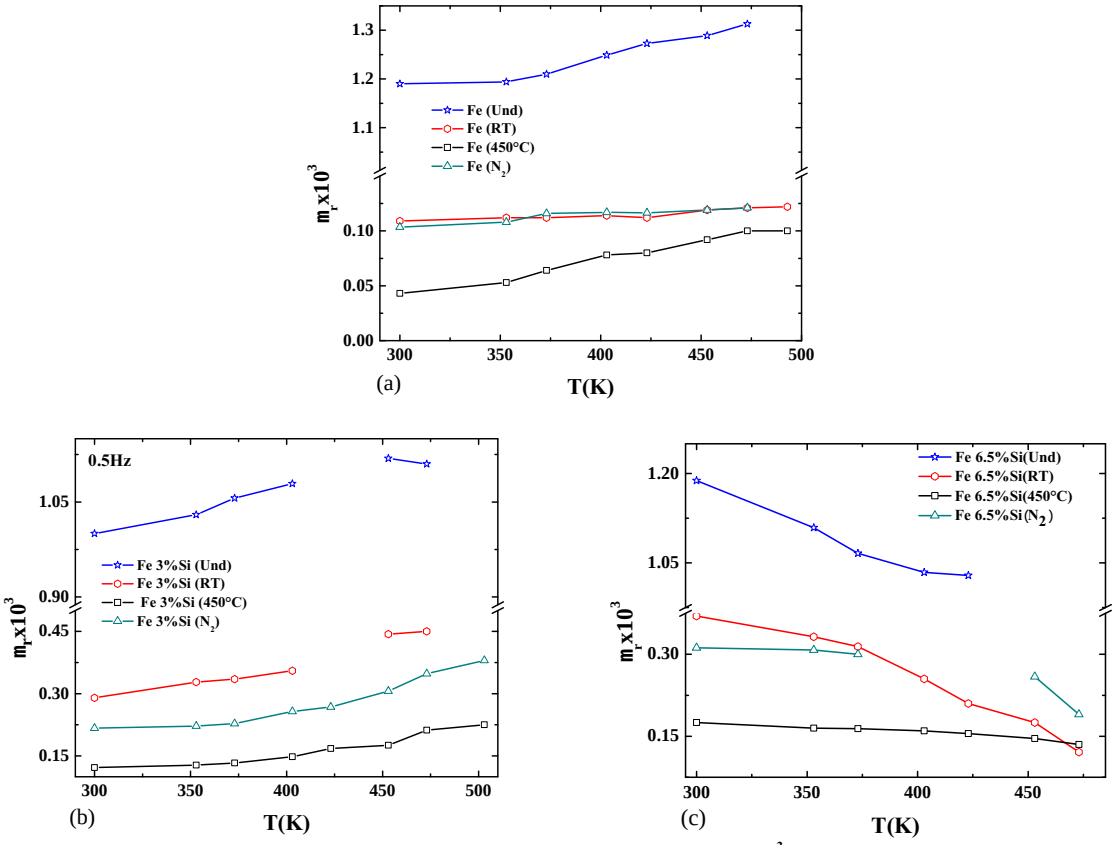

Figure 4.15: Relative initial permeability versus Temperature of HPT-treated (a) Fe, (b) Fe-3 wt%Si and (c) Fe-6.5 wt%Si samples.

4.3.2 Analysis of the Frequency Dependence of Coercivity

The experimental data of the frequency dependence of the coercivity at room temperature (300 K), for HPT-treated Fe, Fe-3 wt%Si, Fe-6.5 wt%Si and Fe-17 wt%Co samples were analyzed by the equations (4.3) and (4.4) (as described in chapter 3). The frequency dependence of coercivity for Fe were also analyzed at 373 K, 423 K and 473 K to see the effect of temperature on the fitting parameters.

$$H_c(f) = a + b.f^c \tag{4.3}$$

$$H_c(f) = d + e.\sqrt{f} + g.f \tag{4.4}$$

In equations the parameters a and d correspond to static coercivity ($H_c(f=0)$), whereas

b, c, e, g are fitting parameters. The coefficient b and the power factor c of equation (4.3) deliver an average of normal and anomalous eddy currents and the coefficient e and g describe the normal and anomalous eddy currents respectively.

The fitting results on experimental data are shown in Figures 4.16 and 4.17 for Fe samples and for Fe-Si/Co samples respectively. The parameters obtained from the such fitting are given in Table 4.4, 4.6 for Fe samples and 4.5, 4.7 for Fe-Si/Co samples. The experimental data are shown by solid curve with symbols, while the curves fitted by Eq. (4.3) and (4.4) by dash and solid curves respectively.

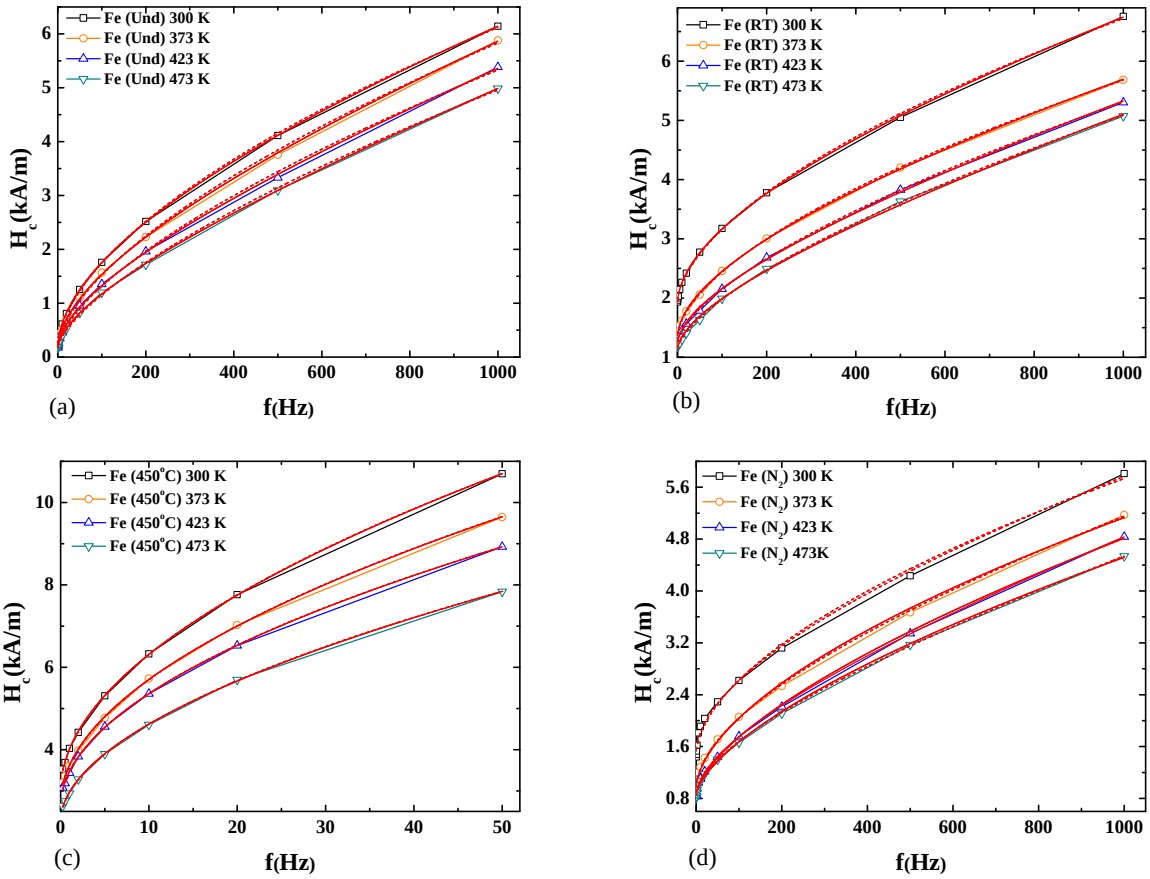

Figure 4.16: Fitting on the frequency dependent coercivity of HPT-treated Fe at different temperature by Eqs. (4.3) and (4.4) (a) un-deformed, (b) deformed at RT, (c) deformed at 450°C and (d) deformed at N_2.

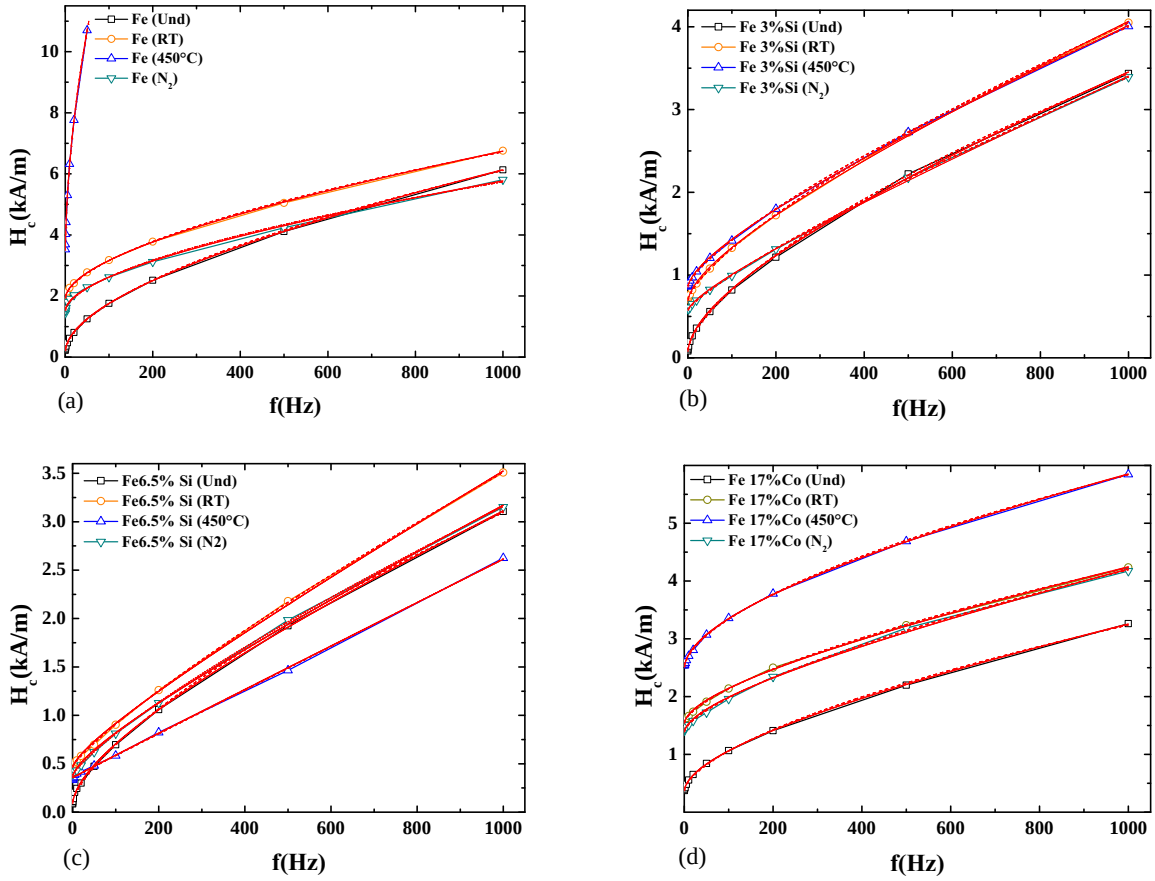

Figure 4.17: Fitting on frequency dependent coercivity of HPT-treated samples at room temperature by Eqs. (4.3) and (4.4) (a) Fe, (b) Fe-3 wt%Si, (c) Fe-6.5 wt%Si and (d) Fe-17 wt%Co.

The values of power factor c obtained by fitting are ranging from 0.5 to 0.8, which agree well with the range mention in formula by A. Zhukove et al. [67] for soft magnetic amorphous materials. It can be seen from the Table 4.4 - 4.7 that the values of fitting parameter b and e describing eddy current behavior of the material significantly decreased in deformed samples as compared to their corresponding un-deformed samples except the case Fe deformed at 450°C, which gives evidence that eddy current effect reduced due to the deformation causing enhancement in resistivity of the materials. While c and g is rather higher in deformed samples, which shows that anomalous effects are relatively increasing in deformed samples.

Furthermore the Parameters b and e obtained for Fe samples measured at elevated temperatures significantly decreased at higher temperature which, indicate that eddy currents

reduced due to an increase in resistivity of the material with the temperature. At 200°C the values almost reduced to half and hence eddy current should be approximately half, which is in accordance with fact that resistivity of iron becomes double at 200°C (373 K) on the other hand with elevated temperature the anomalous eddy current effect increased as can be seen from the values of parameter g obtained at elevated temperatures given in Table 4.4.

From the value of the parameter e and g, the relative permeability (μ_r) was calculated by using relations (4.5) and (4.6) (see chapter 3 section 3.1) designated as μ_r(e) and μ_r(g) given in Table 4.7.

$$e = H_c|_{f=0} R(1 - \frac{1}{\sqrt{2}})\sqrt{\frac{\pi.\mu_o\mu_r}{\rho}} \tag{4.5}$$

$$g = H_c|_{f=0} R^2(1 - \frac{1}{\sqrt{2}})^2\frac{\pi.\mu_o\mu_r}{\rho} \tag{4.6}$$

Sample	*T(K)*	a	Δa	b	Δb	c	Δc
Fe(Und)	300K	189	10	108	3.2	0.58	0.004
	373K	189	22	74	5.7	0.62	0.01
	423K	187	25	54	5.7	0.66	0.02
	473K	180	16	41	3.13	0.70	0.01
Fe(RT)	300K	1922	16	83	5	0.59	0.009
	373K	1354	6	68	1.8	0.60	0.004
	423K	1252	7.6	43	1.7	0.66	0.005
	473K	1143	11	37	2	0.70	0.009
Fe(450°C)	300K	3039	24	969	20	0.53	0.005
	373K	2746	37	875	31	0.53	0.008
	423K	2644	33	818	27	0.52	0.008
	473K	2294	23	669	19	0.54	0.007
Fe(N_2)	300K	1511	47	77	15	0.58	0.028
	373K	968	25	71	7.7	0.60	0.02
	423K	872	19	43	4.4	0.65	0.01
	473K	851	17	41	4.0	0.65	0.01

Table 4.4: Fit parameters at different temperatures for HPT treated Fe samples using Eq.4.3; Δa, Δb and Δc describes the error to a, b and c.

Sample	a	Δa	b	Δb	c	Δc
Fe-3wt%Si(Und)	86	8.0	65	2.0	0.66	0.007
Fe-3wt%Si(RT)	698	2.5	21	0.4	0.73	0.003
Fe-3wt%Si(450°C)	866	4.0	17	0.6	0.75	0.005
Fe-3wt%Si(N_2)	581	4.0	9.0	0.4	0.83	0.006
Fe-6.5wt%Si(Und)	100	9.5	23	1.7	0.70	0.010
Fe-6.5wt%Si(RT)	471	4.0	9.0	0.3	0.80	0.006
Fe-6.5wt%Si(450°C)	358	7.0	2.0	0.30	0.99	0.020
Fe-6.5wt%Si(N_2)	379	5.5	10	0.6	0.80	0.008
Fe-17wt%Co(Und)	372	12	39	3.0	0.62	0.010
Fe-17wt%Co(RT)	1545	5.5	28	1.2	0.66	0.006
Fe-17wt%Co(450°C)	2503	7.0	53	2.0	0.60	0.006
Fe-17wt%Co(N_2)	1398	11	25	2.2	0.70	0.012

Table 4.5: Fit parameters at room temperature for HPT-treated Fe-3 wt%Si, Fe-6.5 wt%Si and Fe-17 wt%Co samples using Eq. 4.3; Δa, Δb and Δc describes the error to a, b and c.

Sample	*T(K)*	d	Δd	e	Δe	g	Δg	μ(e)	μ(g)
Fe(Und)	300K	137	6.4	149	1.4	1.3	0.04	$1*10^6$	20704
	373K	127	9.7	122	2.2	1.9	0.07	$1*10^6$	32643
	423K	127	12	98	2.8	2.1	0.09	$7*10^5$	36079
	473K	121	6.5	82	1.5	2.3	0.05	$5*10^5$	41475
Fe(RT)	300K	1878	6	117	1	1.2	0.05	5654	1861
	373K	1308	12	103	2.6	1.1	0.09	9033	2450
	423K	1203	17	80	4.0	1.6	0.13	6442	3875
	473K	1094	22	72	5	1.70	0.16	6310	4527
Fe(450°C)	300K	2980	21	1022	16	9.8	2	$1*10^5$	7761
	373K	2688	32	927	24	8.1	3.2	$1.4*10^5$	7112
	423K	2609	23	850	17	6.04	2.3	$1.2*10^5$	5464
	473K	2236	22	722	16	10	2.2	$1.2*10^5$	10554
Fe(N_2)	300K	1483	34	103	7.5	1	0.25	8067	2300
	373K	932	14	100	3.2	1.1	0.1	19253	3947
	423K	826	10	77	2.3	1.6	0.08	14533	6479
	473K	808	10	73	2.3	1.4	0.07	13650	5795

Table 4.6: Fit parameters at different temperatures for HPT-treated Fe samples using Eq. 4.4; Δd, Δe and Δg describes the error to d, e and g.

The maximum relative permeability value obtained by using the fitting parameters e and g for un-deformed samples are significantly larger than the values obtained from the experimental data (see Table 4.3) but for deformed samples the μ_{max} values are of the same order of magnitude. Additionally the specific electrical resistivity ρ should increase

due to the severe plastic deformation, however this increase should be less than 20%. The uncertainty in μ_{max}(assuming a constant ρ) as determined from (4.5) and (4.6) is of the same magnitude.

Sample	d	Δd	e	Δe	g	Δg	μ(e)	μ(g)
Fe-3wt%Si(Und)	45	9	35	1.8	1.3	0.015	2.5*10^6	71062
Fe-3wt%Si(RT)	659	10	48	2	1.8	0.07	8821	9035
Fe-3wt%Si(450°C)	830	7	41	1.5	1.9	0.05	4201	7536
Fe-3wt%Si(N_2)	552	10	25	2	2	0.066	3367	42508
Fe-6.5wt%Si(Und)	63	6	49	1.5	1.5	0.044	1*10^6	78909
Fe-6.5wt%Si(RT)	443	12	24	2.6	2.3	0.083	3448	12322
Fe-6.5wt%Si(450°C)	353	8	1.4	1.8	2.2	0.061	1591	14793
Fe-6.5wt%Si(N_2)	350	14	27	3	2	0.095	8928	16282
Fe-17wt%Co(Und)	372	4	63	0.95	0.93	0.03	40277	6436
Fe-17wt%Co(RT)	1533	12	22	2.8	2	0.09	329	4163
Fe-17wt%Co(450°C)	2510	3	57	0.65	1.59	0.02	2437	1702
Fe-17wt%Co(N_2)	1379	5	31	1	1.8	0.035	757	3824

Table 4.7: Fit parameters at room temperature for HPT-treated, Fe-3 wt%Si, Fe-6.5 wt%Si and Fe-17 wt%Co samples using Eq. 4.4; Δd, Δe and Δg describes the error to d, e and g.

Eddy current model for $\mu_r = k/[H_c(f)]^n$

The eddy current model (detail explanation is in chapter 3) modified on the basis of general assumption that permeability and coercivity is reciprocally related [66], which implies that with an increasing coercivity due to an increase of the frequency may cause a reciprocal decrease in permeability. The modified model 4.7 with assumption $\mu_r = k/[Hc(f)]^n$, whereas k and n are fitting parameters was applied on the data of frequency dependence coercivity at room temperature for HPT-treated Fe, Fe-3 wt%Si, Fe-6.5 wt%Si, and Fe-17 wt%Co (P800).

$$f = [\frac{\ln H_{ext} - \ln H_c(0)}{R(1 - \frac{1}{\sqrt{2}})}]^2 . \frac{\rho}{k\pi\mu_o} \tag{4.7}$$

Where $H_c(f=0)$ is extrapolated coercivity to 0 Hz given in Table 4.3. Figure 4.18 shows the result of fitting, it can be seen that the model fits (dash curve) very well with experimental

data of all samples. The value of n for Fe and un-deformed Fe-Si/Co alloys is nearly equal to 1, which implies that relative permeability is much dependent on the coercivity, however the value of n obtained for HPT-deformed Fe-Si/Co alloys is much less than 0.5, which indicate that that the relative permeability is less corelated to the coercivity. The reason might be the general reduction of eddy currents in these samples.

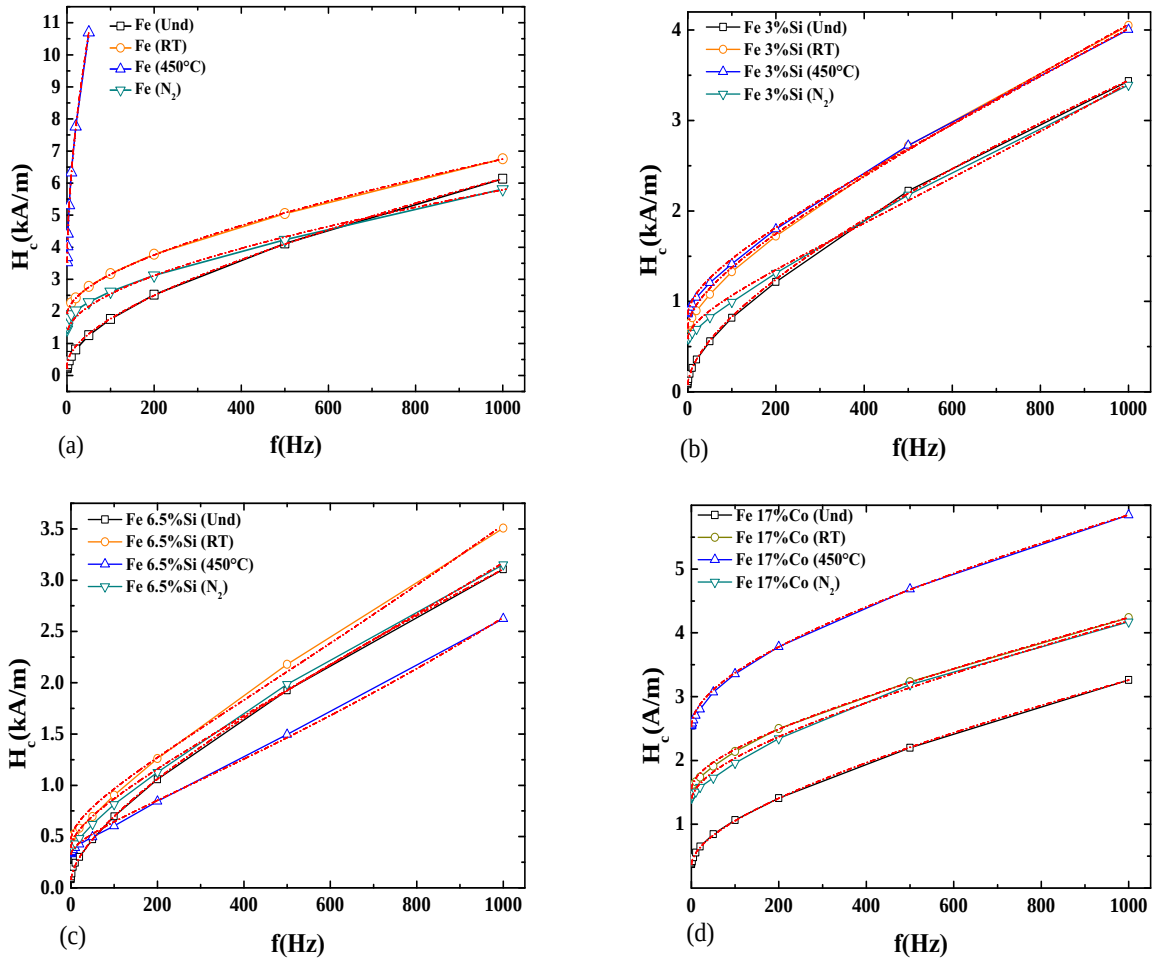

Figure 4.18: Fitting according to model Eq. 4.7 on the data coercivity verses frequency of HPT-treated Fe, Fe-3 wt%Si, Fe-6.5 wt%Si and Fe-17 wt%Co samples, whereas Δk described the error in k.

The value of fitting parameter k also used to calculate the relative permeability at f=0 of all samples by using relation $\mu_r(f) = k/[H_c(f)]^n$ is given in Table 4.8. The maximum relative permeability obtained for un-deformed samples is unreasonable high, however for deformed samples the value is in an aceptable range except for Fe(450°C). Nevertheless

the obtained values of maximum relative permeability follow the general assumption that permeability and coercivity is reciprocally related which can be seen from the general trend that a higher coercivity is accompanied by a lower permeability.

Sample	$a=H_c(f=0Hz)$	*R(m)*	n	Δn	k	Δk	μ_r(f=0)
Fe(Undef)	150	0.00052	1.20	0.004	39429249	1466017	96496
Fe(RT)	1870	0.00045	0.70	0.014	91573	11236	469
Fe(450°C)	3139	0.00050	0.93	0.02	16730641	3742490	9364
Fe(N_2)	1260	0.00042	0.91	0.06	908006	520898	1370
Fe-3wt%Si(Und)	47	0.00050	1.10	0.012	9815376	999191	142102
Fe-3wt%Si(RT)	700	0.00043	0.36	0.033	8346	2309	789
Fe-3wt%Si(450°C)	842	0.00042	0.24	0.032	2624	706	521
Fe-3wt%Si(N_2)	584	0.00042	0.13	0.05	1274	548	556
Fe-6.5wt%Si(Und)	60	0.00042	0.91	0.004	3280738	106082	79041
Fe-6.5wt%Si(RT)	465	0.0005	0.23	0.04	2658	987	647
Fe-6.5wt%Si(450°C)	386	0.00045	0.31	0.04	6767	2465	1068
Fe-6.5wt%Si(N_2)	321	0.00045	0.10	0.02	934	177	524
Fe-17wt% Co(Und)	349	0.00050	0.79	0.01	311700	18807	2880
Fe-17wt% Co(RT)	1540	0.00043	0.22	0.04	904	277	176
Fe-17wt% Co(450°C)	2521	0.00045	0.34	0.03	1636	404	114
Fe-17wt% Co(N_2)	1359	0.00046	0.36	0.07	2973	1625	221

Table 4.8: Fit parameters according to model Eq. 4.8 for HPT-treated Fe Fe-3 wt%Si, Fe-6.5 wt%Si and Fe-17 wt%Co samples, where as Δn, Δk describe the error in n, k.

4.3.3 Analysis of the Frequency Dependence of Losses

According to the statistical theory the losses in electrical steel are divided into hysteresis losses, classical eddy current losses and anomalous losses. The total energy loss in these materials depend not only on magnetic induction, magnetizing frequency, some microstructural features such as grain size and dislocation density but also on externally applied mechanical stress [82].

Total losses for un-deformed and HPT-deformed Fe, Fe-3 wt%Si, Fe-6.5 wt%Si and Fe-17 wt%Co were calculated by integrating the area of the hysteresis loop measured at different frequencies. At 50 Hz about 78% reduction of total core losses were obtained with addition of 3 - 6.5 wt% Si and 64% reduction with 17 wt% Co in pure un-deformed Fe. In HPT deformed samples generally the percentage increase in total losses with increasing frequency were much less than in their corresponding un-deformed samples. For example

the increase in frequency from 0.25 - 50 Hz causes an increase in total losses from about 780% in un-deformed Fe whereas in HPT-deformed Fe this increase was about 100%. The losses were analyzed by fitting the BH (J/m^3) versus f curve with a second order polynomial (4.8) and compared the result with model given in Eq. (4.9) suggested by Moses et. al, [83]. Generally, the three component of losses are analyzed under sinusoidal flux. Here, in this work losses were calculated under triangular magnetizing field.

$$W(f) = W_h + B_1.\sqrt{f} + B_2.f \tag{4.8}$$

$$W_{tot} = W_h + CB_{max}^{1.5}\sqrt{f} + a.\frac{A\pi^2 B_{max}^2}{\rho}.f. \tag{4.9}$$

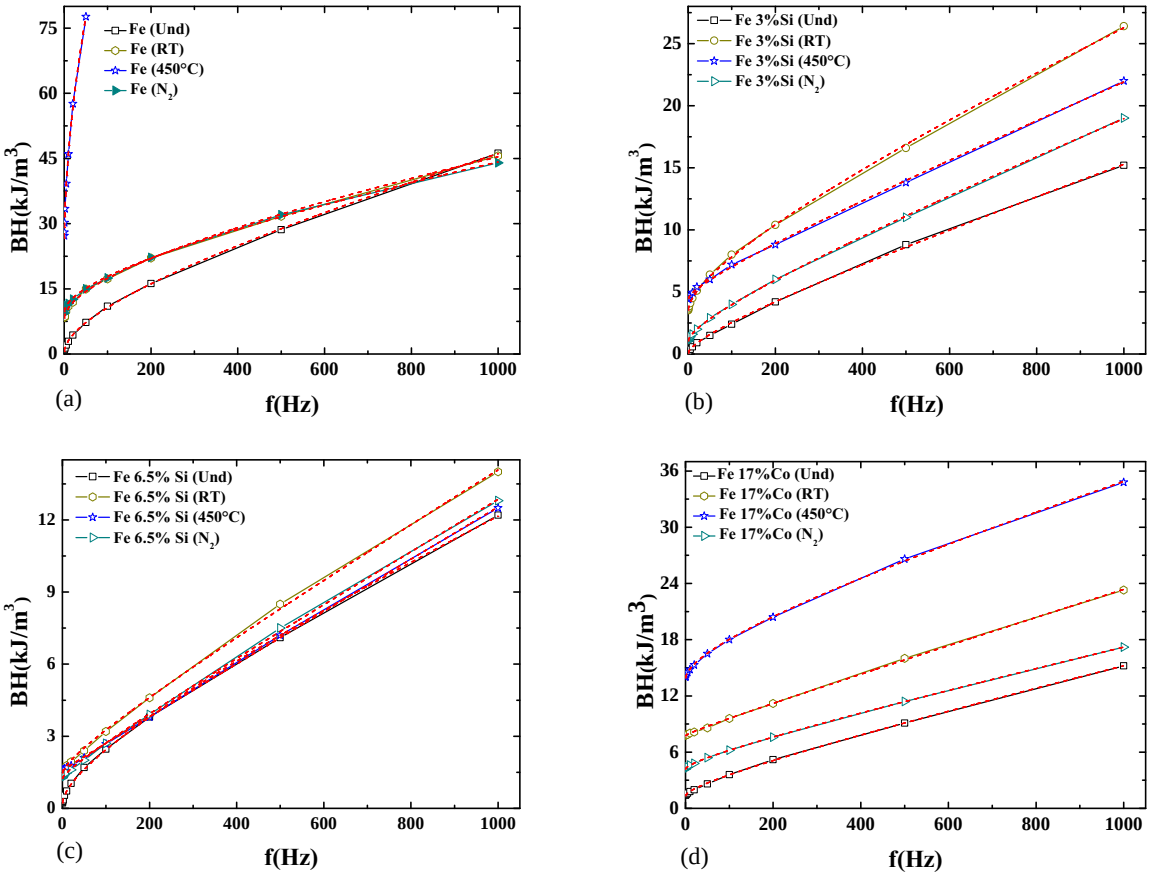

Figure 4.19: Fitting applying Eq. 4.8 on the frequency dependence of the losses; HPT-treated (a) Fe, (b) Fe-3 wt%Si, (c) Fe-6.5 wt%Si and (d) Fe-17 wt%Co samples.

Where W_h (J/m^3) represents the frequency independent hysteresis losses, B_1 and B_2 are fitting parameters. A is the cross section of the sample, B_{max} gives the maximum induction of the material and ρ is the specific electrical resistivity; a describes a constant which is determined by the shape of the driving field. In equation (4.8) and (4.9) second and third term present anomalous eddy current and classical eddy current losses respectively. The coefficient of classical loss term in Eq. (6.4) were directly calculated from the experimental data which agree rather well with the fitting parameter B_2. The fitting parameters and the calculated values are given in Table 4.9.

A well-known equation describe by Bertotti [23] to calculate anomalous eddy current losses is:

$$W_{exc} = CB_{max}^{1.5}\sqrt{f} = 8\sqrt{\frac{GAV_o}{\rho}}B_{max}^{1.5}\sqrt{f}. \tag{4.10}$$

G is a geometry parasmeter which is about 0.2. V_0 forms a characteristic field responsible for the anomalous eddy currents. The estimated values of V_0 are given in Table 4.9.

Sample	W_h*(f=0Hz)*	ΔW_h	B_1	ΔB_1	B_2	ΔB_2	a	aB_2	V_o
Fe(Und)	192	85	866	17	19	0.62	0.05	a.363	756
Fe(RT)	7882	165	845	37	11	1.20	0.06	a.192	1457
Fe(450°C)	23092	472	7158	356	82	47	0.33	a.249	80443
Fe(N_2)	9399	163	729	36	12	1.20	0.07	a.178	1207
Fe-3wt%Si(Und)	86	44	146	10	11	0.32	0.30	a.35	244
Fe-3wt%Si(RT)	3392	64	312	14	13	0.50	0.50	a.26	1537
Fe-3wt%Si(450°C)	4393	56	126	11	13	0.40	0.50	a.25	258
Fe-3wt%Si(N_2)	973	27	176	6	12	0.20	0.50	a.25	503
Fe-6.5wt%Si(Und)	147	24	159	5	7	0.17	0.30	a.25	411
Fe-6.5wt%Si(RT)	1433	44	83	9	10	0.32	0.30	a.33	84
Fe-6.5wt%Si(450°C)	1556	22	8	5	11	0.16	0.4	a.29	1.0
Fe-6.5wt%Si(N_2)	1230	30	48	8	10	0.22	0.35	a.28	33
Fe-17wt% Co(Und)	1283	30	132	7	10	0.22	0.03	a.296	23
Fe-17wt% Co(RT)	7728	43	44	10	14	0.32	0.07	a.215	3.8
Fe-17wt% Co(450°C)	13766	48	315	9	11	0.35	0.10	a.121	168
Fe-17wt% Co(N_2)	4150	7	108	2	9.6	0.05	0.04	a.245	19

Table 4.9: Fit parameters applying Eq. 4.9 for HPT-treated Fe, Fe-Si, Fe-Co samples and the calculated values of B_2 and V_o; ΔW_h, ΔB_1 and ΔB_2 describes the error to ΔW_h, ΔB_1 and ΔB_2.

4.4 Hysteresis Measurements of HPT-Deformed Ni

In this section the effect of HPT-deformation on magnetic properties of pure Nickel (99.999% purity) are studied via frequency dependence hysteresis measurements at room and elevated temperature up to 200°C. Ni is one of the three elements (iron, cobalt being the others) that are strong ferromagnetic at ambient temperature with Curie temperature 358^{o}C (676^{o}F) and magnetic permeability μ_{max} = 1240 at B = 1900G [84]. Pure Ni is seldom used itself as a magnetic material except for certain special purposes, such as magnetostriction applications due to high magnetostriction constants $\lambda_{100} = 46.7 \times 10^{-6}$ and λ_{111} = -11.1 $\times$ 10^{-6} . The crystal structure of Ni is face-centered cubic (FCC) with a lattice constant of 0.35167 nm at 20°C (68°F). Pure nickel is also considered as a good electrical conductor with resistivity at 20°C (68°F) which is 6.8$\times$ $10^{-8}\Omega$m [84].
Polycrystalline Ni was studied in an un-deformed state as well as after a HPT deformation performed at room temperature (RT), liquid nitrogen temperature (N_2) and at 450°C. The HPT parameters are given in Table 4.10 .

Sample	T_{HPT}	n	t	d_o	d_i
Ni	-	0	0.781	7.053	5
Ni	RT	3	0.640	7.010	5
Ni	450°C	3	0.657	7.026	5
Ni	N_2	3	0.653	6.910	5

Table 4.10: HPT parameters as used for the Ni samples; T_{HPT}-HPT treatment temperature, n-number of turns; t-thickness of sample; d_o-outer diameter; d_i-inner diameter.

Sample	$A(m^2)$	$l_{eff}(m)$	N_1	N_2
Ni(Und)	8.1×10^{-7}	0.190	90	62
Ni(RT)	6.4×10^{-7}	0.0188	93	62
Ni(450°C)	6.6×10^{-7}	0.0188	94	57
Ni(N_2)	6.2×10^{-7}	0.186	92	63

Table 4.11: Parameters as used for the hysteresis measurements for pure HPT-treated Ni. N_1-Primary windings, N_2-Secondary windings; $l_{eff}(m)$-Magnetic path length; $A(m^2)$-Cross-sectional area.

Figure 4.23 shows the hysteresis loops of un-deformed and HPT-deformed Ni, at room temperature (RT) liquid nitrogen (N_2), and 450°C (723 K), measured at room temperature

in the frequency range of 0.25 Hz to 1 kHz up to 20 kA/m magnetizing field. Additionally hysteresis measurements were also performed bulk Ni (without HPT-deformation), heat treated Ni (HPT deformed and annealed at 420°C for 1 hr), and electrodeposited nanocrystalline Ni (nc), their respective hysteresis loops are shown in Figure 4.24. The geometrical dimensions and parameters used for hysteresis measurements are given in Table 4.11.

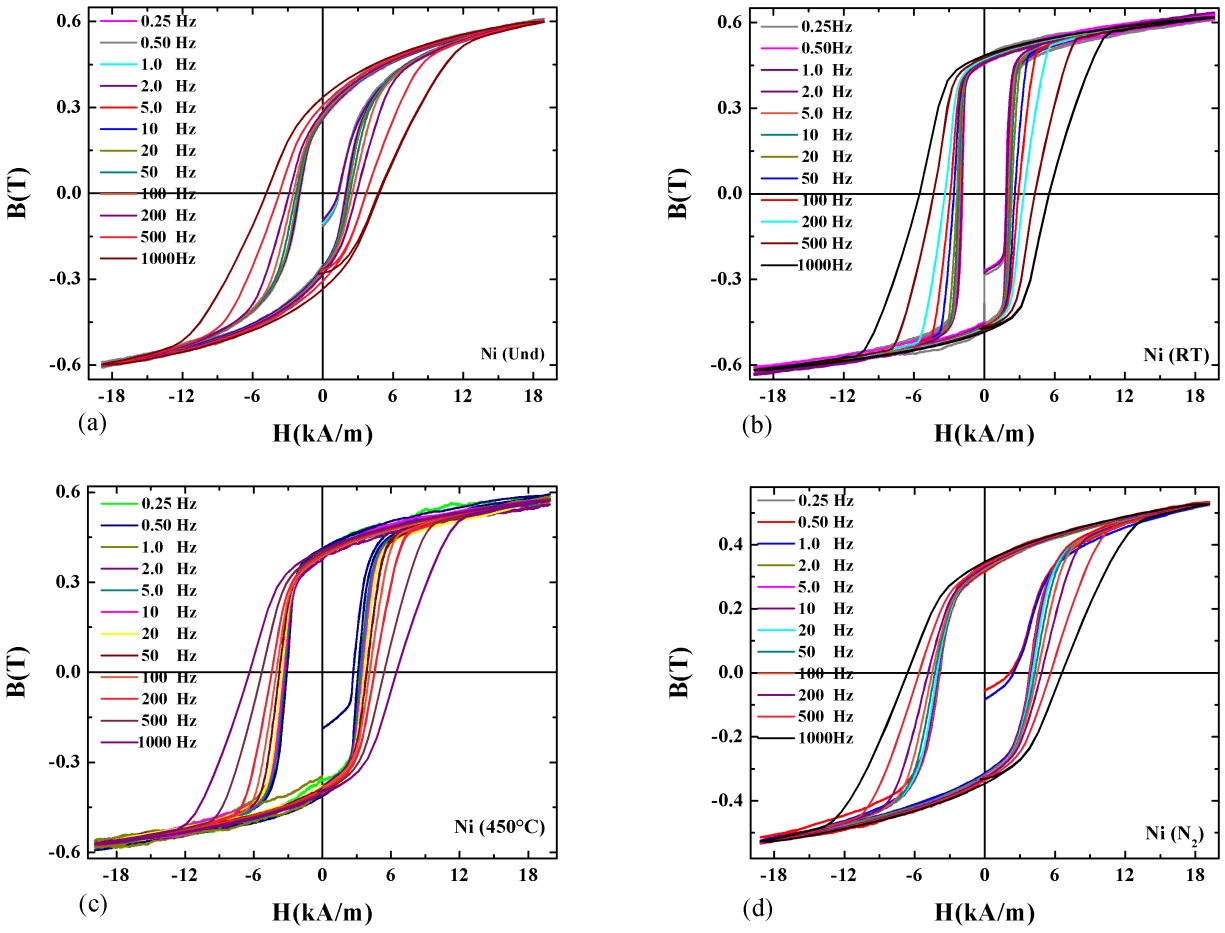

Figure 4.20: Hysteresis loops of HPT-treated Ni (a) un-deformed, (b) deformed at RT (300 K), (c) deformed at 450°C (723 K) and (d) deformed at liquid N_2 temperature (77 K).

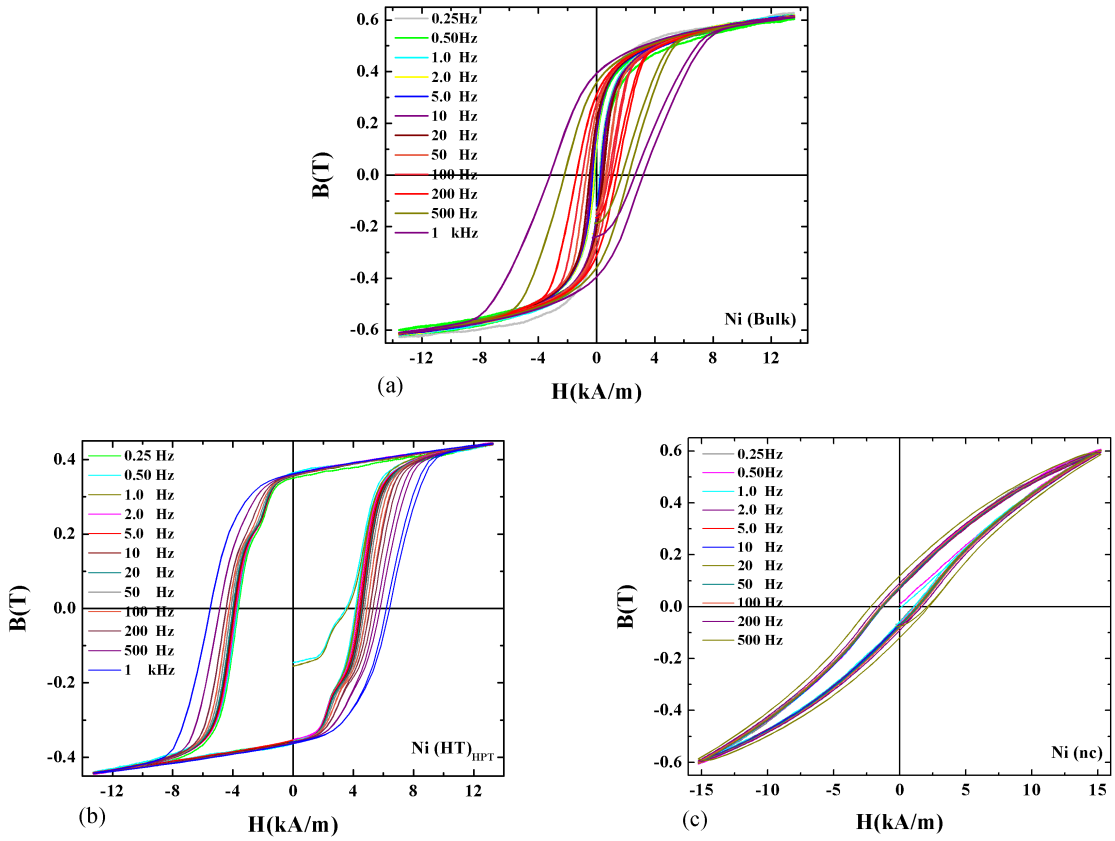

Figure 4.21: Hysteresis loops of Ni (a) Bulk, (b) HPT deformed and heat treated (420°C for 1 hr) and (c) Nano-crystalline Ni.

Measurements results illustrate that HPT-deformation has a strong effect on pure nickel, the coercivity considerably increased with deformation and the squareness ratio also increased about 40 % with deformation, which might be due to the high magnetostriction, which increases the magnetoelastic energy in Ni. For example at 0.5 Hz the coercivity of HPT-deformed Ni is higher than HPT-deformed Fe. Bulk Ni powder showed lowest coercivity whereas HPT-deformed Ni with heat treatment (420°C for 1 h) showed high coercivity (unfortunately the sample was slightly damage during HPT-treatment).

Figure 4.22 shows the coercivity (H_c) plotted against the square root of frequency. The uncertainty in the measurement of the coercivity is within the order of ±2 A/m. Mainly eddy currents are responsible for the strong increase in coercivity with increasing frequency which is obvious from the linear behavior of coercivity with the square root of frequency. Lowest coercivity was observed in recrystallize Ni bulk. HPT-deformed Ni

with heat treatment (420°C for 1 h) showed high coercivity at low frequencies that might be due to dislocations and voids produced during the HPT-deformation which pinned the domain wall motion. At higher frequencies less frequency dependence of coercivity was observed, which can be seen from the slope of coercivity versus square root of frequency curve in Figure 4.22(b), reason might be due to deformation which enhance the resistivity of the material.

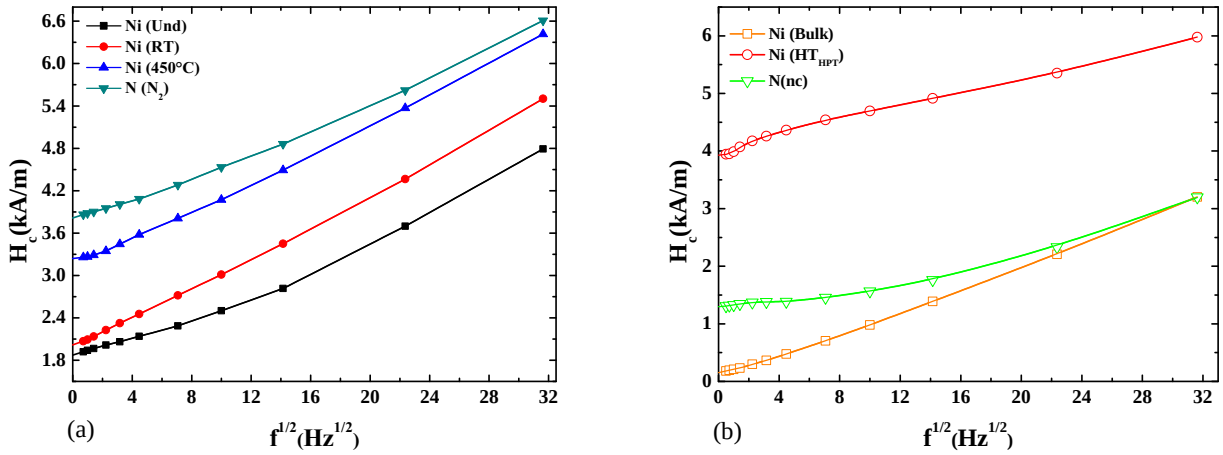

Figure 4.22: Coercivity versus square root of the frequency of (a) HPT-treated Ni and (b) Ni(Bulk), HPT-deformed with heat treatment Ni(HT)$_{HPT}$, nano-crystalline Ni(nc) samples.

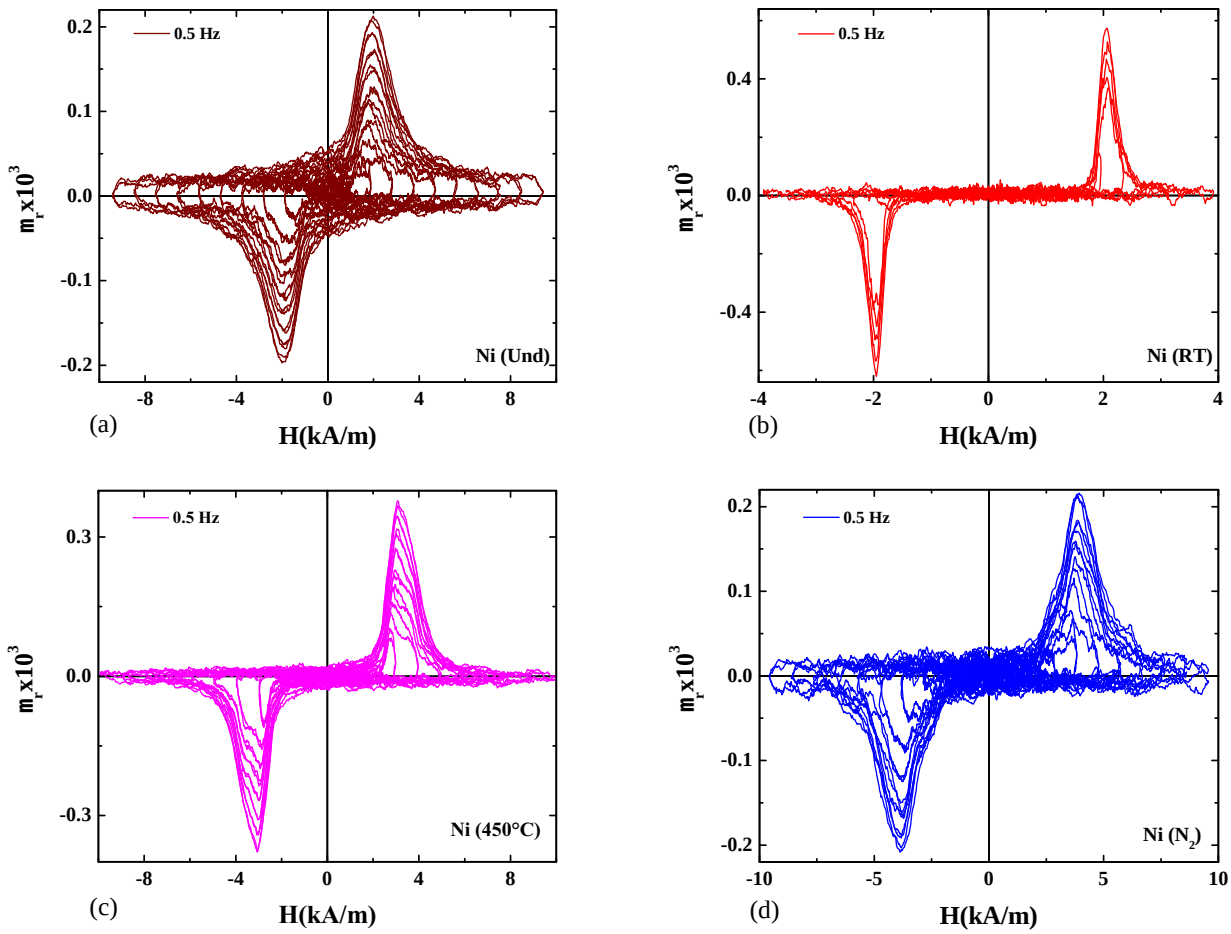

Figure 4.23: Relative permeability versus the field of HPT-treated Ni samples at room temperature.

The relative permeability obtained from the slope of initial hysteresis (B-H) curves is considerably small particularly in deformed samples. The maximum relative permeability was also determined from dB/dt versus field $H(A/m)$ by using the same procedure described in section 4.3. Magnetic parameters extracted from hysteresis loops are given in Table 4.12.

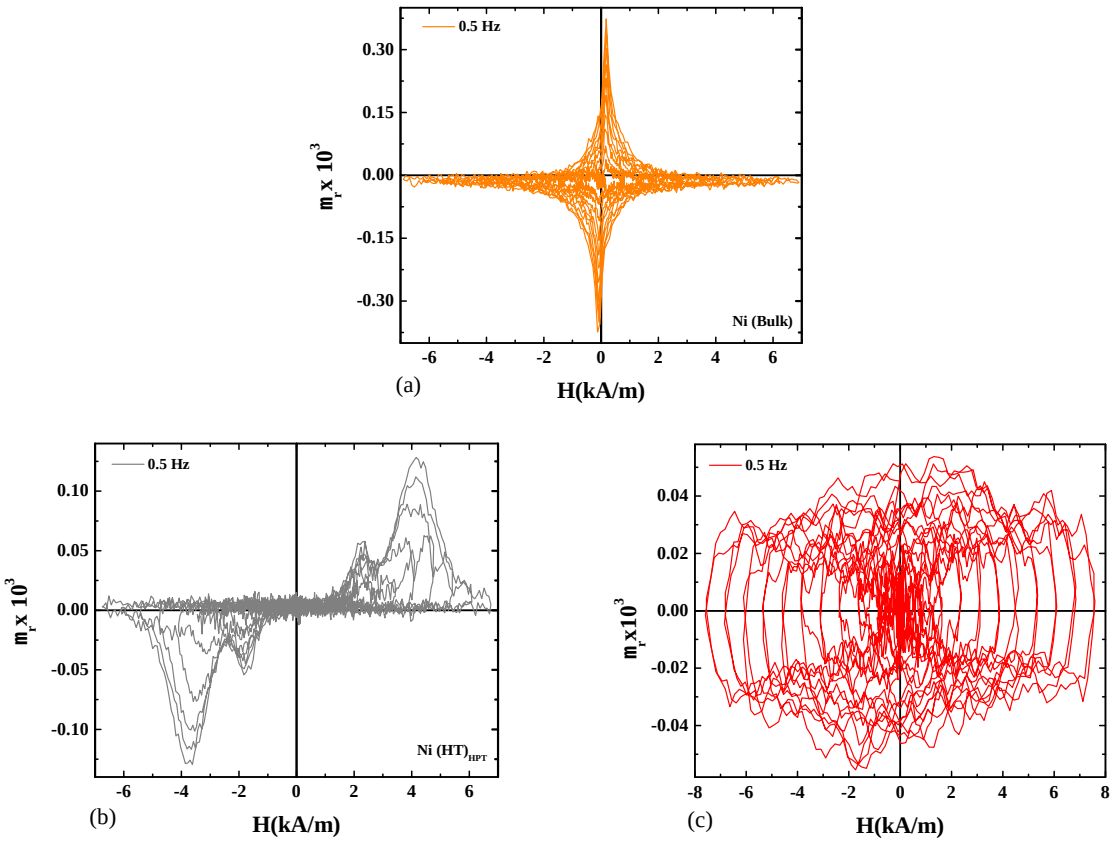

Figure 4.24: Relative permeability versus the field (a) Ni(Bulk),(b) HPT-deformed and heat treated Ni(HT)$_{HPT}$ and (c) Nano-crystalline Ni(nc) samples at room temperature.

The external stresses were estimated by the general formula given in Eq. (4.2). Following data were used to estimate the stress for Ni λ = -50 ppm and $\mu_o M_s$ = 0.61 T [78] (Table 4.12).

Sample	H_c*(f=0Hz)* *(A/m)*	H_c*(f=50Hz)* *(A/m)*	σ *MPa*	μ_{ri}	μ_{max} *dB/dt vs H(t)*	μ_{max} *dB/dH*	B_r/B_s
Ni(Und)	1806	2290	22	41	250 (1979)	91 (1222)	0.48
Ni(RT)	1860	2700	23	19	1000 (2169)	210 (2169)	0.75
Ni(450°C)	3240	3810	39	24	370 (3030)	93 (3002)	0.70
Ni(N_2)	3816	4280	47	16	200 (3869)	121 (3997)	0.62
Ni(Bulk)	151	704	1.8	103	374 (168)	255 (503)	0.20
Ni(HT)$_{HPT}$	3929	4539	48	12	127 (3932)	143 (609)	0.80
Ni(nc)	1290	1454	16	28.7	52 (1156)	68 (696)	0.13

Table 4.12: Magnetic parameters extracted form the hysteresis loop of HPT-treated Ni and Ni(Bulk), HPT-deformed with heat treated (420°C for 1 hr) Ni(HT)$_{HPT}$ and nano-crystalline Ni(nc) samples. The number in (..) are the field values where μ_{max} was determined.

4.4.1 Temperature Dependence of Hysteresis

Temperature dependent hysteresis measurements were made on un-deformed and HPT-deformed pure Ni samples at selected temperature between room temperature (300 K) and 220°C (493 K) with in accuracy of ± 4°C. Figure 4.25 shows the temperature dependence of the coercivity (H_c(T)) at 0.5 Hz. It can be seen that the coercivity decrease with elevated temperature. The decrease of coercivity with increasing temperature is higher in HPT-deformed samples which is most probably due to somewhat relieving of the internal residual stresses. Initial relative permeability was determined at 0.5 Hz from the slope of initial (B-H) curves at measuring temperatures. The initial permeability increased slightly with increasing temperature as shown in Figure 4.25(b) which is in accordance with the general assumption that coercivity and permeability are reciprocally related. The broad maximum might be due to a temperature induced stress relaxation.

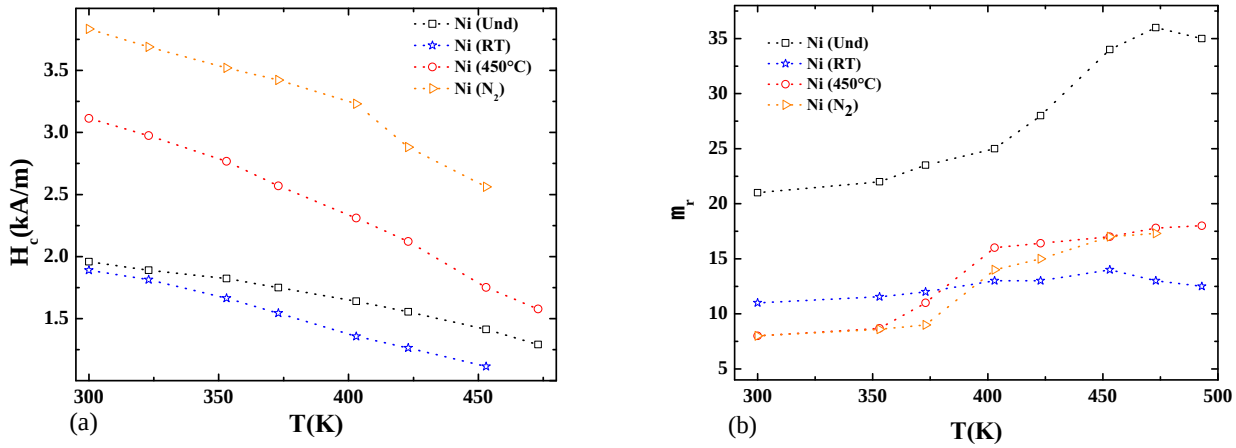

Figure 4.25: Temperature dependent (a) coercivity $H_c(T)$, (b) Relative permeability of HPT-Treated Ni .

4.4.2 Analysis of the Frequency Dependence of Coercivity

The frequency dependence of the coercivity at room temperature as well as at 100°C for HPT-treated samples were analyzed by Eqs. 4.3 and 4.4 using a fitting procedure. Fitting on measured data is shown in Figures 4.26(a) and 4.26(b) at room temperature and at 100°C. The parameters obtained are listed in Table 4.13 and 4.14.

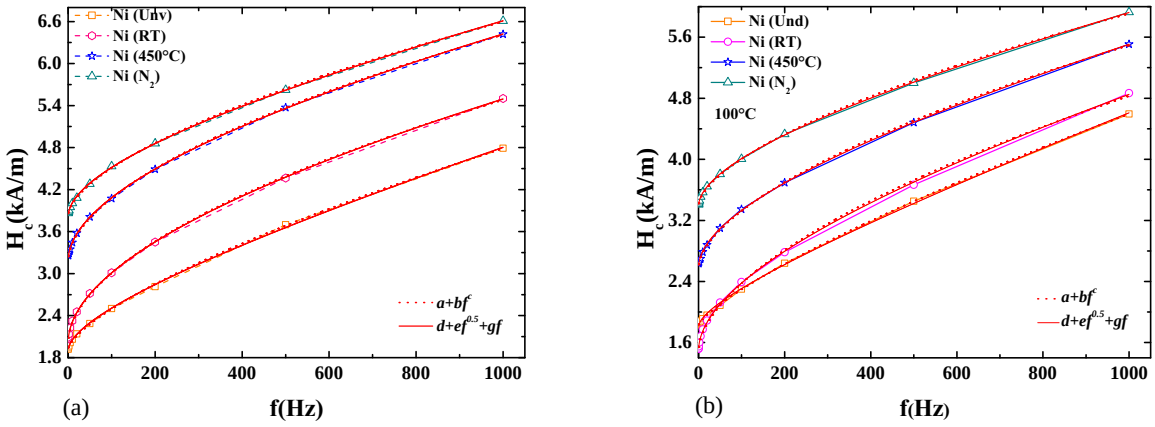

Figure 4.26: (a)Fitting frequency dependent coercivity for HPT-Treated Ni by Eq. 4.3 and 4.4 (a) at room temperature and (b) 100°C (373 K).

The power factor c at room temperature and at 100°C is between 0.5 and 0.8 which is in accordance with the value suggested in formula [67]. The value of parameters b and e describing normal eddy current behavior significantly reduced at 100°C (373 K), which could be attributed to an increase of the resistance with temperature in the materials. Nevertheless the value of g increased at 100°C, which is the indication that the anomalous eddy current damping slightly enhanced at higher temperature. The average relative permeability (μ_r) designated as μ_r(e) and μ_r(g) were calculated by using relations (4.5) and (4.6) from the value of parameter e and g are given in Table 4.14.

Sample	*T(K)*	a	Δa	b	Δb	c	Δc
Ni(Und)	(300K)	1898	11	22	2	0.70	0.012
	(373K)	1830	3.4	13	0.45	0.80	0.005
Ni(RT)	(300K)	2028	12	79	4	0.55	0.008
	(373K)	1514	19	59	6	0.58	0.015
Ni(450°C)	(300K)	3203	8	65	2.6	0.56	0.005
	(373K)	2606	9	45	2.6	0.60	0.009
Ni(N_2)	(300K)	3843	6.8	39	1.7	0.62	0.006
	(373K)	3408	9	34	2.4	0.62	0.01

Table 4.13: Fit parameters for HPT treated Ni samples using Eq. 4.13; Δa, Δb and Δc describe the error to a, b and c.

Sample	*T(K)*	d	Δd	e	Δe	g	Δg	μ(e)	μ(g)
Ni(Und)	(300K)	1892	10.6	47	2	1.4	0.07	483	1174
	(373K)	1800	10	33	2.3	1.8	0.075	263	1565
Ni(RT)	(300K)	2007	5	96	1	0.46	0.04	2537	553
	(373K)	1487	11	81	2.4	0.79	0.08	3290	1178
Ni(450°C)	(300K)	3174	7.6	85	1.6	0.54	0.05	795	380
	(373K)	2576	9	67	2	0.80	0.06	776	689
Ni(N_2)	(300K)	3808	6	63	1.3	0.8	0.04	245	400
	(373K)	3380	3	55	0.70	0.80	0.02	254	438

Table 4.14: Fit parameters for HPT treated Ni samples using Eq. 4.14; Δd, Δe and Δg describe the error to d, e and g.

The values of the maximum relative permeability obtained by using fitting parameters for un-deformed samples are larger than the values (see Table 4.12) calculated through *dB/dt* versus *H(t)* plot but for deformed samples these values agree rather well.

The modified eddy current model (4.7) was applied on frequency dependence of the coercivity as shown in Figure 4.27. It can be seen that model fits (dash curve) very well with experimental data of all HPT-treated samples. The fitting parameters and the relative permeability calculated at f=0 by using relation $\mu_r(f) = k/[H_c(f)]^n$ are given in Table 4.15.

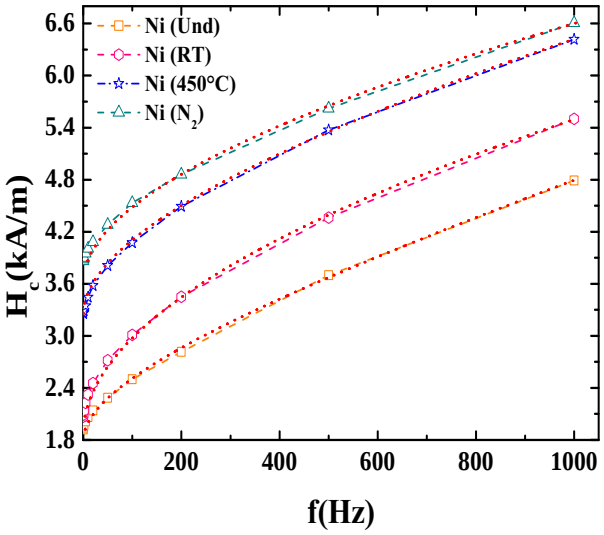

Figure 4.27: Fitting applying model Eq. (4.7) on the coercivity versus frequency data, indicated by dotted line.

Sample	*R(m)*	*a=H_c(f=0Hz)*	*n*	Δn	*k*	Δk	μ_r(f=0)
Ni(Und)	0.00050	1800	0.22	0.04	444	168	85
Ni(RT)	0.00045	1860	1.04	0.04	1249138	501323	496
Ni(450°C)	0.00045	3240	0.4	0.04	1685	599	66
Ni(N_2)	0.00046	3620	0.62	0.09	7130	6341	44

Table 4.15: Fit parameters by using model (4.7) and calculated permeability at $f = 0$ from $k/[H_c(f)]^n$ for HPT-deformed Ni. Δn and Δk represent errors in n and k.

4.4.3 Analysis of the Frequency Dependence of Losses

Frequency dependence of losses were analyzed by fitting the $BH\ (J/m^3)$ versus f curve with a second order polynomial (4.8) and model suggested by Moses et. al, [83] given in equation 4.9. The coefficient of f according to Eq. 4.9 which was obtained by direct calculation agrees with the fitted parameter B_2 for all samples.

The anomalous eddy current losses as described by Bertotti [23] are given in Eq (4.10) is equivalent to coefficient of B_1. The value of V_o was obtained by using parameter B_1, the specific electrical resistivity for Ni $\rho = 6.65 \times 10^{-8}$ Ωm and $B_{max} = 0.6$ T. The fitting parameter and calculated value are given in Table 4.16.

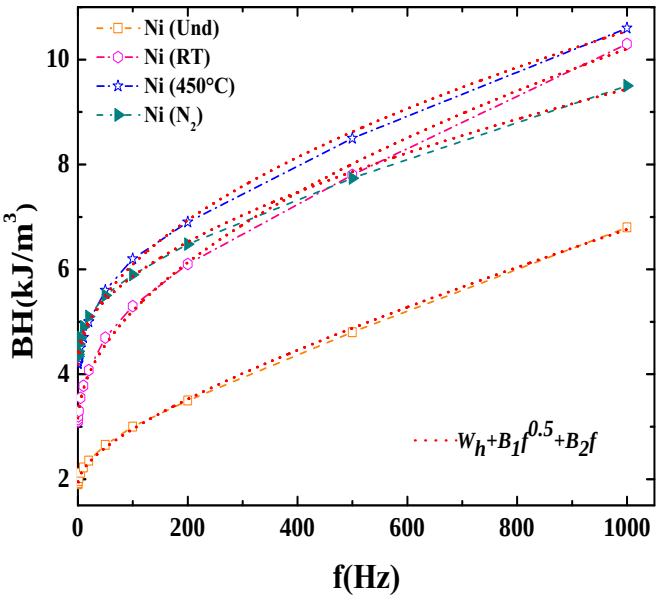

Figure 4.28: Frequency dependence of the losses calculated by integrated hysteresis loops of HPT treated Ni (dotted line indicate fitting).

Sample	$W_h(f=0Hz)$	ΔW_h	B_1	ΔB_1	B_2	ΔB_2	*a(13)*	$A\pi^2 B_{max}^2\ \sigma/6$	V_o
Ni(Und)	1898	22	84	5	2	0.16	0.3	7.5	210
Ni(RT)	3050	52	211	12	0.47	0.38	0.1	5.9	1976
Ni(450°C)	4080	35	200	7.8	0.13	0.26	0.05	6.1	1785
Ni(N_2)	4348	39	148	8.7	0.4	0.28	0.1	5.7	788

Table 4.16: Parameters obtained by fitting Eq.(4.8) on frequency dependence of the losses of HPT treated Ni. ΔW_h and ΔB_1 and ΔB_2 represent errors in W_h,B_1 and B_2.

4.5 Discussion and Conclusions

Soft magnetic metals such as pure Fe, Fe-alloys with Si/Co and pure Ni were deformed by high pressure torsion. The applied strain was chosen in such a way that no further grain refinement is observed. The samples were deformed at 300 K, 450°C (723 K) and liquid nitrogen temperature (77 K) to study the influence of the processed microstructure on the magnetic parameter H_c. A brief discussion and the conclusions are as follows:

The coercivity of HPT treated samples increased generally because of internal stress induced during the HPT-deformations. This is also in accordance with the coercivity versus the Vickers hardness (see Figure 4.2). However the dependence of the coercivity on the HPT temperature is different for each material depending on the microstructure (grain size) as well as the magnetostriction behavior. The dependence of the coercivity of magnetic materials with grain size reaches a maximum value at the single domain particle size, which is close to a grain size of about 100 nm. The coercivity also depends on the magnetocrystalline anisotropy constant. The magnetocrystalline anisotropy is reduced if the grain size becomes smaller than the exchange length. At this grain size a pinning of the domain walls at grain boundaries can be expected. For smaller grain sizes the "effective" anisotropy is reduced due to exchange coupling which causes a dramatic reduction of H_c with decreasing grain size.

A reduction of H_c for small grain sizes can be taken as a hint for exchange coupling between the grains. Therefore the zero frequency extrapolated coercivity (see Tables 4.3 and 4.12) is plotted as a function of the grain size in Figure 4.9. For all materials (except pure Ni) for small grain sizes a decreasing coercivity can be observed. Due to the formation

of platelet type grains the trend here is not as pronounced as the theoretically predicted by reduction of H_c with D^6. In the case of Ni the high magnetostriction dominates the coercivity behavior which is caused by the large magneto-elastic energy. For the coarse grained material states, D^{-1} behavior with decreasing grain size as predicted by the Herzer [49, 52] can be affirmed and is indicated in Figure 4.9. A better agreement with theory can be expected by a stress releasing heat treatment.

The grain size decreases generally with decreasing HPT temperature (see Figure 4.7). On the contrary the Vickers hardness decreases with increase HPT temperature (see Fig. 4.2), which may lead to the conclusion that materials that are deformed at higher temperatures can either partly reduce the local stresses or the larger grains remains still ductile. The coercivities of all samples show a non-uniform dependence on the HPT deformation temperature. This can be due to the exchange coupling, which is caused by a decreasing grain size. Below a grain size of about 100 nm it can be expected that the grains couple magnetically over the grain boundaries. This causes a magnetic softening as soon as the grain size of the alloy becomes smaller than the ferromagnetic exchange length, which is on the order of the domain wall width [51]. The maximum in H_c occurs at a grain size of about 100 nm (single domain particles). For smaller grains the exchange coupling reduces the effective anisotropy as well as the coercivity. Exchange coupled materials show naturally no superparamagnetism. Superparamagnetism occurs at smaller grain sizes (d <10 nm) when thermal fluctuations of the magnetic moment destroy any coupling between the grains.

(i) TEM-based grain size maps of the microstructure processed at different deformation states showed that the size of the microstructural elements decreases rapidly with decreasing HPT temperature. This behavior might be related to the reduced dynamic recovery during HPT at decreasing deformation temperatures.

(ii) This caused magnetic softening for Fe-containing samples at lower HPT processing temperatures which is shown by smaller coercivity values.

(iii) In Ni the rather high magnetostriction dominates the coercivity behavior.

(iv) The Fe-Si samples that exhibit the smallest magnetostriction show also the small-

est effect of the magnetic properties on the HPT deformation.

A modified eddy current model fits very well with the frequency dependence of the coercivity data for all samples. The relative permeability values obtained through this model were in an acceptable rang for HPT-deformed samples however unreasonable large for un-deformed Fe Fe-Si and Fe-Co alloys.

Chapter 5

Magnetic Hysteresis Measurements of High Magnetostrictive Materials

Low cost magnetostrictive materials that exhibit a large magnetostriction at low saturation field combined with a high mechanical strength and a good ductility are of great interest for applications in magnetomechanical sensors and actuators. Substituting iron (Fe) by non magnetic aluminum (Al) or Gallium (Ga) causes a strong increase in magnetostriction [62,63,85]. The reason for this effect is related to the local structure (ordering of Ga pairs [86] and also due to softening of elastic properties [87]. In Fe-Al and Fe-Ga alloys the magnetostriction value depends strongly on the cooling rate, the annealing procedure and the Fe-Al phase diagram including metastable equilibrium conditions among the disordered A2 and an ordered B2 and/or DO3 structure [87, 88]. The system $Fe_{100-x}Al_x$ offers similar options as Fe-Ga however with the advantage of the much cheaper Al but with a lower magnetostriction value [62, 89, 90]. The magnetostrictive properties of these alloys were already studied intensively in the past [61, 63]. For industrial applications the frequency dependent hysteresis properties (coercivity, permeability, losses) are of great importance. Therefore we studied in this work the low field hysteresis behavior on ring shaped bulk samples after a severe plastic deformation procedure.

5.1 Hysteresis Measurement of HPT Treated Fe-Al

Polycrystalline $Fe_{100-x}Al_x$ (x = 15, 20, 22 and 25) samples were produced by high frequency melting, then annealed in vacuum at 1000°C for 72 h and were cooled in a furnace (10°C/min). Afterward the samples were SPD treated at room temperature (RT) as well as at liquid nitrogen temperature (N_2) using the so-called HPT method as described in experimental chapter by applying the parameters given in Table 5.1.

Sample Composition	T_{HPT}	n	*d[mm]*	*h[mm]*	h_{HPT}*[mm]*
$Fe_{85}Al_{15}$	RT	3	8	0.77	0.49
$Fe_{85}Al_{15}$	N_2	3	8	0.96	0.55
$Fe_{80}Al_{20}$	RT	3	8	0.89	0.49
$Fe_{80}Al_{20}$	N_2	3	8	0.97	0.55
$Fe_{78}Al_{22}$	RT	3	8	0.77	0.49
$Fe_{78}Al_{22}$	N_2	3	8	0.93	0.54
$Fe_{75}Al_{25}$	RT	3	8	0.94	0.50
$Fe_{75}Al_{25}$	N_2	3	8	0.99	0.55

Table 5.1: *HPT* parameters as used for the Fe-Al samples. d-sample diameter; h-sample height before *HPT*; h_{HPT}-sample height after *HPT* treatment; n-number of turns during deformation; T_{HPT}-treatment temperature.

Such HPT treatment causes local disorder as well as nanocrystallization which may enhance the magnetostriction in these systems. Analyzing the frequency dependence of the hysteresis loop shall give a basic understanding of the stress and frequency effects on the hysteresis properties of materials with high magnetostriction. The frequency behavior of the hysteresis loop of materials with enhanced magnetostriction was studied in a frequency range between 0.25 Hz and 1 kHz on ring shaped samples equipped with primary and secondary windings. Triangular form of field *H(t)* was applied in order to obtain a constant *dH/dt*, which allows to calculate also the relative and the maximum permeability. The samples were demagnetized before each measurement. The parameters used for hysteresis measurement on ring samples are given in Table 5.2.

The hysteresis loops of $Fe_{100-x}Al_x$ (x = 15, 20, 22, 25) deformed at room temperature (RT) and liquid nitrogen temperature (N_2) are shown in Figure 5.1. The magnetic induc-

Sample	$A(m^2)$	$l_{eff}(m)$	$N_1(m)$	N_2
$Fe_{85}Al_{15}$(RT)	3.5×10^{-7}	0.020	76	45
$Fe_{85}Al_{15}$(N_2)	2.8×10^{-7}	0.02	78	46
$Fe_{80}Al_{20}$(RT)	3.9×10^{-7}	0.02	72	44
$Fe_{80}Al_{20}$(N_2)	3.9×10^{-7}	0.02	76	46
$Fe_{78}Al_{22}$(RT)	2.7×10^{-7}	0.02	72	45
$Fe_{78}Al_{22}$(N_2)	3.0×10^{-7}	0.02	74	46
$Fe_{75}Al_{25}$(RT)	3.9×10^{-7}	0.02	72	42
$Fe_{75}Al_{25}$(N_2)	3.5×10^{-7}	0.02	74	44

Table 5.2: Parameters as used for the hysteresis measurements. N_1-Primary Windings; N_2-Secondary Windings; $l_{eff}(m)$-Magnetic Path length; $A(m^2)$-Cross-sectional Area.

tion achieved with Al 15 % at. was about 1.6 T and saturation magnetization with this composition in literature is 1.65 T [91]. The magnetization decreased with increasing Al concentration (Figure 5.1h). The coercivity of samples deformed at room temperature was higher than the corresponding samples deformed at liquid nitrogen (N_2)temperature. For example the coercivity of $Fe_{85}Al_{15}$ deformed at room temperature was almost 1.6 times higher than the sample deformed in liquid nitrogen environment. This significant increase in coercivity with deformation temperature might be the effect of HPT processing temperature on the grain size as reported in literature [1,53,54]. There the grain size increases with HPT processing temperature. No significant effact was observed on coercivity values obtained for $Fe_{100-x}Al_x$ (x = 20, 22, 25 %) deformed at room temperature. However the coercivity increased for samples deformed in liquid nitrogen (N_2) temperature with increasing the Al concentration. It can be seen from the hysteresis loops that a weak increase in coercivity accured at low frequenceis up to 50 Hz. Eddy current influenced the loop above 50 Hz however this effect was not so much high.

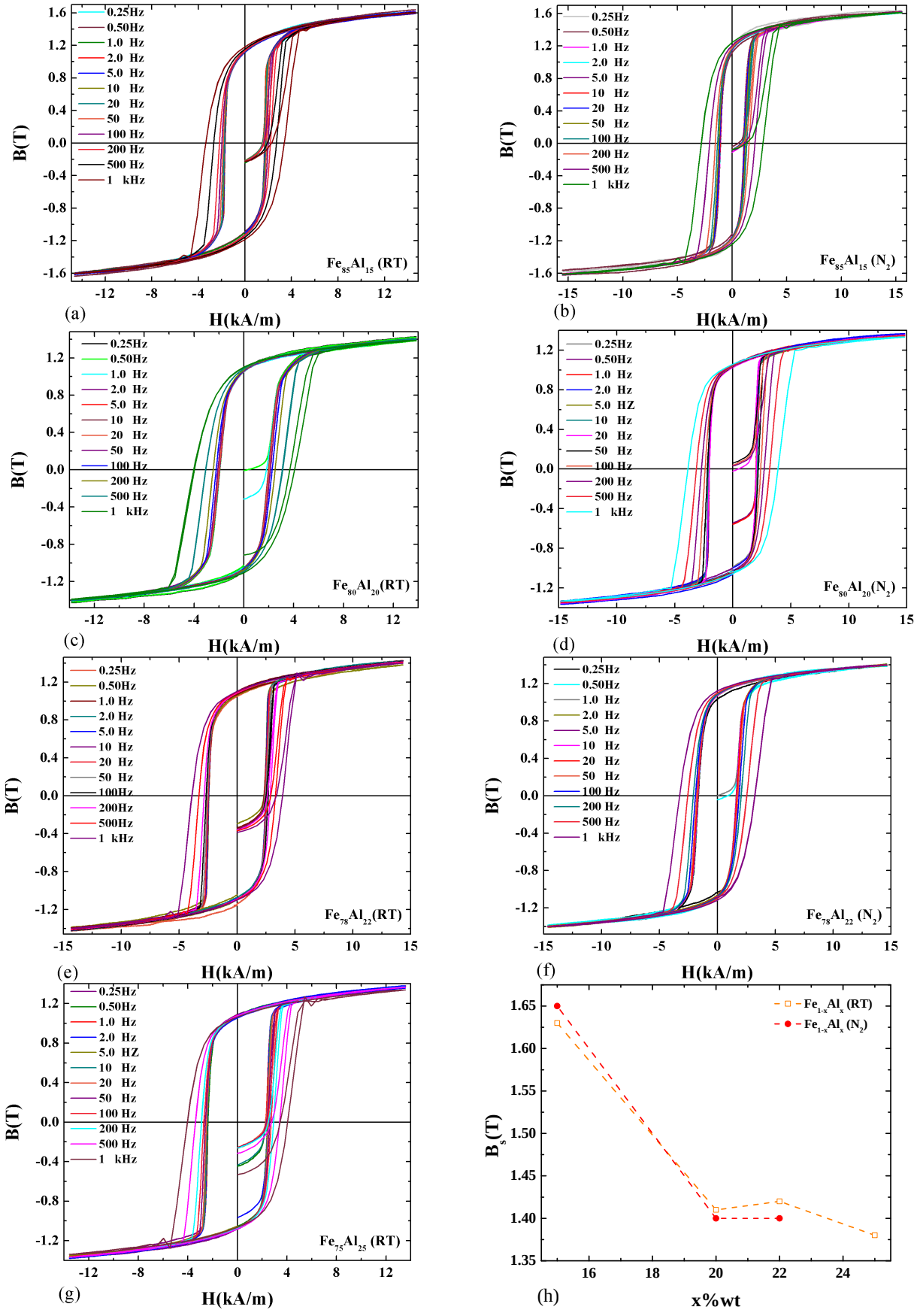

Figure 5.1: Hysteresis loops of HPT-treated Fe-Al system (a) $Fe_{85}Al_{15}$ (RT), (b) $Fe_{85}Al_{15}$ (N_2), (c) $Fe_{80}Al_{20}$ (RT), (d) $Fe_{80}Al_{20}$ (N_2), (e) $Fe_{78}Al_{22}$ (RT), (f) $Fe_{78}Al_{22}$ (N_2), (g) $Fe_{75}Al_{15}$ (RT) and (h) Magnetization as a function of Al concentration.

Figure 5.2 shows the coercivity plotted against the square root of the frequency. The coercivity at zero frequency (0 Hz) is obtained by extrapolating the data to 0 Hz. The effect of eddy currents is obvious regarding the increase of the coercivity with increasing frequency. However this effect is much smaller than in pure iron as well as HPT-deformed Fe at room temperature and liquid nitrogen. For example the increment in coercivity from 0.25 Hz to 50 Hz and 50 Hz to 1 kHz in HPT-deformed Fe at room temperature is 43 % and 144 % respectively whereas HPT-deformed $Fe_{85}Al_{15}$ at room temperature shows an increase of 11 % and 76 % in the same frequency range. The increase of coercivity from 0.25 Hz to 50 Hz in the $Fe_{100-x}Al_x$ system is comparable with that in Fe-3 wt%Si, Fe-6.5 wt%Si and Fe-17 wt%Co, but at higher frequencies the increase becomes much less than in HPT-treated Fe-Si and Fe-Co alloys (for comparison see data in chapter 4) due to an increase of the resistivity of Fe with the addition of Al. Nevertheless, the coercivity increased with increasing Al concentration in $Fe_{100-x}Al_x$ ($15 \leq x \leq 25$) system similar as the magnetostriction. The magnetic parameters derived from their corresponding hysteresis loops are given in Table (5.3), it can be seen that squareness ratio (B_r/B_{max}) is between 0.7 and 0.8 which is a very reliable value for an isotropic polycrystalline cubic material.

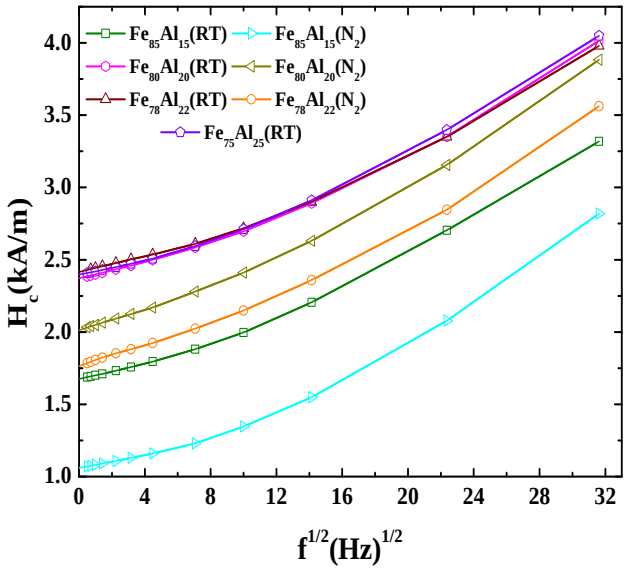

Figure 5.2: Coercivity versus square root of frequency of HPT-treated $Fe_{100-x}Al_x$ (x = $15 \leq x \leq 25$) samples.

The initial permeability was determined by the slope of the initial BH-curve and the initial relative permeability (μ_{ri}) was calculated by μ_i/μ_o. The maximum relative permeability was determined from *dB/dt* versus field *H (A/m)* data by using the relation $(\mu_o)^{-1}(\Delta\ B/\Delta\ t)\ (\Delta\ t/\Delta\ H)$. From the slope of the triangular field *H (t)*, $\Delta\ H/\Delta\ t$ was calculated i.e $4fH_{max}$. $\Delta\ B/\Delta\ t$ was taken directly from the minor loop measurement data i.e *dB/dt*. Figure 5.3 shows the graphs of maximum relative permeability versus field. The maximum differential permeability was also determined by means of direct differentiation of the hysteresis loop (*dB/dH*). Magnetic properties of all samples extracted from measured hysteresis loops are given in Table 5.3; the number in small bracket (..) are the field values where μ_{max} was determined. The values of initial relative permeability obtained for all HPT treated $Fe_{100-x}Al_x$ (x = $15 \leq x \leq 25$) samples were rather small because of large stress effect due to deformation. A decline in the maximum relative permeability was observed with increasing Al concentration. The reduced relative permeability for the HPT treated $Fe_{78}Al_{22}$ (RT) indicates that the larger amount of Al increased disorder as well as the higher stress state causing a strong broadening of the relative permeability of this sample. Magnetic permeability decreases and the coercive force increases with the increase of stress in deformed samples and this behavior makes the material magnetically less soft.

It should be mentioned that the "true" coercivity $H_c(f = 0)$ of a (soft) magnetic material depends generally on the microstructure (grain size) and additionally on external stresses (λ-effective magnetostriction, σ-stress) neglecting the magnetocrystalline ansiotropy: This effect can be explained by a simple formula 5.1 which describes the coercivity of soft magnetic materials [5].

$$H_c = \frac{\lambda\sigma}{\mu_o.M_s} \tag{5.1}$$

Using this relation the internal stress σ was estimated assuming a "polycrystalline" magnetostriction value of λ = 75 to 120 ppm [18] and specific electrical resistivity $\rho = 9 \times 10^{-7}$ Ωm.

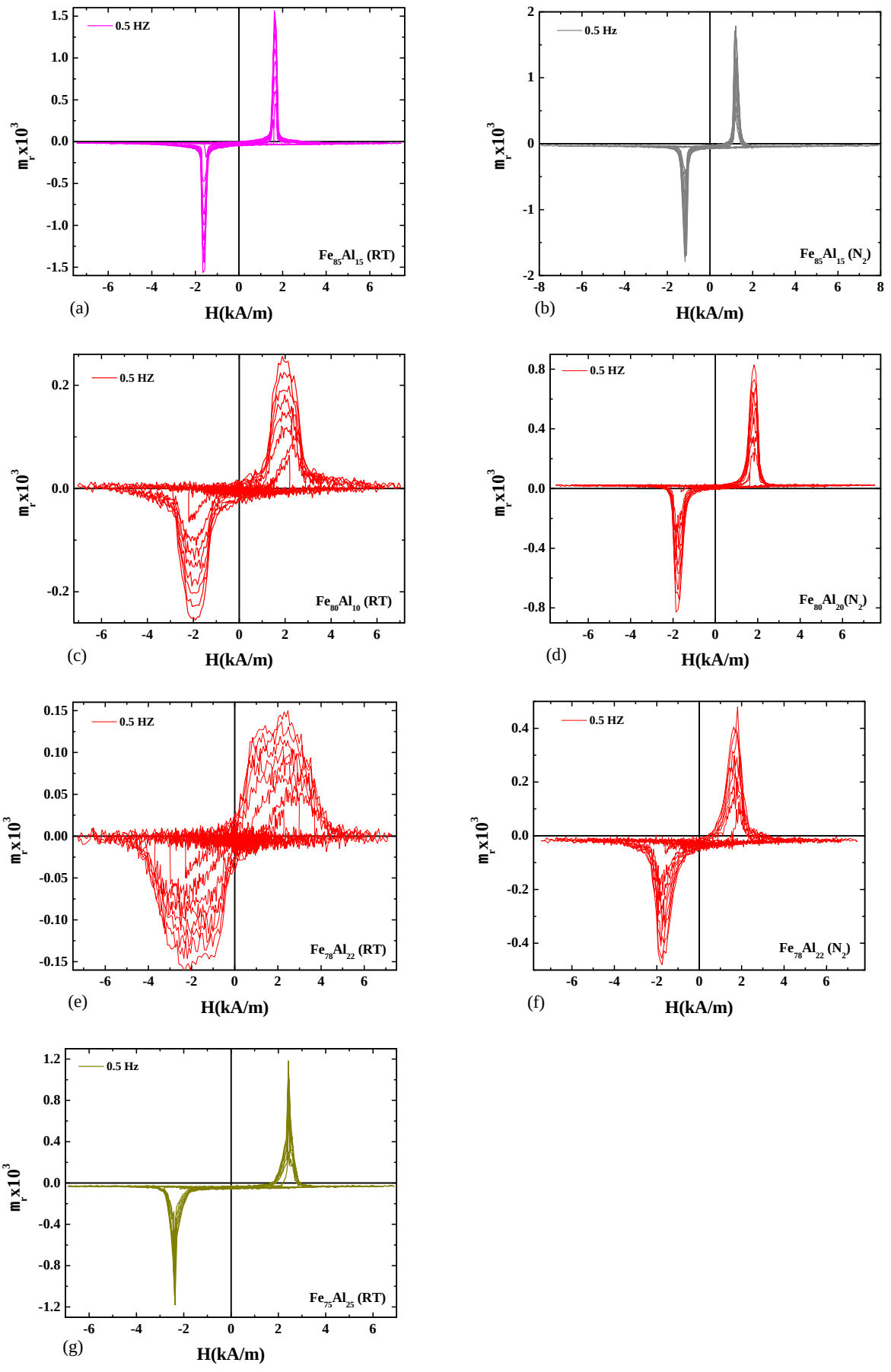

Figure 5.3: Relative permeability versus the field of HPT treated $Fe_{100-x}Al_x$ (x = 15 $\leq$ x $\leq$ 25) samples.

Sample	H_c(*f=0Hz*) *A/m*	H_c(*f=50Hz*) *A/m*	μ_{ri}	μ_{max} *dB/dt vs H(t)*	μ_{max} *dB/dH*	σ MPa	B_r/B_{max}
$Fe_{85}Al_{15}$(RT)	1675	1881	52	1565 (1600)	348 (1040)	28	0.70
$Fe_{85}Al_{15}(N_2)$	1060	1230	78	1740 (1200)	557 (826)	17.5	0.72
$Fe_{80}Al_{20}$(RT)	2371	2585	40	256 (1870)	238 (1776)	37	0.77
$Fe_{80}Al_{20}(N_2)$	2012	2280	44	828 (1825)	377 (1875)	31.7	0.76
$Fe_{78}Al_{22}$(RT)	2415	2610	39	155 (2290)	294 (1253)	43	0.77
$Fe_{78}Al_{22}(N_2)$	1763	2024	43	480 (1800)	306 (1040)	31.7	0.78
$Fe_{75}Al_{25}$(RT)	2398	2594	24	1180 (2430)	381 (2140)	48.7	0.77

Table 5.3: Magnetic hysteresis Parameters of HPT-treated $Fe_{100-x}Al_x$ (x = $15 \leq x \leq 25$) samples.

5.1.1 Temperature Dependence of Hysteresis

Temperature dependent hysteresis measurements were performed from room temperature up to 220°C in order to study the influence of the temperature on the magnetic properties. Hysteresis loops were taken at selected temperature with in accuracy of ± 2°C Figure 5.4 shows the coercivity, magnetization and initial permeability measured as function of temperature at constant frequency $f = 0.5$ Hz. It can be seen that the coercivity and magnetization decreased while permeability increased. According to the Globus relation [92]

$$\mu_i = \frac{M_s^2 D}{\sqrt{K_1}} \tag{5.2}$$

Where D is grain size, M_s is saturation magnetization and anisotropy constant K_1. Generally anisotropy field K_1 decreases much faster with elevated temperature than M_s which lead to an increase in μ_i. It can also be seen in Figure 5.4 that the rate of increase of μ_i with temperature decreases by increasing Al-content.

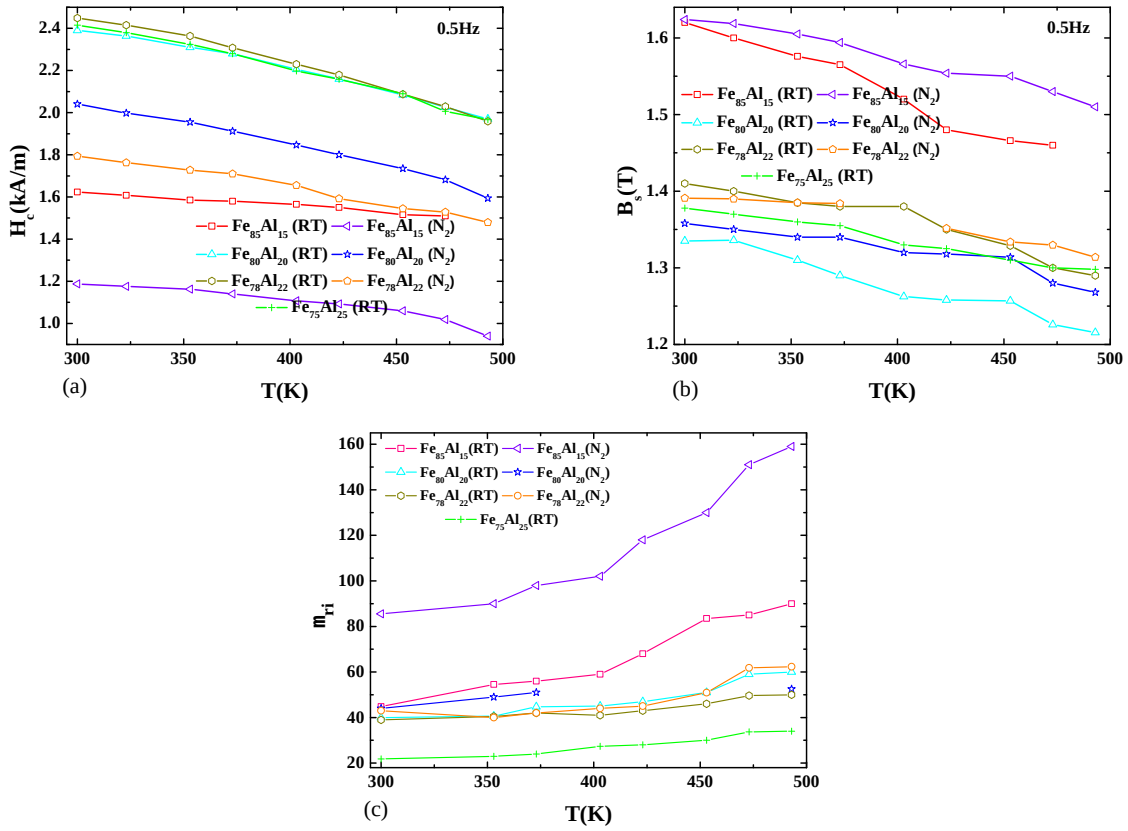

Figure 5.4: (a) coercivity versus temperature (b) saturation magnetization versus temperature and (c) initial relative permeability versus temperature (K) of HPT treated $Fe_{100-x}Al_x$ (x = $15 \leq x \leq 25$) samples.

5.1.2 Analysis of the Frequency Dependence of Coercivity at room temperature

Frequency dependence of coercivity $H_c(f)$ was analyzed by fitting the data by two general equations 5.3 and 5.4 as already described in chapter 3:

$$H_c(f) = a + b.f^c \tag{5.3}$$

$$H_c(f) = d + e.\sqrt{f} + g.f \tag{5.4}$$

In Eq.(5.3) it is assumed that $H_c(f)$ scales with some unknown power of f and in Eq. (5.4) $H_c(f)$ expressed into different powers of f. The fit parameters a and d corresponds

to coercivity at zero frequency i.e $H_c(f=0)$. b,c, e and g are fitting parameters. The coefficient b and the power factor c in Eq.(5.3) deliver an average of normal and anomalous eddy currents. The coefficients e and g describe the normal eddy and anomalous eddy currents respectively. The result of the fitting is shown in Figure 5.5 and the fitting parameters are given in Tables 5.4.

Frequency dependence of the coercivity in amorphous materials, has been analyzed by the Eq. 5.5 [67] derived for triangular wave form of the field with $H_c(t) = 4fH_o(t)$.

$$H_c(f) = H_c(0) + B(fH_o)^{\frac{1}{n}} \tag{5.5}$$

With H_o is the field amplitude, $H_c(0)$ is the coercivity at zero frequency, the coefficient depending on intrinsic parameters of materials, and n can vary between 1 and 3 depending on the geometry and on the microstructure of the material as well as on the considered frequency range [67]. Eq.(5.4) and (5.3) are set equivalent; from this the coefficient b can be expressed as $B = b/(H_0)^{1/n}$ which correlates then the dynamic coercivity field. The value of power factor cs iobtained by fitting which is in accordance with the range mentioned [67]. The high value of $i.e.$(c = 0.8) means also that normal and anomalous eddy currents are existing.

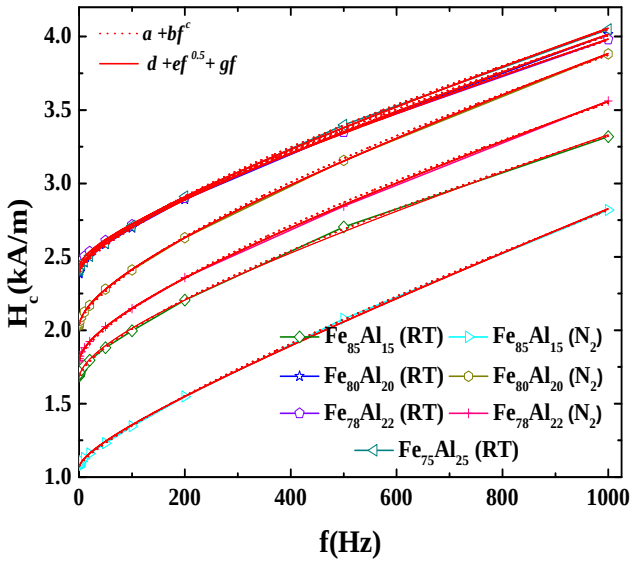

Figure 5.5: Fitting applying Eqs. (5.3) and (5.4) on experimental data of coercivity versus frequency of HPT treated $Fe_{100-x}Al_x$ ($15 \leq x \leq 25$) samples.

Sample	a	Δa	b	Δb	c	Δc
$Fe_{85}Al_{15}$(RT)	1688	3.7	12	0.66	0.70	0.007
$Fe_{85}Al_{15}(N_2)$	1076	3	6.7	0.33	0.80	0.007
$Fe_{80}Al_{20}$RT)	2394	4.7	10.5	0.76	0.73	0.01
$Fe_{80}Al_{20}(N_2)$	2040	5	15	0.97	0.70	0.01
$Fe_{78}Al_{22}$(RT)	2442	4	8.9	0.58	0.75	0.01
$Fe_{78}Al_{22}(N_2)$	1800	7.3	13	1.3	0.70	0.01
$Fe_{75}Al_{25}$(RT)	2410	1.9	10	0.30	0.70	0.004

Table 5.4: Fitting parameters applying Eq. (5.3) on the frequency dependence of the coercivity for HPT treated $Fe_{100-x}Al_x$ ($15 \leq x \leq 25$) samples; Δa, Δb and Δc describes the error to a, b and c.

Sample	d	Δd	e	Δe	g	Δg	μ(e)
$Fe_{85}Al_{15}$(RT)	1668	7	26	1.6	0.83	0.05	456
$Fe_{85}Al_{15}(N_2)$	1059	4.5	17.4	1.0	1.22	0.03	507
$Fe_{80}Al_{20}$(RT)	2374	1.0	24	0.23	0.89	0.007	192
$Fe_{80}Al_{20}(N_2)$	2018	1.0	31	0.26	0.90	0.008	443
$Fe_{78}Al_{22}$(RT)	2421	2.6	21	0.55	0.89	0.01	141
$Fe_{78}Al_{22}(N_2)$	1778	2.6	28	0.59	0.89	0.02	466
$Fe_{75}Al_{25}$(RT)	2390	4.4	24	0.98	0.92	0.30	189

Table 5.5: Fitting parameters applying Eq. (5.4) on the frequency dependence of the coercivity for HPT treated $Fe_{100-x}Al_x$ ($15 \leq x \leq 25$) samples; Δd, Δe and Δg describes the error to d, e and g.

Eddy current model for μ_r = constant:

The frequency dependence of H_c was also analyzed by an eddy current model based on the material parameters. Details description is given in chapter 3. Here the model equation is rewritten

$$H_c(f) = H(f=0).exp[(R(1-1/\sqrt{2}).\sqrt{\frac{\pi.f\mu_o\mu_r}{\rho}}] \tag{5.6}$$

R is the mean radius of sample, the specific resistivity (for Fe-Al ρ is between 1×10^{-7} and 9×10^{-7} mΩ) is (nearly) independent of the deformation. Fitting by model equation (5.6) on the experimental data of the frequency dependence of coercivity is shown in Figure 5.6. The maximum permeability was estimated from the frequency dependence of H_c. Fitting

parameters are summarized in Table 5.6. From the values it can be observed that the relative permeability increased which corresponds a decrease in the coercivity of samples.

Eq.(5.3) and (5.6) are equivalent. If one makes a series expansion of formula (5.6) and compare there coefficients a relation 5.7 can be obtained. From this relation an average relative permeability was calculated. The vlaues are reasonable for all samples and agree well with the values determined through *dB/dt* versus *H(t)* plots (for comparison see Table 5.3). Calculated vlaues are given in Table 5.5.

$$e = H_c|_{f=0} R. \sqrt{\frac{\pi . \mu_o \mu_r}{\rho}} \tag{5.7}$$

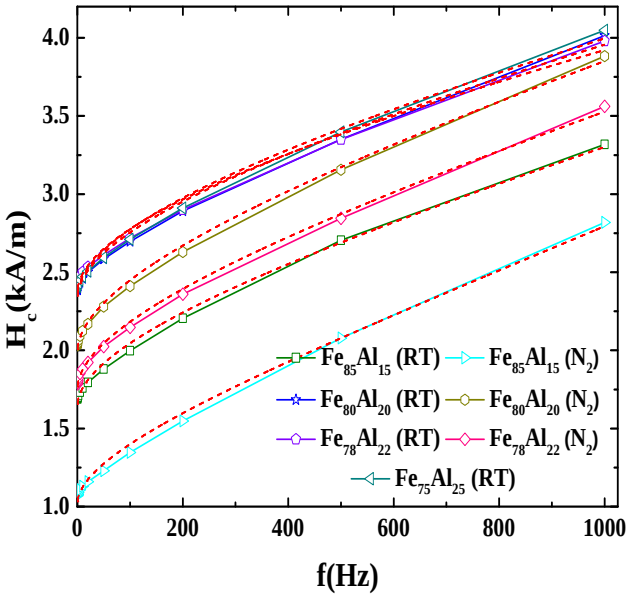

Figure 5.6: Fit applying the model Eq. (5.6) on experimental data of the coercivity versus frequency of of HPT-treated $Fe_{100-x}Al_x$ ($15 \leq x \leq 25$) samples.

Sample	*R(m)*	*a*	Δa	μ_r *(f=0)*	$\Delta\mu_r$
$Fe_{85}Al_{15}$(RT)	0.00033	1639	10	760	23
$Fe_{85}Al_{15}(N_2)$	0.00030	1016	11.6	1918	68
$Fe_{80}Al_{20}$(RT)	0.00036	2329	15	366	17
$Fe_{80}Al_{20}(N_2)$	0.00035	1986	9.0	605	15
$Fe_{78}Al_{22}$(RT)	0.00030	2367	17	479	26
$Fe_{78}Al_{22}(N_2)$	0.00032	1748	8.7	813	21
$Fe_{75}Al_{25}$(RT)	0.00038	2343	15	333	16

Table 5.6: Fitting parameters applying model Eq. (5.6) on the frequency dependence of the coercivity for HPT-treated $Fe_{100-x}Al_x$ ($15 \leq x \leq 25$) samples; Δa and $\Delta\mu_r$ describes the error to a, and μ_r.

5.1.3 Analysis of the Frequency Dependence of Losses

The frequency dependence of losses is shown in Figure 5.7. The losses were determined by a direct integration procedure of the hysteresis loops which were measured as a function of the frequency. The losses increased with increasing Al concentration. The average losses of $Fe_{100-x}Al_x$ x = (15, 20, 22, 25) as compared to HPT-treated Fe, under same HPT-treatment conditions are about a factor 2 smaller. In comparison to HPT-treated Fe-3 wt%Si and Fe-6.5 wt%Si at room and at liquid N_2 temperature the losses at low frequencies in HPT-treated Fe-Al system is approximately a factor 2 and 4 higher respectively, but at higher frequency the losses decreased. This may be due to the fact that at higher frequencies the skin depth (δ) becomes smaller than the sample dimension. Consequently the internal field becomes extremely inhomogeneous.

The frequency dependence of losses were analyzed using two different polynomial equations written as:

$$W_{tot} = BH = W_h + W_e.f^c \tag{5.8}$$

$$W_{tot} = BH = W_h + W_c + W_a = W_h + B_1.\sqrt{f} + B_2.f \tag{5.9}$$

In both cases so-called normal and anomalous eddy current losses are assumed. Table 5.7 gives the fitting parameters using Eq. (5.8) and Table 5.8 using Eq. (5.9). Where as W_h

delivers the frequency independent hysteresis losses (in J/m^3) as obtained by extrapolating the total losses to $f = 0$. Regarding the numbers and comparing with standard values of Fe-Si, the pure hysteresis losses in the HPT treated Fe-Al systems are about 100 times larger. Parameter c indicates according to formula (5.8) anomalous losses. When the value becomes larger than 0.5 anomalous losses becomes important. The values of the parameters B_1 and the parameter B_2 indicate that the contribution of these anomalous eddy current losses seems to be rather small as compared with the pure hysteresis losses as well as with the normal eddy current losses.

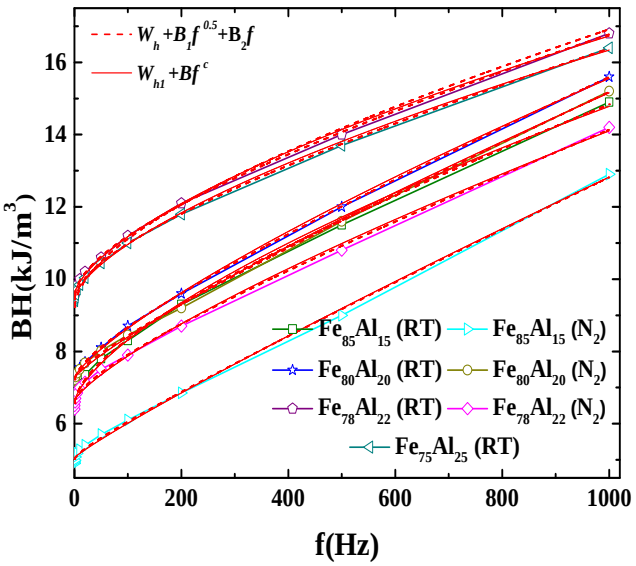

Figure 5.7: Fitting according to equation (5.8) and (5.9) on the frequency dependence of the losses of HPT-treated $Fe_{100-x}Al_x$ ($15 \leq x \leq 25$) samples.

According to a model suggested by Moses et.al, for Fe-Si [83] one can write the losses according to Eq. (5.10)

$$W_{tot} = W_h + a.\frac{A\pi^2 B_{max}^2}{\rho}.f + CB_{max}^{1.5}\sqrt{f} \tag{5.10}$$

Where W_h is hysteresis losses (rate independent)and the second term presents classical eddy current losses derived theoretically [60]. A is the cross-section of the sample, B_{max} is induction, a describes a constant which is determined by the shape of the driving field.

The classical eddy current losses were directly calculated from (5.10) and agree well with fitted parameter B_2. The calculated result using Eq. (5.10) are summarized in Table (5.8).

According to formula (5.9) the parameter B_1 indicates the "anomalous" eddy current losses, which can also be described by Bertotti [23] as in Eq. 5.11

$$W_{exc} = CB_{max}^{1.5}\sqrt{f} = 8\sqrt{\frac{GAV_o}{\rho}}B_{max}^{1.5}\sqrt{f}. \tag{5.11}$$

G is a geometry parameter which is about 0.2. V_0 forms a characteristic field responsible for the anomalous eddy currents. The estimated values of V_0 given in Table 5.8 are somewhat high for soft magnetic materials which might be due to the effect of a high magnetostriction of such material. Values as found for $a.A\pi^2B_{max}^2/\rho$ can be compared with that of B_2, this gives than values for a between 0.5 and 1 which is very reasonable.

Sample	W_{h1}*(f=0Hz)*	ΔW_{h1}	B	ΔB	c	Δc
$Fe_{85}Al_{15}$(RT)	6588	70	77	14.6	0.70	0.03
$Fe_{85}Al_{15}(N_2)$	5060	52	14	3.4	0.91	0.03
$Fe_{80}Al_{20}$(RT)	7268	27	38	3.4	0.80	0.01
$Fe_{80}Al_{20}(N_2)$	7263	40	24	3.8	0.84	0.02
$Fe_{78}Al_{22}$(RT)	9557	38	83	9.0	0.65	0.02
$Fe_{78}Al_{22}(N_2)$	6630	68	34	8.7	0.78	0.04
$Fe_{75}Al_{25}$(RT)	9460	34	72	7.5	0.66	0.02

Table 5.7: Fit parameters applying Eq. (5.8) on the frequency dependence of the losses of HPT-treated $Fe_{100-x}Al_x$ ($15 \leq x \leq 25$) samples; ΔW_{h1}, ΔB_1 and ΔB_2 are estimated errors of W_{h1}, B_1 and B_2.

Sample	W_h*(f=0Hz)*	ΔW_h	B_1	ΔB_1	B_2	ΔB_2	$a.A\pi^2B_{max}^2/\rho$	V_o
$Fe_{85}Al_{15}$(RT)	6490	47	147	10.5	3.7	0.34	a.9.83	1060
$Fe_{85}Al_{15}(N_2)$	4997	49	40	11	6.5	0.40	a.7.9	98
$Fe_{80}Al_{20}$(RT)	7176	11	96	2.4	5.4	0.08	a.8.0	652
$Fe_{80}Al_{20}(N_2)$	7186	30	66	6.6	5.9	0.22	a.7.9	312
$Fe_{78}Al_{22}$(RT)	9474	20	144	4.5	2.74	0.15	a.5.8	1966
$Fe_{78}Al_{22}(N_2)$	6539	55	89	12	4.8	0.40	a.6.7	649
$Fe_{75}Al_{25}$(RT)	9378	14	132	3.2	2.84	0.10	a.9.2	1060

Table 5.8: Fit parameters applying Eq. (5.9) on the frequency dependence of the losses of HPT-treated $Fe_{100-x}Al_x$ ($15 \leq x \leq 25$) samples; ΔW_h, ΔB_1 and ΔB_2 are estimated errors of W_h, B_1 and B_2.

5.2 Quenched and Annealed Fe-Ga

Substituting Fe by non magnetic Ga causes a dramatic increase in magnetostriction [61–63]. The high magnetostriction is due to local structure (ordering of Ga pairs [63]) and also due to softening of the elastic constants [61]. For dynamic applications we studied in this work the frequency dependence of the hysteresis loop and analyzed these data using different assumptions of eddy current based models.

High purity Iron (99.99%), and Gallium (99.999%) were weighted stoichiometrically with an excess of 1 wt % of Ga. The elements were melted three times in an induction furnace under Argon atmosphere using a water cooled Cu-curicibal. Finally four ingots were put together and re-melted in a bigger water cooled Cu-crucible (Hukin-Tiegel) under the same conditions as mention in [93]. From the big piece ("MA" or "Master Alloy") first a cylindrical disc was machined and then two rings were cut out. These two rings were sealed in a quartz ampoule under 15 mbar Argon atmosphere with Tantal foil as oxygen getter material. One sample was quenched in cold water ("Q" or "Quenched"), while the other was slowly cooled in the oven ("ASC" or "Annealed, Slowly cooled").

5.2.1 Hysteresis Measurements of Quenched and Annealed $Fe_{81}Ga_{19}$

Figure 5.8 shows the frequency dependence of the hysteresis loops measured on the quenched "Q" and annealed "A" $Fe_{81}Ga_{19}$ at room temperature in frequency range from 0.25 Hz to 100 Hz. Dimensions of ring samples and measurement parameters for hysteresis are given in Table 5.9. The applied field *H(t)* was in triangular wave form in order to obtain a constant *dH/dt*, which allows to calculate also the relative and the maximum permeability. The samples were demagnetized before each measurement. Saturation induction could not be achieved under applied field. The effect of eddy current is obvious regarding the increase of coercivity (and remanence) with frequency. Nevertheless with increasing frequency the coercivity of quenched samples increased sharply, for example the coercivity of the quenched sample was almost double than that of the annealed sample at 100 Hz. It should be noted that the remanence of both samples is significantly below that for isotropic cubic material with $K_1 > 0$ (easy axis in (100)) expected $0.866 M_s$ [94]

indicating also magnetically a strong texture of the material. In this measurement the "Q" sample shows a ratio of Mr/Ms = 0.06 (which also exhibit very high textured according to XRD [93]) whereas the "A" samples achieves a ratio of 0.15. Both plots are obviously not linear indicating the importance of excess frequency dependent effects.

Sample	$A(m^2)$	$l_{eff}(m)$	N_1	N_2
$Fe_{81}Ga_{19}$(Q)	8.75×10^{-7}	0.02	125	45
$Fe_{81}Ga_{19}$(A)	7.30×10^{-7}	0.02	125	46

Table 5.9: Parameters as used for the hysteresis measurements. N_1-Primary windings, N_2-Secondary windings, $l_{eff}(m)$-Magnetic path length, $A(m^2)$-Cross-sectional area.

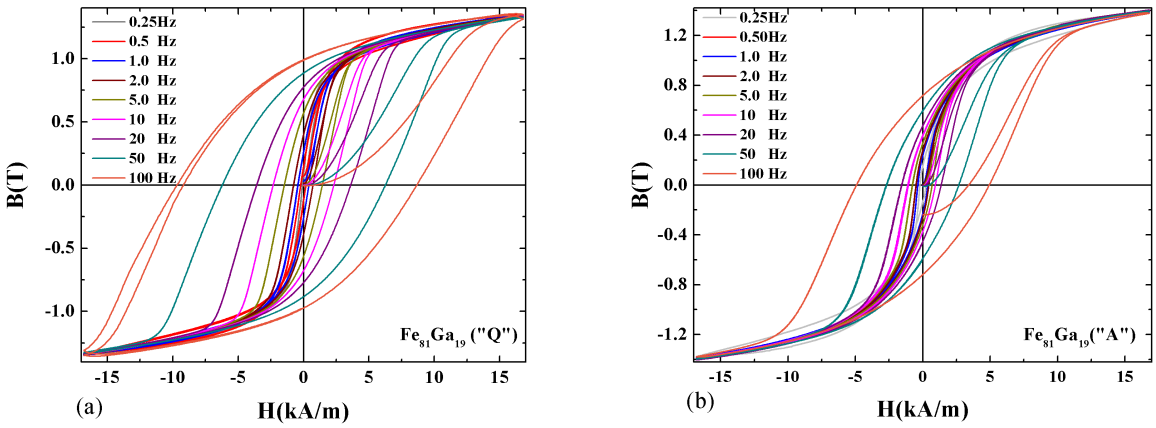

Figure 5.8: Hysteresis loop of $Fe_{81}Ga_{19}$ measured at different frequencies: (a) on quenched (Q) and (b) on annealed (A) at room temperature.

Figure 5.9 shows the coercivity plotted against the square root of frequency. Both curves are extrapolated to 0 Hz to obtain the coercivity at 0 Hz which the so called "true" coercivity. The annealed $Fe_{81}Ga_{19}$(A) sample shows significant lower values for $H_c(f=0)$ that may be due to the stress relaxed state in this sample which was found also by XRD [93]. Magnetic properties of the materials extracted from the hysteresis are given in Table 5.10.

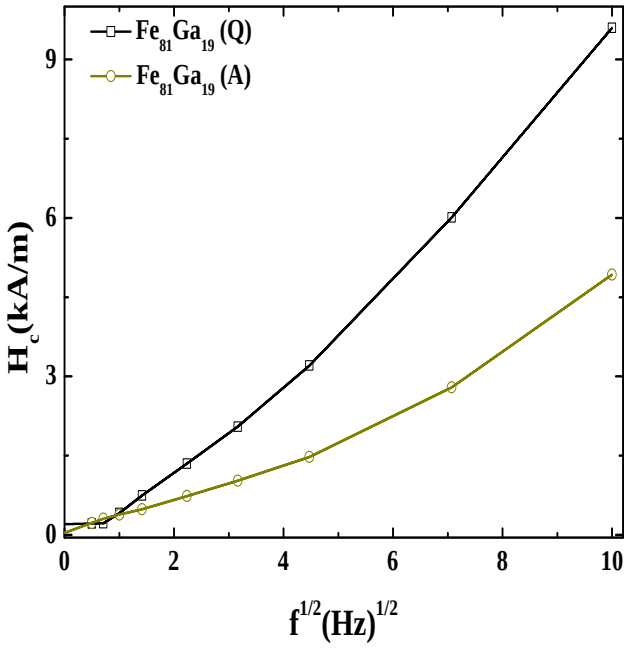

Figure 5.9: Extrapolated coercivity as a function of square root of frequency of $Fe_{81}Ga_{19}$ quenched (Q) and annealed (A) samples.

The initial permeability was determined by the slope of the initial BH-curve and the initial relative permeability (μ_{ri}) was calculated as μ_i/μ_o. The maximum relative permeability can be determined using the plot of *dB/dt* versus the field *H(t)* and relation $(\mu_o)^{-1}(\Delta\ B/\Delta\ t)\ (\Delta\ t/\Delta\ H)$. The triangular field *H(t)* allows to calculate $\Delta\ H/\Delta\ t$ from $4fH_{max}$. $\Delta\ B/\Delta\ t$ taken directly from the minor loop measurement data i.e *dB/dt*. Figure 5.3 shows the graphs of the relative permeability versus field. The differential permeability was also determined by means of direct differentiation of hysteresis loop (*dB/dH*). Magnetic parameter extracted from measured hysteresis loops are given in Table 5.10; the number in small bracket (..) is the field values where μ_{max} was determined. Figure 5.10 shows the relative permeability versus field and comparison of quenched (Q) and annealed $Fe_{81}Ga_{19}$ samples indicates clearly that the permeability broadens strongly due to the quenching process close to H_c which causes local stress.

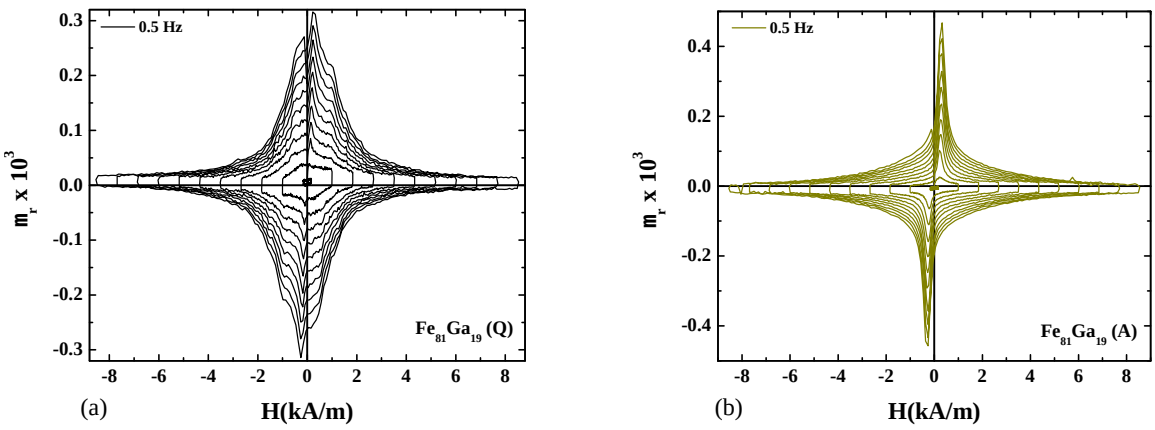

Figure 5.10: Relative permeability versus the field at room temperature measured at 0.5 Hz of $Fe_{81}Ga_{19}$ (a) quenched (Q) and (b) annealed (A) samples.

Sample	H_c*(f=0Hz)* *A/m*	H_c*(f=50Hz)* *A/m*	μ_{ri}	μ_{max} *dB/dt vs H(t)*	μ_{max} *dB/dH*	σ MPa	B_r/B_{max}
$Fe_{81}Ga_{19}$(Q)	204	6009	38	320 (239)	180 (445)	6.6	0.1
$Fe_{81}Ga_{19}$(A)	40	2792	105	460 (298)	442 (445)	1	0.1

Table 5.10: Magnetic hysteresis Parameters of $Fe_{81}Ga_{19}$ quenched (Q) and annealed (A) samples. The number in (..) is the field values where μ_{max} was determined.

5.2.2 Analysis of the Frequency Dependence of Coercivity

The frequency dependence of the coercivity was analyzed using Eqs. (5.3) and (5.4). The parameters a and d correspond to zero frequency coercivity $H_c(f=0)$ and were not considered as a free fit parameters. There values were considered from extrapolated data of H_c versus square root of frequency given in Table 5.10 . The result of the fitting is shown in Figure 5.11 and the fit parameters are given in Table 5.11.

The annealed (A) sample shows significant lower values for $H_c(f=0)$ that may be due to the stress relaxed state in this sample which was found also by XRD [93]. The dynamic coefficients b and e represent an average of normal and anomalous eddy currents with much larger values for the quenched (Q) sample.

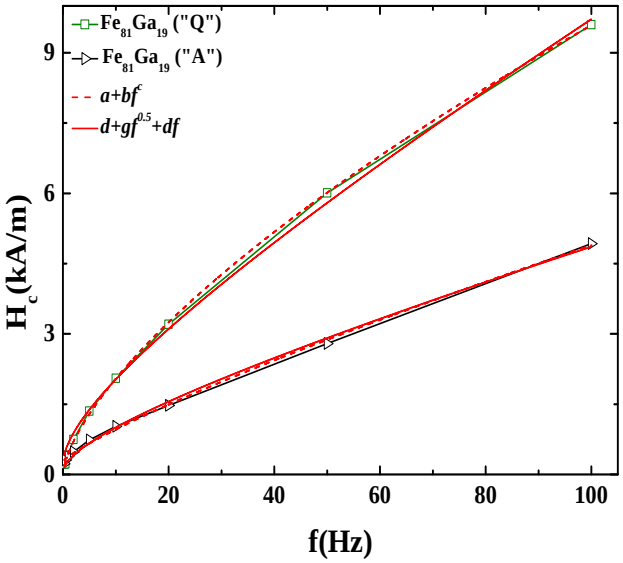

Figure 5.11: Fitting according to Eqs. 5.3 and 5.4 on experimental data of coercivity versus frequency of quenched and annealed $Fe_{81}Ga_{19}$ samples.

Sample	a	b	Δb	c	Δc
$Fe_{81}Ga_{19}$(Q)	204	349	21	0.72	0.01
$Fe_{81}Ga_{19}$(A)	40	192	30	0.70	0.04
	d	e	Δe	g	Δg
$Fe_{81}Ga_{19}$(Q)	204	404	46	54	5
$Fe_{81}Ga_{19}$(A)	40	222	21	26	2

Table 5.11: Fit parameters according to Eqs. (5.3) and (5.4) on experimental data of coercivity versus frequency of $Fe_{81}Ga_{19}$(Q) and (A) samples, where Δb, Δc, Δe, Δg describe the errors of b c, e,and g respectively.

According to an analysis of the frequency behavior of the coercivity in amorphous materials, the power factor can be described by a general formula (5.5) which was derived for triangular wave form of the field with $H_c(t) = 4fH_o t$ [67]:

In Eq. (5.3) the power factor c close to 2/3 (see Table 5.11) which according to [67] corresponds to a high frequency solution or to the fact that also anomalous eddy current damping of the domain walls occur. From the parameters of Eq. (5.4) given in Table (5.11) one can see that here normal eddy currents are visible described by parameter e however the anomalous eddy current damping (g) becomes especially at higher frequencies

dominant. Generally the "Q" sample shows higher normal eddy current effects.

Eddy current model for μ_r = constant:

The frequency dependence of H_c can be also analyzed by the model equation (5.6). Assuming that the specific resistivity (for Fe-Ga ρ is about 9×10^{-7} Ω m [93]) is (nearly) independent of the heat treatment, the maximum permeability was estimated from the frequency dependence of H_c. It is worth to note that the maximum permeability calculated from Eq.(5.6) were 1.6×10^5 and 8.8×10^5 for sample "Q" and "A" respectively. These values are unrealistically large for a high magnetostrictive materials. The experimental values of μ_{max} determined from the dB/dt versus $H(t)$ plot, which were $\mu_{max} = 320$ (sample Q) and $\mu_{max} = 460$ (sample A) (Table 5.10) gave more realistic numbers.
If one plots now $H_c(f)$ as determined experimentally and compares it with the trend given by formula (5.6) it becomes evident that according to this simple assumption H_c increases with f more and more whereas the experimental curve starts to saturate for high frequency values - see Figure 5.12. This unrealistic behavior of our model describing $H_c(f)$ and taking also into consideration that the achieved permeability values with the model were unreasonably high leading to an assumption which may be more realistic.

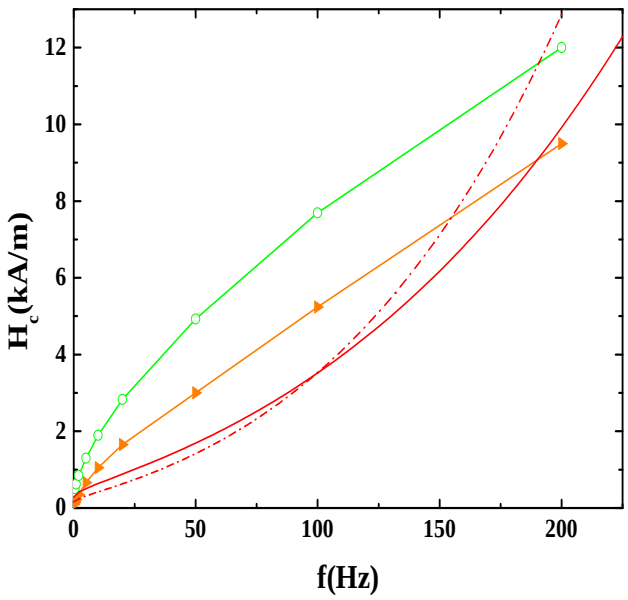

Figure 5.12: Fitting according to Eq. (5.6) on experimental data of coercivity versus frequency of $Fe_{81}Ga_{19}$ quenched (Q) and annealed (A) samples.

Eddy current model for $\mu_r = k/[H_c(f)]^n$:

Generally it can be assumed that the permeability scales reciprocal with the coercivity [72]. This leads to the assumption that with f increasing coercivity causes a reciprocal decreasing permeability. This leads to an improved eddy current model which assumes that $\mu_r(f)$ can be described by the simple formula: $\mu_r = k/[H_c(f)]^n$.

$$f = [\frac{\ln H_{ext} - \ln H_c(0)}{R(1 - \frac{1}{\sqrt{2}})}]^2 . \frac{\rho}{k\pi\mu_o} \tag{5.12}$$

Where k is the free parameter. When the model with this assumption was applied on the experimental curve delivered at least the correct shape of $H_c(f)$ (see Figure 5.13). Here, we expressed Eq. 5.12 in term of $f(H_c)$ since with $H_c(f)$ the problem is analytically difficult to solve. The results of fitting Eq. (5.12) to the experimental data by assuming $n = 1$ are given in Table 5.12. The much better agreement with the theoretical model is obvious from Figure 5.13. However the values as obtained for $\mu_r(f = 0)$ were for a polycrystalline material with high magnetostriction still unrealistic large. This means that the assumption of $\mu_r = k/[H_c(f)]^n$ with $n = 1$ was not sufficient to describe $H_c(f)$ with realistic values of the permeability. Therefore in order to study the effect of this reciprocity more general we also used n as a free fit parameter. This delivered fit results which agreed again very well with the experimental behavior of $H_c(f)$. The results of the fit are given in Table 5.13. Note that the error in *"k"* is now significantly bigger, which is a hint that this model is also problematic. A rather good agreement with experimental data has been achieved. It is obvious that the obtained value for the power factor n were close to one and consequently the calculated relative permeability is similar to that given in Table 5.13. This means that also this assumption cannot solve the problem of the too high permeability value.

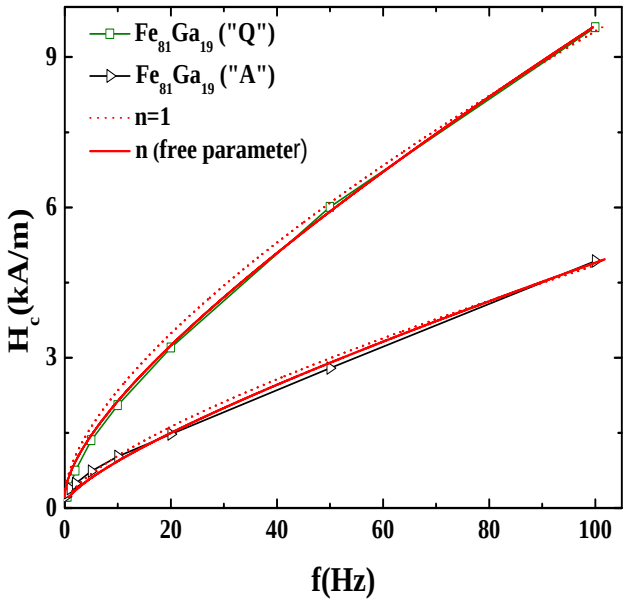

Figure 5.13: Fitting applying model Eq. 5.12 on the experimental data of the coercivity versus frequency of $Fe_{81}Ga_{19}$ (Q) and (A).

Sample	*R*	$H_c(f=0)$	$k\times10^6$	$\Delta k\times10^5$	$\mu_r(f=0)\times10^4$
$Fe_{81}Ga_{19}$(Q)	0.00153	204	15	2	7.6
$Fe_{81}Ga_{19}$(A)	0.0017	40	9.7	2	24

Table 5.12: Fit parameters according to model Eq. 5.12 assuming n=1 on experimental data of coercivity versus frequency of $Fe_{81}Ga_{19}$(Q) and $Fe_{81}Ga_{19}$(A) samples.

Sample	$H_c(f=0)$	$k\times10^6$	$\Delta k\times10^5$	n	$\mu_r(f=0)\times10^4$
$Fe_{81}Ga_{19}$(Q)	204	4.8	9.8	0.9	4.7
$Fe_{81}Ga_{19}$(A)	40	3.6	12	0.88	14

Table 5.13: Fit parameters according to model Eq. 5.12 using n as a free parameter on experimental data of coercivity versus frequency of $Fe_{81}Al_{19}$(Q) and $Fe_{81}Ga_{19}$(A).

5.2.3 Analysis of the Frequency Dependence of Losses

The hysteresis loops measured at different frequencies were integrated and these data were used to estimate the frequency dependence of the losses as shown in Figure 5.14. The estimated losses are a factor 25 higher than that of a conventional Fe-Si steel which might be due to the much larger magnetostriction of Fe-Ga. These curves were analyzed by fitting with a second order polynomial of the type given in Eq.(5.9). The fitting is

shown by dotted line in Figure 5.14 and the results of such fit are summarized in Table 5.14.

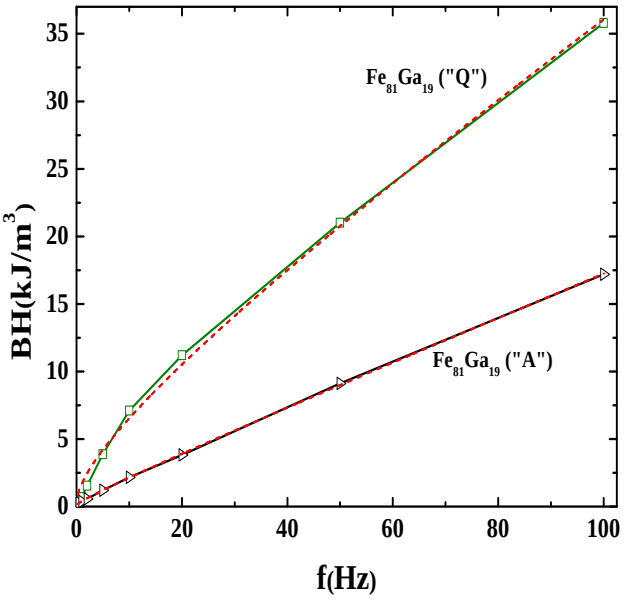

Figure 5.14: Fitting using Eq. 5.9 on the frequency dependence of losses of $Fe_{81}Ga_{19}$ quenched (Q) and annealed (A) samples.

The *BH* (J/m^3) versus f curves were also analyzed using a model as suggested by Moses et al. [83]. The calculated coefficient of f according to Eq. (5.10) agrees well with the fitted parameter B_2. The coefficient B_1 can be explained assuming anomalous eddy current losses as described by Bertotti [23]. The estimated values of V_o (Table 5.14) from Eq. (5.11) were unreasonably high for $Fe_{81}Ga_{19}$ (Q), which is a soft magnetic material like e.g. Fe-Si.

Sample	$W_h(f=0Hz)$	ΔW_h	B_1	ΔB_1	B_2	ΔB_2	$a.A\pi^2 B_{max}^2/\rho$	V_o
$Fe_{81}Al_{19}$(Q)	196	0	1274	172	231	21	1.6	6497
$Fe_{81}Al_{19}$(A)	75	0	162	15	155	1.8	0.85	88

Table 5.14: Fit parameters applying Eq. (5.9) on the frequency dependence of the losses for $Fe_{81}Ga_{19}$ (Q) and (A)samples; ΔW_h, ΔB_1 and ΔB_2 are estimated errors to W_h, B_1 and B_2.

5.3 Discussion and Conclusions

High magnetostrictive materials such as Fe-Al and Fe-Ga alloys behaves as a magnetically soft material, which is very important for technical applications. In $Fe_{100-x}Al_x$ ($15 \leq x \leq 25$) alloys, decrease in saturation magnetization and relative permeability while increase in coercivity was observed with increase of Al contents. The coercivity of samples deformed at liquid nitrogen (N_2) temperature was significantly less than the coercivity of the same samples deformed at room temperature (RT). The frequency dependence of the coercivity as well as that of the losses for $Fe_{100-x}Al_x$ ($15 \leq x \leq 25$) samples can be well explained using a simple eddy current model. This leads to permeability values which can be well compared with the values which were determined from a direct measurement of *dB/dt* versus *H(t)* as well as from a direct differentiation of the loop. Also the the normal eddy current losses obtained from analysis of frequency dependence of losses by fitting equation (coefficient B_2) and by model suggested by Moses et. al, were well compared.

The frequency dependence of the hysteresis as well as the losses were measured on quenched (cold water "Q") and annealed (slowly cooled in the oven "A") polycrystalline $Fe_{81}Ga_{19}$ samples. The coercivity and consequently the hysteresis loop exhibits unexpected strong frequency dependence. The data were analyzed using different dynamic hysteresis based model. The annealed sample exhibits lower coercivity and lower hysteresis losses as compared to quenched sample, however both samples shows strong frequency dependence. Analyzing the frequency dependence of the coercivity by eddy current model, the relative permeability was estimated. Although the model fit very well with the experimental data, however unrealistically high value of the relative permeability was obtained. The model can explain the experimental data only by assuming a much larger sample cross-section as really used.

Classical and excess eddy current losses were separated by analysing the frequency dependence of the losses. The classical losses (B_2) were calculated using the material parameters. Here good agreement between the fitted and the calculated values were found. The excess eddy current losses (B_1) are rather high and deliver unexpected large values for the characteristic field V_o which might be due to the high magnetostriction of this material. The

results of these analysis show however that in all cases anomalous eddy current effects are necessary in order to achieve agreement between experiment and model. No direct correlation could be found between the parameters describing frequency dependence of the coercivity and that of the losses.

Chapter 6

Magnetic and Microstructural Investigation of SPD Pearlitic Steel

The Pearlitic steel grade R260 is carbon-manganese steel used for rail tracks transporting heavy load therefore must be high strength as well as high wear resistance against environments. The chemical composition of fully pearlitic steel grade R260 is 0.76 wt.%C, 0.35 wt.%Si, 1 wt.% Mn, 0.014 wt.% S, 0.017 wt.% P, and 97.86 wt.% iron. The strength can be enhanced by controlled shaping of the pearlitic microstructure, especially the pearlite morphology during isothermal annealing. With thermal treatment the size of pearlite colonies and interlamellar distance in cementite is reduced. In consequence, the properties of a pearlitic rail steel and the durabilityof rail sections change [95–97]. Strength properties of rail steel enhanced with increased carbon content. While addition of manganese causes a decrease in the pearlitic transition point, thus contributing to reduction in size of pearlite colonies. Such steels are characterized by high stability and low level of additive elements, as well as high metallurgical purity and a low content of gases, especially hydrogen (below 2 ppm) and oxygen (below 20 ppm) [98].

In ferromagnetic materials a well established correlation exists between the elastic/plastic deformation and the associated changes in magnetic properties. The properties are influenced by dislocations and other imperfections such as inclusions and inhomogeneities in the materials. It is also well known, that during the fatigue process the dislocation den-

sities changes very rapidly. These dislocations interact and impede the free movement of magnetic domain walls and lead to changes in magnetic properties such as coercivity [99].

Pearlitic steel R260 has been investigated magnetically by hysteresis measurements. The samples were plastically deformed by HPT technique as described in experimental chapter with shear rate ϵ = (0, 1, 2, 4, 8 and 16) at room temperature in order to study the effect of severe plastic deformation on the microstructure and possible correlation with magnetic properties such as coercivity, permeability etc.

6.1 Microstructure

Microstructures of SPD pearlitic steel grade R260 samples were investigated by Transmission Electron Microscopy (TEM). Micrographs for samples deformed with shear rate ϵ = (0, 8, 16) are shown in Figure 6.1.

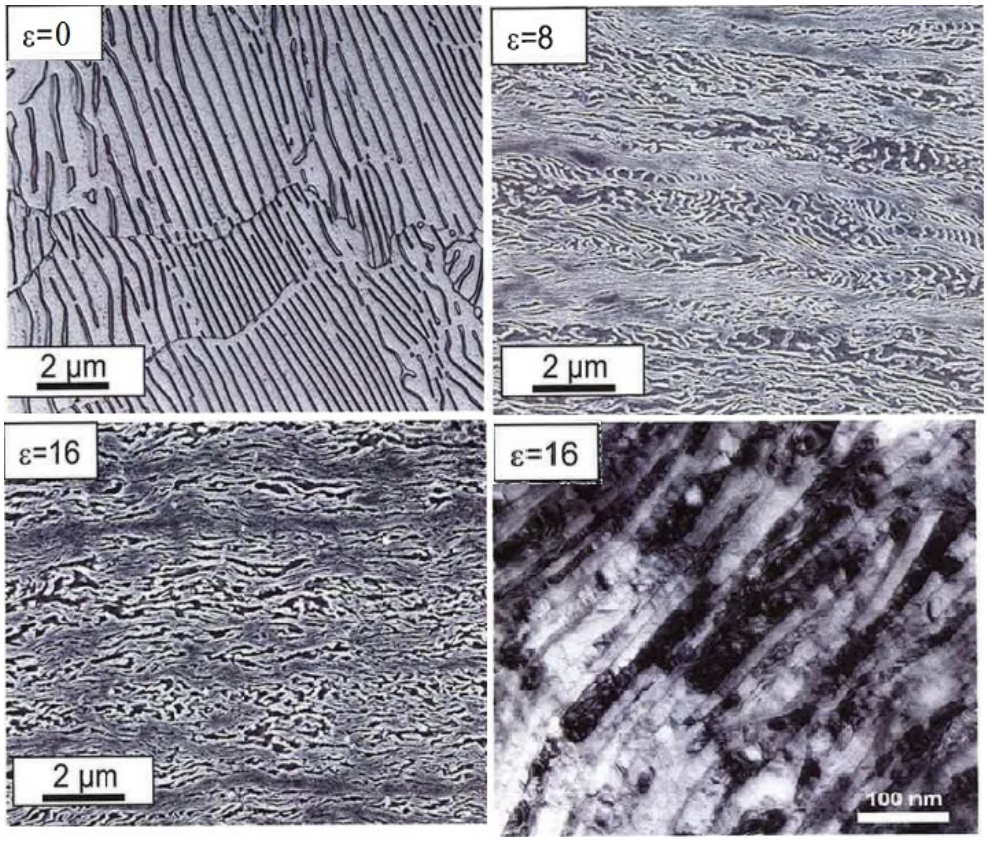

Figure 6.1: Microstructure photographs of SPD treated pearlitic steel (R260).

It can be observed from micrographs that the lamellas are aligned parallel to the shear direction while the distance between them is decreasing with increasing shear strain. The shear deformation leads to an elongation and alignment of the cementite lamellae parallel to the pressing direction and are severely deformed, as can be seen from smaller interlamellar distance and a smaller thickness of cementite lamellae. Pearlite morphology and hardness test have shown that the smaller the interlamellar distance, the higher the steel strength. Vicker hardness increased from 240 HV to $\sim$ 800 HV at a shear rate $\epsilon = 16$. More over fragmentation of carbides appeared with SPD deformation.

6.2 Magnetic Hysteresis Measurements of SPD Pearlitic Steel R260

Magnetic hysteresis were measured on ring shape samples with a hysteresigraph set-up described in the experimental chapter. All samples with their dimensions and parameters used for hysteresis measurements are listed in Table 6.1. All magnetic measurements were performed under triangular magnetizing current in order to obtain constant dH/dt.

Sample	$A(m^2)$	$l_{eff}(m)$	N_1	N_2
$P_1(\epsilon=0)$	7.40×10^{-7}	0.022	68	61
$P_2(\epsilon=1)$	7.46×10^{-7}	0.022	57	63
$P_3(\epsilon=2)$	7.40×10^{-7}	0.022	67	62
$P_4(\epsilon=4)$	7.50×10^{-7}	0.022	68	67
$P_5(\epsilon=8)$	7.50×10^{-7}	0.022	63	62
$P_6(\epsilon=16)$	7.50×10^{-7}	0.022	58	61

Table 6.1: Parameters as used for the hysteresis measurements of pearlitic steel (R260). N_1-Primary Windings, N_2-Secondary Windings, $l_{eff}(m)$-Magnetic Path length, $A(m^2)$-Cross-sectional Area.

Figure 6.2 shows the frequency dependence hysteresis of all measured samples. The shear strain effect can be seen from the broadening of the loops area at very low frequencies.

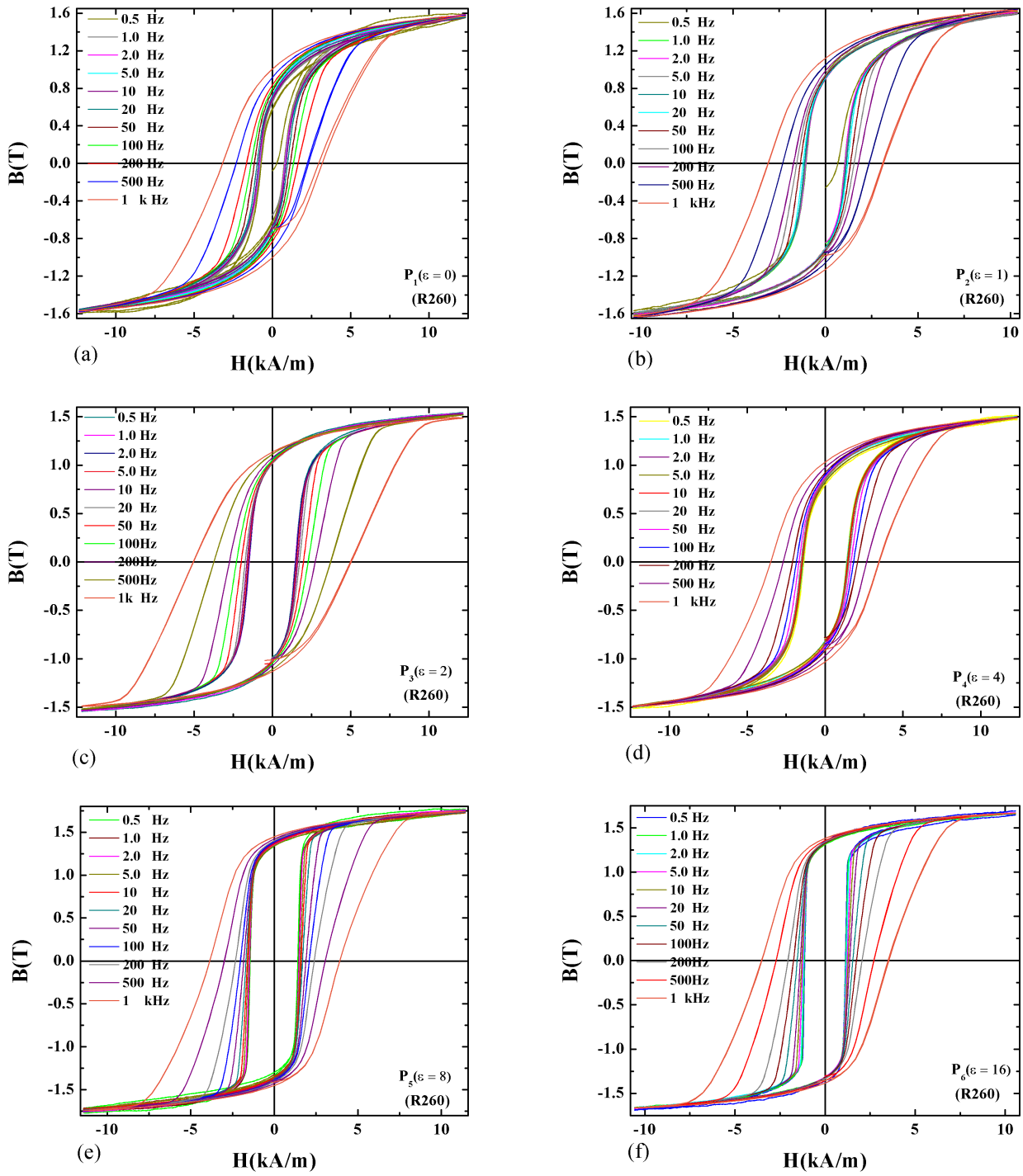

Figure 6.2: Hysteresis loops of SPD treated pearlitic steel (R260) (a) $P_1(\epsilon{=}0)$, (b) $P_2(\epsilon{=}1)$, (c) $P_3(\epsilon{=}2)$, (d) $P_4(\epsilon{=}4)$, (e) $P_5(\epsilon{=}8)$ and (f) $P_6(\epsilon{=}16)$.

The coercivity at 0.5 Hz increased radically from 656 A/m with $\epsilon = 0$ to 1016 A/m and 1426 A/m with $\epsilon = 1$ and $\epsilon = 2$ respectively but a further increase in the deformation up to $\epsilon = 16$ lead to decrease in the coercivty. This might be due to the fact that with

increasing shear rate the dislocation density increases but when the grain size becomes below 100 nm the dislocation decreases again and exchange coupling may occure. The broadening of hysteresis loops at higher frequencies is due to eddy currents but this effect is much smaller than for HPT-deformed pure iron as already discussed in chapter 4.

Figure 6.3 shows the coercivity plotted against the square root of frequency. The coercivity at 0 Hz was obtained by extrapolating coercivity data versus square root of frequency up to 0 Hz. At zero shear rate ($\epsilon = 0$) the curve showed more linear behavior which indicate that the classical eddy current effect dominates. Increasing shear deformation produced dislocations and other imperfections in crystal structure which result in an increase of the resistance of the sample, consequently the eddy current effect is reduced. An increasing coercivity has been observed with shear strain rate up to $\epsilon = 4$ but at higher shear strain the coercivity decreases. The same trend was observed for the squareness ratio B_r/ B_s. The magnetic parameters derived from the hysteresis loop are given in Table 6.2.

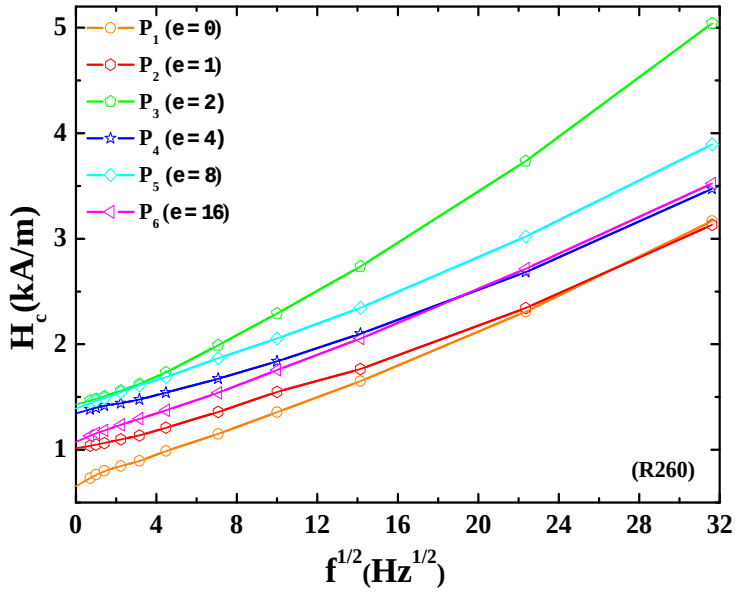

Figure 6.3: Coercivity versus square root of frequency of SPD treated pearltic steel (R260).

The initial permeability was determined from the slope of the initial BH-curve and the relative permeability (μ_{ri}) was calculated as μ_i/μ_o. The maximum relative permeability μ_{max} at a field *H (A/m)*was determined experimentally using minor loop measurements from which the plot of *dB/dt* (T/s) versus the field *H (A/m)* can be derived and then

according to formula (3.25) $\mu_{max}(H)$ can be calculated - see Figure 6.4.

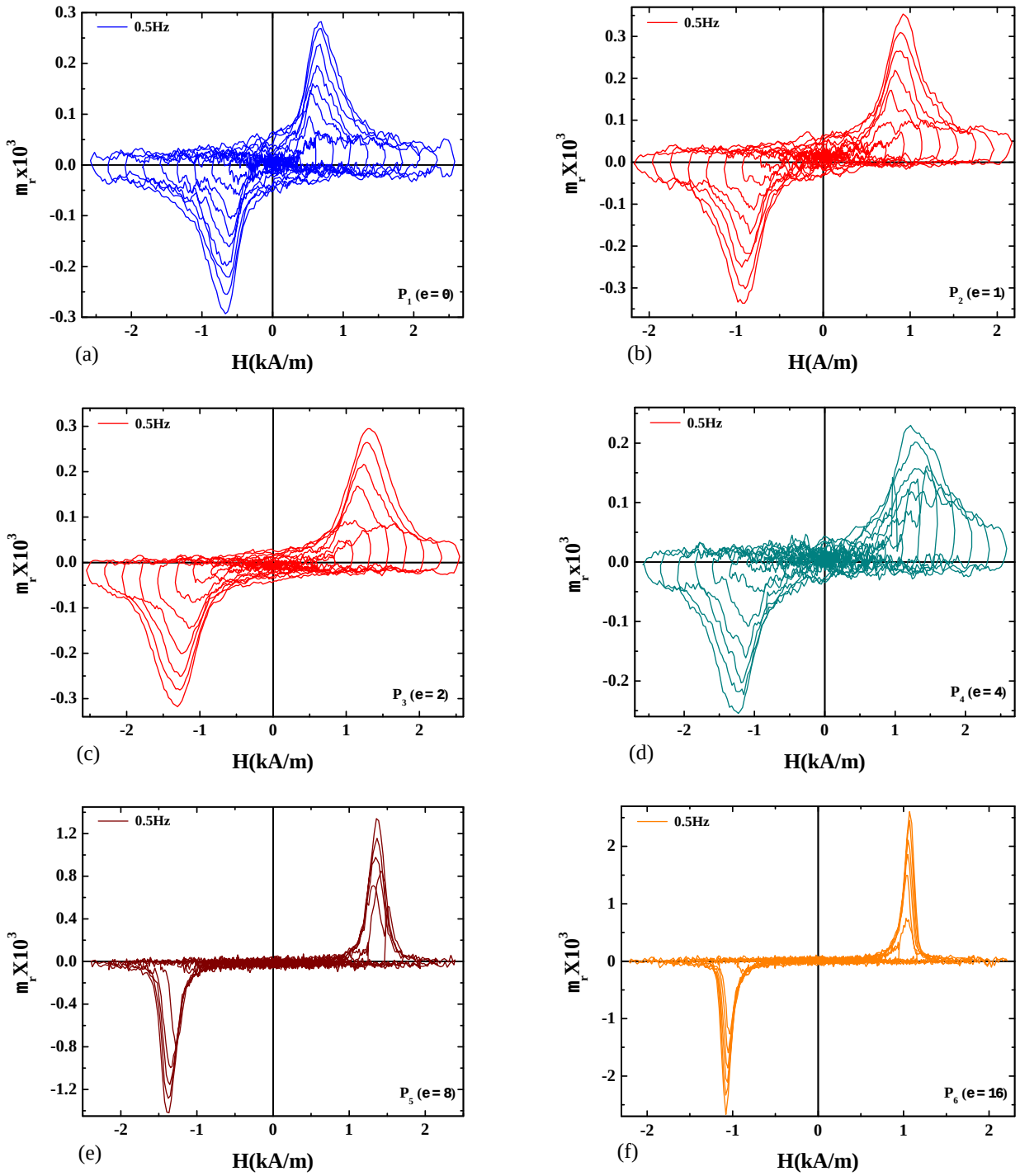

Figure 6.4: Relative permeability versus the field of SPD treated pearlitic steel (R260) (a) $P_1(\epsilon=0)$, (b) $P_2(\epsilon=1)$, (c) $P_3(\epsilon=2)$,(d) $P_4(\epsilon=4)$, (e) $P_5(\epsilon=8)$ and (f) $P_6(\epsilon=16)$.

In the measurements of minor loop a triangular field $H(t)$ was used which allows to calculate $\Delta H/\Delta t$ from $H_{max}/T/4$; $\Delta B/\Delta t$ is obtained directly from the measurement.

Additionally, the maximum relative permeability μ_{max} can also be determined from the direct differentiation of hysteresis loop (dB/dH). The number in small brackets (..) describes the field where the relative permeability value μ_{max} was determined. The magnetic permeability derived and calculated from hysteresis measurements are presented in Table 6.2.

Sample	H_c*(f=0Hz)* *(A/m)*	H_c*(f=50Hz)* *(A/m)*	μ_{ri}	μ_{max} *dB/dt vs H(t)*	μ_{max} *dB/dH*	B_r/B_{max}
$P_1(\epsilon=0)$	656	1148	140	287 (665)	180 (552)	0.37
$P_2(\epsilon=1)$	1016	1358	114.6	343 (912)	205 (760)	0.58
$P_3(\epsilon=2)$	1426	1975	51	304 (1308)	219 (522)	0.66
$P_4(\epsilon=4)$	1344	1673	69.6	241 (1212)	201 (814)	0.57
$P_5(\epsilon=8)$	1388	1862	68	1375 (1377)	955 (1515)	0.76
$P_6(\epsilon=16)$	1074	1540	51	2617 (1078)	786 (1247)	0.86

Table 6.2: Magnetic Properties of SPD treated pearlitic steel (R260), the number in (..) describes the field where the relative permeability μ_{max} was determined.

6.2.1 Analysis of the Frequency Dependence of Coercivity

The coercivity is strongly influenced by the stress state of the sample therefore for a basic understandings of the stress and frequency effects on the coercivity the experimental data describing the frequency dependence of the coercivity of rail steel samples (R260) were analyzed by the general formulas 3.16 and 3.17 described in chapter 3. The fitting results are shown in Figure 6.5. The experimental data are shown by solid curves with symbols, while the fitting results are shown by dashed and solid curves respectively.

The parameters extracted from the fitting by the corresponding formulas are given in Tables 6.3 and 6.4. The value of power factor c describing the eddy current behavior is between 0.6 and 0.7 which agree well with the value described in formula [67]. From the value of parameter e, the relative permeability (μ_r) calculated by using relation (3.20) and is given in Table 6.4 as $\mu_r(e)$.

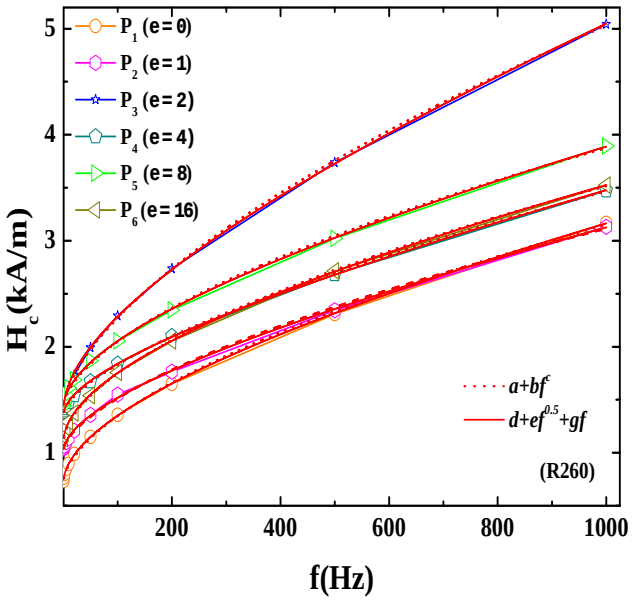

Figure 6.5: Fitting according to Eqs. (3.16) and (3.17) on coercivity versus frequency data of SPD treated pearlitic steel (R260).

Sample	a	Δa	b	Δb	c	Δc
$P_1(\epsilon{=}0)$	734	11	39	3.0	0.60	0.01
$P_2(\epsilon{=}1)$	1027	11	26.5	2.7	0.63	0.01
$P_3(\epsilon{=}2)$	1436	6.7	46	1.6	0.63	0.004
$P_4(\epsilon{=}4)$	1379	4.4	21.5	0.92	0.67	0.006
$P_5(\epsilon{=}8)$	1438	12	38.7	3.4	0.60	0.01
$P_6(\epsilon{=}16)$	1117	5.6	44	1.6	0.58	0.005

Table 6.3: Fit parameters according to Eq. (3.16) on the coercivity versus frequency data of SPD pearlitic steel (R260). Δa, Δb and Δc describe error to a, b and c.

Sample	d	Δd	e	Δe	g	Δg	μ(e)
$P_1(\epsilon{=}0)$	707	4.7	58	1.0	0.62	0.03	682
$P_2(\epsilon{=}1)$	1000	7.4	44.7	1.6	0.70	0.05	205
$P_3(\epsilon{=}2)$	1388	9.0	77.7	1.9	1.20	0.06	316
$P_4(\epsilon{=}4)$	1349	4.2	40.5	0.90	0.85	0.03	90
$P_5(\epsilon{=}8)$	1411	5.4	57.6	1.0	0.65	0.04	163
$P_6(\epsilon{=}16)$	1093	2.8	61	0.58	0.50	0.02	311

Table 6.4: Fit parameters according to Eq. (3.17) on the coercivity versus frequency data of SPD pearlitic steel (R260). Δd, Δe and Δg describe error to d, e and g.

The frequency dependence of the coercivity of SPD treated rail steel samples (R260) was also analyzed by the eddy current model given below as explained in chapter 3.

$$f = [\frac{\ln H_{ext} - \ln H_c(0)}{R(1-\frac{1}{\sqrt{2}})}]^2 . \frac{\rho}{k\pi\mu_o} \tag{6.1}$$

With the assumption $\mu_r(f) = \mathrm{k}/[\mathrm{Hc(f)}]^n$, whereas k and n are fitting parameters. Figure 6.6 presents the fitting result and fitting parameters are given in Table 6.5.

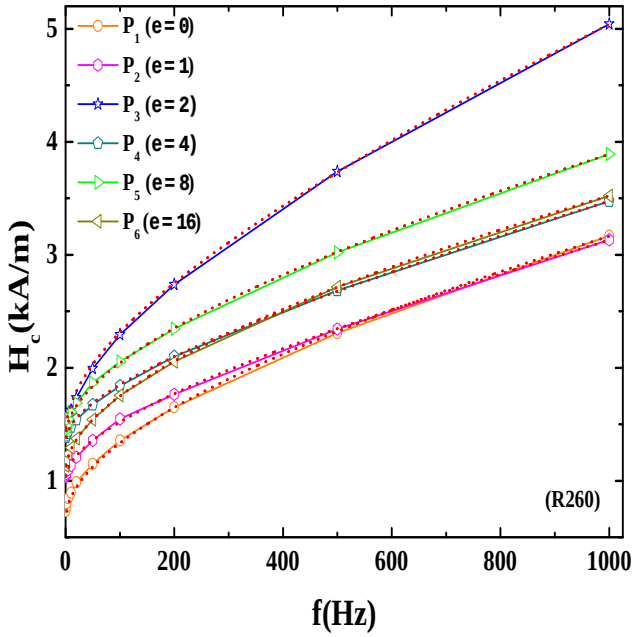

Figure 6.6: Fitting according to Eq. (6.1) on the coercivity versus frequency data of SPD pearlitic steel (R260).

Sample	a=$H_c(f$=0$Hz)$	$R(m)$	n	Δn	k	Δk	μ_r(f=0)
$P_1(\epsilon$=0)	655	0.0005	0.83	0.02	200315	36062	192
$P_2(\epsilon$=1)	1013	0.0005	0.36	0.02	2300	379	144
$P_3(\epsilon$=2)	1427	0.0005	0.5	0.0	11111	0	294
$P_4(\epsilon$=4)	1343	0.0005	0.2	0.01	464	58	110
$P_5(\epsilon$=8)	1389	0.0005	0.53	0.02	8517	1295	184
$P_6(\epsilon$=16)	1075	0.0005	0.75	0.007	66030	3790	352

Table 6.5: Fit parameters according to equation (6.1) on the coercivity versus frequency data of SPD treated pearltic steel (R260) and the calculated permeability μ_r at $f = 0$ from $\mu_r(f) = k/[Hc(f)]^n$.

The model fits (dash curve) very well with the experimental data of all samples. However, the value of n varies from 0.2 to 0.8 in a nonsystematic manner. The value of fitting

parameter k is also used to calculate the relative permeability at f=0 of all samples by using relation $\mu_r(f)$ = k/[Hc(f)]^n is given in Table 6.5. The values calculated from this relation do not agree well with the values obtained experimentally as given in Table 6.2. μ_r behaves in this case not reciprocal to H_c which is a consequence of the unusual behaviour of the power factor n.

6.2.2 Analysis of the Frequency Dependence of Losses

The frequency dependent losses were calculated at different frequencies by integrating the area of the hysteresis loops. The hysteresis losses were much higher in the deformed samples (ϵ= 1, 2, 4, 8, 16) as compared to un-deformed sample (ϵ= 0). For example eddy currents effect start to become significant above 20 Hz which can be seen from the broadening of the hysteresis loops. The losses also increased with shear rate due to role of the internal stresses. However the calculated losses for P_1 (ϵ=0) were a factor 2.5 smaller than that of pure un-deformed iron and for P_6 (ϵ=16) factor 2 smaller than HPT-deformed iron at room temperature.

The losses were analyzed by fitting the *BH (J/m)* versus f curve with a second order polynomial Eq. (6.2) and were also analyzed using a model suggested by Moses et. al, [83] given in Eq. (6.3).

$$W(f) = W_h + B_1.\sqrt{f} + B_2.f \tag{6.2}$$

$$W_{tot} = W_h + CB_{max}^{1.5}\sqrt{f} + a.\frac{A\pi^2 B_{max}^2}{\rho}.f \tag{6.3}$$

Where W_h represents the frequency independent hysteresis losses, B_1 and B_2 are fitting parameters. $A(m^2)$ is the cross section of the sample, B_{max} gives the maximum induction of the material and ρ is the specific electrical resistivity; a describes a constant which is determined by the shape of the driving field. The coefficient of classical eddy current losses term in Eq. (6.3) can be directly calculated from the experimental data.

According to Bertotti the anomalous losses are described as

$$W_{exc} = CB_{max}^{1.5}\sqrt{f} = 8\sqrt{\frac{GAV_o}{\rho}}B_{max}^{1.5}\sqrt{f}. \tag{6.4}$$

G is a geometry parameter which is about 0.2. V_0 forms a characteristic field responsible for the anomalous eddy currents. V_0 was calculated by using the value of fitting parameter B_1 and coefficient of $\sqrt{f}$ in Eq. (6.3). The fitting parameter and calculated values are given in Table 6.6.

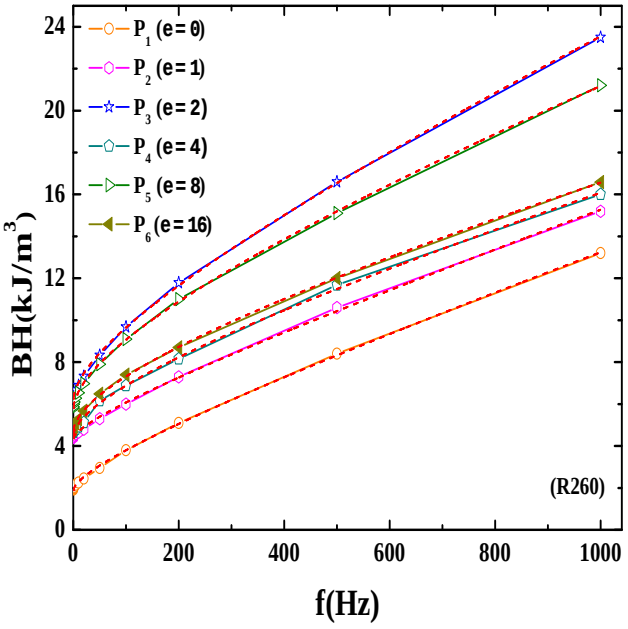

Figure 6.7: Total losses versus frequency for SPD pearlitic steel (R260) and analyzed by applying Eq.(6.2) shown by dotted line.

Sample	$W_h(f$=0Hz)	$\Delta\ W_h$	B_1	$\Delta\ B_1$	B_2	$\Delta\ B_2$	*aB2*	V_o
$P_1(\epsilon$=0)	1833	29.7	120	6.7	7.6	0.02	a.187	37
$P_2(\epsilon$=1)	4308	42	98	9.5	7.9	0.03	a.188	27
$P_3(\epsilon$=2)	6114	58	262	13	9.2	0.42	a.164	194
$P_4(\epsilon$=4)	4424	45	188	16	5.7	0.5	a.167	99
$P_5(\epsilon$=8)	5667	72	271	6.5	7.0	0.2	a.178	205
$P_6(\epsilon$=16)	4626	28	219	6.3	5.0	0.2	a.177	134

Table 6.6: Fit parameters according to Eq. (6.3) on frequency of dependence total losses for pearlitic steel (R260). ΔW_h, ΔB_1 and ΔB_2 describe error to W, e and g.

6.3 Conclusions

Pearlitic rail steel (R260) samples were plastically deformed with shear rates (ϵ = 1, 2, 4, 8, 16). It was observed that with increasing shear strain the lamellas were aligned in the shear direction and the distance between them decreased while the vicker hardness increased from 240 HV to 800 HV at a shear rate $\epsilon = 16$.

The coercivity and hence hysteresis losses increased extensively because with deformation dislocation density increases which may causes strong pinning sites nevertheless, the calculated losses are lower than HPT deformed Fe.

The relative permeability calculated from eddy current model do not satisfy to the experimentally obtained values due to nonsystematic manner of fitting parameter n of model.

Chapter 7

Magnetic Measurements of Pipeline Steels

Pipelines made of steel are used for the transportation of crude oil, refined oil, natural gas and petrochemicals. With passing time the pipelines are affected by these chemicals as well as the continuously changing environmental effects for example oil and gas contain hydrogen sulfide (H_2S) which seriously cause corrosion and cracking problems [100]. Magnetic investigation provides the promising non-destructive technique for predicting the failures in structure of the material [57], since ferromagnetic properties like hysteresis loops, domains, and magnetostriction of steel are very sensitive to local stress areas, dislocations, or scratches [101]. For this purpose in this chapter three different categories of steel segments, X52, X56, and X60 grade oil-pipelines were obtained from out-of-service tubes and investigated in order to see the anisotropic and stress effect as a result of environmental degradation on the magnetic hysteresis. Table 7.1 gives chemical composition according to API 5L standards for each magnetically investigated steel in this work.

Elements	*X52*	*X56*	*X60*
C	0.21	0.10	0.08
Mn	1.21	1.51	1.09
Si	0.05	0.31	0.26
P	0.021	0.014	0.010
S	0.019	0.002	0.004
Cr	0.02	0.03	0.01
Ni	0.02	0.02	0.02
V	0.00	0.00	0.08
Ti	0.00	0.02	0.00
Cu	0.05	0.01	0.30

Table 7.1: Chemical composition of pipeline steels X-52, X-56, X-60.

7.1 Microstructure

Figures 7.1 show a typical longitudinal and transverse section microstructures for X52, X56, and X60 grade pipeline steels. X52 (see Figure.7.1a, b) contain elongated ferritic (white) and pearlite (black) phases texture along the rolling direction. The pearlitic content is about 25% due to high carbon content (0.21 %) and the grain size ranges from 4 to 20 μm. Figure 7.1(c,d) shows the microstructure of X56 steel along longitudinal and transverse direction respectively consisting of uniformly distributed mixed ferrite, pearlite. From grain distribution no texture can be seen. In X60 steel only a small texture can be observed (see Figure.7.1c, d).

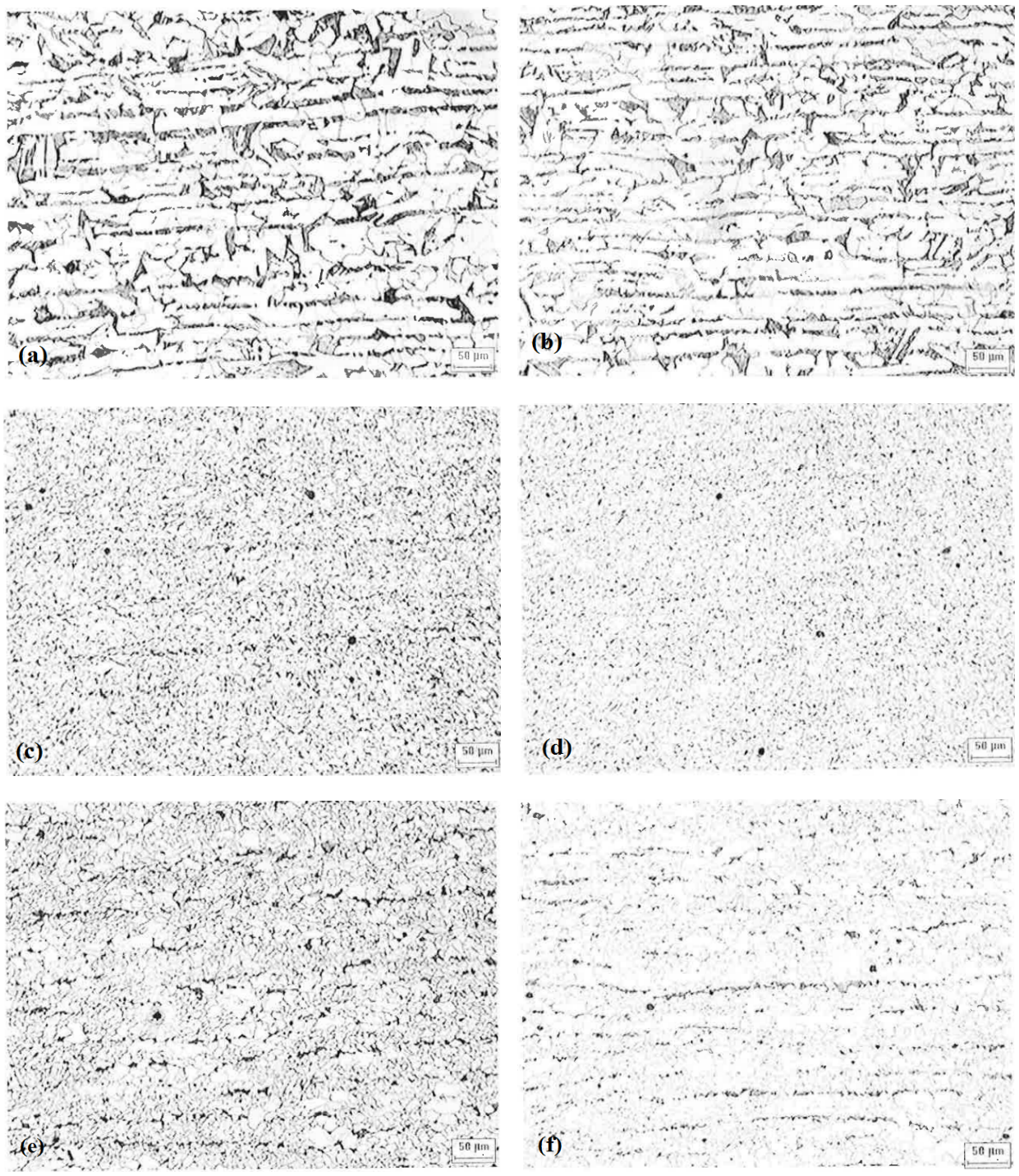

Figure 7.1: Microstructure of a longitudinal (left) and transversal (right) section of X52 (a, b), X56 (c, d) and X60 (e, f).

7.2 Magnetic Hysteresis of X52, X56 and X60 Pipeline Steels

In order to measure the magnetic properties in different crystallographic texture, steel segments with dimension (60×39×3) mm were cut parallel (longitudinal or along the axial direction), perpendicular (transverse) and at an angle of 45°of the pipe axis and designated as *L-sample*, *T-sample*, and *M-sample* respectively. To make a magnetically closed circuit, frame shaped sample (sample geometry is shown in chapter 2, Figure 2.6) were made by cutting from steel segment such that the thin legs of frame are oriented parallel, perpendicular and at 45°angle to the pipe axis for the L, T and M samples, respectively. The connecting regions of the legs have a cross-section being five times larger than that of the legs itself. Therefore, the influence of these connecting regions on the measurements has been neglected as described in experimental chapter 2 (section 2.3.3).

The frequency dependent magnetic hysteresis measurements were carried out from 0.25 Hz to 100 Hz at room temperature. The applied AC magnetic field *H(t)* was in triangular wave form to obtain constant *dH/dt*. This also allows an accurate determination of the permeability. The samples were demagnetized before each measurement. The magnetic hysteresis measurements parameters are given in Table 7.2.

Sample	$A(m^2)$	$l_{eff}(m)$	N_1	N_2
X52L	1.65×10^{-5}	0.143	360	98
X52M	1.66×10^{-5}	0.143	360	98
X52T	1.65×10^{-5}	0.142	280	64
X56L	1.62×10^{-5}	0.144	250	76
X56M	1.66×10^{-5}	0.143	250	76
X56T	1.64×10^{-5}	0.143	250	76
X60L	1.67×10^{-5}	0.142	250	76
X60M	1.67×10^{-5}	0.143	250	76
X60T	1.69×10^{-5}	0.142	250	76

Table 7.2: Parameters as used for the hysteresis measurements. N_1-Primary Windings, N_2-Secondary Windings, $l_{eff}(m)$-Magnetic Path length, $A(m^2)$-Cross-sectional Area of the thin leg.

Here l_{eff} is the magnetic path length which is equal to sum of lengths taken from the centre of all four sides of window frame (shown by dotted lines in Figure 2.7) while the area of cross-section is taken only of the thin leg.

Figure 7.2 shows the frequency dependent hysteresis loops of X52 (L), X52 (T), and X52 (M) samples. The polarization is about 1.94 T at a field of 10 kA/m, but the sample is not yet saturated. The coercivity obtained at 0.25 Hz is double that of pure un-deformed Fe but 4.7 factors less than HPT-deformed Fe (see Data in chapter 4). This high coercivity at low frequency is due to the density of inclusions (impurities) and residual stresses effects. Eddy current contribution causes an increasing coercivity as is visible from the increasing hysteresis loop area with increasing frequency. For example in the X 52 L sample the coercivity obtained at 50 Hz was 2464 A/m while in un-deformed pure Fe and HPT-deformed (room temperature) was 1250 A/m and 2750 A/m at 50 Hz respectively. The coercivity is twice that of pure un-deformed Fe and comparable to HPT-deformed Fe.

To demonstrate the texture effect, hysteresis loops measured at 0.5 Hz for the longitudinal, transversal and at an angle of 45°are plotted in one graph as shown in Figure 7.2(d). The slope of hysteresis curves measured in three directions illustrate that the sample posses magnetically anisotropic behavior, with a magnetic easy axis in the pipe axial (longitudinal) direction and the hard axis along the transverse direction. The strong texture effect because of the shape anisotropy is more visible in minor loops and the loops of dB/dt versus H for all samples of X52 as shown in Figure 7.6. The texture is in accordance with the microstructure (see Figure7.1(a, b)). From the microstructure it can be seen that the grains have long needle like shape (cylindrical in shape) and lie along the longitudinal direction as the internal demagnetizing field will be less along the length of the grains as compared to the width of grains that's why the easy axis of magnetization is parallel to the long axis.

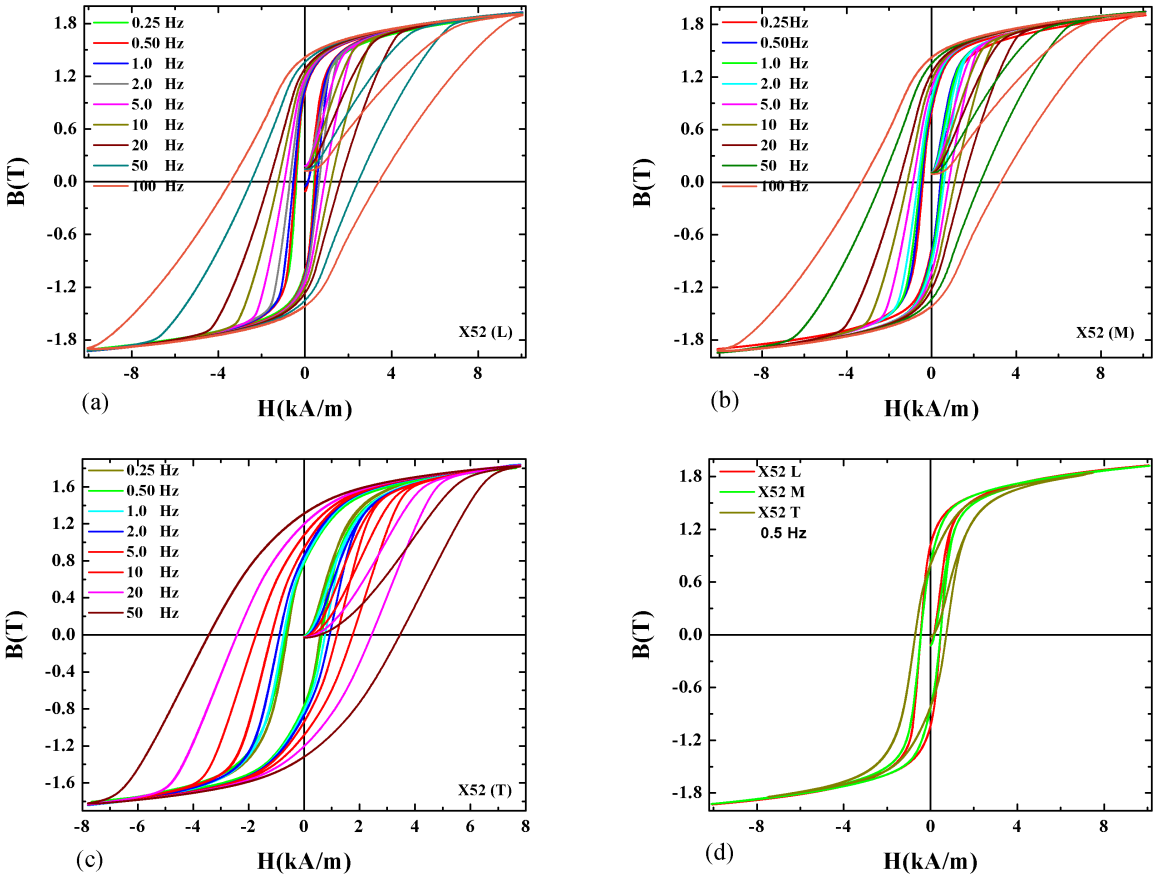

Figure 7.2: Hysteresis loops for X52 steel (a) L, (b) M, (c) T and (d) Comparison of texture of X52 at 0.5 Hz.

The frequency dependence hysteresis loops for X56 and X60 steel are shown in Figures 7.3 and 7.4 respectively. The magnetization is about 1.95 T at a applied field of 6 kA/m but also here it is clear that the sample is not saturated. The frequency dependent behavior is similar in all samples. The comparison of the hysteresis of all three samples for X56 shows isotropic behavior (Figure 7.3 d) whereas sample X60 steel as visible in Figure 7.4 d shows rather small anisotropy which is also in agreement with their corresponding microstructures (Figure 7.1(c, d)).

Figure 7.5 shows the coercivity plotted against the square root of the frequency of the X52, X56, and X60 samples. The linear behavior indicates the major contribution of classical eddy currents in enhancing the coercivities with frequency. The coercivity of X52 sample in transverse direction is somewhat higher because of the hard axis of

magnetization. Whereas in X56 and X60 the coercivity is the same in all three directions.

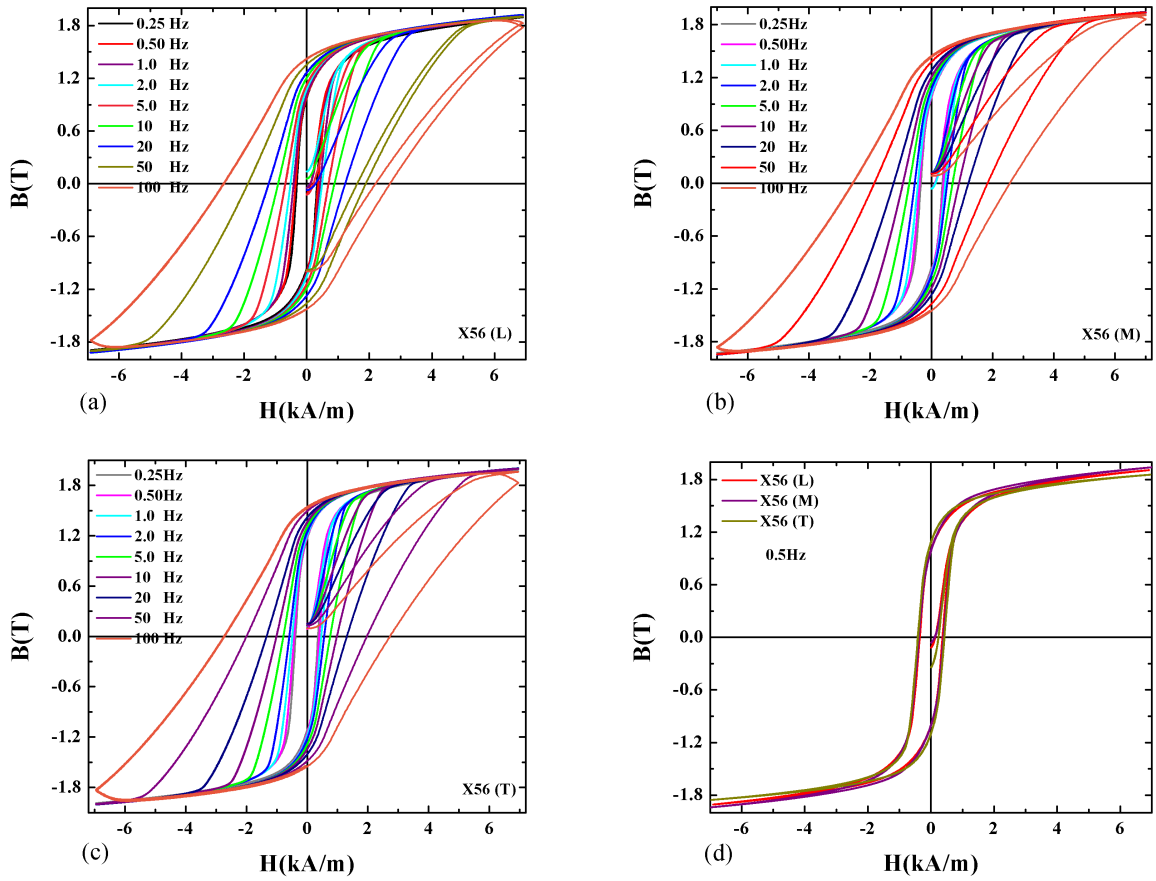

Figure 7.3: Hysteresis loops for X56 steel (a) L, (b) M, (c) T and (d) Comparison of texture at 0.5 H.

The magnetic parameters derived from the hysteresis loops within 2% accuracy of all investigated samples are given in Table 7.3. The ratio of remanent polarization to saturation polarization is clearly below the theoretical value of 0.75 for a cubic isotropic material [101]. The difference in remanence values along (L), transverse (T), and in 45°(M) to the pipe axis strongly indicate the presence of a texture in particular direction in X52 and X60 samples.

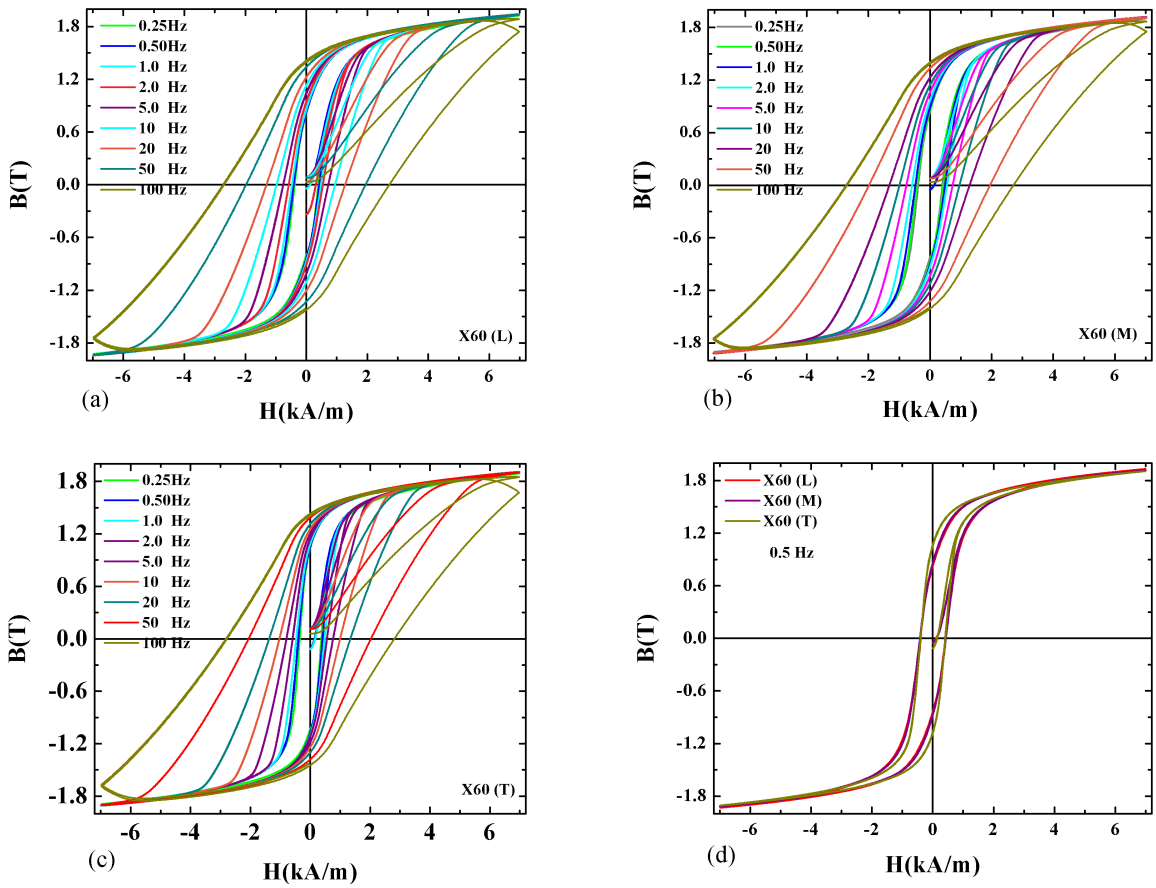

Figure 7.4: Hysteresis loops for X60 steel (a) L, (b) M, (c) T and (d) Comparison of texture at 0.5 H.

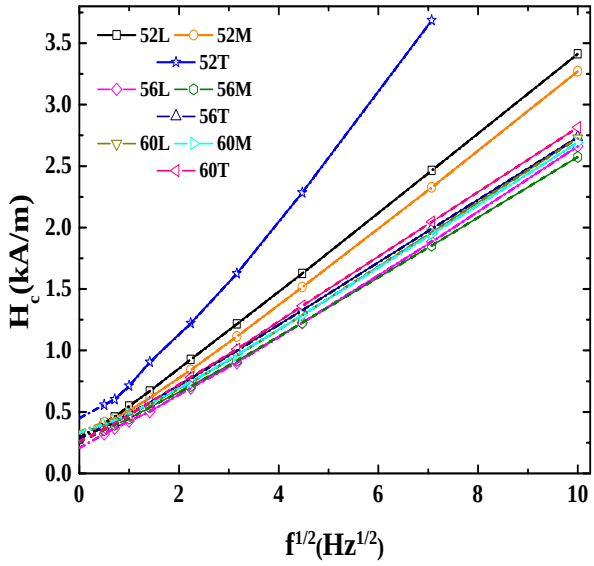

Figure 7.5: Coercivity versus square root of frequency of X52, X56, X60.

The initial relative permeability (μ_{ri}=μ_i/ μ_0) was determined from the slope of initial BH curve and the maximum relative permeability μ_r was determined experimentally using minor loop measurements from which the plot of *dB/dt (T/s)* versus the field *H (A/m)* can be derived and then according to Eq. (3.25), μ_{max}(H) can be calculated as shown in Figures 7.6, 7.7 and 7.8. In the measurements a triangular field *H(t)* was used which allows to calculate Δ H/Δt from H_{max}/T/4; ΔB/Δt is obtained directly from the measurements. The maximum relative permeability μ_{max} can also be determined from the direct differentiation of hysteresis loop (*dB/dH*). The number in the small brackets (...) against each maximum relative permeability value presents the field value where μ_{max} was determined (Table 7.3). Note that this field is not identical with the coercivity.

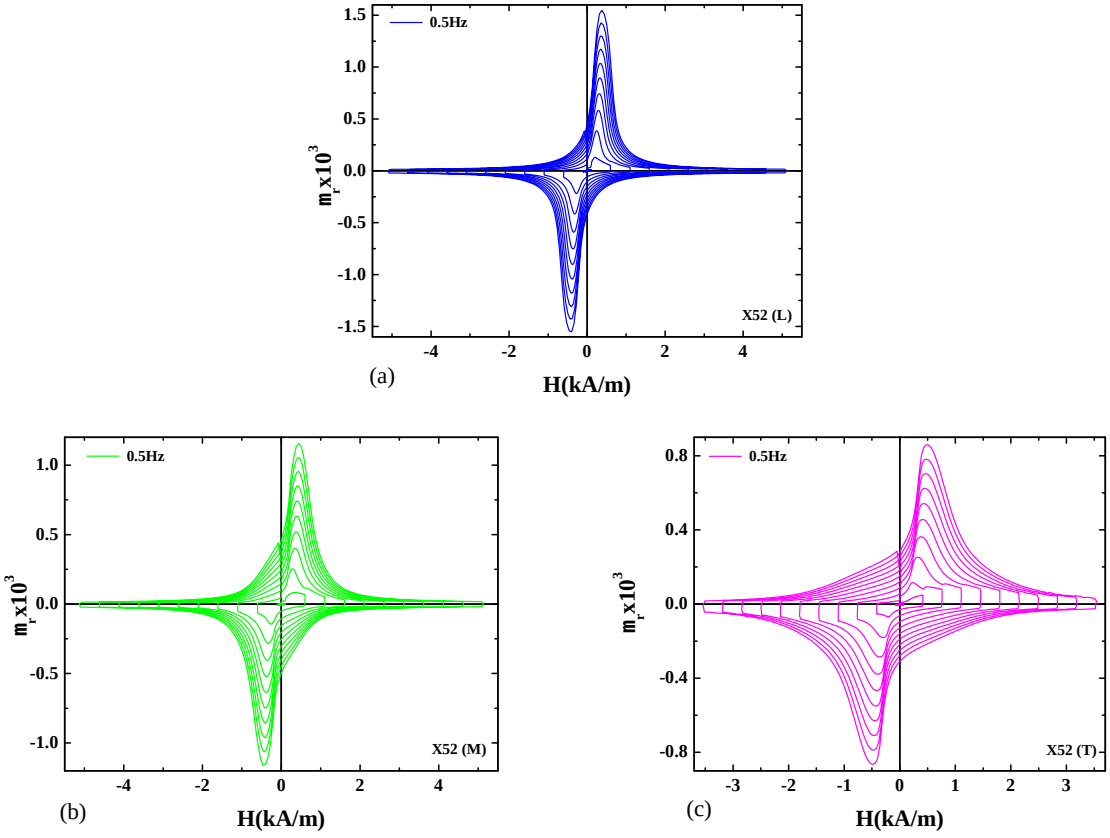

Figure 7.6: Relative permeability μ_r versus field *H(t)* for pipeline steel X52 (a) X52 (L), (b) X52 (M), (c) X52 (T).

The effect of texture in the samples X52 and X60 can also be observed from a significant broadening from the middle of permeability versus field *H(t)* curves when measuring along

the tranverse (T) and longitudinal (L) direction respectively (see Figures 7.6c and 7.8a). This indicates that a high induction is required to align the moment in the hard axis. No texture effect can be seen from μ_r versus *H(t)* curves for the sample X56 which is also in agreement with the hysteresis loops and microstructure (see Figure 7.7 and 7.1(c-d)).

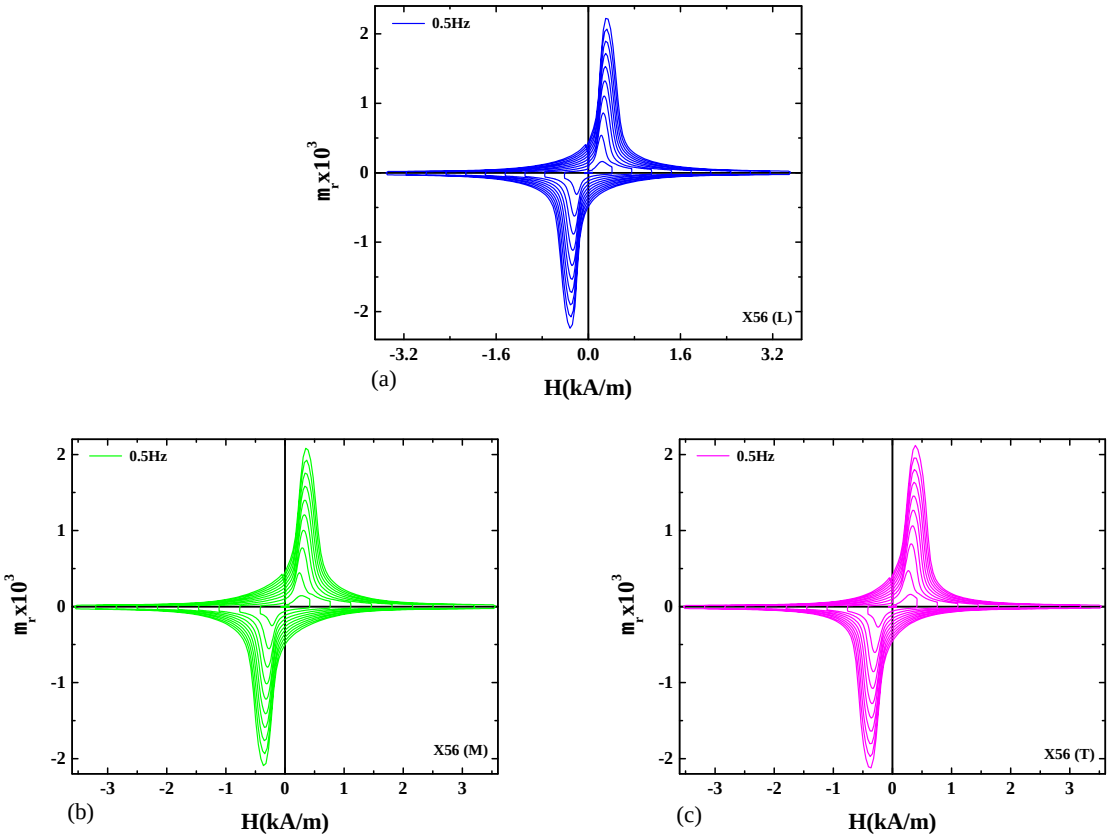

Figure 7.7: Relative permeability μ_r versus field *H(t)* for pipeline steel X56 (a) X56 (L), (b) X56 (M) and (c) X56 (T).

Static or quasi-static coercivity of the soft magnetic materials depends generally on the microstructure (grain size) and additionally on external stresses (λ-effective magnetostriction, σ-stress) neglecting the magnetocrystalline ansiotropy ($\lambda\sigma > K$). This effect can be explained in a simple relation which describes the coercivity of soft magnetic materials.

$$H_c = \frac{\lambda\sigma}{\mu_o.M_s} \tag{7.1}$$

The internal stress σ was estimated from this relation and is given in Table 7.3 by assuming

a "polycrystalline" magnetostriction value of λ = -14 ppm [78] and specific electrical resistivity $\rho = 1\times10^{-7}$ Ωm.

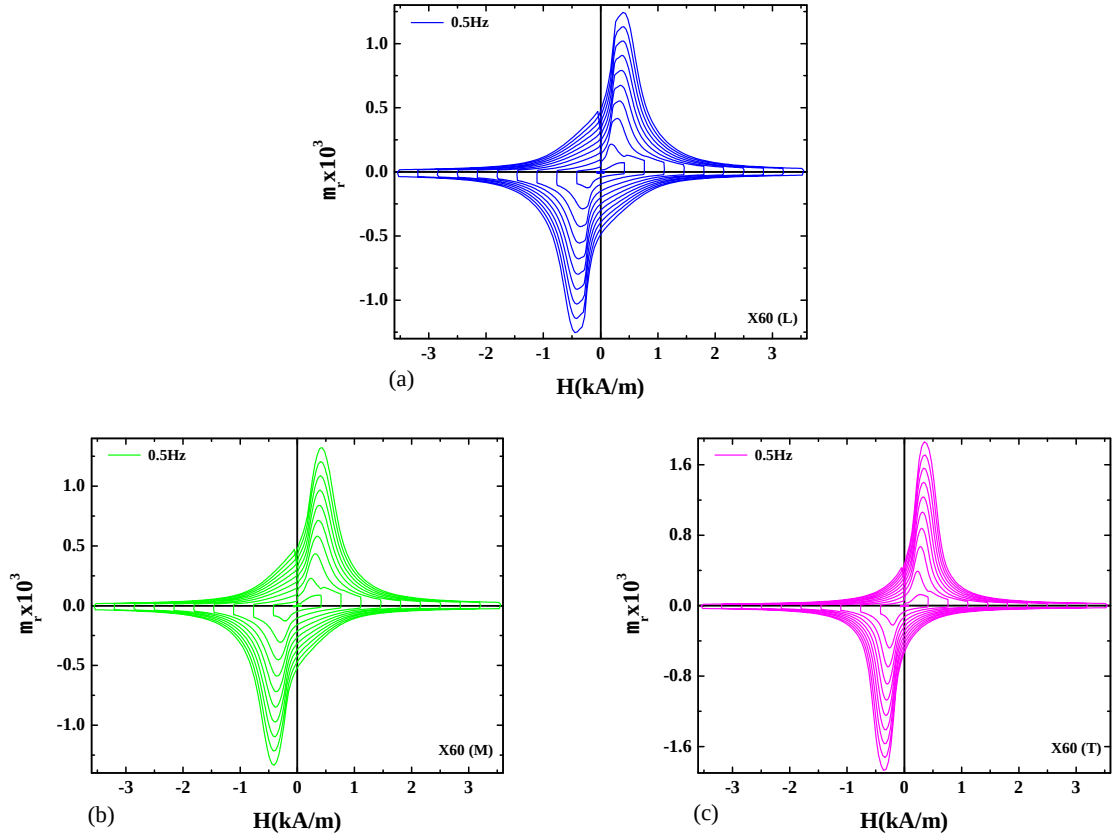

Figure 7.8: Relative permeability μ_r versus field *H(t)* for pipeline steel X60 (a) X60 (L), (b) X60 (M) and (c) X60 (T).

Sample	H_c(f=0Hz) *(A/m)*	H_c(f=50Hz) *(A/m)*	μ_{ri}	μ_{max} *dB/dt vs H(t)*	μ_{max} *dB/dH*	σ *(MPa)*	B_r/B_{max}
X52L	339	2464	123	1550 (389)	411 (359)	12.5	0.53
X52M	292	2326	104	1156 (422)	425 (200)	10.8	0.45
X52T	449	3685	57	862 (483)	353 (364)	17.4	0.43
X56L	246	1883	198	2230 (310)	875 (208)	9.0	0.51
X56M	303	1853	114	2087 (357)	657 (383)	11.0	0.51
X56T	308	1990	51	2120 (376)	921 (430)	11.3	0.59
X60L	322	1962	128	1245 (797)	354 (430)	11.8	0.44
X60M	261	1947	134	1329 (421)	414 (488)	9.6	0.45
X60T	332	2046	117	1866 (356)	627 (325)	12.0	0.57

Table 7.3: Magnetic properties derived from hysteresis loops of samples X52, X56 and X60.

7.2.1 Analysis of the Frequency Dependence of Coercivity

The experimental data of the frequency dependence of the coercivity of steel pipeline X52, X56, and X60 samples were analyzed using the equations 3.16 and 3.17 described in chapter 3 section 3.2.2. The experimental data are shown by the solid curves with symbols, while the curves fitted using equations (3.16) and (3.17) are denoted by dash and solid curves respectively in Figure 7.9.

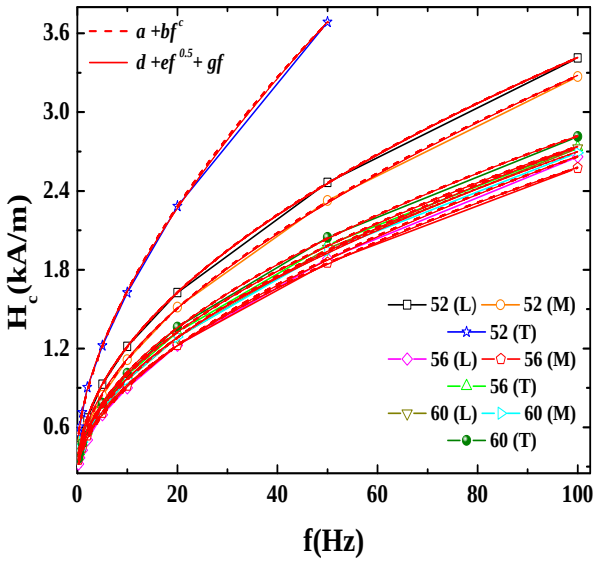

Figure 7.9: fit according to Eqs.3.16 and 3.17 on coercivity versus frequency of X52, X56, and X60 steel pipeline samples.

The values extracted from the curve fitting of the corresponding equations are given in Table 7.4. The value of power factor c from (3.16) is between 0.5 and 0.6 which agree well with the value described in formula described by A.Zhukov et al. [67]. From the value of parameter e, the relative permeability denoted as μ_r(e) was calculated by using relations (3.20) given in Table 7.4. The values of maximum relative permeability obtained by using fitting parameters are in acceptable range.

Sample	a	Δa	b	Δb	c	Δc
X52L	263	4.5	287	3.0	0.52	0.002
X52M	294	11	226	7.0	0.56	0.006
X52T	426	16	295	11	0.60	0.009
X56L	239	4.0	183	2.7	0.56	0.003
X56M	264	4.0	186	2.9	0.55	0.003
X56T	267	5.6	217	4.0	0.53	0.004
X60L	296	8.6	184	6.0	0.56	0.006
X60T	303	9.0	185	6.5	0.56	0.007
X60M	245	6.6	233	4.8	0.52	0.004

Table 7.4: Fit parameters according to Eq. (3.16) for X52, X56, and X60 pipeline steel samples.Whereas, Δa, Δb and Δc describe error to a, b and c.

Sample	d	Δd	e	Δe	g	Δg	$\mu(e)$
X52L	247	4.9	302	2.9	1.5	0.30	3800
X52M	256	13.6	261	8.0	4.2	0.80	3796
X52T	359	15	351	11	1.7	1.50	2910
X56L	210	6.0	210	3.7	3.5	0.35	3489
X56M	241	6.3	208	3.7	2.6	0.36	2256
X56T	251	6.3	233	3.7	1.6	0.35	2740
X60L	264	11.5	212	6.7	3.5	0.65	1941
X60M	274	11.6	211	6.8	3.1	0.70	3159
X60T	230	6.4	247	3.7	1.2	0.40	1934

Table 7.5: Fit parameters according to Eq. (3.17) for X52, X56, and X60 pipeline steel samples. Whereas, Δd, Δe and Δg describe error to d, e and g.

Eddy current model for $\mu_r = k/[Hc(f)]^n$:

Eddy current model Eq. (3.15) was applied on the frequency dependence of coercivity. In this model it is assumed that the permeability is reciprocal proportional to the some power of the coercivity i.e. $\mu_r = \mathrm{k}/[\mathrm{Hc(f)}]^n$. The model fits very precisely to the experimental data as shown in Figure 7.10. The value of the fitting parameter n is close to 1. From the relation $\mu_r = k/[Hc(f)]^n$ the maximum relative permeability is calculated at $f = 0$. The fitting parameters by model and calculated value of relative permeability are given in Table 7.6. The maximum relative values calculated through the model and from the frequency dependent data analysis (Table 7.5) are in good agreement. However the relative permeability values calculated from both methods are bit higher than the experimentally determined values given in Table 7.3.

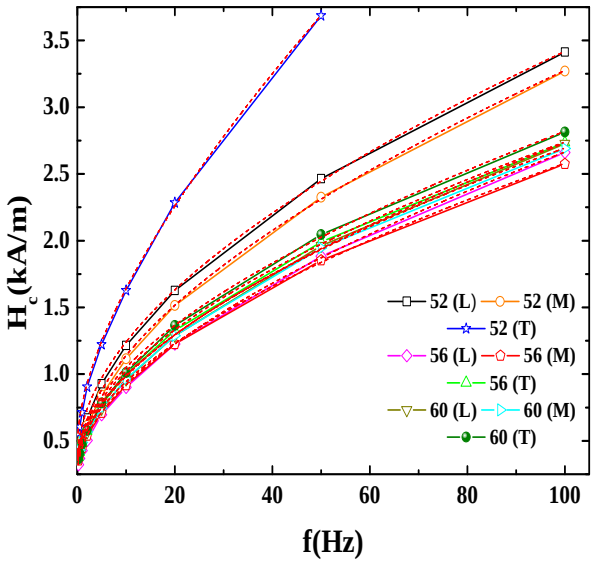

Figure 7.10: Fitting according to Eq. (3.15) on experimental data of coercivity versus frequency of X52, X56, and X60 pipeline steel.

Sample	$R(m)$	$a{=}H_c(f{=}0Hz)$	n	Δn	k	Δk	μ_r(f=0)
X52L	0.0023	339	1.13	0.025	2599646	530672	3595
X52T	0.0023	292	1.1	0.02	1953428	313814	3792
X52M	0.0023	449	0.80	0.02	277498	53398	2228
X56L	0.0023	246	1.06	0.016	1136144	148830	3319
X56T	0.0023	303	1.0	0.03	694647	150922	1931
X56M	0.0023	308	1.12	0.03	1649654	349935	2692
X60L	0.0023	322	1.0	0.03	626180	161679	1944
X60T	0.0023	261	1.17	0.02	2590830	371999	3854
X60M	0.0023	332	1.1	0.03	1165603	336351	2206

Table 7.6: Fit parameters according to model (3.15) for X52, X56, and X60 pipeline steel samples. Δn and Δk describe error to n and k.

7.2.2 Analysis of the Frequency Dependence of Losses

The total losses for pipeline steel samples X52(L), X56(L) and X60(L) were calculated by integrating the area of the frequency dependence of hysteresis loops. The total losses W_{tot} divides into static hysteresis loss W_h, classical eddy current loss W_{cl}, and excess loss W_{ex}.

$$W_{tot} = W_h + W_{cla} + W_{exc} \tag{7.2}$$

The losses were analyzed by fitting the BH (J/m^3) versus f curve with a second order

polynomial (7.3). The fitting results are shown in Figure 7.11

$$W(f) = W_h + B_1.\sqrt{f} + B_2.f \tag{7.3}$$

Where W_h represents the frequency independent hysteresis losses, B_1 and B_2 are fitting parameters which describe the anomalous and normal eddy current losses. A is the cross-sectional area of the sample, B_{max} gives the maximum induction of the material and ρ is the specific electrical resistivity; a describes a constant which is determined by the shape of the driving field.

According to formula (5.9) the parameter B_1 indicates the *normal* eddy current losses, which can be described by Bertotti [23] Eq. 7.4

$$W_{exc} = CB_{max}^{1.5}\sqrt{f} = 8\sqrt{\frac{GAV_o}{\rho}}B_{max}^{1.5}\sqrt{f}. \tag{7.4}$$

G is a geometry parasmeter which is about 0.2. V_0 forms a characteristic field responsible for the anomalous eddy currents. The estimated values of V_0 are given in Table 7.7 are more or less as expected for soft magnetic materials, which means $V_0 < H_c$.

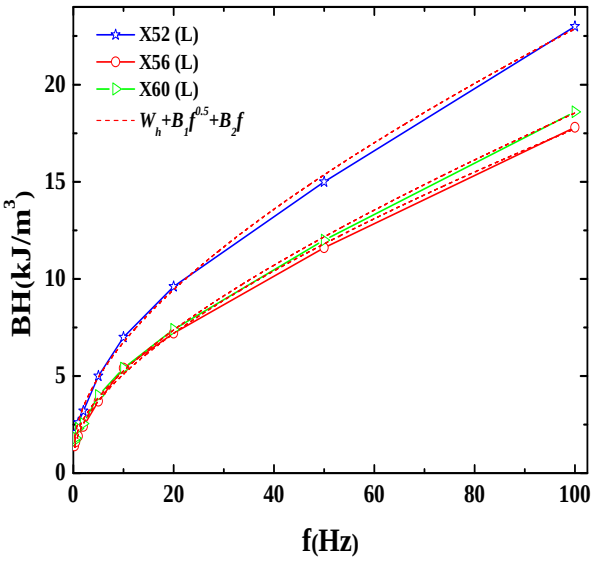

Figure 7.11: Total losses per cycle with frequency of X52 (L), X56 (L), and X60 (L). The dotted indicates the fitting result.

Sample	$W_h(f=0Hz)$	ΔW_h	B_1	ΔB_1	B_2	ΔB_2	V_o
X52L	958	163	1660	95	53	9	190
X56L	691	72	1251	72	45	7	108
X60L	967	75	1141	44	62	4.3	90

Table 7.7: Fit parameters according to Eq. (6.3) on frequency of dependence total losses for X52, X56, and X60 pipeline steel. ΔW_h, ΔB_1 and ΔB_2 describe error to W_h, e and g.

7.3 Conclusions

Hysteresis properties of pipeline steel X52, X56, and X60 were measured on window frame shaped samples parallel, perpendicular and at angle of 45°to the pipe axis. The shape of hysteresis loops of X52 and X60 illustrate the longitudinal texture while nearly no texture was observed in X56 sample. The squareness ratio (B_r/B_s) fall between 0.45 and 0.60 which is well below the theoretical value of 0.75 for a cubic isotropic material, showing also the presence of a texture. These results are in agreement with the results as observed in the microstructures of corresponding samples. Frequency dependence of the coercivitiy show no remarkable difference along three directions of corresponding samples except X52, which shows high frequency dependence along transverse direction. The coercivities of all samples were observed higher than pure Fe (un-deformed) due to residual stress effects. The relative permeability obtained by eddy current model were in agreement with experimental value.

Chapter 8

Magnetization and Microstructural Investigation of Resin coated Fe-Powder

Soft magnetic composites (SMC) are ferromagnetic (pure Fe, Co, Ni or their alloys) powder and some resin (plastic) bonded filler. These composite materials have generally isotropic magnetic properties, high electrical resistivity which leads to a significant reduction in eddy current losses in alternating current applications [102].

In this chapter resin coated compact Fe-powder samples containing different Fe contents were magnetically examined. Saturation magnetization, at room temperature was measured by Pulse field magnetometer (PFM) (Hirst). The geometry used for all samples was 20 mm x 15 mm x 4 mm. The frequency dependence of hysteresis were carried out on ring shaped samples by hysteresigraph in frequency range from 0.25 Hz to 100 Hz. This has the advantage that the sample geometry-dependent demagnetizing field become zero (closed ring). Additionally, microstructure and the powder morphology were examined by scanning electron microscopy to see the particle size and distribution in the matrix. Magnetic properties of composite materials are affected by powder particle size and shape [103]. Usually coarse particles are preferable for low frequency applications where high permeability is required while for high frequency applications fine particle compos-

ites are preferred to avoid eddy current losses. Spherical or granular shape particles with low open porosity are suitable since insulation of iron particles can be achieved with a minimum amount of dielectric.

8.1 Microstructure of Resin coated Fe-Powder

The microstructure was investigated using standard optical microscopy. Figure 8.1(a, b, and c) shows the typical microstructures of three samples S_3 S_8 and S_9 as an example. From the microstructure it can be observed that iron powder (white part) coated with resin is not uniformly distributed in the resin matrix. The particles are irregular in shape and have very high open porosity. The iron powder is composed of approximately 73 wt% of the coarse particles.

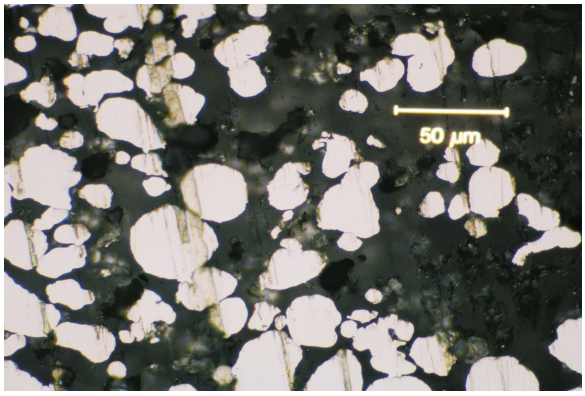

(a)

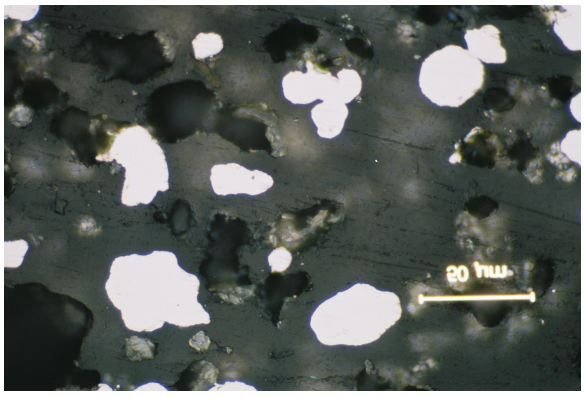

(b)

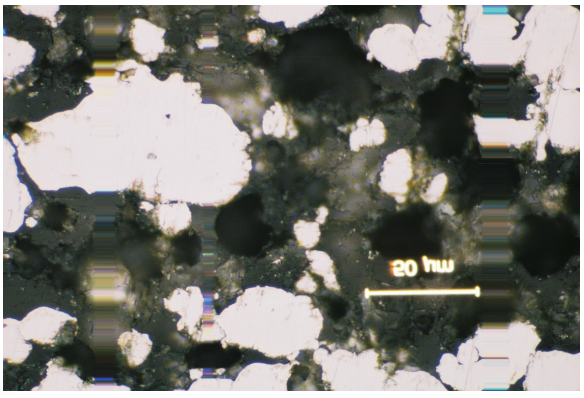

(c)

Figure 8.1: Microstructure of resin coated Fe-Powder samples (a) S_3, (b) S_8 and (c) S_9.

8.2 Magnetization Measurements of Resin coated Fe-Powder

Figure 8.2 shows the M(H) loops of all samples in a pulsed magnetometer measured up to 4 T (40 kOe) at room temperature. The magnetic field was applied along the direction of sample's thickness (4 mm). Magnetization for samples S_3, S_8 and S_9 were also measured by applying a field along the direction of long axis (20 mm) (Figure 8.3 shows the applied field direction) to see the demagnetizing effect. Saturation magnetization in all samples was found between 125 emu/g to 182 emu/g depending upon the amount of Fe contents in the given sample. The sample S_8 considered as reference and its data according to ISO standard is given in Table 8.1. The given value of Fe-contents (Table 8.1) of reference sample S_8 according to ISO standard is about 75 % .

The percentage of iron contents in the measured samples were estimated by comparing the saturation magnetization of these samples with the saturation magnetization of pure iron which is about 215 emu/g using following formula:

%age of resin contents = (215-saturation magnetization of sample)× 100/215

%age of iron contents = 100- %age of resin contents.

The estimated percentage of Fe contents in S_8 is about 72 % which is 3 % less than given by ISO standard 8.1. The percentage of iron Fe contents in all samples is given in Table 8.2.

Demagnetization effect can be seen in Figure 8.2 while applying the field along the direction of long axis (20 mm) of samples S_3, S_8 and S_9. Demagnetizing field can be calculated as:

$$H_{int} = H_{ext} + H_d \tag{8.1}$$

Where H_{int}, H_{ext} and H_d are internal, external and demagnetizing field. Demagnetizing field is given as H_d = -N.M(H), where M(H) is magnetization and N is a demagnetizing factor (dimensionless) depending on shape of the sample geometry .

In the case of amorphous compounds such as Fe powder in a resin (plastic) matrix, the demagnetizing factor is determined by the geometric shape of the sample plus demagnetizing factor which is determined by an average shape of the powder particles. Since the geometry used for all samples was approximately the same, the inclination of M(H) loops in Figure 8.4 indicates a different demagnetizing effect due to different geometry of the Fe-powder particles in plastic (resin) matrix.

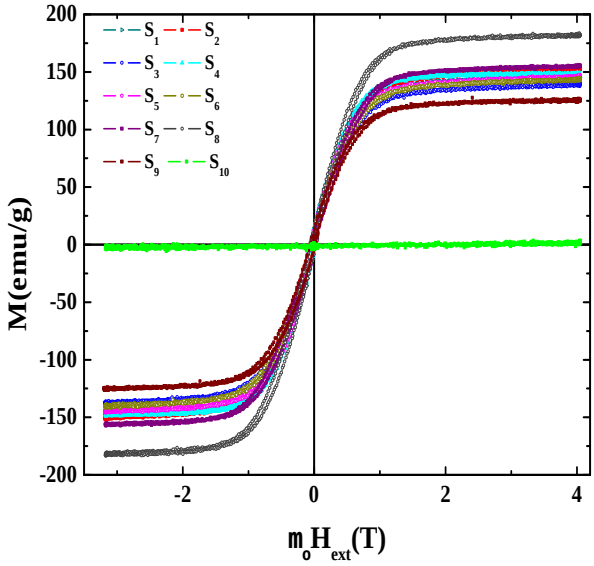

Figure 8.2: Magnetization M(H) loops of resin coated Fe-Powder.

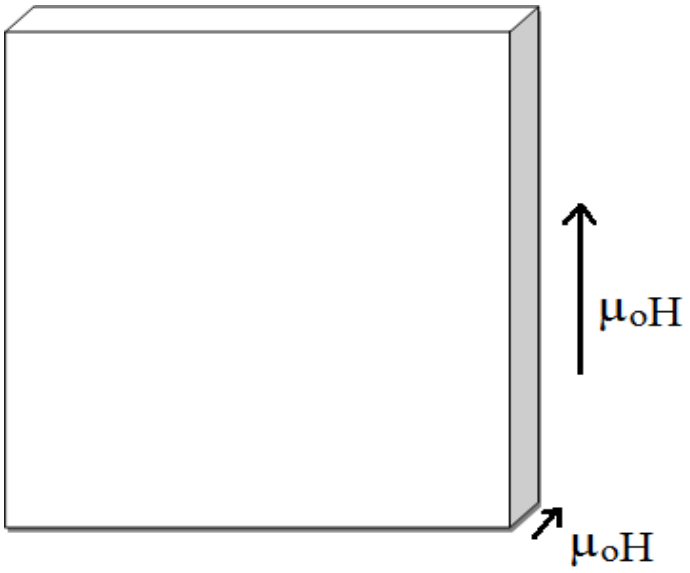

Figure 8.3: Schematic diagram for resin coated Fe-Powder sample to show applied field directions.

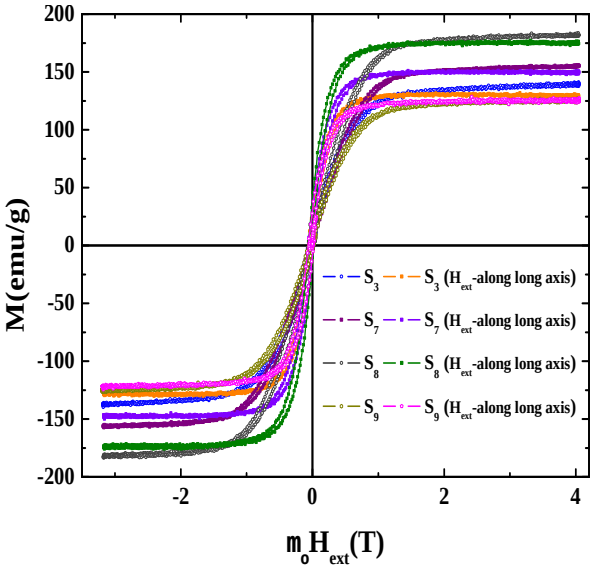

Figure 8.4: Magnetization loops of resin coated Fe-Powder to see demagnetizing effect.

Main Features	Test standard	unit	Minimum value
Tensile strength at 23^{o}C 150^{o}C	ISO 178	Mpa	$\geq$150$\geq$120
Density	ISO 1183	g/cm3	3.5$\pm$0.2
Modulus of elasticity at 23^{o}C&150^{o}C	ISO 178	Gpa	About 14.5& 11.5
Iron content	–	%	About 75
Glass content	–	%	About 7
Resin content	–	%	About 18
Temperature index	IEC 216	^{o}C	About 155
Volume resistivity	IEC 167	Ohm cm	$\geq 1\times10^6$

Table 8.1: Data according to ISO standard for Sample S_8.

Sample	$M_s(emu/g)$	$M_s(T)$	$H_c(A/m)$	*% Glass+resin*	*% Fe-Contents*
S_1	146	1.44	3.2×10^4	32	68
S_2	151	1.50	3.5×10^4	30	70
S_3	138	1.36	3.5×10^4	35.8	64.2
S_4	148	1.46	3.2×10^4	31	69
S_5	144	1.42	3.2×10^4	33	67
S_6	142	1.40	3.2×10^4	34	66
S_7	155	1.53	3.0×10^4	29	72
S_8	182	1.80	3.0×10^4	15	85
S_9	126	1.25	3.0×10^4	41.4	58.6

Table 8.2: Saturation magnetization and % of Fe-contents resin coated Fe-powder.

8.3 Hysteresis Measurements of Resin coated Fe-Powder

The dimensions and parameters for the measurements of hysteresis loops on ring shaped samples are given in Table 8.3. Figures 8.5 and 8.6 present the frequency dependence of hysteresis loops of all samples measured at room temperature from 0.5 Hz to 100 Hz. The maximum average field was ∼23 kA/m. The hysteresis loops of all samples look very similar in the applied field and nearly frequency independent up to 10 Hz (see inset). The excessively low value of induction B is a consequence of (*i*) low applied field to magnetically saturate the material and (*ii*) non magnetic plastic particles present in the material, which do not contribute in magnetization. The shape of the hysteresis loops (inclination to the right) seems to be a consequence of the fact that the individual grains have a strong demagnetizing fields and the applied field (23 kA/m) was not enough to overcome the demagnetizing effect. The increase of polarization (J) with increasing Fe-contents can be seen in Figure 8.7 plotting hysteresis loop at 0.5 Hz of all samples in one graph.

Sample	$A(m^2)$	$l_{eff}(m)$	N_1	N_2
S_1	$3.56*10^{-5}$	0.0685	396	72
S_2	$2.92*10^{-5}$	0.0688	396	72
S_3	$3.46*10^{-5}$	0.0689	396	74
S_4	$3.36*10^{-5}$	0.0683	392	78
S_5	$3.49*10^{-5}$	0.0688	400	76
S_6	$2.75*10^{-5}$	0.0687	400	76
S_7	$1.05*10^{-5}$	0.0314	350	64
S_8	$1.43*10^{-5}$	0.0398	212	60
S_9	$2.87*10^{-5}$	0.0702	390	80
S_{10}	$2.70*10^{-5}$	0.0628	400	95

Table 8.3: Dimensions and parameters used for the hysteresis measurements of Fe-Powder. N_1-Primary Windings, N_2-Secondary Windings, $l_{eff}(m)$-Magnetic Path length, $A(m^2)$-Cross-sectional Area.

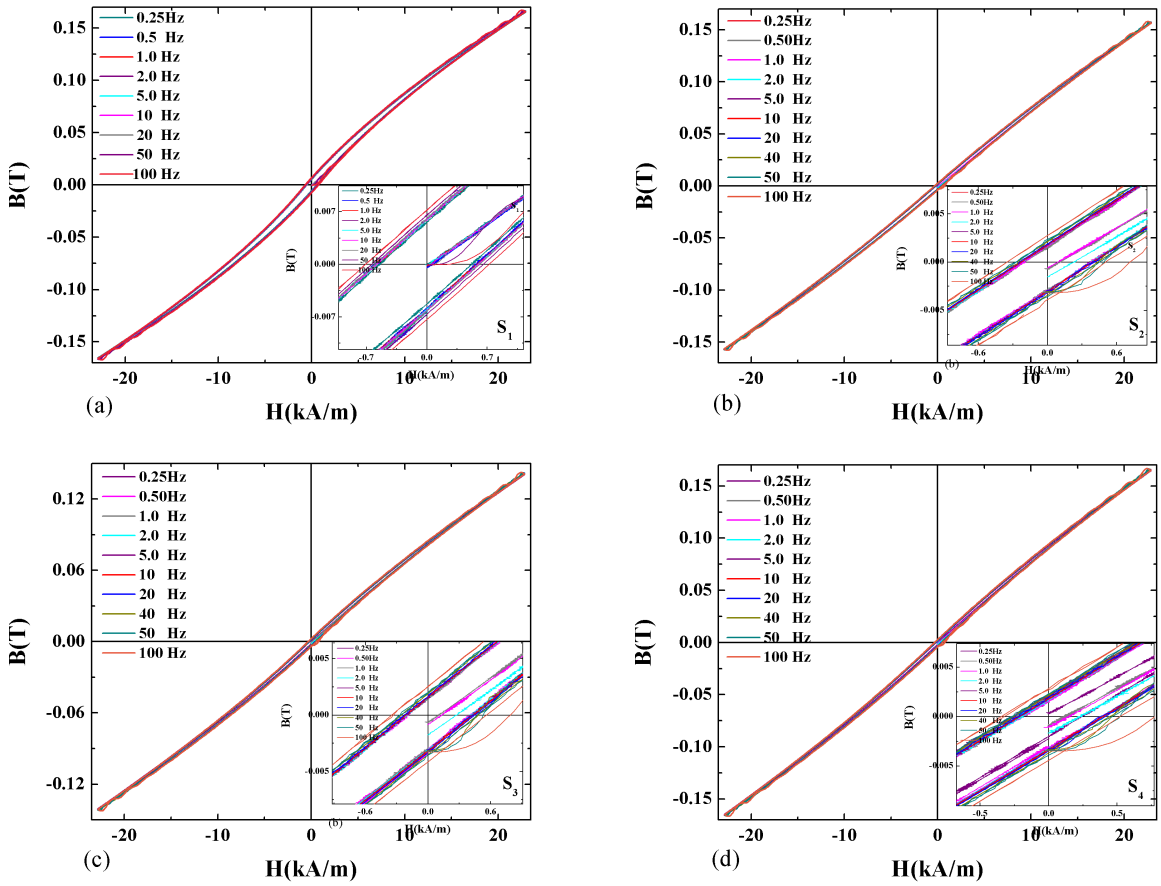

Figure 8.5: Frequency dependent hysteresis loops of resin coated Fe-Powder samples (a) S_1, (b) S_2, (c) S_3 and (d) S_4.

Figure 8.8 shows the frequency dependence of the coercive field. The frequency dependence is much lower than pure (bulk) iron (described in chapter 4) that is due to isolated Fe particles in resin matrix which reduces the eddy currents. The sample S_1 has significantly higher coercive field than other samples, the reason could be an impurity in the Fe in this sample.

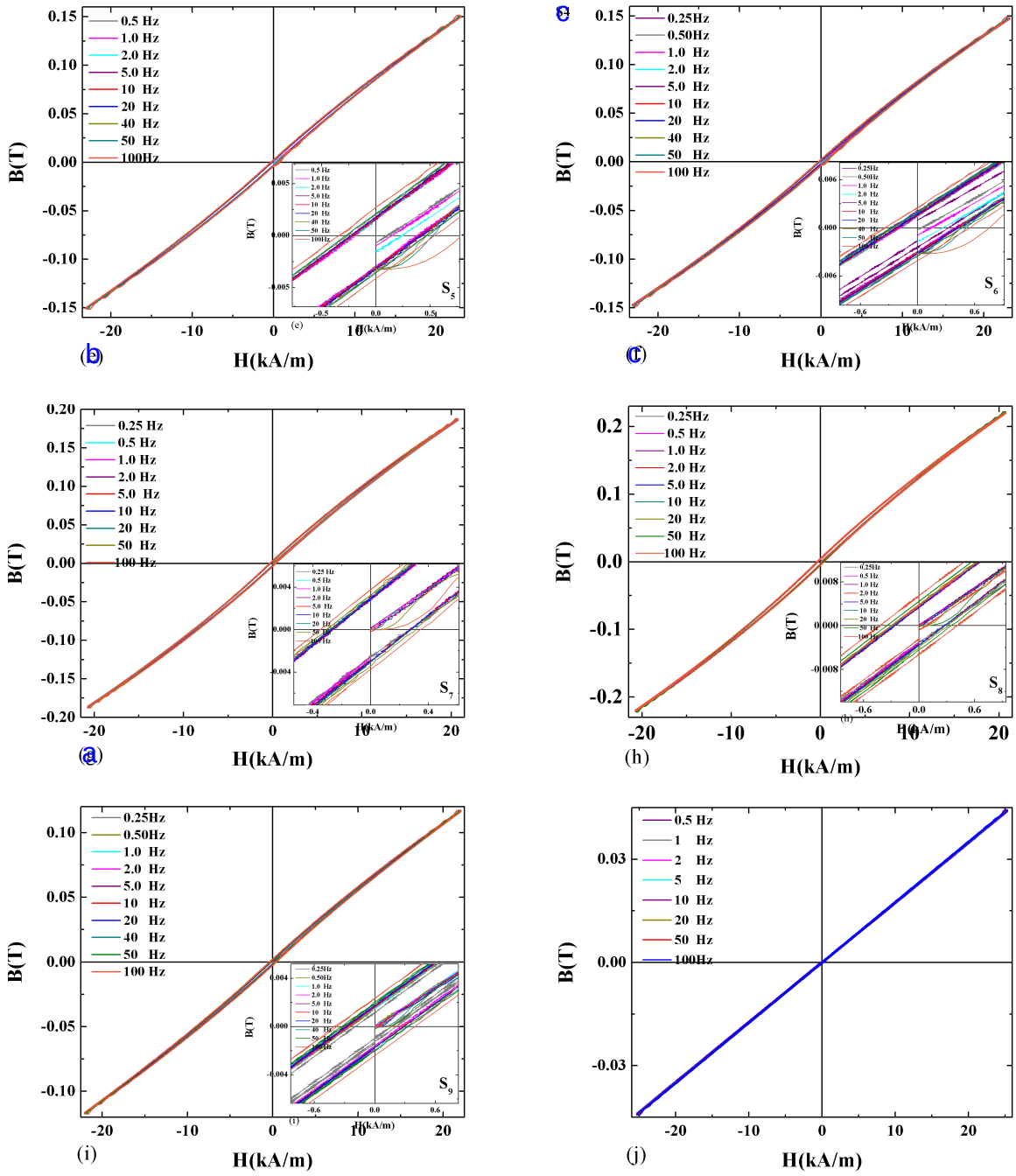

Figure 8.6: Frequency dependent hysteresis loops of resin coated Fe-Powder (e) S_5, (f) S_6, (g) S_7, (h) S_8, (i) S_9 and (j) S_{10}.

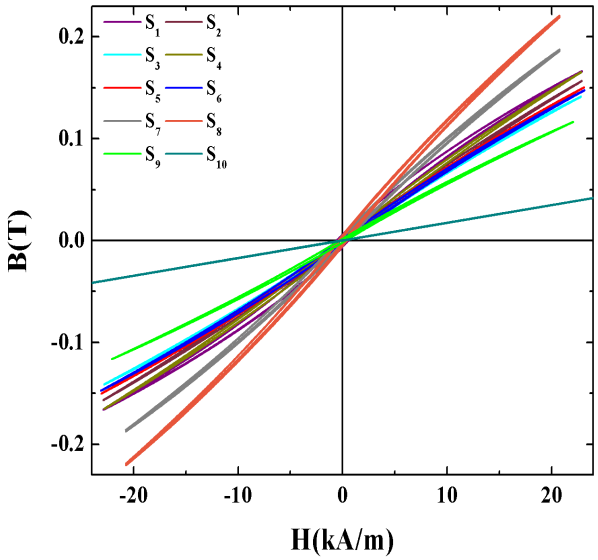

Figure 8.7: Hysteresis loops at 0.5 Hz of all resin coated Fe-Powder samples.

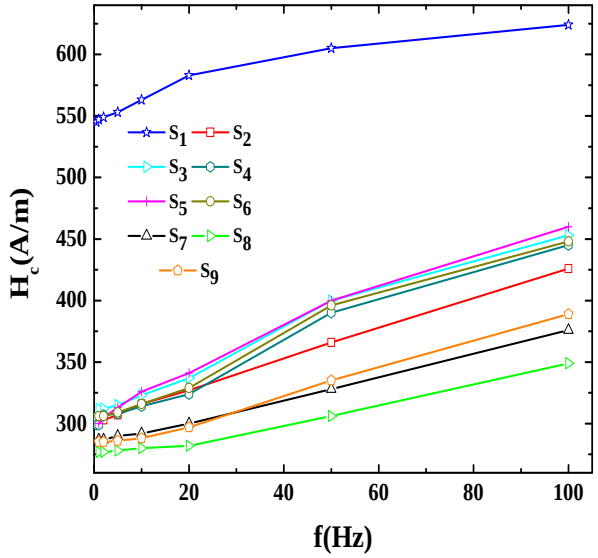

Figure 8.8: Coercivity versus frequency of resin coated Fe-Powder.

The magnetic properties of samples derived from the hysteresis loops at 0.5 Hz are given in Table 8.4. The coercivity (H_c) at zero frequency (0 Hz) was obtained by extrapolating the almost frequency independent coercivities to 0 Hz (H_c at low frequencies). The initial relative permeability (μ_{ri}) was determined by the slope of initial BH-curive. The maximum relative permeability was determined from dB/dt versus field H (A/m) data by using the relation $(\mu_o)^{-1}(\Delta\ B/\Delta\ t)(\Delta\ t/\Delta\ H)$. $\Delta\ B/\Delta\ t$ was taken directly from the minor loop

measurement data i.e dB/dt and $\Delta\ H/\Delta\ t$ (slope) was derived from triangular field H (t) i.e $4H_{max}/T$. Figures 8.9 and 8.10 show the graphs of relative maximum permeability versus field. The maximum differential permeability was also determined by means of direct differentiation of the hysteresis loop. The number in small bracket (..) are the field values where μ_{max} was determined. The values of initial relative permeability obtained for all resin coated Fe-powder samples were significntly low reason, could be a stray field produced by individual isolated Fe particles in resin matrix and resin also contributed in reducing the permeability of the material. The shapes of the loops are different from the usual behaviour, which might be associated with the isolated Fe particles.

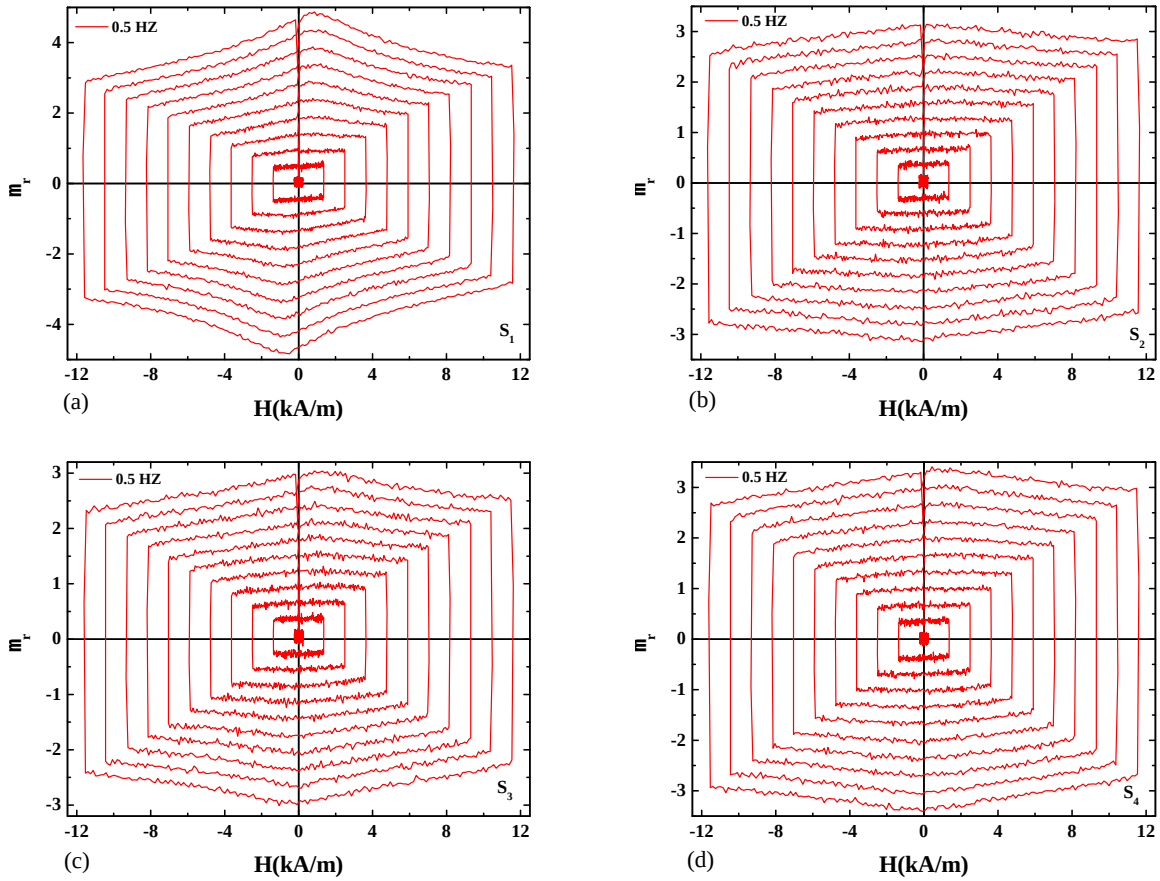

Figure 8.9: Relative permeability versus field of resin coated Fe-powder samples (a) S_1, (b) S_2, (c) S_3 and (d) S_4.

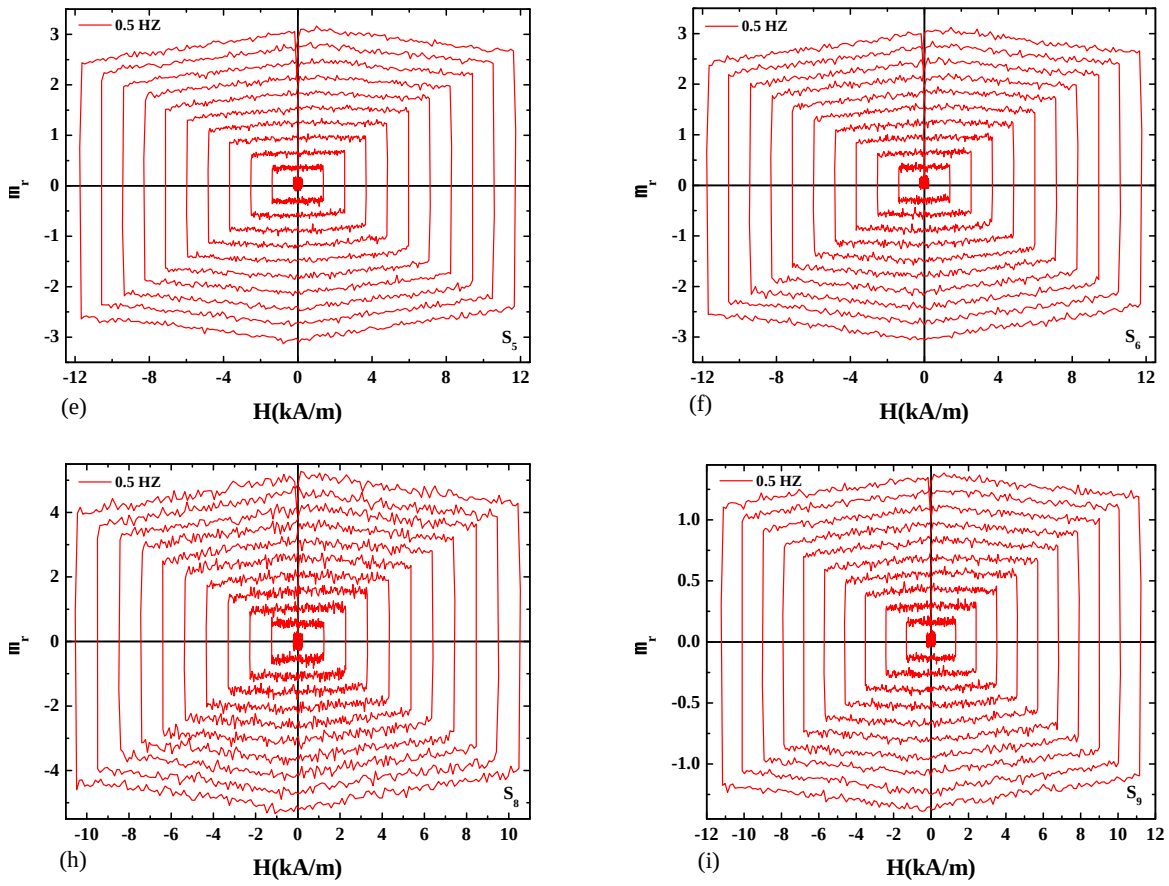

Figure 8.10: Relative permeability versus field of resin coated Fe-powder samples (e) S_5 (f), S_6, (g) S_8, and (h) S_9.

Sample	H_c(f=0Hz) (A/m)	H_c(f=100Hz) (A/m)	μ_{ri}	μ_{max} dB/dt *vs* $H(t)$	μ_{max} dB/dH
S_1	543	624	5.0	4.83 (616)	3.4 (876)
S_2	301	426	5.3	3.20 (218)	2.5 (577)
S_3	312	453	5.0	3.04 (483)	2.0 (473)
S_4	299	445	4.9	3.40 (310)	2.8 (564)
S_5	295	460	4.5	3.10 (357)	3.0 (447)
S_6	306	448	5.6	3.05 (376)	1.7 (668)
S_7	287	396	6.8	5.10 (396)	4.5 (373)
S_8	277	349	6.8	5.05 (421)	4.7 (515)
S_9	275	389	4.0	1.20 (356)	2.8 (396)

Table 8.4: Magnetic properties of risen coated Fe-powder, the number in (..) are the field values where μ_{max} was determined.

8.4 Conclusions

Resin coated Fe-powder containing different Fe contents were investigated with respect to microstructure, magnetization and frequency dependence of hysteresis. Microstructure show high porosity and irregular Fe particles. The saturation magnetization were found between 125 emu/gm to 182 emu/gm. %age of Fe contents were calculated from the saturation magnetization. Hysteresis loops of all samples show same behavior and are nearly frequency independent. Magnetic polarization increases with increasing Fe contents. The initial and maximum relative permeability values obtained were significantly low, which could be associated with stray field produced by isolated Fe particles in resin matrix.

Summary

Severe Plastic Deformation (SPD) is used to produce bulk highly deformed soft magnetic materials. This treatment can leads to recrystallisation of material after which a nanocrystalline state is achieved. This method was applied on a set of well known soft magnetic materials such as: pure Fe, Ni, Fe-3 wt%Si, Fe-6.5 wt%Si, Fe-17 wt%Co, different steels samples and high magnetostrictive $Fe_{100-x}Al_x$ (x = $15 \leq x \leq 25$) and $Fe_{81}Ga_{19}$ alloys. These materials were SPD-treated by high pressure torsion (HPT) technique at liquid nitrogen (N_2) temperature, room temperature (RT) and at 450°C. Frequency dependent hysteresis measurements were carried out on ring shaped samples by using a full automized hysteresigraph controlled by a Labview program. The hysteresis measurements were performed at room temperature and also at elevated temperatures(up to 200°C).
The magnetic properties such as coercivity, permeability, remanence, and also the shape of the hysteresis loop were greatly influenced by deformations in the materials. The coercivity (H_c) of a magnetic materials is strongly dependent on the grain size [52] and increases with decrease in grain size, reaching a maximum value at the single domain particle size, which is close to 100 nm and then decreases sharply when the grain size becomes smaller than 100 nm. At this stage exchange length becomes comparable to the grain size, which causes a reduction of the "effective" anisotropy and consequently of the coercivity as the coercivity roughly depends on the magnetocrystalline anisotropy constant.
In the present work the coercivity values obtained for all HPT treated samples were considerably high, which could be explained as due to dominant effect of internal stresses induced during deformation. However the dependence of coercivity on the HPT temperature was different for each material, depending on the microstructure (grain size) as well as the magnetostriction of the material. In the case of pure Fe, Fe-3 wt%Si, Fe-6.5 wt%Si, Fe-17 wt%Co alloys and pure Ni, the coercivity of the samples deformed at 450°C was significantly high as compared to samples deformed at liquid nitrogen temperature and room temperature. One of the possible reasons for this behavior could be the bigger grain size of samples deformed at 450°C as reported in literature [1]. According to these considerations the grain size increases with HPT processing temperature. The

frequency dependence of the coercivity was analyzed and explained by an eddy current based model originating from the Maxwell equation and material parameters such as electrical resistivity and magnetic permeability. An important parameter is the average maximum relative permeability, which was derived by using the model and compared with the experimental values determined from the measurement of *dB/dt* versus *H(t)* as well as from the direct differentiation of the Hysteresis loop B(H). Frequency dependent hysteresis measurements of high magnetostrictive system $Fe_{100-x}Al_x$ ($15 \leq x \leq 25$) shows that the coercivity increases while the saturation magnetization decreases with Al concentration. The coercivity of samples deformed at liquid N_2 temperature was also lower than the coercivity of samples deformed at room temperature. The maximum relative permeability derived from the eddy current based model was well comparable with the experimental values obtained from *dB/dt* versus *H(t)* measurement as well as from the direct differentiation of the hysteresis loop.

High magnetostrictive $Fe_{81}Ga_{19}$ samples, one quenched in cold water and other annealed (slowly cooled in oven) exhibited an unexpected strong frequency dependent coercivity. The maximum relative permeability derived from the eddy current model as well as from the frequency dependent analysis using a general equation for calculating the permeability delivers unreasonably high values. The maximum permeability as determined directly from a *dB/dt* versus *H* plot as well as from a direct differentiating method delivers values (between 150 and 450) which are reasonable from a magnetic understanding of a high magnetostrictive system.

Microstructure and magnetic hysteresis studies were made on pearlitic rail steel (R260) samples which were plastically deformed with shear rates (ϵ = 1, 2, 4, 8, 16). Microstructure shows that the distance between lamellas decreases with increasing shear strain while the vicker hardness increases from 240 HV to 800 HV at a shear rate $\epsilon = 16$. SPD deformation results in extensive increase in coercivity and hence hysteresis losses.

Hysteresis properties of sample of API 5L grade X52, X56, and X60 pipeline steel were measured along, perpendicular and at angle 45°to the pipe axis, on window frame shaped samples. Hysteresis loops of X52 and X60 illustrate the effect of texture induced

anisotropy. The squareness ratio (B_r/B_s) was observed well below the theoretical value for a cubic isotropic material, representing also the presence of a texture. These results are in agreement with the texture as observed in the microstructures.

Bibliography

[1] A. Vorhauer, K. Rumpf, P. Granitzer, S. Kleber, H. Krenn, and R. Pippan. Magnetic properties and microstructure of a FeCo ferritic steel after severe plastic deformation. *Materials Science Forum*, 503 - 504:299–304, 2006.

[2] M. Faleschini. *Severe plastic Deformation of Tungsten Alloy and its influence on fracture behaviour*. PhD thesis, Enrich Schmid Institute of Material Science, Austerian Academy of Sciences Department of Materials Physics, 2006.

[3] S. Scheriau and R. Pippan. Severe plastic deformation of steels. *BHM Berg- und Httenmnnische Monatshefte*, 153:242–246, 2008.

[4] N. Mehmood. *Investigation of New High Magnetostrictive materials*. PhD thesis, Technische Universitt Wien Fakultt fr Physik, 2009.

[5] S. Scheriau, M. Kriegisch, S. Kleber, N. Mehboob, R. Grssinger, and R. Pippan. Magnetic characteristics of hpt deformed soft-magnetic materials. *Journal of Magnetism and Magnetic Materials*, 322(20):2984 – 2988, 2010.

[6] G. Herzer. *Handbook of Magnetic Materials*. Elsevier, Science B.V., 1997.

[7] D. Jiles. *Introduction to Magnism and Magnetic materials*. Chapman and Hall, 1991.

[8] M. E. McHenry and D. E. Laughlin. Nano-scale materials development for future magnetic applications. *Acta Materialia*, 48(1):223 – 238, 2000.

[9] W. Roderwald H. Warlimont E. Adler, G. W. Reppel. Matching P/M and the physics of magnetic materials. *International Journal of Powder Metallurgy*, 25(4):319, 1989.

[10] N. M. Talijan. Magnetic properties of sintered high energy Sm-Co and Nd-Fe-B magnets. *Science of Sintering*, 38:73–82, 2006.

[11] V. Jancarik, A. Gruskova, J. Slama, and R. Dosoudil. Study of Sr and Ba hexa-ferrite prepared by low temperature auto-combustion method. *Journal of electrical engineering*, 57(8/S):163–166, 2006.

[12] O. S. Rodriguez-Fernández L. García-Cerda and P. J. Reséndiz-Hernández. Study of $SrFe_{12}O_{19}$ synthesized by the sol-gel method. *Journal of Alloys and Compounds*, 369(1-2):182–184, 2004.

[13] A. Jafari-H. Sheikh E. Paimozd, A .Ghasemi. Influence of acid catalysts on the structural and magnetic properties of nanocrystalline barium ferrite prepared by sol-gel method. *Journal of Magnetism and Magnetic Materials*, 320(23):L137 – L140, 2008.

[14] H. Gavrila V. Ionita. Crystalline and amorphous soft magnetic materials and their applications status of art and challenges. *Journal of Optoelectronics and Advanced Materials*, 4(2):173 – 192, 2002.

[15] C. Beatrice and F. Fiorillo. Measurement and prediction of magnetic losses in Mn-Zn ferrites from dc to the megahertz range. *IEEE Transactions on Magnetics*, 42(10):2867 –2869, 2006.

[16] W. J. Carr and R. Smoluchowski. The magnetostriction of single crystals of iron-silicon alloys. *Phys. Rev.*, 83:1236–1243, 1951.

[17] E. Tatsumoto and T. Okamoto. Temperature dependence of the magnetostriction constants in iron and silicon iron. *Journal of the Physical Society of Japan*, 14(11):1588–1594, 1959.

[18] R. C. Hall. Single crystal anisotropy and magnetostriction constants of several ferromagnetic materials including alloys of NiFe, SiFe, AlFe, CoNi, and CoFe. *Journal of Applied Physics*, 30(6):816–819, 1959.

[19] T. Sourmail. Evolution of strength and coercivity during annealing of feco based alloys. *Scripta Materialia*, 51(6):589 – 591, 2004.

[20] Y. T. Zhu, T. C. Lowe, and T. G. Langdon. Performance and applications of nanostructured materials produced by severe plastic deformation. *Scripta Materialia*, 51(8):825 – 830, 2004.

[21] V. Varyukhin, B. Efros, V. Ivchenko, N. Efros, and E. Popova. Effect of severe platic deformation an atomic structure of metals at study of field ion microscopy method. *Rev. Adv. Mater. Sci.*, 10:422–426, 2005.

[22] G. Herzer. Soft magnetic nanocrystalline materials. *Scripta Metallurgica et Materialia*, 33(1011):1741 – 1756, 1995.

[23] G. Bertotti. *Hysteresis in Magnetism.* Academic Press, 1998.

[24] J. B. Goodenough. Summary of losses in magnetic materials. *IEEE Transactions on Magnetics*, 38(5):3398 – 3408, 2002.

[25] J. E. Brittain. A steinmetz contribution to the ac power revolution. *Proceedings of the IEEE*, 72(2):196 – 197, 1984.

[26] R.M Bozorth. *Ferromagnetism.* Toronto: D. Van Nostrand Co, 1951.

[27] A. Boglietti, A. Cavagnino, M. Lazzari, and M. Pastorelli. Predicting iron losses in soft magnetic materials with arbitrary voltage supply: an engineering approach. *IEEE Transactions on Magnetics*, 39(2):981 – 989, 2003.

[28] A. Goldman. *Modern Ferrite Technology.* Springer, 2006.

[29] F. Fiorillo. *Measurement and Characterization of Magnetic Materials.* Elsevier, Academic Press, 2004.

[30] Y. Chen and P. Pillay. An improved formula for lamination core loss calculations in machines operating with high frequency and high flux density excitation. 2002.

[31] G. Bertotti. General properties of power losses in soft ferromagnetic materials. *IEEE Transactions on Magnetics*, 24(1):621 –630, 1988.

[32] G. Bertotti. Physical interpretation of eddy current losses in ferromagnetic materials. i. theoretical considerations. *Journal of Applied Physics*, 57(6):2110 –2117, 1985.

[33] G. Bertotti. Physical interpretation of eddy current losses in ferromagnetic materials. ii. analysis of experimental results. *Journal of Applied Physics*, 57(6):2118 –2126, 1985.

[34] G. Bertotti, G. D. Schino, A. F. Milone, and F. Fiorillo. On the effect of grain size on magnetic losses of 3% non-oriented SiFe. *Le Journal de Physique Colloques*, 46(6):385, 1985.

[35] F. Fiorillo and A. Novikov. An improved approach to power losses in magnetic laminations under nonsinusoidal induction waveform. *IEEE Transactions on Magnetics*, 26(5):2904 –2910, 1990.

[36] H. Gleiter. Nanocrystalline materials. *Progress in Materials Science*, 33(4):223 – 315, 1989.

[37] R. Z. Valiev, I. V. Alexandrov, N. A. Enikeev, M. Y. Murashkin, and I.P. Semenova. Towards enhancement of properties of UFG metals and alloys by grain boundary engineering using spd processing. *Rev. adv. Mater. Sci.*, 25:1–10, 2010.

[38] A. Vorhauer. *On the influence of temperature during severe plastic deformation and subsequent annealing*. PhD thesis, University of Leoben, 2005.

[39] R. Z Valiev, R. K Islamgaliev, and I. V Alexandrov. Bulk nanostructured materials from severe plastic deformation. *Progress in Materials Science*, 45(2):103 – 189, 2000.

[40] R. Z. Valiev and I. V. Alexandrov. Development of severe plastic deformation techniques for the fabrication of bulk nanostructured materials. *Annales de Chimie Science des Matriaux*, 27(3):3 – 14, 2002.

[41] R. Z. Valiev, Y. V. Ivanisenko, E. F. Rauch, and B. Baudelet. Structure and deformaton behaviour of armco iron subjected to severe plastic deformation. *Acta Materialia*, 44(12):4705 – 4712, 1996.

[42] S. Bayramoglu, C. Hakan Gür, Igor V. Alexandrov, and M. M. Abramova. Characterization of ultra-fine grained steel samples produced by high pressure torsion via magnetic barkhausen noise analysis. *Materials Science and Engineering: A*, 527(45):927 – 933, 2010.

[43] R. Z. Valiev and T. G. Langdon. Principles of equal-channel angular pressing as a processing tool for grain refinement. *Progress in Materials Science*, 51(7):881 – 981, 2006.

[44] R. Grössinger, R. Sato, D. Holzer, and M. Dahlgren. Properties, benefits, and application of nanocrystalline structures in magnetic materials. *Advanced Engineering Materials*, 5(5):285–290, 2003.

[45] A. Vorhauer and R. Pippan. On the homogeneity of deformation by high pressure torsion. *Scripta Materialia*, 51(9):921 – 925, 2004.

[46] A. Vorhauer, T. Hebesberger, and R. Pippan. Disorientations as a function of distance: a new procedure to analyze local orientation data. *Acta Materialia*, 51(3):677 – 686, 2003.

[47] T. Hebesberger, H.P. Stwe, A. Vorhauer, F. Wetscher, and R. Pippan. Structure of Cu deformed by high pressure torsion. *Acta Materialia*, 53(2):393 – 402, 2005.

[48] O. Crisan, M. Angelakeris, K. Simeonidis, Th. Kehagias, Ph. Komninou, M. Giersig, and N.K. Flevaris. Structure effects on the magnetism of agco nanoparticles. *Acta Materialia*, 54(19):5251 – 5260, 2006.

[49] G. Herzer. Grain size dependence of coercivity and permeability in nanocrystalline ferromagnets. *IEEE Transactions on Magnetics*, 26(5):1397 –1402, 1990.

[50] G. Herzer. Nanocrystalline soft magnetic materials. *Physica Scripta*, T49:307–314, 1993.

[51] P. Marín, M. Vázquez, and A. Hernando. Magnetic hardening during the amorphous to nanocrystalline transformation in fesibcunb alloys: theoretical considerations. *Journal of Magnetism and Magnetic Materials*, 196-197:221–223, 1999.

[52] G. Herzer. Grain structure and magnetism of nanocrystalline ferromagnets. *IEEE Transactions on Magnetics*, 25(5):3327 –3329, 1989.

[53] Y.Y. Wang, P.L. Sun, P.W. Kao, and C.P. Chang. Effect of deformation temperature on the microstructure developed in commercial purity aluminum processed by equal channel angular extrusion. *Scripta Materialia*, 50(5):613 – 617, 2004.

[54] Y.C. Chen, Y.Y. Huang, C.P. Chang, and P.W. Kao. The effect of extrusion temperature on the development of deformation microstructures in 5052 aluminium alloy processed by equal channel angular extrusion. *Acta Materialia*, 51(7):2005 – 2015, 2003.

[55] A. Yamashita, D. Yamaguchi, Z. Horita, and TG. Langdon. Influence of pressing temperature on microstructural development in equalchannel angular pressing. *Mater Sci Eng*, A287:100, 2000.

[56] J.A. Ewing. *Magnetic induction in iron and other metals*. Electrician series. The D. Van Nostrand company, 1892.

[57] D. C. Jiles. Review of magnetic methods for nondestructive evaluation. *NDT International*, 21(5):311–319, 1988. cited By (since 1996) 108.

[58] G. Bida and A. Nichipuruk. Coercive force measurements in nondestructive testing. *Russian Journal of Nondestructive Testing*, 36:707–727, 2000.

[59] G. S. Korzunin, V. K. Chistyakov, F. F. Rimshev, and V. M. Shevnin. Developing techniques for testing magnetic properties of electric steels. iii. apparatus for sheet steel (review article). *Russian Journal of Nondestructive Testing*, 37:397–421, 2001.

[60] S.E. Zirka, Y.I. Moroz, P. Marketos, and A.J. Moses. Loss separation in nonoriented electrical steels. *IEEE Transactions on Magnetics*, 46(2):286 –289, 2010.

[61] A.E. Clark, M. Wun-Fogle, J.B. Restorff, T.A. Lograsso, and J.R. Cullen. Effect of quenching on the magnetostriction on $Fe_{1-x}Ga_{\ x}$ (0.13<x <0.21). *Magnetics, IEEE Transactions on*, 37(4):2678 –2680, 2001.

[62] A. E. Clark, J. B. Restorff, M. WunFogle, D. Wu, and T. A. Lograsso. Temperature dependence of the magnetostriction and magnetoelastic coupling in $Fe_{100-x}Al_x$ (x = 14.1, 16.6, 21.5, 26.3) and $Fe_{50}Co_{50}$. *Journal of Applied Physics*, 103(7):310, 2008.

[63] A. E. Clark, J. B. Restorff, M. Wun-Fogle, T.A. Lograsso, and D.L. Schlagel. Magnetostrictive properties of body-centered cubic Fe-Ga and Fe-Ga-Al alloys. *Magnetics, IEEE Transactions*, 36(5):3238 –3240, 2000.

[64] P. Oser. Ein hysteresograph zur charakterisierung weichmagnetischer materialien. Master's thesis, Der Technischen Universitt Wien, 2008.

[65] B. D. Cullity and C. G. Graham. *Introduction to magnetic materials*. IEEE Press Wiley, 1972.

[66] R. S. Turtelli, J. P. Sinnecker, A. P. Madrigal, R. Grössinger, I. Skorvnek, T. Krenicky, and E. Estevez-Rams. An unusual temperature dependence of the coercive field in the melt-spun $Fe_{80-x}\ Si_{20}Nb_x$ (x = 12 , 20). *Fuel and Energy*, 304, 2006.

[67] A. Zhukov, M. Vzquez, J. Velzquez, C. Garca, R. Valenzuela, and B. Ponomarev. Frequency dependence of coercivity in rapidly quenched amorphous materials. *Materials Science and Engineering: A*, 226-228:753 – 756, 1997.

[68] K. Y. Mulyukov, S. B. Khaphizov, and R. Z. Valiev. Grain boundaries and saturation magnetization in submicron grained nickel. *phys. stat. sol. (a)*, 133:447–454, 1992.

[69] V. V. Stolyarov, Ch. Sh Salimgareev, R. Z. Valiev, J. Kloda?, and K. Chrst. High coercive state in submicrograined highly deformed fe-cr-co alloy. *physica status solidi (a)*, 129(2):529–537, 1992.

[70] K. Y. Mulyukov, G. F. Korznikova, and R. F. Valiev. Microstructure and magnetic properties of submicron grained cobalt after large plastic deformation and their variation during annealing. *physica status solidi (a)*, 125(2):609–614, 1991.

[71] A. J. Otter. Annealing cycles for magnet steel and variation in b-h characteristics. *Tri-University Meson Facility, Design Note n TRI-DN-69-3, University of British Columbia Vancouver*, 1969.

[72] R. Grössinger, R. S. Turtelli, N. Mehmood, S. Heiss, H. Müller, and C. Bormio-Nunes. Giant magnetostriction in rapidly quenched Fe-Ga? *Journal of Magnetism and Magnetic Materials*, 320(20):2457–2465, 2008.

[73] R. Laxmanan V. Das S. Chang, C. bye. Texture and magnetic properties of rapidly quenched fe-6.5wtribbon. *IEEE Transactions on Magnetics*, 20:553–558, 1984.

[74] Y. Feng, Y. F. Liang, Y. L. Wang, J. P. Lin, and G. L. Chen. Fe-6.5wt.%Si High Silicon Steel Sheets Produced by Cold Rolling. *Materials Science Forum*, 638 - 642:1428–1433, 2010.

[75] G. Bertotti and M. Pasquale. Physical interpretation of induction and frequency dependence of power losses in soft magnetic materials. *IEEE Transactions on Magnetics*, 28(5):2787 –2789, 1992.

[76] G. Herzer and H. R. Hilzinger. Recent developments in soft magnetic materials. *Physica Scripta*, T24:22–28, 1988.

[77] M. Pasquale, C.P. Sasso, M. Velluto, and S.H. Lim. Stress sensing with Co based ferrite composites. *Journal of Magnetism and Magnetic Materials*, 242-245:1460 – 1463, 2002.

[78] R. Groessinger, N. Mehboob, M. Kriegisch, A. Bachmaier, and R. Pippan. Frequency dependence of the coercivity of soft magnetic materials. *IEEE Transactions on Magnetics*, 48(4):1473 –1476, april 2012.

[79] A. H. Qureshi and L. N. Chaudhary. Influence of plastic deformation on coercive field and initial susceptibility of Fe-3.25% Si alloys. *Journal of Applied Physics*, 41(3):1042–1043, 1970.

[80] M. Pasnak and R. H. Lundsten. Effects of high temperature on magnetic properties of core materials. *Journal of Applied Physics*, 30(4):S107–S108, 1959.

[81] A. A. Sattar, H. M. El-Sayed, and W. R. Agami. Physical and magnetic properties of calcium-substituted Li-Zn ferrite. *Journal of Materials Engineering and Performance*, 16:573–577, 2007.

[82] V. Permiakov, L. Dupr, Alexandre Pulnikov, and Jan Melkebeek. Loss separation and parameters for hysteresis modelling under compressive and tensile stresses. *Journal of Magnetism and Magnetic Materials*, 272-276:E553–E554, 2004.

[83] S. E. Zirka, Y. I. Moroz, P. Marketos, and A. J. Moses. Evolution of the loss components in ferromagnetic laminations with induction level and frequency. *Journal of Magnetism and Magnetic Materials*, 320(20):e1039 – e1043, 2008.

[84] J. R. Davis, editor. *Nickel, Cobalt, and their alloys.* ASM International., 2000.

[85] A. E. Clark, M. Wun-Fogle, J. B. Restorff, and T. A. Lograsso. Magnetostrictive properties of galfenol alloys under compressive stress. *Materials Transactions*, 43(5):881–886, 2002.

[86] S. Pascarelli, M. P. Ruffoni, R. Sato Turtelli, F. Kubel, and R. Grössinger. Local structure in magnetostrictive melt-spun $Fe_{80}Ga_{20}$ alloys. *Phys. Rev. B*, 77:184406, May 2008.

[87] J. R. Cullen, A. E. Clark, M. Wun-Fogle, J. B. Restorff, and T. A Lograsso. Magnetoelasticity of FeGa and FeAl alloys. *Journal of Magnetism and Magnetic Materials*, 226-230, (Part 1):948–949, 2001. Proceedings of the International Conference on Magnetism.

[88] D. Martín Rodríguez, F. Plazaola, J.S. Garitaonandia, and G.J. Cuello. Structural study of the re-entrant spin-glass behaviour of feal alloys. *Journal of Magnetism and Magnetic Materials*, 316(2):e488 – e491, 2007. Proceedings of the Joint European Magnetic Symposia.

[89] O. Ikeda, R. Kainuma, I. Ohnuma, K. Fukamichi, and K. Ishida. Phase equilibria and stability of ordered b.c.c. phases in the Fe-rich portion of the FeGa system. *Journal of Alloys and Compounds*, 347(12):198 – 205, 2002.

[90] N. Mehmood, R. Sato Turtelli, R. Grssinger, and M. Kriegisch. Magnetostriction of polycrystalline $Fe_{100-x}Al_x$ (x=15, 19, 25). *Journal of Magnetism and Magnetic Materials*, 322(912):1609 – 1612, 2010. Proceedings of the Joint European Magnetic Symposia.

[91] J. E. Noakes, H. Sato, and Anthony Arrott. Measurements of pressure dependence of magnetic moment in iron-aluminum alloys. *Journal of Applied Physics*, 42(4):1608–1609, 1971.

[92] G. C. Jain, B. K. Das, R. S. Khanduja, and S. C. Gupta. Effect of intragranular porosity of initial permeability and coercive force in a manganese zinc ferrite. *Journal of Materials Science*, 11:1335–1338, 1976.

[93] M. Kriegisch, R. Groessinger, N. Mehboob, F. Kubel, and R. Sato Turtelli. Hysteresis measurements of high magnetostrictive Fe-Ga. submitted.

[94] J. B. Restorff, M. Wun-Fogle, A. E. Clark, and K. B. Hathaway. Induced magnetic anisotropy in stress-annealed galfenol alloys. *IEEE Transactions on Magnetics*, 42(10):3087 –3089, oct. 2006.

[95] P. Clayton. Tribological aspects of wheel-rail contact: a review of recent experimental research. *Wear*, 191(12):170 – 183, 1996. 4th International Conference on Contact Mechanics and Wear of Rail-Wheel Systems.

[96] L. Deters and M. Proksch. Friction and wear testing of rail and wheel material. *Wear*, 258(78):981 – 991, 2005. Contact Mechanics and Wear of Rail/Wheel Systems.

[97] S. Zakharov, I. Komarovsky, and I. Zharov. Wheel flange/rail head wear simulation. *Wear*, 215(12):18 – 24, 1998.

[98] K. Aniolek J. Herian. The structure and properties of steel with different pearlite morphology and its resistance to abrasive wear. *International Scientific Journal*, 31:83–86, 2008.

[99] D. O. Thompson. *Review of Progress in Quantitative Nondestructive Evaluation*. Springer, 1993.

[100] G. T. Park, S. U. Koh, H. Gyo Jung, and K. Y. Kim. Effect of microstructure on the hydrogen trapping efficiency and hydrogen induced cracking of linepipe steel. *Corrosion Science*, 50(7):1865 – 1871, 2008.

[101] R. Grössinger, F. Keplinger, N. Mehmood, J.H. Espina-Hernandez, J. Araujo, C. Eisenmenger, K. Poppenberger, and J.M. Hallen. Magnetic and microstructural investigations of pipeline steels. *IEEE Transactions on Magnetics*, 44(11):3277 – 3280, 2008.

[102] H. Shokrollahi and K. Janghorban. Soft magnetic composite materials (SMCs). *Journal of Materials Processing Technology*, 189(13):1 – 12, 2007.

[103] B. Weglinski. Soft Magnetic Powder Composites-Dielectromagnetics and Magnetodielectrics. *Reviews on Powder Metallurgy and Physical Ceramics*, 4(2):79–154, 1990.

List of Publications

1. S. Scheriau, M.Kriegisch, S. Kleber, **N. Mehboob**, R.Grssinger, R. Pippan. Magnetic characteristics of HPT deformed soft-magnetic materials, *Journal of Magnetism and Magnetic Materials*, 322:2984-2988, 2010.

2. **N. Mehboob**, M. Rotter, M. Doerr, E. Royaniana, H. Mller, A. Grytsiv, Y. Skourski, Thermal expansion and magnetostriction of $GdAg_2$, and relations to the magnetoelastic paradox, *Solid State Communications*, 151:1112-1116, 2011.

3. R. Groessinger, **N. Mehboob**, M. Kriegisch, A. Bachmaier, and R. Pippan, 3. Frequency Dependence of the Coercivity of Soft Magnetic Materials, *IEEE Transactions on magnetics*, 48(4):1473-1476, 2012.

4. R. Grssinger, **Nasir Mehboob**, D. Suess, R. Sato Turtelli, An eddy current model describing the frequency dependence of the coercivity of polycrystalline Galfenol, *IEEE Transactions on magnetics*, (accepted) 2012.

5. R. Groessinger, M. haas, E. bauer, **N. Mehboob**, M. katter, M. Dahlgren, Magnetocaloric Properties and Thermal Conductivity of Gd, LaFeCoSi and LaFeSiH, *Thermag V*, (accepted) 2012.

6. M.Kriegisch, R.Groessinger, **N.Mehboob**, F.Kubel,R.Sato Turtelli, Hysteresis measurements of SPD treated high magnetostrictive materials Journal of Applied Physics, (submitted) 2012.

7. P. Fulmek, **N. Mehboob**, P. Haumer, M. Kriegisch, R. Grssinger, Magnetic characterisation of industrial high strength steel *Soft Magnetic Material Conference (SMM19)* 2009.

8. **N. Mehboob**, R. Groessinger, P. Oser, M. Kriegisch, P. Fulmek, I. Tomas, Temperature dependent measurements of hysteresis properties of soft magnetic materials, *Soft Magnetic Material Conference (SMM19)* ID 12-G, 2009.

9. R. Grssinger, N. Mehboob, M. Kriegisch, R.Sato Turtelli, Hysteresis measurements of SPD-treated Fe- Al, *Soft Magnetic Material Conference (SMM20)*, S05-P274, 2010.

10. R. Grssinger, **N. Mehboob**, M. Kriegisch, F. Kubel, A. Bachmaier, , R. Pippan. M. Zehetbauer, Soft Magnetic and Magnetostrictive properties of SPD nanomaterials, *Soft Magnetic Material Conference (SMM20)*, 2010.

11. R. Grssinger, N. Mehboob, M. Kriegisch, F. Kubel, A. Bachmaier, R. Schfer, R. Pippan, (Invited Paper 2.4011) Magnetic properties of Severely Plastically Deformed Nanomaterials, *4^{th} International Conference on Rapidly Quenched and Metastable Materials (RQ14) Salvador - Brasil*, 2011.

CURRICULUM VITAE

Personal

Name: Nasir Mehboob

Father's Name: Mehboob Alam

Date of Birth: 29-05-70

Nationality: Pakistani

Marital Status: Married

House # 15L-31, Street # 3

Sirsyed Colony, Tipu Road

Rawalpindi, Pakistan

Email; nasir29may@yahoo.com

Phone: +92-51-5501781

Education

Since Sept. 2008: Ph. D research, Institute for Solid State Physics, TU Wien, Austria

Oct. 2007-Aug.2008: Master Thesis

Title: Magnetostriction of $GdAg_2$, $PrFe_4As_{12}$, and $GdVO_3$ measured with a Capacitance Dilatometer.

Supervisor: Dr. Habil Mortin Rotter, Institute for Physical chemistry, University of Vienna, Austria

2001: Master of Science (M. Sc) Physics, Allama Iqbal Open University, Islamabad, Pakistan.

2000: Master of Science (M. Sc) Mathematics, University of Punjab , Lahore, Pakistan.

1992: Bachelor of Science (B. Sc), University of Punjab, Pakistan.

1990: Higher Secondary School Certificate (HSSC), Govt. Asghar Mall College Rawalpindi, Pakistan.

1987: Secondary School Certificate (SSC), F. G Sir Syed School, Rawalpindi, Pakistan.

Employment

July 2001 – Oct. 2006: Lecturer, Sultana Foundation, Islamabad, Pakistan.